

Swept Away

Numerical and Experimental Investigations into Swept Wind Turbine Blades

Fritz, E.K.

DOI

[10.4233/uuid:55415991-053c-4c74-b31a-3db8724bfab7](https://doi.org/10.4233/uuid:55415991-053c-4c74-b31a-3db8724bfab7)

Publication date

2024

Document Version

Final published version

Citation (APA)

Fritz, E. K. (2024). *Swept Away: Numerical and Experimental Investigations into Swept Wind Turbine Blades*. [Dissertation (TU Delft), Delft University of Technology]. <https://doi.org/10.4233/uuid:55415991-053c-4c74-b31a-3db8724bfab7>

Important note

To cite this publication, please use the final published version (if applicable). Please check the document version above.

Copyright

Other than for strictly personal use, it is not permitted to download, forward or distribute the text or part of it, without the consent of the author(s) and/or copyright holder(s), unless the work is under an open content license such as Creative Commons.

Takedown policy

Please contact us and provide details if you believe this document breaches copyrights. We will remove access to the work immediately and investigate your claim.



Swept Away

NUMERICAL AND EXPERIMENTAL INVESTIGATIONS INTO
SWEPT WIND TURBINE BLADES

Erik Fritz



SWEPT AWAY

**NUMERICAL AND EXPERIMENTAL INVESTIGATIONS INTO
SWEPT WIND TURBINE BLADES**

SWEPT AWAY

NUMERICAL AND EXPERIMENTAL INVESTIGATIONS INTO SWEPT WIND TURBINE BLADES

Dissertation

for the purpose of obtaining the degree of doctor
at Delft University of Technology,
by the authority of the Rector Magnificus, Prof.dr.ir. T.H.J.J. van der Hagen,
chair of the Board for Doctorates,
to be defended publicly on Wednesday 6, November 2024 at 17:30 o'clock

by

Erik FRITZ

Master of Science in Energy Engineering,
RWTH Aachen University, Aachen, Germany,
born in Heidelberg, Germany.

This dissertation has been approved by the candidate's promotors

Promotor: Prof. dr. ir. C.J. Simao Ferreira

Promotor: Dr. ir. R. De Breuker

Composition of the doctoral committee:

Rector Magnificus,	chairperson
Prof. dr. ir. C.J. Simao Ferreira,	Technical University of Delft
Dr. ir. R. De Breuker,	Technical University of Delft

Independent members:

Prof. dr. ir. R. Benedictus,	Technical University of Delft
Dr. C. Braud,	École centrale de Nantes, France
Prof. dr. C.L. Bottasso,	Technical University of Munich, Germany
Dr. G.R. Pirrung,	Technical University of Denmark, Denmark
Prof. dr. S.J. Watson,	Technical University of Delft, reserve member

Other member:

Dr. ir. K. Boorsma,	TNO
---------------------	-----

This research was funded with Topsector Energiesubsidie from the Dutch Ministry of Economic Affairs under grant no. TEHE119018.



Keywords: Wind turbine aerodynamics, swept blades, numerical modelling, wind tunnel experiments, field experiments

Printed by: Gildeprint

Front & Back: Illustration of a wind turbine rotor with swept blades

Copyright © 2024 by E. Fritz

ISBN 978-94-6366-897-2

An electronic version of this dissertation is available at

<http://repository.tudelft.nl/>.

CONTENTS

Summary	ix
Samenvatting	xi
I Introduction	1
1 Introduction	3
1.1 Current state of wind energy and wind turbine technology	3
1.2 Theory of blade sweep	4
1.2.1 Aerodynamic effects of blade sweep	5
1.2.2 Structural effect of blade sweep	6
1.3 Research questions	6
1.4 Research methods	7
1.4.1 Numerical modelling	7
1.4.2 Wind tunnel experiments	9
1.4.3 Field experiments	9
1.5 Dissertation outline	10
II Extending blade element momentum theory to swept blades	19
2 Correcting blade element momentum theory for swept blades	21
2.1 Introduction	22
2.2 Methodology	23
2.2.1 Sweep parametrisation.	23
2.2.2 Numerical modelling	23
2.3 Sweep correction model	25
2.3.1 Velocity induced by a semi-infinite helical vortex filament	26
2.3.2 Velocity induced by the additional/missing vortex filament	29
2.3.3 Velocity induced by the bound vortex on itself	30
2.3.4 Implementation of the sweep correction in BEM.	33
2.4 Simulation results.	34
2.4.1 The straight reference case.	34
2.4.2 Varying the sweep parameters	36
2.4.3 Varying the operating conditions	39
2.5 Conclusions.	41
2.A Nomenclature.	42

3	The reference wind tunnel experiment with straight blades	49
3.1	Introduction	50
3.2	Methodology	51
3.2.1	Scaled wind turbine model.	51
3.2.2	Experimental setup and measurement system	54
3.2.3	Deriving blade-level aerodynamics from PIV measurements.	56
3.3	Results	59
3.3.1	Determination of the combined pitch and twist offset	59
3.3.2	Flow fields	60
3.3.3	Blade aerodynamics	60
3.3.4	Lift polar	64
3.4	Conclusions.	64
3.A	Sensitivity to chosen control volume	65
3.B	Nomenclature.	67
4	The wind tunnel experiment with swept blades	75
4.1	Introduction	76
4.2	Methodology	76
4.2.1	Scaled wind turbine model.	76
4.2.2	Experimental setup and measurement system	77
4.2.3	Deriving blade-level aerodynamics from PIV measurements.	80
4.3	Results	81
4.3.1	Determination of the combined pitch and twist offset	81
4.3.2	Flow fields	83
4.3.3	Blade aerodynamics	83
4.3.4	Lift polar	86
4.4	Conclusions.	87
4.A	Nomenclature.	88
5	Validating the BEM correction model for swept blades	93
5.1	Introduction	94
5.2	Methodology	94
5.3	Results	95
5.3.1	Aerodynamic characteristics of the original blade design	95
5.3.2	Combined pitch and twist offset	99
5.3.3	Validation using an inverse BEM approach	101
5.4	Conclusions.	104
5.A	Step-by-step discussion of the impact of blade sweep during the BEM so- lution process.	106
5.B	Nomenclature.	108
III	Towards swept blade tips in the field	111
	The TIADE project	113
6	Optimising the pressure sensor layout on wind turbine airfoils	115
6.1	Introduction	116

6.2	Methodology	117
6.2.1	Selected airfoils and their operating conditions	117
6.2.2	Generating airfoil polars using XFOIL	119
6.2.3	Estimating lift based on a discrete number of pressure sensors	121
6.2.4	Approaches to defining the pressure sensor layout.	122
6.3	Results	125
6.3.1	Cosine spacing.	125
6.3.2	Optimised sensor layout	125
6.3.3	Potential for reducing the number of sensors	129
6.4	Conclusions.	130
6.A	Nomenclature.	131
7	Aeroelastic model validation using field measurements	141
7.1	Introduction	142
7.2	Methodology	143
7.2.1	Experimental setup	143
7.2.2	Data reduction.	145
7.2.3	Numerical modelling	150
7.2.4	Estimation of the angle of attack	150
7.3	Results	152
7.3.1	How representative is a ten-minute average pressure distribution?	152
7.3.2	Model validation based on long-term ten-minute averaged experimental data	154
7.3.3	Model validation based on long-term time-resolved experimental data	158
7.4	Conclusions.	161
7.A	Nomenclature.	162
8	Design of a swept wind turbine blade tip for field experiments	171
8.1	Introduction	172
8.2	Methodology	172
8.2.1	Limitations imposed by the project	172
8.2.2	Numerical modelling	173
8.3	Results	173
8.3.1	Crossflow-corrected versus fully-corrected BEM simulations	174
8.3.2	Application of steady twist compensation	175
8.3.3	Determination of the allowable sweep extent	175
8.3.4	Effect of blade sweep on extreme loads	176
8.3.5	Effect of blade sweep on fatigue loads	179
8.3.6	Effect of blade sweep on energy production	182
8.4	Conclusions.	182
8.A	Nomenclature.	183

IV Conclusion	189
9 Conclusions and future research	191
9.1 Key findings of the conducted research	192
9.2 Recommendations for future research	196
9.2.1 Numerical modelling	196
9.2.2 Experimental testing	196
9.2.3 Swept blade design for state-of-the-art turbines	197
Acknowledgements	201
Curriculum Vitæ	205
List of Publications	207

SUMMARY

In the transition from fossil fuels to renewable energy sources, the advancement and deployment of wind turbine technology plays a crucial role. A notable trend in wind turbine design is the ever-growing rotor size, which entails that wind turbine blades have become very slender and flexible structures.

This increasing flexibility offers an opportunity for tailoring the aeroelastic behaviour of wind turbine blades. One such aeroelastic tailoring technique is blade sweep, defined as a displacement of the blade axis in the rotor plane. Blade sweep couples bending and torsion deformations and can thus be used to passively alleviate loads on the blade.

For the design, optimisation, and certification of wind turbine blades, blade element momentum theory (BEM) remains the aerodynamic simulation method most relied upon. However, BEM-based numerical tools inherently assume a straight blade geometry and, hence, cannot accurately model the additional flow complexities introduced by blade sweep.

This dissertation starts by presenting a newly developed BEM correction model for swept blades. The focus is on accurately modelling the azimuthal displacement of trailed vorticity and the curved bound vortex self-induction while maintaining BEM's streamtube-independent approach and rapid calculation speed. The developed model shows good agreement with mid-fidelity modelling (lifting line simulations), which intrinsically can model the two aforementioned effects of blade sweep.

To validate the BEM correction model for swept blades beyond the comparison with lifting line simulations, two wind tunnel campaigns are conducted, one with straight blades, being thrust-scaled versions of the IEA 15 MW reference wind turbine blades, and one with swept blades. While the former is intended to provide a baseline for the accuracy of numerical modelling, the latter then provides means to assess the impact of blade sweep and how this is captured in low-fidelity numerical simulations. The validation is conducted based on blade-aerodynamic quantities derived from flow fields measured using particle image velocimetry (PIV). It is demonstrated that the application of the BEM correction model improves the match with the experimental data compared to simulations without the correction model being applied.

Furthermore, this dissertation covers three diverse research efforts conducted within the framework of the TIADE project, a field experiment on a full-scale wind turbine. Firstly, a robust approach to optimise the spacing of pressure sensors for aerodynamic measurements on wind turbine airfoils is presented. The approach considers the expected turbine operating conditions and improves the lift prediction accuracy compared to a simpler, cosine sensor spacing over a wide range of angles of attack. Given that two fundamentally different optimisation routines arrive at close-to-identical solutions, it can be concluded that an optimal solution exists for placing pressure sensors around an airfoil to conduct aerodynamic measurements.

Secondly, pressure measurements obtained on the TIADE research wind turbine over multiple months are employed to validate aeroelastic simulations. The validation is performed based on both ten-minute average data and time-resolved data and using both the integrated sectional forces and the underlying pressure distributions. Generally, a reasonably good agreement between simulated and measured data is found. This indicates that BEM-based aeroelastic algorithms are still valid tools to simulate modern, multi-megawatt wind turbines and their slender and flexible blades.

Finally, a design study of a blade with swept tip for the TIADE field experiment and thus under realistic geometric and load restrictions is conducted. Simulations suggest that flapwise fatigue and extreme blade root loads can be reduced. The same holds for the fore-aft and yawing moments at the turbine tower base. Simultaneously, the turbine performance in terms of power output remains unaffected. These results highlight the potential benefits of blade sweep as an alternative tip geometry for modular blades or as a conscious design choice for future generations of blades.

In conclusion, this dissertation contributes to a more accurate understanding and numerical modelling of swept blade aerodynamics. By moving from fundamental analyses all the way to more applied investigations of swept blade tips for a field experiment, the presented research helps pave the way towards swept blades being a valid option in future wind turbine designs.

SAMENVATTING

In de overgang van fossiele brandstoffen naar duurzame energiebronnen speelt de ontwikkeling en inzet van windturbine-technologie een cruciale rol. Een opvallende trend in het ontwerp van windturbines is de steeds groter wordende rotordiameter, waardoor de bladen van windturbines zeer slanke en flexibele constructies zijn geworden.

Deze toenemende flexibiliteit biedt de mogelijkheid om het aero-elastische gedrag van windturbinebladen aan te passen. Een manier om dit te bereiken is door gebruik te maken van gekromde bladen, waarbij de kromming wordt gedefinieerd als een verplaatsing van de bladas in het rotorvlak. Gekromde bladen koppelen buig- en torsievervormingen en kunnen daarom worden gebruikt om de belasting op het blad passief te verlichten.

Voor het ontwerp, de optimalisatie en certificering van windturbinebladen blijft de blade element momentum theory (BEM) de meest gebruikte aerodynamische simulatiemethode. BEM-gebaseerde numerieke algoritmen gaan echter uit van een rechte bladgeometrie. Zij kunnen daarom de extra stromingscomplexiteit die door bladkromming ontstaat niet nauwkeurig modelleren.

Dit proefschrift begint met de presentatie van een nieuw ontwikkeld BEM-correctiemodel voor gekromde bladen. De focus ligt op het nauwkeurig modelleren van de azimuthale verplaatsing van getrokken wervelingen en de zelfinductie van gekromde gebonden wervelingen met behoud van BEM's stroombuis-onafhankelijke benadering en snelle rekensnelheid. Het ontwikkelde model toont goede overeenkomst met mid-fidelity modellering (hijlslijnsimulaties), die intrinsiek de twee bovengenoemde effecten van gekromde bladen kan modelleren.

Om het BEM-correctiemodel voor gekromde bladen verder te valideren dan alleen door vergelijking met hijlslijnsimulaties, worden twee windtunnelcampagnes uitgevoerd. De eerste campagne gebruikt rechte bladen, die stuwkracht-geschaalde versies zijn van de referentiebladen van de IEA 15 MW-windturbine. De tweede campagne richt zich op gekromde bladen. De eerste is bedoeld om een referentie te bieden voor de nauwkeurigheid van numerieke modellering, waar de tweede de mogelijkheid biedt om de impact van bladkromming te beoordelen en hoe nauwkeurig dit wordt weergegeven in low-fidelity numerieke simulaties. De validatie wordt uitgevoerd op basis van blad-aerodynamische grootheden afgeleid van stromingsvelden gemeten met particle image velocimetry (PIV). Dit onderzoek toont aan dat de toepassing van het BEM-correctiemodel de overeenkomst met de experimentele data verbetert ten opzichte van simulaties zonder toepassing van het correctiemodel.

Verder behandelt dit proefschrift drie verschillende onderzoeksactiviteiten die zijn uitgevoerd in het kader van het TIADE project, een veldexperiment op een windturbine op ware grootte. Allereerst wordt een robuuste benadering gepresenteerd voor het optimaliseren van de plaatsing van druksensoren voor aerodynamische metingen op windturbineprofielen. De aanpak houdt rekening met de verwachte operationele condities

van de turbine en verhoogt de nauwkeurigheid van de liftvoorspelling over een breed scala aan invalshoeken, in vergelijking met een eenvoudigere sensorplaatsing volgens een cosinusverdeling. Aangezien twee fundamenteel verschillende optimaliseringsroutines tot bijna identieke oplossingen leiden, kan worden geconcludeerd dat er een optimale oplossing bestaat voor het plaatsen van druksensoren rond een aerodynamisch profiel.

Ten tweede worden drukmetingen aan de TIADE onderzoekswindturbine gedurende meerdere maanden gebruikt om aero-elastische simulaties te valideren. De validatie wordt uitgevoerd op basis van zowel tien minuten statistieken en tijdreeksen en met gebruik van zowel de geïntegreerde sectionele krachten als de onderliggende drukverdelingen. Over het algemeen wordt een redelijk goede overeenkomst gevonden tussen de gesimuleerde en gemeten gegevens. Dit geeft aan dat op BEM gebaseerde aero-elastische algoritmen nog steeds valide zijn om moderne multi-megawatt windturbines en hun slanke en flexibele bladen te simuleren.

Tot slot wordt een ontwerpstudie uitgevoerd voor een blad met gekromde tip. Deze wordt ontworpen voor het TIADE veldexperiment, daarom wordt rekening gehouden met realistische geometrische restricties en belastingsbeperkingen. Simulaties suggereren dat extreme en vermoeiingsbelastingen aan de bladwortel in klaprichting verminderd kunnen worden. Hetzelfde geldt voor de voor-achter- en giermomenten aan de basis van de turbinetoren. Tegelijkertijd blijven de prestatie van de turbine in termen van vermogen onaangetast. Deze resultaten benadrukken de potentiële voordelen van bladkromming als een alternatieve tipgeometrie voor modulaire bladen of als een bewuste ontwerpkeuze voor toekomstige generaties bladen.

Concluderend kan gesteld worden dat dit proefschrift bijdraagt aan een nauwkeuiger begrip en numerieke modellering van de aerodynamica van gekromde bladen. Door van fundamentele analyses helemaal over te gaan naar meer toegepaste onderzoeken van gekromde bladtips voor een veldexperiment, helpt het gepresenteerde onderzoek een weg te banen voor gekromde bladen als een mogelijke ontwerpkeuze voor toekomstige windturbines.



I

INTRODUCTION



1

INTRODUCTION

1.1. CURRENT STATE OF WIND ENERGY AND WIND TURBINE TECHNOLOGY

Global warming is arguably the largest challenge our generation faces. In striving to become a sustainable society, a transition from fossil fuels to renewable energy sources is inevitable. Wind energy, and thus wind turbines, are a key technology in this transition. The technology's importance is reflected in the extent to which it has penetrated the global and particularly the European energy market. At the end of 2022, a total capacity of 906 GW was installed globally [1].

Europe alone accounts for 255 GW of installed wind energy capacity, of which 225 GW are installed onshore and 30 GW offshore [2]. A big milestone was reached in 2023 when wind surpassed natural gas for the first time in terms of annual energy production. Contributing 18 % to the EU's electricity generation, wind energy ranks second only behind nuclear power generation [3]. In their central scenario, WindEurope predicts Europe's installed wind capacity to grow to 323 GW [4] by 2030, showcasing that the development of wind energy is far from its end.

Alongside the growth in installation, wind turbines have also undergone physical growth while the technology matured. The first generation of electricity-producing wind turbines, built around the turn of the 19th century, had a diameter in the range of 10 – 25 m and a power rating of approximately 10 – 20 kW [5]. In the 1970s, motivated by the oil crisis, wind turbine technology received a surge of attention, leading to the development of prototype rotors in the megawatt range with diameters of approximately 50 – 100 m. Many of these prototypes were ill-fated, and commercially built wind turbines actually grew at a slower pace [6]. It should also be noted that during this time, no consensus had yet been reached on the turbine design, so some prototypes still featured downwind designs and/or two blades. Nowadays, the wind turbine industry has converged to three blades and an upwind design, referred to as the Danish concept [7].

In 2022, the average power rating for newly installed onshore turbines was 4.1 MW and for offshore turbines 8.0 MW [2]. However, the latest generation of offshore wind



turbines has reached power ratings in the 15 MW range and rotor diameters of 240 m [8], making them the largest rotating machines in the world. A visual representation of this turbine growth is given in Figure 1.1.

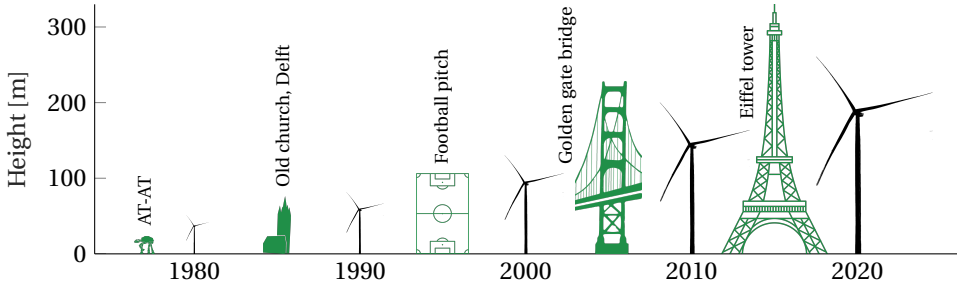


Figure 1.1: Historical development of the size of commercially produced wind turbines

As a consequence of this growth, wind turbine blades have become extremely slender and flexible structures, which poses both challenges and opportunities. Compared to older blades, which were shorter and stiffer, the interaction of aerodynamic forces and the blade's structural response gains importance. This necessitates detailed aeroelastic stability analyses to detect and avoid phenomena such as flutter occurring in modern wind turbine blade designs [9].

An opportunity of modern wind turbine blades' flexibility lies in the fact that their aeroelastic behaviour can be tailored [10]. One such aeroelastic tailoring technique is blade sweep, which couples bending and torsion deformations. This mechanism of bend-twist coupling has the potential to reduce both ultimate and fatigue loads and, consequently, to increase the longevity of wind turbine blades. Additionally, the reduced blade loading opens up the opportunity of building lighter blades, which in turn, means reduced manufacturing costs. The theory behind blade sweep is explained in more detail in the next section.

1.2. THEORY OF BLADE SWEEP

Blade sweep was first introduced in the context of wind turbines by Liebst [11]. It is defined as a displacement of the blade axis in the rotor plane as schematically depicted in Figure 1.2. While displacing the blade axis in the direction of rotation is referred to as forward sweep, a displacement against the direction of rotation is called backward or aft sweep.



Figure 1.2: Schematic representation of a blade with aft sweep

1.2.1. AERODYNAMIC EFFECTS OF BLADE SWEEP

In the context of this thesis, three aerodynamic effects of blade sweep are discussed, which are presented schematically in Figure 1.3.

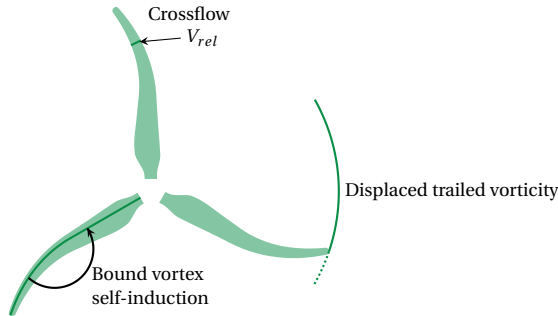


Figure 1.3: Schematic representation of the sweep-induced changes in blade aerodynamics

One major change in blade aerodynamics due to blade sweep is known as *crossflow principle*. For a straight blade, the local inflow velocity V is approximately perpendicular to the blade axis. However, if blade sweep is applied, this velocity is oriented at an angle that is a function of the global sweep angle ζ and the local sweep angle Λ , see Figure 1.4.

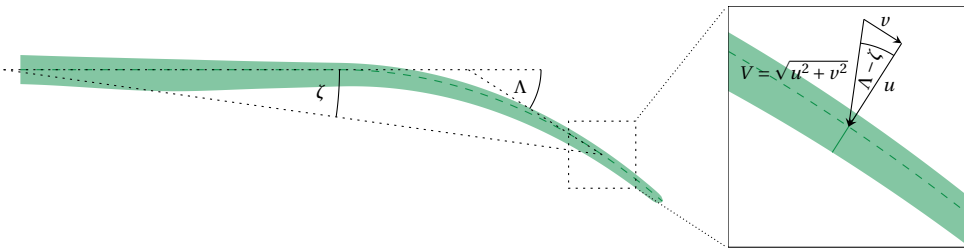


Figure 1.4: Schematic of the crossflow principle

Considering the flow component $v = V \sin(\Lambda - \zeta)$, which is aligned with the local blade axis, equally large on the pressure and suction side of the airfoil, it has a negligible influence on the pressure forces. The local forces – lift, pressure drag and pitching moment – are then a function of the velocity component perpendicular to the local blade axis $u = V \cos(\Lambda - \zeta)$. The angle of attack α as measured in the direction of u increases when compared to the angle of attack measured in alignment with V by $1/\cos(\Lambda - \zeta)$. Considering a constant lift slope $\partial c_l/\partial \alpha$, the local lift force per unit blade length $L = \frac{1}{2} \rho u^2 c c_l$ becomes proportional to $\cos(\Lambda - \zeta)$. The same is true for the drag force and the pitching moment. At the same time, the infinitesimal blade length exceeds the corresponding infinitesimal radial length in the swept part of the blade by a factor of $1/\cos(\Lambda - \zeta)$. Therefore, the absolute blade forces, i.e. the sectional forces multiplied by the blade length, would be identical between straight and swept blades if not for further changes to the blade aerodynamics.



The relevance of two angles Λ and ζ is a small but important distinction from aircraft aerodynamics. Here, only the local sweep angle Λ needs to be considered due to the generally straight flight of aircraft [12].

While the occurrence of crossflow is a well-known effect of blade sweep, the displacement of the trailed vorticity and the self-induction of the curved bound vortex have been discussed far less. An essential part of the research presented in this dissertation deals with the appropriate numerical modelling of these two effects and their integration into existing low-fidelity algorithms.

1.2.2. STRUCTURAL EFFECT OF BLADE SWEEP

From a structural viewpoint, blade sweep couples bending and torsional deformations [13]. In operation, a section of a wind turbine blade experiences forces perpendicular and aligned with its chord line, F_x and F_y , respectively. These forces act at the aerodynamic centre, generally assumed to be at the quarter chord location [7]. In conventional blade designs, the aerodynamic centre is sought to be close to the shear centre, which is defined as the location where an acting force will not induce a torsional deformation of the blade's regarded section. By sweeping the blade, the blade section, and thus its aerodynamic centre, is placed at a distance from its shear centre. As a consequence, the acting forces do not only entail flapwise and edgewise deformations but also a torsional deformation. This principle of bend-twist coupling is visualised in Figure 1.5.

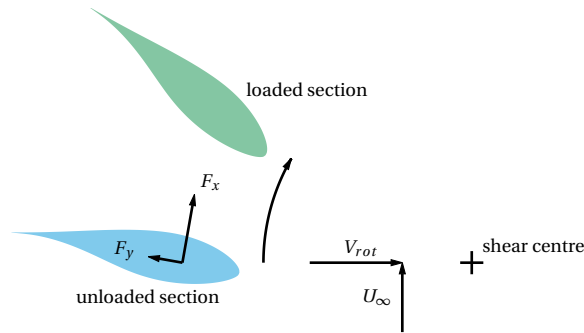


Figure 1.5: Schematic of the bend-twist coupling principle of swept blades, adapted from Larwood and Zuteck [13]

When sweeping a blade forward, the sweep-induced torsion twists the cross-section to higher angles of attack. As long as the regarded cross-section is acting in the linear part of the lift curve, this increase in angle of attack is equivalent to higher loads. In contrast to that, aft sweep enforces a torsion to lower angles of attack, also referred to as twist to feather. In the linear region of the lift curve, this corresponds to lower loads on the blade section.

1.3. RESEARCH QUESTIONS

Blade sweep is not a completely novel concept in the field of wind turbine technology. However, the complete lack of commercial wind turbines equipped with swept blades,

demonstrates that this concept has not reached market maturity. This can be attributed in part to remaining uncertainties regarding the additional complexity in blade-level aerodynamics. Fundamental research in the area of low-fidelity numerical modelling and wind tunnel experiments offers an opportunity to increase the understanding of swept blade aerodynamics and build a solid base on which design choices for novel, swept wind turbine blades can be made. In light of this, Part II of this thesis aims to answer the research questions

1. How does blade sweep influence the aerodynamics of wind turbine blades?
2. How can swept blade aerodynamics be modelled more accurately with low-fidelity simulation tools?

On the path of demonstrating the added value of swept blade tips, another challenge is posed. There are concerns about whether commonly used low-fidelity numerical tools can still be applied to simulate the aerodynamics and aeroelasticity of modern, multi-megawatt wind turbines. Field experiments offer a unique opportunity for conducting validation studies of such simulation methods. Once the tools' validity is ensured, reliable investigations into novel design concepts, such as blade sweep, can be conducted. Therefore, Part III of this thesis aims to answer the research questions

3. How can field data be used for model validation beyond average integral values?¹
4. Can a blade's aeroelastic performance be tailored through a swept tip design?

1.4. RESEARCH METHODS

To answer these questions, the research performed in the context of this dissertation is built on three pillars introduced in the following sections: Numerical modelling, wind tunnel experiments and field experiments.

1.4.1. NUMERICAL MODELLING

Various numerical models exist to simulate the aerodynamics of wind turbines. These models differ considerably in their fidelity to the flow physics of a real wind turbine, which they aim to replicate. Similarly, they show a wide variety of computational effort required for simulations. Therefore, some models are more suited for the detailed analysis of a single flow case to investigate very specific aerodynamic phenomena, while others are more suited for the evaluation of the turbine's performance over a wide range of operating conditions. When applying blade sweep, the advanced blade geometry introduces additional complexity of flow physics, which needs to be understood and correctly modelled.

BLADE ELEMENT MOMENTUM THEORY

Blade element momentum theory (BEM) was first developed by Glauert in 1935 [15]. Despite being the lowest fidelity tool discussed in this section, BEM is crucial in the design and certification process of modern wind turbines and is used throughout the industry [16]. Its rapid calculation speed makes it the only tool suitable to run the many

¹Research question 3 is directly inspired by the work of van Kuik et al. [14]



loadcases a wind turbine will experience throughout its lifetime. BEM couples the one-dimensional momentum theory of flow passing through an actuator disc with the local forces acting on the wind turbine blade. The standard equations used in BEM algorithms are given in many textbooks on rotor aerodynamics, see e.g. [17, 7, 18]. Many implementations exist in which BEM algorithms are coupled to structural solvers [19, 20, 21, 22]. Such aeroelastic simulation tools solve the aerodynamic loading and structural response iteratively until convergence is reached.

It should be noted that BEM was originally developed for much shorter, stiffer blades than the state-of-the-art. With increasing turbine size, the ability of such low-fidelity tools to predict the aeroelastic performance of modern, flexible wind turbine blades needs to be continuously re-evaluated. Additionally, BEM algorithms, in their basic implementation, assume a straight blade shape. Thus, physical inaccuracies are inevitable when simulating swept wind turbine blades with currently available BEM tools.

In this dissertation, ...

BEM simulations play a central role. In Part II, a BEM correction model is developed and validated that extends BEM towards swept blade geometries by more accurately modelling the sweep-induced changes to wind turbine blade aerodynamics. In Part III, simulation results from a BEM algorithm coupled to a structural solver are compared to measurements from a field experiment to assess the code's accuracy. Additional simulations are run to predict the changes in performance and loads when sweeping the tip of a blade.

VORTICITY-BASED METHODS

Vorticity-based methods represent a lifting body and the surrounding flow-field through a combination of basic vortex elements, for which analytical flow solutions exist, in a Lagrangian reference frame. These methods can be applied both in two-dimensional and three-dimensional space. Multiple variations exist which differ in their representation of the lifting body. The two most commonly used vorticity-based algorithms are lifting line and panel methods. While lifting line algorithms generally discretise the lifting body using multiple connected vortex filaments, panel methods discretise the lifting body's surface using the name-giving panels. In both methods, the wake of the lifting body is represented by a combination of trailed and shed vortex filaments. For a detailed description of vorticity-based methods, the reader is referred to dedicated textbooks, such as [23, 24].

When simulating swept blades, vorticity-based methods have the advantage of modelling the geometry of the blades and wake. Therefore, advanced geometries such as sweep can be represented fairly accurately. To exploit this geometric representation as well as the computational efficiency of BEM, researchers at the Danish University of Technology (DTU) have developed the so-called near wake model, which couples a lifting-line-based near wake solver with a BEM-based far wake formulation [25, 26]. This model was recently adapted and used to study the aerodynamics of swept wind turbine blades [27, 28, 29].

In this dissertation, ...

Lifting line simulations are used to validate the BEM correction model for swept blades. Results from a panel code are used to verify post-processing methods employed in the wind tunnel data analysis. Additionally, 2D panel code simulations are run to obtain airfoil-level aerodynamic solutions used in Part III.

1.4.2. WIND TUNNEL EXPERIMENTS

Wind tunnel experiments are a standard practice in the wind energy community to investigate aerodynamic, aeroelastic and acoustic characteristics of wind turbine and airfoil models [30]. Since such experiments are conducted in controlled and repeatable conditions, the uncertainties are – in most cases – manageable. This allows studying aerodynamic phenomena with a high degree of detail and accuracy. A downside of such experiments lies in the reliance on scaled geometries. When scaling a rotor geometry, it is generally not possible to preserve various similarity parameters, such as geometric similarity, Reynolds number or non-dimensionalised loads, at the same time. Nonetheless, wind tunnel experiments are vital in improving the understanding of wind turbine aerodynamics. Equally important, the gathered data can be used to validate and improve numerical models that aim to simulate reality as closely as possible.

Swept wind turbines have hardly been studied in the wind tunnel, the only exception being a non-rotating swept blade tip tested by Barlas et al. [31]. Here, pressure measurements were obtained at four radial sections and compared to simulations of varying fidelity. Additionally, flow patterns visualised using tufts were compared to surface streamlines simulated using Computational Fluid Dynamics (CFD).

In this dissertation, ...

Results from two wind tunnel experiments on a model HAWT are presented: One with straight blades and one with swept blades equipped. Particle image velocimetry (PIV) is used to gain deeper insight into the flow field around the individual blades. Spanwise distributions of the inflow conditions, circulation and blade loading are derived and used to validate low- to mid-fidelity numerical simulations.

1.4.3. FIELD EXPERIMENTS

Field experiments are extremely valuable in researching wind turbine aerodynamics, simply because they are conducted on the actual subject of interest. Neither the model assumption made for numerical simulations, nor the scaling effects of wind tunnel experiments apply here. At the same time, field experiments are subject to larger uncertainties since they are conducted in uncontrolled conditions. Additionally, the high cost of such full-scale research efforts limits the frequency with which these are performed. The research conducted in this PhD project is part of the TIADE (Turbine Improvements for ADditional Energy) project, which revolves around a field experiment on a 3.8 MW research turbine. This project will be introduced in more detail in Part III.

The only publicly reported field campaign on a turbine with swept blades is the STAR (Sweep Twist Adaptive Rotor) project, run by Sandia National Laboratories and Knight & Carver in 2007 – 2009 [32]. In this project, a sub-megawatt wind turbine was equipped



with swept blades and produced 10 – 12 % more energy than the straight baseline configuration while maintaining the baseline’s flapwise blade root load envelope [33]. Recently, Barlas et al. [34] tested a swept blade tip mounted on a one-armed rotor test rig. Field measurements were compared against multi-fidelity numerical simulations and showed good agreement.

In this dissertation, ...

Pressure measurements from the TIADE field experiment are used to evaluate the accuracy of aerodynamic and aeroelastic simulations of a modern multi-megawatt wind turbine. Furthermore, this field campaign defines the design space limits for a numerical study of potential swept tip geometries.

1.5. DISSERTATION OUTLINE

The remainder of this thesis is subdivided into three parts. Part II deals with extending the capability of low-fidelity numerical modelling, namely BEM algorithms, to swept blades. The numerical developments are validated using wind tunnel experimental data.

- **Chapter 2** proposes a new numerical correction model to blade element momentum theory. The model corrects the axial induction factor for two purely aerodynamic effects of blade sweep, which are not included in the basic form of BEM. These effects are the changes in induction due to the displaced trailed vorticity and due to the curved bound vortex’s induction on itself. This correction model retains BEM’s streamtube-independent approach, is easy to implement and requires very little additional computational effort. With this extension, the aerodynamic algorithms most relied on in industrial wind turbine blade design can more accurately account for blade sweep.
- **Chapter 3** presents a wind tunnel experimental analysis of a scaled model of the IEA 15 MW RWT. The experimental dataset consists of flow fields in the direct vicinity of the blade measured using PIV. Flow fields, as well as the derived distributions of blade-level aerodynamic quantities, were previously unavailable for scaled versions of the IEA 15 MW RWT and can be used for numeric model validation. Additionally, the results serve as reference case for the following chapter.
- **Chapter 4** builds upon the experiment presented in the previous chapter. Instead of the original straight blades, swept blades are tested and, again, flow fields are measured using PIV. The experiment yields a unique aerodynamic dataset for swept, rotating wind turbine blades, which can be used twofold: To study the effect of sweep on the blade’s aerodynamics and to validate numerical simulations.
- **Chapter 5** utilises results from Chapters 2 - 4. The experimental results obtained in the two wind tunnel campaigns are used to validate numerical simulations based on blade element momentum theory. The straight-bladed experimental data enables the creation of a baseline regarding numerical accuracy. Then, the data from the swept blade experiment is used to validate the sweep correction model presented in Chapter 2.

Part III concerns the generation of high-quality field data and their use in validating low-fidelity numerical simulations. Finally, the validated tool is used to explore the design possibilities of a swept wind turbine tip for field experiments.

- **Chapter 6** presents a novel approach to optimise the layout of pressure sensors on wind turbine airfoils. It is demonstrated that the accuracy in lift estimation based on pressure measurements can be increased considerably when optimising the sensor layout. This is particularly valuable in field experiments, where the number of sensors is limited by geometrical and financial restrictions.
- **Chapter 7** evaluates the accuracy of aeroelastic simulations of a multi-megawatt wind turbine by comparing numerical results against data collected in the TIADE field campaign. This field data consists of multiple months of pressure measurements obtained using an optimised sensor layout. The model validation is based on both integrated blade loads and pressure distributions.
- **Chapter 8** elevates the topic of blade sweep from theory and wind tunnel experiments to the application on a full-scale turbine. A numeric design study is conducted aiming at a suitable swept tip design for the multi-megawatt TIADE research turbine. Sweep-induced changes in ultimate and fatigue loads, as well as energy production, are analysed numerically highlighting the potential of swept blades in reducing blade loads while maintaining the turbine's performance.

Part IV concludes this dissertation.

- **Chapter 9** summarises and connects key findings from the previous chapters and relates these to the research questions posed in the present chapter. Finally, suggestions for future research on the topic of swept wind turbine blades are given.

A graphical representation of this dissertation's contents is given on the following two pages.



Extending BEM to swept blades II

*How does blade sweep influence the aerodynamics of wind turbine blades?
How can swept blade aerodynamics be modelled more accurately
with low-fidelity simulation tools?*



Chapter 2

BEM correction model

*Where are the limits of blade element
momentum theory in simulating
swept blades?*

How can they be overcome?

Chapters 3 & 4

Wind tunnel experiments

*Can sweep-induced changes in blade
aerodynamics be determined
experimentally?*

If so, what changes occur?



Chapter 5

Validation BEM correction model

*Can the developed BEM correction
model be validated using the wind
tunnel experimental data?*

*How large is the impact of the
proposed corrections?*



III Towards swept blade tips in the field

*How can field data be used for model validation beyond average integral values?
Can a blade's aeroelastic performance be tailored through a swept tip design?*

Chapter 6

Optimising sensor layout

Can the quality of pressure measurements be improved by optimising the sensor layout?

What implications does this have for experimental setups?

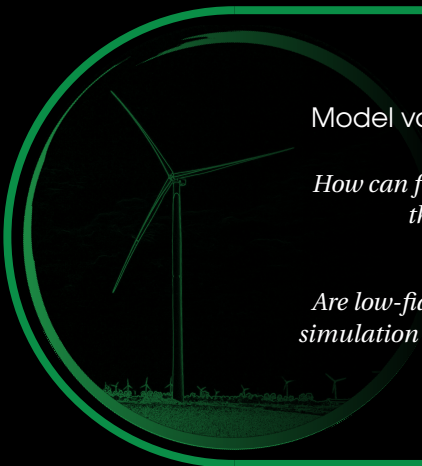


Chapter 7

Model validation using field data

How can field data be used to quantify the accuracy of the numerical simulation results?

Are low-fidelity tools still suited for the simulation of modern, multi-megawatt wind turbines?

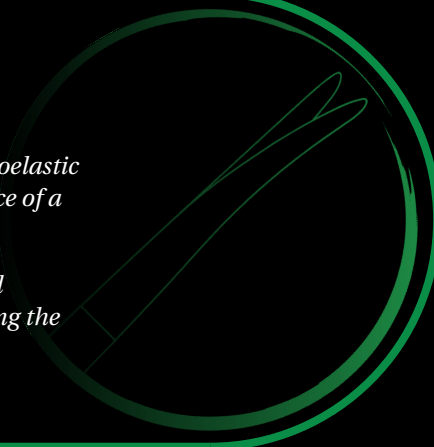


Chapter 8

Swept tip design

How do sweep-induced aeroelastic effects affect the design space of a swept blade tip?

What is the achievable load reduction while maintaining the desired rotor performance?



BIBLIOGRAPHY

- [1] GWEC. *Global Wind Report 2023*. Feb. 2023.
- [2] WindEurope. *Wind energy in Europe: 2022 Statistics and the outlook for 2023-2027*. Feb. 2023.
- [3] Ember. *European Electricity Review 2024*. Feb. 2024.
- [4] WindEurope. *Wind energy in Europe, Scenarios for 2030*. Sept. 2017.
- [5] P. Gipe and E. Möllerström. “An overview of the history of wind turbine development: Part I—The early wind turbines until the 1960s”. In: *Wind Engineering* 46.6 (Dec. 2022). Publisher: SAGE Publications, pp. 1973–2004. ISSN: 0309-524X. DOI: [10.1177/0309524X221117825](https://doi.org/10.1177/0309524X221117825).
- [6] P. Gipe and E. Möllerström. “An overview of the history of wind turbine development: Part II—The 1970s onward”. In: *Wind Engineering* 47.1 (Sept. 2022), pp. 220–248. ISSN: 0309-524X. DOI: [10.1177/0309524X221122594](https://doi.org/10.1177/0309524X221122594).
- [7] M. Hansen. *Aerodynamics of wind turbines*. Sterling, VA: Earthscan, 2008. ISBN: 978-1-84407-438-9.
- [8] VisualCapitalist. *Animation: The World's Biggest Wind Turbines*. June 2022.
- [9] P. Veers et al. “Grand challenges in the science of wind energy”. In: *Science* 366.6464 (Oct. 2019), eaau2027. DOI: [10.1126/science.aau2027](https://doi.org/10.1126/science.aau2027).
- [10] P. S. Veers et al. “Trends in the Design, Manufacture and Evaluation of Wind Turbine Blades”. In: *Wind Energy* 6.3 (2003), pp. 245–259. ISSN: 1099-1824. DOI: [10.1002/we.90](https://doi.org/10.1002/we.90).
- [11] B. S. Liebst. “Wind turbine gust load alleviation utilizing curved blades”. In: *Journal of Propulsion and Power* 2.4 (July 1986), pp. 371–377. DOI: [10.2514/3.22897](https://doi.org/10.2514/3.22897).
- [12] S. F. Hoerner. *Fluid-dynamic lift*. Published by Liselotte A. Hoerner, 1985.
- [13] S. Larwood and M. Zuteck. “Swept wind turbine blade aeroelastic modeling for loads and dynamic behavior”. In: *AWEA Windpower*. AWEA Windpower, Jan. 2006.
- [14] G. A. M. van Kuik et al. “Long-term research challenges in wind energy – a research agenda by the European Academy of Wind Energy”. In: *Wind Energy Science* 1.1 (Feb. 2016), pp. 1–39. ISSN: 2366-7451. DOI: [10.5194/wes-1-1-2016](https://doi.org/10.5194/wes-1-1-2016).
- [15] H. Glauert. “Airplane propellers”. In: *Aerodynamic Theory*. Vol. 4. Berlin: Julius Springer, 1935.
- [16] J. N. Sørensen. *General Momentum Theory for Horizontal Axis Wind Turbines*. Vol. 4. Research Topics in Wind Energy. Cham: Springer International Publishing, 2016. ISBN: 978-3-319-22113-7. DOI: [10.1007/978-3-319-22114-4](https://doi.org/10.1007/978-3-319-22114-4).



- [17] J. G. Leishman. *Principles of helicopter aerodynamics*. 2nd ed. Cambridge aerospace series 18. Cambridge: Cambridge University press, 2006. ISBN: 978-0-521-85860-1.
- [18] T. Burton, D. Sharpe, N. Jenkins, and E. Bossanyi. *Wind Energy Handbook*. John Wiley & Sons, June 2011. ISBN: 978-1-119-99392-6.
- [19] T. J. Larsen and A. M. Hansen. *How 2 HAWC2, the user's manual*. Risø National Laboratory, 2007.
- [20] C. Lindenburg. *PHATAS User's manual version 11737*. Tech. rep. WMC-2016-005. (Confidential). LM Wind Power, 2020.
- [21] J. Jonkman and M. Sprague. *OpenFAST Documentation — OpenFAST v3.5.2 documentation*. Golden, CO, US, 2023.
- [22] DNV. *Bladed Theory Manual v4.15*. 2023.
- [23] J. Katz and A. Plotkin. *Low-speed aerodynamics*. Cambridge University Press, Feb. 2001. ISBN: 978-0-511-81032-9. DOI: [10.1017/cbo9780511810329](https://doi.org/10.1017/cbo9780511810329).
- [24] E. Branlard. *Wind turbine aerodynamics and vorticity-based methods*. Springer International Publishing, 2017. ISBN: 978-3-319-85583-7. DOI: [10.1007/978-3-319-55164-7](https://doi.org/10.1007/978-3-319-55164-7).
- [25] H. A. Madsen and F. Rasmussen. “A near wake model for trailing vorticity compared with the blade element momentum theory”. In: *Wind Energy* 7.4 (2004), pp. 325–341. DOI: [10.1002/we.131](https://doi.org/10.1002/we.131).
- [26] G. R. Pirrung, H. A. Madsen, T. Kim, and J. Heinz. “A coupled near and far wake model for wind turbine aerodynamics”. In: *Wind Energy* 19.11 (Mar. 2016), pp. 2053–2069. DOI: [10.1002/we.1969](https://doi.org/10.1002/we.1969).
- [27] A. Li, G. Pirrung, H. A. Madsen, M. Gaunaa, and F. Zahle. “Fast trailed and bound vorticity modeling of swept wind turbine blades”. In: *Journal of Physics: Conference Series* 1037 (June 2018), p. 062012. DOI: [10.1088/1742-6596/1037/6/062012](https://doi.org/10.1088/1742-6596/1037/6/062012).
- [28] A. Li, M. Gaunaa, G. R. Pirrung, N. Ramos-García, and S. G. Horcas. “The influence of the bound vortex on the aerodynamics of curved wind turbine blades”. In: *Journal of Physics: Conference Series* 1618 (Sept. 2020), p. 052038. DOI: [10.1088/1742-6596/1618/5/052038](https://doi.org/10.1088/1742-6596/1618/5/052038).
- [29] A. Li, G. R. Pirrung, M. Gaunaa, H. A. Madsen, and S. G. Horcas. “A computationally efficient engineering aerodynamic model for swept wind turbine blades”. In: *Wind Energy Science* 7.1 (Aug. 2021), pp. 129–160. DOI: [10.5194/wes-2021-96](https://doi.org/10.5194/wes-2021-96).
- [30] C. L. Bottasso and F. Campagnolo. “Wind Tunnel Testing of Wind Turbines and Farms”. In: *Handbook of Wind Energy Aerodynamics*. Ed. by B. Stoevesandt, G. Schepers, P. Fuglsang, and S. Yuping. Cham: Springer International Publishing, 2021, pp. 1–57. ISBN: 978-3-030-05455-7. DOI: [10.1007/978-3-030-05455-7_54-1](https://doi.org/10.1007/978-3-030-05455-7_54-1).

- [31] T. Barlas, G. R. Pirrung, N. Ramos-García, S. G. Horcas, R. F. Mikkelsen, A. S. Olsen, and M. Gaunaa. “Wind tunnel testing of a swept tip shape and comparison with multi-fidelity aerodynamic simulations”. In: *Wind Energy Science* 6.5 (Oct. 2021), pp. 1311–1324. DOI: [10.5194/wes-6-1311-2021](https://doi.org/10.5194/wes-6-1311-2021).
- [32] T. D. Ashwill. *Sweep-twist adaptive rotor blade : final project report*. Tech. rep. SAND2009-8037. Sandia National Laboratories (SNL), Albuquerque, NM, and Livermore, CA (United States), Feb. 2010. DOI: [10.2172/973353](https://doi.org/10.2172/973353).
- [33] T. Ashwill, G. Kanaby, K. Jackson, and M. Zuteck. “Development of the sweep-twist adaptive rotor (STAR) blade”. In: *48th AIAA aerospace sciences meeting including the new horizons forum and aerospace exposition*. American Institute of Aeronautics and Astronautics, Jan. 2010. DOI: [10.2514/6.2010-1582](https://doi.org/10.2514/6.2010-1582).
- [34] T. Barlas, G. R. Pirrung, N. Ramos-García, S. González Horcas, A. Li, and H. A. Madsen. “Atmospheric rotating rig testing of a swept blade tip and comparison with multi-fidelity aeroelastic simulations”. In: *Wind Energy Science* 7.5 (Oct. 2022), pp. 1957–1973. ISSN: 2366-7443. DOI: [10.5194/wes-7-1957-2022](https://doi.org/10.5194/wes-7-1957-2022).





II

EXTENDING BLADE ELEMENT MOMENTUM THEORY TO SWEEPED BLADES



2

CORRECTING BLADE ELEMENT MOMENTUM THEORY FOR SWEEPED BLADES

To this day, blade element momentum theory (BEM) remains a crucial tool in the design, optimisation and certification process of wind turbines. What separates BEM algorithms from other, higher fidelity simulation tools is the rapid calculation speed, which enables the simulation of millions of load cases that wind turbines will experience during their lifetime. One shortcoming of BEM is that it inherently assumes a straight blade geometry and, therefore, cannot account for the aerodynamic effects of blade sweep.

This chapter introduces an efficient correction model that enables the extension of the blade element momentum method for swept blades. The proposed extension corrects the axial induction regarding two aspects: the azimuthal displacement of the trailed vorticity system and the induction of the curved bound vortex on itself. The proposed model retains the streamtube-independent approach of BEM and adds little computational effort.

Following a brief introduction in Section 2.1, Section 2.2 presents the sweep parametrisation used to generate various swept blade geometries. Furthermore, the numerical tools used in this study, namely the baseline BEM algorithm and the lifting line implementation used for comparison, are discussed. The sweep correction function for BEM is derived in Section 2.3. A comparison between results from lifting line and BEM simulations is shown in Section 2.4, validating the newly developed BEM extension. Finally, conclusions are presented in Section 2.5.

Parts of this chapter have been published in E. Fritz, C. Ferreira, K. Boorsma, *An efficient blade sweep correction model for blade element momentum theory*, *Wind Energy* **25**, 12 (2022).



2.1. INTRODUCTION

To study the benefits of swept blades, several numerical investigations have been performed in the past, ranging from low to high fidelity tools and from purely aerodynamic to aeroelastic. Suzuki et al. [1] used a hybrid Navier-Stokes/Vortex-Panel solver to simulate the NREL Phase VI rotor with aft sweep. The results showed no significant change in power. Kaya et al. [2] employed computational fluid dynamics (CFD) to study the NTNU rotor with various sweep configurations. The power coefficient increased for a forward swept blade while backward sweep led to a decrease in power production due to a lower thrust coefficient. Contrary results were obtained by Chattot [3] using a lifting line code based on the Goldstein model to study the NREL 6 kW rotor where backward sweep resulted in a slight power increase while the forward sweep reduced the rotor power. Picot et al. [4] studied the effect of swept blades on a free-yawing, stall controlled downwind rotor using HAWC2. They show that the bend-twist-coupling delays stall to higher wind speeds, thereby, increasing the rated power. Sessarego et al. [5] used the lifting line module of MIRAS to simulate the NREL 5 MW turbine in complex inflow conditions. Their results indicate that blade sweep can positively affect power and thrust performance of the turbine. Next to increased annual energy production, Larwood et al. [6] report a positive impact of blade sweep on flapwise bending loads. This is in line with a study by Verelst and Larsen [7], who simulated the NREL 5 MW rotor for various sweep configurations using HAWC2. Their study showed that backward sweep can be used to reduce flapwise fatigue and extreme loads. Using the lifting line code AWSM coupled to a structural solver, Grasso et al. [8] show that an aft swept blade oscillates less than a straight reference blade when hit by a gust, indicating the potential for a reduction of fatigue loading.

The studies presented above mainly rely on numerical models of medium and higher fidelity, such as lifting line models, CFD, and hybrid vortex panel/CFD. The computational cost of these methods prohibits their use in the concept design and certification phase of wind turbines, where many design variations and load cases are calculated. In wind turbine applications, such calculations are generally performed using codes based on blade element momentum theory. BEM, however, assumes a straight blade geometry located in the rotor plane and, thus, cannot account for the effect of sweep on the induction. This effect is neglected in the studies presented above [4, 7] where the BEM-based tool HAWC2 is used. In order to further investigate and exploit the benefits of swept wind turbine blades, BEM based tools need to be extended to account for the effects of blade sweep. One such approach is presented by Li et al. [9]. The employed model is based on the near wake model originally adapted for wind turbine applications by Madsen and Rasmussen [10] and further developed by Pirrung et al. [11]. It combines a lifting line representation of the near wake consisting of the first quarter revolution of the wake with a far wake BEM implementation. In their work, Li et al. [9, 12] extend this near wake model to be able to account for swept blade geometries. Contrary to BEM, the near wake model models the coupling of the solutions of multiple streamtubes.

This chapter introduces a novel method to extend BEM so that it can account for the effect of blade sweep. For this purpose, a sweep correction model is derived that is applied to the axial induction. The proposed model retains the streamtube-independent approach of BEM and adds little computational effort.

2.2. METHODOLOGY

2.2.1. SWEEP PARAMETRISATION

Blade sweep is defined as displacement of the blade axis in the rotational plane. A schematic of a blade with aft sweep is shown in Figure 2.1.

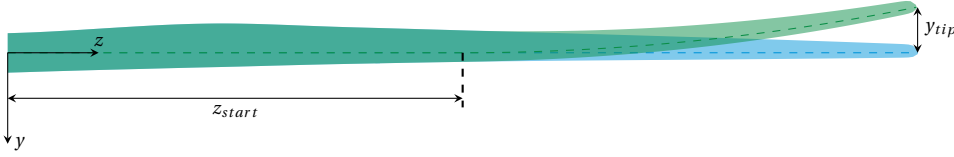


Figure 2.1: Schematic of an aft swept blade

For the parametrisation of the blade sweep, a power law equation is chosen that was previously also applied by Zuteck [13], Verelst and Larsen [7] and Larwood et al. [6]

$$y_{\Lambda} = \begin{cases} 0 & \text{for } z \leq z_{start} \\ y_{tip} \left(\frac{z - z_{start}}{R - z_{start}} \right)^{\gamma} & \text{for } z > z_{start} \end{cases} \quad (2.1)$$

Here, y_{Λ} is the inplane displacement of the blade axis, y_{tip} is the tip displacement, z_{start} is the sweep starting position, γ is the sweep exponent and R is the blade radius. The local sweep angle Λ can be determined as $\Lambda(z) = \tan^{-1}(\partial y / \partial z)$. The local aerofoil orientation is kept perpendicular to the blade pitching axis. In order to maintain the same tip radius as the unswept reference blade, the swept coordinates are scaled by $(1 + y_{tip}^2 / R^2)^{-1/2}$. Several other approaches for sweep parametrisation can be found in the literature. Kaya et al. [2] report a parametrisation similar to Equation 2.1, based on y_{tip} , z_{start} and a third sweep parameter. Hansen [14] uses a combined linear-quadratic shape function to allow for combinations of fore and aft sweep. Li et al. [9] employ Bézier curves parameterised by sweep starting position, tip displacement, and tip sweep angle to describe the blade axis shape. The sweep correction model proposed in Section 2.3 is independent of the parametrisation variables and, thus, also applicable to all methods mentioned above.

2.2.2. NUMERICAL MODELLING

BLADE ELEMENT MOMENTUM THEORY

Despite the availability of numerical models of higher fidelity, such as CFD and vorticity-based methods, the blade element momentum theory remains a crucial model to analyse the aerodynamic performance of rotors such as wind turbines or propellers. This is due to its rapid calculation speed which makes it suitable for the calculation of vast numbers of loadsets required e.g. for wind turbine certification.

The BEM algorithm couples the momentum theory of an actuator disc with the blade element theory. To this purpose, the blade is discretised by a number of blade elements where the local loads are calculated by interpolating aerofoil polars based on the inflow conditions. Similarly, the actuator disc is discretised using concentric annuli that correspond to a number of streamtubes for which the momentum equations are solved



independently. Many correction models exist to improve the accuracy of BEM algorithms, e.g. correction models for obtaining 3D polars, unsteady aerofoil aerodynamics, tilt/cone/yaw angles, tower effects, etc. In the baseline algorithm used in this study, only Prandtl's tip and root correction and Glauert's correction for heavily loaded rotors are implemented as presented by Burton et al. [15]

Based on an initial guess for the axial induction factor a and the tangential induction factor a' , the local inflow angle ϕ is calculated as

$$\phi = \tan^{-1} \left(\frac{U_\infty (1 - a)}{\omega r (1 + a')} \right), \quad (2.2)$$

where U_∞ is the freestream velocity, ω is the rotational speed and r is the radial position of the regarded annulus. Together with information of the blade pitch and local twist, the inflow angle is used to calculate the local forces from aerofoil polars. The normal force F_N in turn yields the local thrust coefficient

$$C_T = \frac{F_N dr N_b}{\frac{\rho}{2} U_\infty^2 A_{ann}}. \quad (2.3)$$

Here, dr is the radial extent of the annulus, N_b is the number of blades, ρ is the density of air and A_{ann} is the annulus surface area. At high values for thrust coefficient or axial induction, respectively, BEM theory becomes invalid and the momentum relation needs to be replaced with an empirical model. Glauert's correction model gives the following relation between axial induction factor a and thrust coefficient C_T :

$$a = \begin{cases} \frac{1}{2} - \frac{\sqrt{1-C_T}}{2}, & \text{for } C_T < C_{T_2} \\ 1 + \frac{C_T - C_{T_1}}{4\sqrt{C_{T_1} - 4}}, & \text{for } C_T \geq C_{T_2} \end{cases}, \quad (2.4)$$

where $C_{T_1} = 1.816$ and $C_{T_2} = 2\sqrt{C_{T_1}} - C_{T_1}$.

Prandtl's tip correction is applied to correct the momentum theory for the effects of finite numbers of blades. At the blade tip, a trailing tip vortex occurs which leads to large values of induction and therefore altered inflow conditions. Similar effects occur at the blade root. The Prandtl factors for tip and root correct for this increase in induction and can be calculated as

$$f_{tip} = \frac{2}{\pi} \cos^{-1} \left(e^{-\frac{N_b}{2} \left(\frac{R}{r} - 1 \right) \sqrt{1 + \left(\frac{\lambda_r}{1-a} \right)^2}} \right) \quad (2.5a)$$

$$f_{root} = \frac{2}{\pi} \cos^{-1} \left(e^{-\frac{N_b}{2} \left(\frac{r_{root}}{r} - 1 \right) \sqrt{1 + \left(\frac{\lambda_r}{1-a} \right)^2}} \right), \quad (2.5b)$$

where r_{root} and R are the root and tip radius and λ_r is the local tip-speed ratio. The total Prandtl factor $f_P = f_{tip} \cdot f_{root}$ is then used to correct the annulus-averaged induction factors to account for the induction at the blade.

$$a_b = \frac{a}{f_P} \quad (2.6a)$$

$$a'_b = \frac{a'}{f_p} \quad (2.6b)$$

Equations 2.2 to 2.6 are solved iteratively until convergence is reached.

A BEM algorithm as described here inherently assumes a straight blade located in the rotor plane. Thus, it can account neither for the displacement of the trailed vorticity due to blade sweep, nor for the induction of the curved bound vortex representing a swept blade on itself. To include both effects, a correction model is developed in Section 2.3 that can represent the changes in induction as a function of the sweep shape and the radial position of the evaluation point.

LIFTING LINE THEORY

In the lifting line theory, the rotor blade is represented by a bound vortex filament running through the quarter chord point of the specified blade cross-sections. The rotor wake is represented by a system of trailed and shed vorticity usually referred to as vortex lattice. In this study, steady conditions are assumed so that no shed vorticity occurs. Wake self-induction is neglected leading to a wake represented by concentric helical vortex filaments trailing at the edges of the numerical elements by which the blade is discretised. No vortex core model is applied to the induction of the trailed vorticity elements. For the representation of the wake, an azimuthal increment of $\Delta\theta = 1^\circ$ is chosen and a downstream wake extension of $L_{wake} = 10D$ is simulated, where D is the rotor diameter. The trailed vortices are convected by $U = U_\infty(1 - a_{rotor})$, where a_{rotor} is the rotor averaged axial induction factor in the rotor plane, and the helix lead angle is calculated as $\delta = \tan^{-1}\left(\frac{(1-a_{rotor})R}{\lambda r}\right)$. In this study, a_{rotor} is calculated by a BEM simulation with equivalent operating conditions as described in Section 2.2.2.

Local loads are calculated based on the inflow conditions and interpolated aerofoil polars which are provided as input. Based on the loads, the bound circulation and the resulting wake circulation can be calculated. The induced velocity is determined by evaluating the Biot-Savart law. As described in Section 2.2.2, a curved bound vortex representing a swept blade induces a velocity on itself. In this study, simulations are run with and without accounting for the bound vortex self-induction. A more detailed discussion of the vortex core model and radius used in the calculation of the bound vortex's self-induction follows in Section 2.3.3. Knowing the local induction at the rotor blade, the inflow conditions, the blade loads and the bound and trailed vorticity can be updated. At the same time, the prescribed wake geometry is kept constant. This way, the loads are calculated in an iterative procedure until convergence is reached. Next to the prescribed wake approach described here, the free wake lifting line code AWSM [16] is employed to evaluate the influence of the wake discretisation approach on the aerodynamic solution. The lifting line theory is capable of representing the blade axis and the wake in three-dimensional space and, therefore, is appropriate to simulate swept blade designs.

2.3. SWEEP CORRECTION MODEL

By sweeping the blade, two main changes are made to the vorticity system.

1. The release point of trailed vorticity is moved ahead or aft of a straight reference



blade in the azimuthal direction. Based on Equation 2.1, it is obvious that the largest displacement occurs at the tip. Modern wind turbine blades are designed to achieve an almost constant circulation distribution along their span, meaning that the majority of vorticity is trailed at the root and tip. Thus, the effect of sweep can be approximated by the effect of the changing tip vortex position. Compared to a reference case with a straight blade, the sweep will add or subtract a piece of the helical vortex filament that describes the tip vortex. For realistic sweep configurations and wind turbine blade dimensions, this additional/missing part of the tip vortex can be approximated as straight vortex filament and the induced axial velocity of a swept blade $u_{ind,\Lambda}$ can be described as

$$u_{ind,\Lambda} = u_{ind,ref} + u_{ind,VF}, \quad (2.7)$$

where the swept case, reference case and the additional/missing vortex filament are denoted with the subscripts " Λ ", " ref " and " VF ". Consequently, the axial induction factor of a swept blade configuration can be expressed as

$$a_{\Lambda} = a_{ref} \left(1 + \frac{u_{ind,VF}}{u_{ind,ref}} \right). \quad (2.8)$$

2. The bound vortex is curved and, in contrast to a straight vortex filament, induces a velocity on itself.

2.3.1. VELOCITY INDUCED BY A SEMI-INFINITE HELICAL VORTEX FILAMENT

The tip vortex of a wind turbine blade rotating in clockwise direction as seen from upstream can be described by a helical vortex filament, its curve defined as $y = -R \sin \theta$, $z = R \cos \theta$ and $x = \theta l$. A schematic of this filament is shown in Figure 2.2.

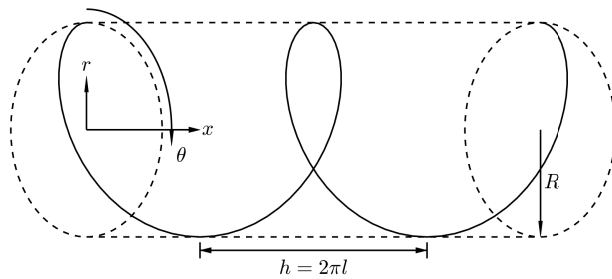


Figure 2.2: Schematic of a helical vortex filament.

Kawada [17] and Hardin [18] independently derived the equations describing the velocity field induced by an infinitely extending helical vortex filament. Often overlooked, Kawada's contribution is related by Fukumoto et al. [19]. Using the Kawada-Hardin

equations, the velocity field is calculated by means of the Kapteyn series. Extended to account for the tip vortices of multiple equispaced blades, the equation for the induced velocity along the helix axis reads

$$u_x = \frac{N_b \Gamma}{2\pi l} \left\{ \begin{array}{l} 1 \\ 0 \end{array} \right\} - \frac{\Gamma R}{\pi l^2} \sum_{n=1}^{N_b} \sum_{m=1}^{\infty} m \left\{ \begin{array}{l} I_m(mr/l) K'_m(mR/l) \\ I'_m(mR/l) K_m(mr/l) \end{array} \right\} \cos(m\chi_n), \quad (2.9)$$

where l is the helix pitch, $\chi = \theta - x/l$ and $\chi_n = \chi + 2\pi(n-1)/N_b$. $I_m(x)$ and $K_m(x)$ are the modified Bessel functions of first and second kind and the prime indicates their derivative with respect to the argument. The upper line in the notation " $\{ \}$ " represents the solution for $r < R$ while the lower line states it for $r \geq R$. With multiple blades present, the wake exhibits a periodicity. The term $\sum_{n=1}^{N_b} \cos(m\chi_n)$ then becomes zero if m is not a multiple of N_b , a circumstance referred to as "Kawada cancellation". Okulov [20] presents a more efficient approximation to the velocity field to which Wood et al. [21] apply the Kawada cancellation. While [21] still contained a typographic mistake, the correct equations are given by Wood et al. [22].

$$u_x = \begin{cases} \left(\frac{N_b \Gamma}{2\pi l} + \frac{\Gamma}{2\pi l} \sqrt{\frac{c_R}{c_r}} \left(\frac{N_b U}{1-U} + \frac{1}{24} \left[\frac{9(R/l)^2+2}{c_R^3} + \frac{3(r/l)^2-2}{c_r^3} \right] \log\left(1 + \frac{U}{1-U}\right) \right) \right) & \text{for } r < R \\ \left(\frac{\Gamma}{2\pi l} \sqrt{\frac{c_R}{c_r}} \left(\frac{N_b}{1-U} + \frac{1}{24} \left[\frac{9(R/l)^2+2}{c_R^3} + \frac{3(r/l)^2-2}{c_r^3} \right] \log\left(1 + \frac{1}{U-1}\right) \right) \right) & \text{for } r \geq R \end{cases}, \quad (2.10)$$

with

$$c_R = \sqrt{1 + \left(\frac{R}{l}\right)^2}, \quad (2.11)$$

$$c_r = \sqrt{1 + \left(\frac{r}{l}\right)^2}, \quad (2.12)$$

$$U = \left(\frac{r(c_R+1)}{R(c_r+1)} \exp(c_r - c_R) \right)^{N_b}. \quad (2.13)$$

Okulov [20] presents additional terms to further improve the accuracy of this approximation. Wood et al. [22] compare Okulov's extended approximation to other approximations of the Kawada-Hardin equations. They conclude that, while increasing the accuracy at high helix pitch values, Okulov's additional terms do not significantly improve the accuracy for wind turbine relevant helix pitch angles ($l \approx 0.1$). Thus, the additional terms are omitted from the discussion.

Equation 2.10 gives an expression for the evaluation of the induction of an infinite helical vortex filament. The tip vortex of a wind turbine blade, however, only spans downstream of the rotor and, thus, resembles a semi-infinite helical vortex filament. It should be noted, that the problem of induction by a helical vortex filament is not symmetrical. Nonetheless, dividing the solution of Equation 2.10 by two gives a good approximation of the semi-infinite vortex filament's induction. This will be demonstrated by comparing this approach to results obtained when evaluating the Biot-Savart law for



a discretised helical vortex filament only spanning downstream of the rotor. Both methods are compared for multiple helical vortex filaments defined by the axial induction factor a , tip-speed ratio λ , number of blades N_b , wake extension L_{wake}/D and the azimuthal increment $\Delta\theta$. The latter two parameters are only relevant for the discretisation of the filament when calculating the induction using the Biot-Savart law. The helix configurations are listed in Table 2.1, where the bold script indicates the parameter variation compared to Helix 1.

Table 2.1: Helix parametrisation

	a [-]	λ [-]	N_b [-]	L_{wake}/D [-]	$\Delta\theta$ [°]
Helix 1	0.3	9	1	10	1
Helix 2	0.2	9	1	10	1
Helix 3	0.3	7	1	10	1
Helix 4	0.3	9	3	10	1
Helix 5	0.3	9	1	100	1
Helix 6	0.3	9	1	10	5

Figure 2.3 shows the ratio of induced velocity calculated using the Biot-Savart law (subscript *BS*) over the solution of Equation 2.10 divided by two (subscript $\infty/2$, denoting a semi-infinite helix) as a function of the radial position.

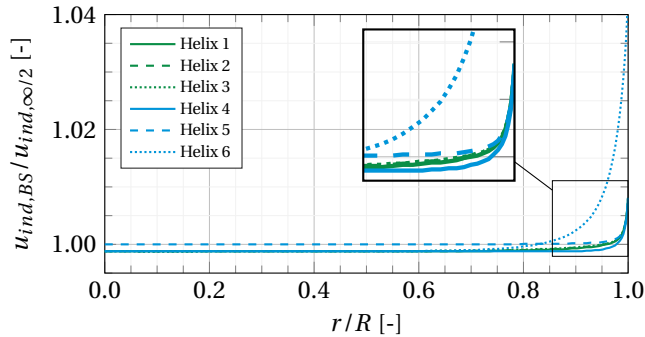


Figure 2.3: Ratio of induction when evaluating a helical vortex filament using Equation 2.10 and Biot-Savart law

The influence of the input parameters when compared to the baseline helix 1 can be summarised as follows:

- Changes in the axial induction a (helix 2) or tip-speed ratio λ (helix 3) have no significant influence on the agreement of Equation 2.10 and the Biot-Savart evaluation.
- A larger number of blades (helix 4) will result in more evenly spread vorticity, thereby, reducing the impact of the symmetry assumption. The results of helix 4 show the best agreement between the Biot-Savart law and the analytical solution.

- Instead of an exact representation of the helical vortex filament, the Biot-Savart law is used to evaluate a set of straight vortex filaments that approximate the helix shape. Whereas Equation 2.10 is a solution for an infinite helical vortex filament, the discretised helical filament spans a finite length L_{wake} downstream of the rotor. By increasing the discretised wake length (helix 5), deviations in the helix centre can be reduced while the error at the tip remains unchanged. Additionally, the azimuthal increment defines how closely the curved helical shape is approximated. By increasing the azimuthal increment (helix 6), this approximation becomes worse which increases the error particularly in the proximity of the vortex itself.

Based on these observations, the helical filament of the tip vortex will be discretised using the parameters of helix 4, see Table 2.1 for all simulations presented in this section. As such, assuming symmetry of the velocity induced by a helical vortex filament extending infinitely both upstream and downstream of the rotor plane introduces an error smaller than 0.5%. It should be noted that in this section, the wind turbine wake is treated as a helix with constant radius while the wake expands behind a real wind turbine. However, Wood [23] demonstrates that the approximation of the Kawada-Hardin equation for the axial induced velocity presented here remains accurate when compared to a Biot-Savart evaluation of an expanding wake.

2.3.2. VELOCITY INDUCED BY THE ADDITIONAL/MISSING VORTEX FILAMENT

The effect of blade sweep is approximated by adding/subtracting a straight piece of vortex filament located in the rotor plane from the semi-infinite vortex representing the tip vortex of the blade. A schematic of both a forward and backward swept case is given in Figure 2.4. For simplicity, the trailing vortex is also plotted as straight line while in reality, it is a helical vortex filament.

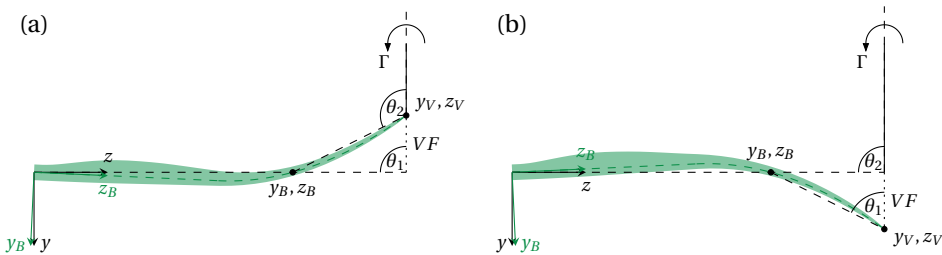


Figure 2.4: Schematic of the additional/missing vortex filament (dotted line) for an aft swept blade (a) and forward swept blade (b).

Considering the Biot-Savart law, the velocity induced at a given point by a straight vortex filament of length $d\mathbf{l}$ can be calculated as

$$\mathbf{v}_{ind} = \frac{\Gamma}{4\pi} \int \frac{\mathbf{r} \times d\mathbf{l}}{|\mathbf{r}|^3}, \quad (2.14)$$



where \mathbf{r} is the distance vector between the vortex filament and the evaluation point and Γ is the filament's circulation. The induced axial velocity of the additional/missing vortex filament can then be expressed as

$$u_{ind,VF} = \frac{\Gamma}{4\pi(z_V - z_P)} (\cos\theta_2 - \cos\theta_1), \quad (2.15)$$

where z_V and z_P refer to the radial position along the blade pitch axis of the trailed vortex and the evaluation point on the blade, respectively. Given that $\cos\theta_1 = 0$ for backward sweep and $\cos\theta_2 = 0$ for forward sweep, Equation 2.16 can be simplified to

$$u_{ind,VF} = -\frac{\Gamma}{4\pi(z_V - z_P)} \text{sgn}(y_{tip}) \cos\theta_\Lambda. \quad (2.16)$$

Here, θ_Λ is the angle between the trailing vortex filament and the swept blade axis (θ_2 for backward sweep and θ_1 for forward sweep). This angle can be calculated as

$$\theta_\Lambda = \tan^{-1}\left(\frac{z_V - z_P}{y_V - y_P}\right) + \tan^{-1}\left(\frac{y_P}{z_P}\right), \quad (2.17)$$

where the coordinates of the evaluation point y_P, z_P and of the tip vortex starting point y_V, z_V are given in the rotated blade coordinate system with axes y_B, z_B . Note, that the length of the additional/missing vortex filament is not only a function of the sweep parameters y_{tip}, z_{start} and γ , but also of the radial position of the evaluation point.

Figure 2.5 shows the velocity induced by such a vortex filament with unit circulation for forward swept blade geometries with varying sweep parametrisation in green. For comparison, the difference in induced velocity between lifting line simulations of the straight reference blade and the swept blade geometries are plotted in light blue. In the lifting line simulations, vorticity is only trailed at the tip. Overall, very good agreement can be observed, the differences visible inboard of 80 % blade span only appear large due to the logarithmic ordinate. Identical results (with inverted sign) are obtained when sweeping the blade backward instead of forward while keeping the other sweep parameters constant.

The analysis shown here and in Section 2.3.1 underlines that the axial induction of the tip vortex can be approximated for any swept blade configuration with good accuracy by the sum of Equation 2.10 divided by two and Equation 2.16. Figure 2.6 shows the ratio of the induced velocity simulated using a lifting line approach to the approximation just described. For this simplified case, where vorticity is only trailed at the tip, the maximum error increases the further the tip is displaced and the further outboard the sweep begins. However, even for the extreme cases with sweep parameters $z_{start} = 0.75R$ and $y_{tip} = \pm 0.2R$, the maximum error remains below 2.5 % indicating a good approximation of the axial induction.

2.3.3. VELOCITY INDUCED BY THE BOUND VORTEX ON ITSELF

In lifting line theory, a wind turbine blade is represented by the bound vortex which is discretised by a number of vortex filaments. If this bound vortex forms a straight line, it does not induce a velocity on itself. If, however, the bound vortex is curved, it is essential to consider its self-induction. In lifting line theory, this is done by evaluating the

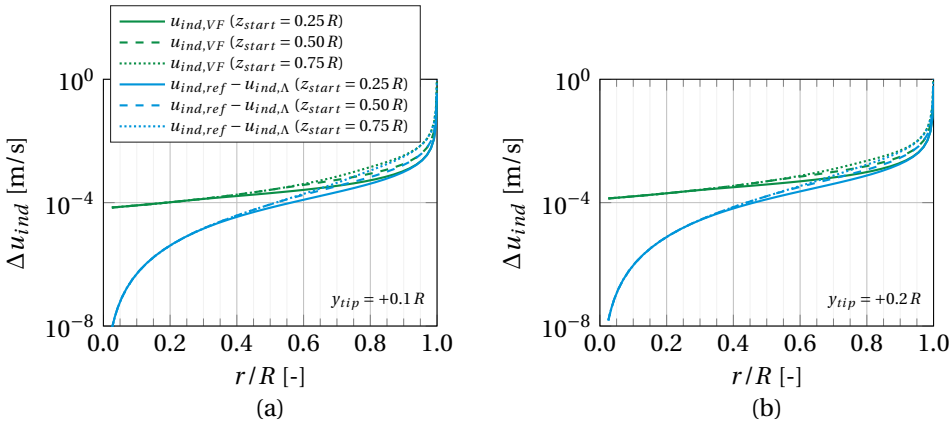


Figure 2.5: Difference in axial induction between swept and reference geometry. Simulated using a lifting line approach (light blue) and approximated by a straight vortex filament (green) for swept geometries with $y_{tip} = +0.1R$ (a) and $y_{tip} = +0.2R$ (b).

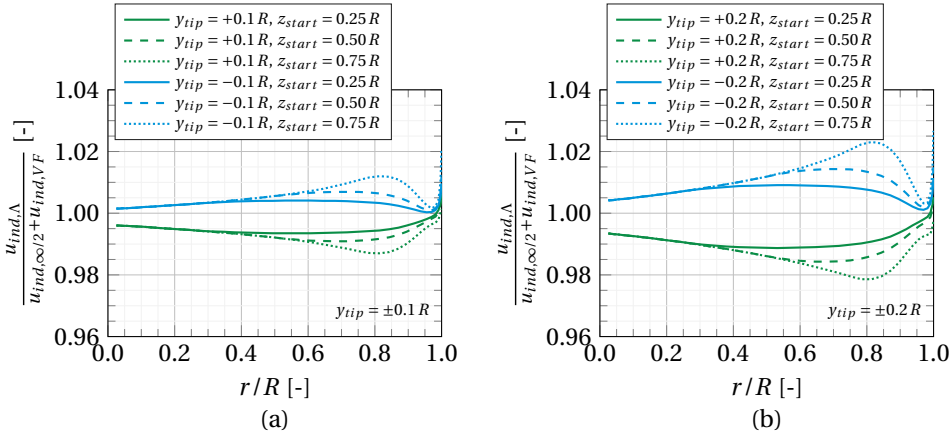


Figure 2.6: Ratio of induced axial velocity simulated using a lifting line approach to the sweep model for swept geometries with $y_{tip} = \pm 0.1R$ (a) and $y_{tip} = \pm 0.2R$ (b)

Biot-Savart law. The induced velocity behaves singular in the direct vicinity of a vortex filament. To avoid this effect, regularisation models are used. In this study, the bound vortex filaments are regularised using a Lamb-Oseen multiplication factor

$$K = 1 - \exp\left(\frac{-\alpha r^2}{r_c^2}\right), \quad (2.18)$$

where r is the distance between evaluation point and vortex filament, r_c is the viscous core radius and $\alpha = 1.25643$ [24]. The choice of the viscous core radius has a strong influence on the velocity induced by the curved bound vortex on itself. This is demonstrated exemplarily in Figure 2.7 (a). Here, the self-induction of a swept vortex filament



with unit circulation strength is plotted. According to Equation 2.1, the sweep is defined by $z_{start} = 0.5R$, $y_{tip} = -0.2R$ and $\gamma = 2$, where the unswept reference length of the vortex filament is $R = 100$ m, which is comparable to the length of modern wind turbine blades. A blade of this length will have a chord distribution approximately ranging from a maximum of $c = 5$ m to $c = 1$ m towards the tip. Along this line of thought, the chosen viscous core radii are also related to a mean chord of $c = 3$ m in Figure 2.7 (a). The filament is discretised using $N_{elem} = 50$ elements. It is obvious, that larger viscous core radii lead to reduced self-induction. When lowering the viscous core radius, the self-induction increases. There is a lower limit of the viscous core radius beyond which the self-induction reaches a converged state that is equivalent to calculating the induced velocity without viscous core radius model.

In the swept part of the bound vortex where self-induction is most present, the highest contribution to the locally induced velocity comes from the discretised vortex filaments in the proximity of the evaluation point. Assuming that the circulation distribution does not rapidly change over the span, the following correction model is proposed to account for the bound vortex's self-induction in BEM algorithms. At the beginning of a BEM simulation, a one-time evaluation of the bound vortex's self-induction is conducted using the Biot-Savart law. For each blade element i , the sum of velocities induced by each other blade element j based on a unit strength circulation distribution is calculated.

$$\mathbf{V}_{ind,\Gamma_b=1,i} = \sum_{j=1}^{N_{elem}} K_j \frac{1}{4\pi} \int \frac{\mathbf{r}_{i,j} \times d\mathbf{l}_j}{|\mathbf{r}_{i,j}|^3} \quad (2.19)$$

This value of induced velocity per bound circulation strength is stored as a property of the respective blade element. During the iterative solution of each streamtube, the axial component of this relative induction $u_{ind,\Gamma_b=1,i}$ is multiplied by the currently calculated circulation of the blade element, thus, approximating the velocity that the entire bound vortex would induce.

$$u_{ind,\Gamma_b,i} = u_{ind,\Gamma_b=1,i} \Gamma_{b,i} \quad (2.20)$$

The resulting change in the axial induction factor is

$$\Delta a_{\Gamma_b} = -\frac{u_{ind,\Gamma_b,i}}{U_\infty} \quad (2.21)$$

The benefit of this correction model is that the streamtube-independent approach of most BEM algorithms can be retained.

On a real wind turbine blade, the bound circulation is distributed over the blade's surface instead of being lumped at the quarter chord point. Thus, a discussion regarding a reasonable viscous core radius size follows based on the example of a flat plate. The chordwise circulation distribution of a flat plate is given by

$$\gamma(x) = 2U_\infty \alpha \sqrt{\frac{1-x}{x}}, \quad (2.22)$$

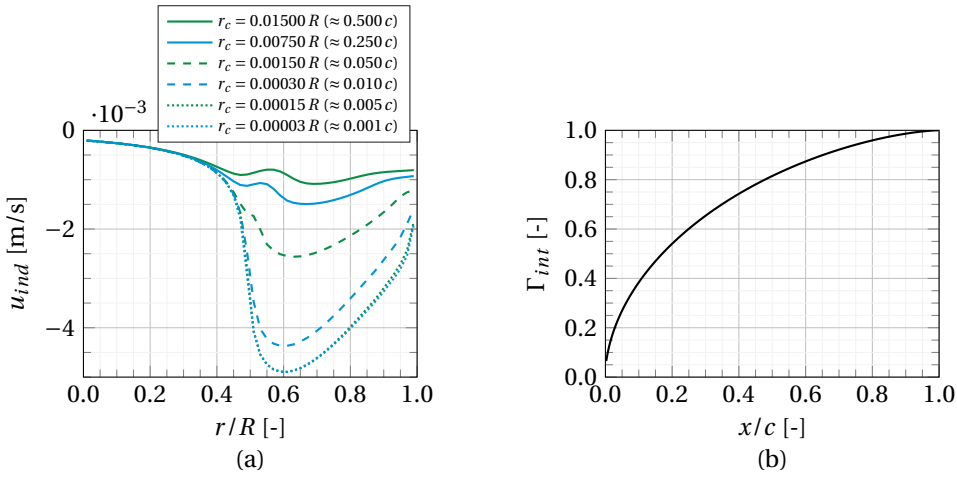


Figure 2.7: Self-induced velocity of a swept vortex filament defined by $R = 100$ m, $N_{elem} = 50$, $z_{start} = 0.5 R$, $y_{tip} = -0.2 R$, $\gamma = 2$ for different viscous core radii (a) and relative integrated circulation of a flat plate (b)

where α is the angle of attack and x is the chordwise coordinate, see e.g. Katz and Plotkin [25]. The relative integrated circulation

$$\Gamma_{int} = \frac{\int_0^x \gamma(x) dx}{\int_0^c \gamma(x) dx} \quad (2.23)$$

is shown in Figure 2.7 (b). Representing the flat plate by a lifting line at the quarter chord location, it can be observed that a viscous core radius of $r_c = 0.25 c$ would encompass approximately 80 % of the bound circulation. Deeming this a good approximation of real conditions, all simulations run for this study use this viscous core radius. In Figure 2.7 (a), the self-induction of a swept bound vortex with $r_c \approx 0.25 c$ is plotted as solid light blue line.

2.3.4. IMPLEMENTATION OF THE SWEEP CORRECTION IN BEM

Combining the results of Sections 2.3.1 to 2.3.3, the axial induction factor of swept blades can be approximated. The resulting sweep correction can be implemented inside of the iterative loop that solves the local blade element loads in equilibrium with the annulus momentum theory. Inside the iterative loop, the rotor averaged induction factor a_{rotor} is not known. Therefore, the calculation of the helix pitch of the tip vortex (Equation 2.10) is based on the local induction factor a . Consequently, the helix pitch does not only change with the radial position but also during each iteration in which the local axial induction factor a is updated until convergence is reached. This approach can be justified by considering that blade sweep results in changes especially in the near wake induction. Slight changes in the tip vortex helix pitch due to the varying local induction have a relatively smaller impact on the axial induction compared to the additional/missing vortex filament introduced by the sweep.

It should be noted, that both the velocity induced by the vortex filament represent-



ing the shifted tip vortex position (Equation 2.16) and the velocity induced by the semi-infinite helical vortex filament representing the wake (Equation 2.10) are linearly proportional to the tip vortex strength. When calculating the correction for the axial induction factor (Equation 2.8), the division of the two induced velocity terms ensures that the circulation is cancelled from the equation. Consequently, this correction term is independent of the tip vortex strength. Numerically, this also guarantees the correction model's independence from the blade discretisation, which can have an influence on how the tip vortex strength is distributed over the outermost elements.

Given the assumption that the effect of sweep is described only by an additional/missing vortex filament at the blade tip and the bound vortex's self-induction, the influence on the tangential induction factor a' is negligible. Therefore, the tangential induction is not corrected. By placing the sweep correction inside the iterative loop, the solution process remains streamtube-independent and minimal computational effort is added. The implementation of the sweep correction in BEM is shown in Algorithm 1.

Algorithm 1 BEM algorithm with sweep correction

- 1: Calculate velocity induced by bound vortex with unit circulation strength on itself (Equation 2.19)
 - 2: **for** $i = 1 : N_{annuli}$ **do**
 - 3: Initial guess a, a'
 - 4: **while** not converged **do**
 - 5: Calculate inflow conditions (Equation 2.2)
 - 6: Calculate loads based on polars
 - 7: Update induction factors (Equations 2.3 - 2.4)
 - 8: Correct axial induction for displacement of trailed vorticity (Equations 2.8, 2.10 and 2.16) and bound vortex's self-induction (Equation 2.21)
 - 9: Apply Prandtl correction (Equations 2.5a - 2.6)
 - 10: Check convergence
 - 11: **end while**
 - 12: **end for**
-

2.4. SIMULATION RESULTS

2.4.1. THE STRAIGHT REFERENCE CASE

The IEA 15 MW rotor is chosen as baseline geometry for the numerical investigations presented in this study. Details of this reference turbine are taken from the report by Gaertner et al. [26] and the corresponding GitHub repository [27]. To simplify the geometry, slight modifications were done, namely, the tilt and cone angle were set to zero and the prebend was neglected. The main characteristics of the modified IEA 15 MW rotor model are listed in Table 2.2.

Initially, the straight reference blade is simulated using the BEM algorithm described in Section 2.2.2, the lifting line algorithm described in Section 2.2.2 and the free wake lifting line code AWSM [16]. The subscript *ref* represents the straight reference blade. The operational conditions are $U_\infty = 10 \text{ m s}^{-1}$, $\lambda = 9$ and $\beta_{pitch} = 0^\circ$.

Table 2.2: Parameters of the modified IEA 15 MW reference wind turbine. Compared to the original report [26], the prebend, tilt and cone are removed.

Parameter	Value	Unit
Number of blades	3	-
Rotor diameter	240.00	m
Rated power	15.00	MW
Rated wind speed	10.59	m s^{-1}
Rated pitch angle	0.00	deg
Design tip-speed ratio	9.00	-
Tip prebend	0.00	m
Tilt angle	0.00	deg
Cone angle	0.00	deg

Figure 2.8 shows the spanwise distribution of axial induction (a) and the circulation distribution (b). There is good agreement between the numerical tools. It can be observed, that the lifting line approaches give lower axial induction values along almost the entire blade. This is in line with observations documented by Schepers et al. [28, 29] for comparisons between BEM and lifting line models of rotors with high induction values. Furthermore, the axial induction calculated using the free wake lifting line code AWSM is lower than that of the prescribed wake lifting line approach described in Section 2.2.2. This discrepancy can be attributed to the wake discretisation approach. The lower axial induction leads to slightly higher values of the bound circulation for the lifting line calculations. Independent of the numerical model, the IEA 15 MW turbine has a constant circulation distribution for large parts of the blade span. The circulation gradient, which represents the strength of the trailed vorticity, is largest at the blade tip. Thus, the assumption of vorticity mostly being trailed at the tip as made in the derivation of the sweep correction model, is in good agreement with the simulation results.

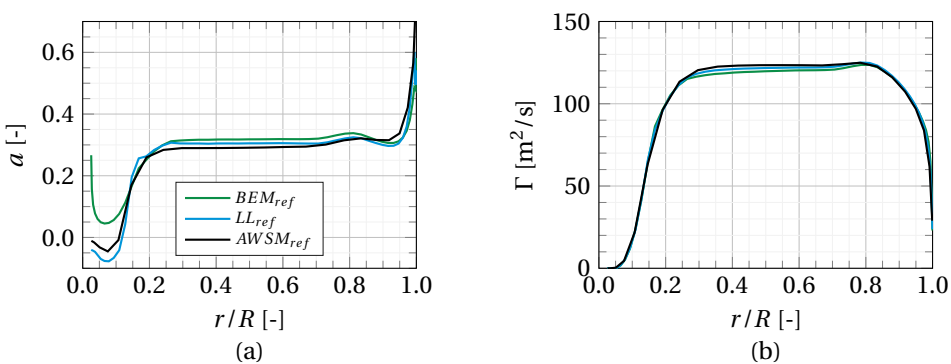


Figure 2.8: Spanwise distribution of the axial induction factor (a) and circulation (b) of the straight reference blade, case: $U_\infty = 10 \text{ m s}^{-1}$, $\lambda = 9$, $\beta_{pitch} = 0^\circ$

The normal and tangential load distributions are plotted in Figure 2.9. In line with



the induction and circulation distributions, the different numerical models agree well for the blade loads. Given the overall congruence between the two lifting line codes, the inaccuracy introduced by the prescribed wake formulation is deemed negligible. Thus, changes in the aerodynamic blade characteristics due to sweep are analysed based on the lifting line algorithm with prescribed wake for the remainder of this chapter. The cylindrical wake used in this approach matches the wake assumptions made in the derivation of the sweep correction model for BEM. Consequently, this model is well suited for the validation of the extended BEM algorithm.

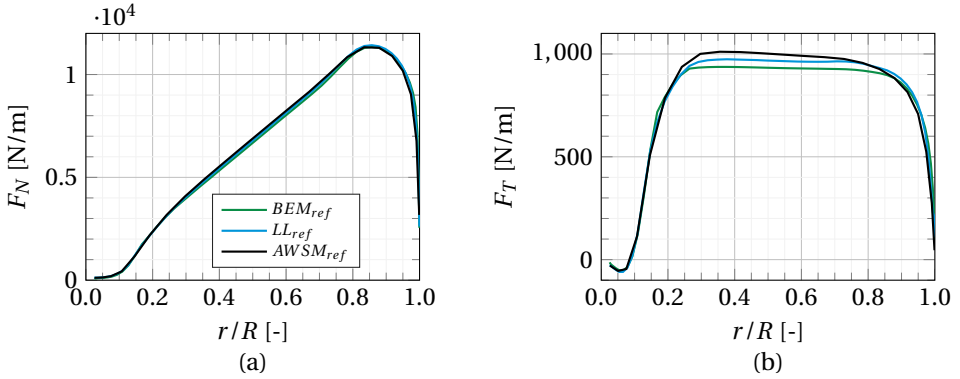


Figure 2.9: Spanwise distribution of the normal force (a) and tangential force (b) of the straight reference blade, case: $U_\infty = 10 \text{ m s}^{-1}$, $\lambda = 9$, $\beta_{pitch} = 0^\circ$

2.4.2. VARYING THE SWEEP PARAMETERS

For the simulations presented in this section, the sweep starting position z_{start} and the tip displacement y_{tip} are varied while keeping the sweep exponent γ constant. The parameter variation is listed in Table 2.3 and a graphical representation of the resulting blade geometries is shown in Figure 2.10.

Table 2.3: Sweep parameter variation

Parameter	Value
z_{start}	$[0.25, 0.50, 0.75] R$
y_{tip}	$[-0.2, -0.1, +0.1, +0.2] R$
γ	2

Both the prescribed wake lifting line model as well as the extended BEM model are employed for simulating the swept blade geometries. The lifting line results are denoted as LL , the subscripts ref and Λ represent the straight and swept blade simulations, respectively. Additionally, the subscript Γ_b indicates that the velocity induced by the bound vorticity on the blade itself has been taken into account. While the BEM simulations employ the correction model described in Section 2.3.3 to do so, the lifting line simulations directly evaluate the velocities induced by the bound vortex on itself. The

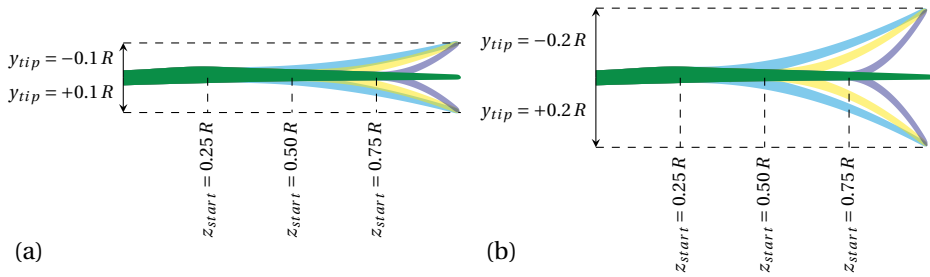


Figure 2.10: Swept blade geometries for $y_{tip} = \pm 0.1 R$ (a) and $y_{tip} = \pm 0.2 R$ (b)

operational conditions remain $U_\infty = 10 \text{ m s}^{-1}$, $\lambda = 9$ and $\beta_{pitch} = 0^\circ$. Exemplary, the simulation results of a swept blade with $z_{start} = 0.5 R$, $y_{tip} = -0.2 R$ and $\gamma = 2$ are graphically compared to those of the straight reference blade.

The sweep-induced change of the axial induction factor a is plotted in Figure 2.11 (a). Firstly, the results of the simulations not modelling the bound vortex induction are discussed (solid lines). As expected for the presented case with aft sweep, the axial induction factor drops towards the tip. This is due to the aft displacement of the tip vortex in azimuthal direction, resulting in a "missing" part of vortex filament compared to the straight blade. Contrary to this, a forward sweep will cause an increase in axial induction close to the tip. The results from the extended BEM simulation show good agreement with the lifting line simulations. The changes in normal force F_N are depicted in Figure 2.11 (b). Due to the decreased induction, the blade tip experiences higher angles of attack, which entail increased sectional loads. These results demonstrate that the sweep correction model enables BEM to account for the sweep-induced changes in the trailed vorticity system.

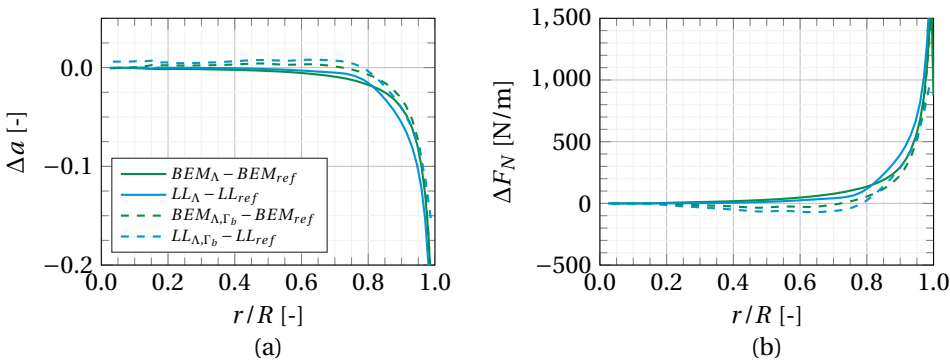


Figure 2.11: Spanwise distribution of sweep-induced changes to the axial induction factor (a) and normal force (b), case: $U_\infty = 10 \text{ m s}^{-1}$, $\lambda = 9$, $\beta_{pitch} = 0^\circ$, $y_{start} = 0.5 R$, $x_{tip} = -0.2 R$, $\gamma = 2$

Along with the normal force, also the tangential force and the bound circulation in-



crease at the tip for aft swept blades. Since their sweep-induced variation resembles that of the normal force in shape, plots of these changes have been omitted for brevity. The increased circulation at the tip moves the large circulation gradient indicating the tip vortex to even higher radial positions. This further supports the assumption of vorticity mostly being trailed at the tip as made in the derivation of the sweep correction model. In contrast to that, forward sweep decreases the bound circulation at the tip, and, therefore, the peak of the circulation gradient is moved further inboard and is slightly smoothed out. Thus, forward sweep is less aligned with the model assumptions than aft sweep.

In a second set of simulations, the induction of the bound vortex on itself is included, see the dashed lines in Figure 2.11. For aft swept blades the induction at the tip is still lower compared to straight reference blade. More inboard, however, the curved bound vortex increases the axial induction. Sweeping the blade forward has a comparable effect with inverted sign. As a consequence of the induction distribution, the normal force reduces at midspan and increases at the tip. Thus, blade sweep causes a load redistribution over the blade span. The BEM algorithm underpredicts the velocity induced by the bound vortex on itself slightly when compared to the lifting line model. Nonetheless, the agreement between the two models is very good. As mentioned in Section 2.3.3, the velocity induced by the bound vortex on itself is highly dependent on the chosen viscous core radius, here 25% of the local chord. If a lower core radius were chosen, the load changes around the sweep starting point would appear stronger.

In order to validate the sweep correction model for all swept cases, the integrated flapwise moment at the blade root is calculated as

$$M_f = \int_{r_{root}}^R F_N(r) r dr . \quad (2.24)$$

The linear weighting of the force due to the radially increasing moment arm stresses the changes in blade loads due to sweep which mainly occur at the tip. The baseline flapwise moments of the straight reference case for BEM and the lifting line code are $M_{f,BEM,ref} = 5.99 \cdot 10^7$ Nm and $M_{f,LL,ref} = 6.04 \cdot 10^7$ Nm. Thus, the difference in flapwise moment between the two baseline simulations is $\frac{M_{f,LL,ref} - M_{f,BEM,ref}}{M_{f,LL,ref}} = 0.8\%$. Based on the parameter variation listed in Table 2.3, simulations are conducted and the changes in flapwise moment compared to the straight reference case are shown in Figure 2.12, both for simulations accounting for and neglecting the bound vortex's self-induction.

Again, we first discuss the simulations neglecting the influence of the curved bound vortex on itself. The results confirm that both numerical models show the same trend for all sweep configurations. In comparison with the lifting line simulations, it can be observed that the relative change in flapwise moment is mostly underpredicted by the extended BEM code with the exception of the cases with $z_{start} = 0.25R$ and $y_{tip} < 0$. The difference between the models grows with increasing tip deflection and sweep starting position. Furthermore, the relative change in flapwise moment generally matches slightly better for aft swept cases as was explained on the basis of the circulation distribution. Larger deviations between the lifting line and extended BEM code can primarily be found for the cases with $z_{start} = 0.75R$ and $y_{tip} = \pm 0.2R$. It should be noted, that for these cases the tip displacement is almost equal to the spanwise extent of the blade

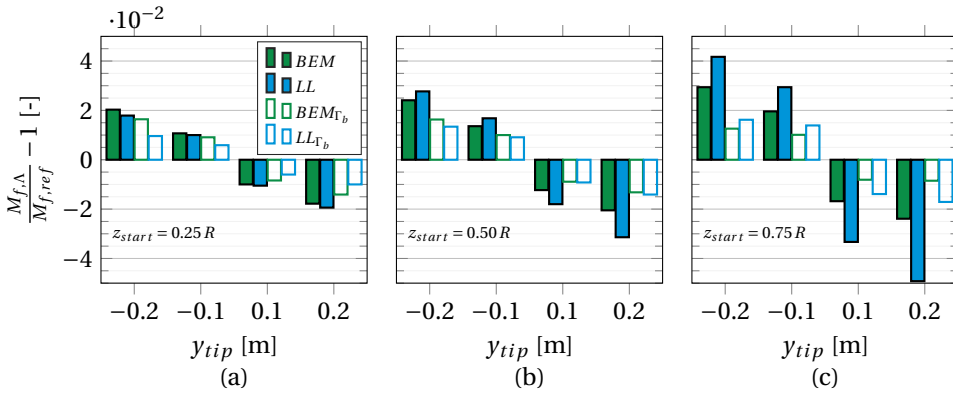


Figure 2.12: Relative change in flapwise moment for $z_{start} = 0.25 R$ (a), $z_{start} = 0.50 R$ (b), $z_{start} = 0.75 R$ (c), case: $U_\infty = 10 \text{ m s}^{-1}$, $\lambda = 9$, $\beta_{pitch} = 0^\circ$

that is being swept, resulting in a local sweep angle of nearly $\Lambda = 60^\circ$ at the tip. In such conditions, considerable crossflow will occur and the validity of either numerical model is questionable. A better solution would be the application of models that resolve the three-dimensional blade geometry such as panel methods or CFD.

Accounting for the induction of the curved bound vortex on itself leads to a load redistribution as shown in Section 2.4.2. Figure 2.12 confirms this for all swept configurations that were simulated. While the flapwise root bending moment still increases for all aft swept blades and reduces for all forward swept blades, the extent of these changes is smaller compared to the simulations without bound vortex self-induction. The largest influence of the bound vortex occurs for the swept blades with $z_{start} = 0.75 R$. Those cases have the highest curvature in the swept part of the blade. As a consequence, the influence of the regularisation applied to the bound vortex's induced velocity reduces. The agreement between the lifting line and BEM simulations is reasonably good.

2.4.3. VARYING THE OPERATING CONDITIONS

The results presented in Section 2.4.2 demonstrate the effect of different sweep geometries on the aerodynamic performance of the wind turbine blade. Those simulations are conducted at operating conditions close to the rated conditions of the IEA 15 MW reference wind turbine. This section will extend that analysis to the whole range of operational conditions using the example of a swept blade with $z_{start} = 0.5 R$, $y_{tip} = -0.2 R$ and $\gamma = 2$. Within the documentation of the IEA 15 MW reference wind turbine [26, 27], the operating conditions are defined for wind speeds of $3 \text{ m s}^{-1} \leq U_\infty \leq 25 \text{ m s}^{-1}$. The tip speed ratio λ and the pitch angle β_{pitch} are plotted in Figure 2.13.

The accuracy of the sweep correction model throughout the operating conditions is, again, investigated based on the blade root flapwise moment. Figure 2.14 (a) displays the absolute values of M_f as a function of the wind speed for the straight reference blade. Throughout the operational range, differences due to the employed numerical model are small compared to the variation due to the operating conditions. The impact of sweep can be seen when plotting the relative change in flapwise moment due to



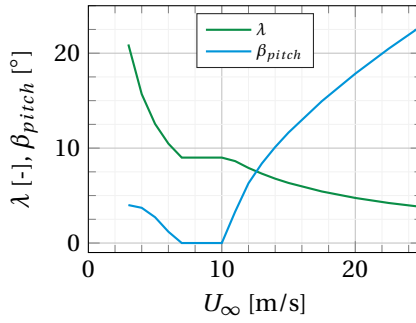


Figure 2.13: Operating conditions of the IEA 15 MW reference wind turbine

sweep per model, as done in Figure 2.14 (b). For most operating conditions (with the exception of below rated conditions for simulations including the bound vortex induction), the change in flapwise moment is underpredicted by the extended BEM model. The difference between the two models grows with increasing wind speed. At very high wind speeds, the BEM results even show a decrease in flapwise moment when sweeping the blade. In these conditions, negative induction and negative thrust occur in the outboard part of the blade. Exemplary, Figure 2.15 depicts the axial induction and normal force distribution at $U_\infty = 25 \text{ m s}^{-1}$ of the simulations neglecting the bound vortex influence. Since the sweep correction model for the altered trailed vorticity system is applied as a scaling of the axial induction factor it scales positive and negative values alike. In the case of aft sweep, it reduces the absolute value of axial induction for both positive and negative induction. This leads to increased negative thrust in the outboard region which reduces the integrated flapwise moment of the swept blade at very high wind speeds. The load redistribution caused by the influence of the bound vortex on itself as described in Section 2.4.2 is consistent throughout the operating range and expresses itself through a shift of the change in flapwise moments to lower values.

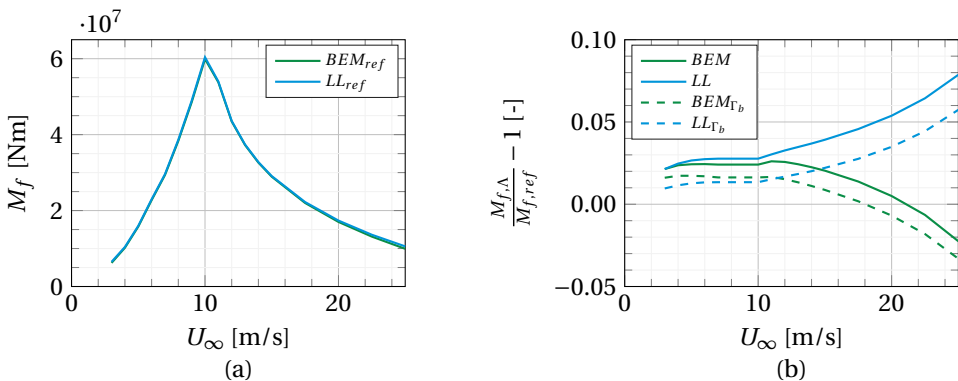


Figure 2.14: Flapwise moment at the blade root (a) and its changes due to sweep (b) along the operating conditions, case: $z_{start} = 0.5R$, $y_{tip} = -0.2R$, $\gamma = 2$

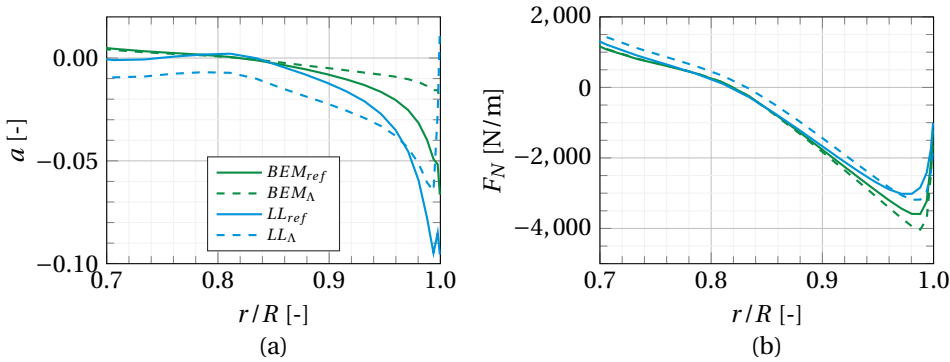


Figure 2.15: Spanwise distribution of axial induction (a) and normal force (b), case: $U_{\infty} = 25 \text{ m s}^{-1}$, $\lambda = 3.8$, $\beta_{pitch} = 22.91^{\circ}$, $z_{start} = 0.5R$, $y_{tip} = -0.2R$, $\gamma = 2$

2.5. CONCLUSIONS

In the present chapter, an efficient correction model is presented that enables BEM codes to approximate the changes of axial induction due to blade sweep. The model consists of two separate corrections, one of which corrects for the altered trailed vorticity system and the other for the self-induction of the curved bound vortex. The former correction is based on the assumption that these changes in induction can be summarised in the altered release point of the tip vortex. This effect is modelled by adding/subtracting the induction of a straight vortex filament representing the displacement of the tip vortex to/from the induction of the helical tip vortex filament. Since no analytical solution exists for the induction of a semi-infinite helical vortex filament, an approximation of the Kawada-Hardin equations describing the induction of an infinite helical vortex filament is divided by two. While the introduced inaccuracy is demonstrated to be small, the model would, nonetheless, benefit from the derivation of an analytical solution of the velocity induced by a semi-infinite helical vortex filament.

The influence of the curved bound vortex on itself is accounted for by evaluating the Biot-Savart expression for the swept bound vortex with unit circulation during the initialisation of the BEM simulation. The thus calculated induced velocity per circulation strength is stored as property of the individual blade elements. This relative velocity is multiplied by the local circulation to obtain an approximation of the velocity induced by the entire curved bound vortex.

The proposed correction function is placed inside the iterative loop of a BEM algorithm, ensuring that the effect of sweep is accounted for during the convergence procedure. Additionally, the streamtube-independent approach of BEM is retained, and thus, only minimal additional computational effort is introduced.

Simulations of the IEA 15 MW reference wind turbine using the extended BEM algorithm are compared to a lifting line model with prescribed wake. For the reference case of a straight blade, good agreement is found between BEM and lifting line model regarding the distribution of circulation, induction, and local forces. Due to its ability to model the three-dimensional blade axis and rotor wake, the lifting line model can predict the



changes in induction introduced by the blade sweep. Aft swept geometries result in a reduced axial induction particularly around the tip while forward swept geometries exhibit increased induction values. When the curved bound vortex is accounted for, the changes in induction at the tip are counteracted by a change of induction with inverted sign around the sweep starting point. This effect leads to a load redistribution for swept blade geometries.

Initially, a set of swept blade geometries with varying sweep start position and tip displacement (both forward and aft sweep) are simulated at rated conditions. The trends of increased/decreased axial induction, as calculated by the lifting line, are approximated well with the correction model used in the BEM simulations. Consequently, the circulation distribution and the local blade loads are also in very good agreement between the two numerical models. In the second part of the study, simulations are conducted along the operational range of the wind turbine. Limitations to the proposed model are found for wind speeds far above rated. In such conditions, low axial induction occurs, and the scaling due to the sweep correction function has limited effect. Furthermore, the circulation distribution departs from the favourable shape of constant values along large parts of the blade for high wind speeds. Hence, the assumption of the sweep correction model that most of the vorticity is trailed at the blade tip and root is being violated.

2.A. NOMENCLATURE

Latin letters	continues on next page...
A_{ann}	Annulus area
a, a'	Axial and tangential induction factor
a_{rotor}	Rotor-averaged axial induction factor
C_T	Rotor thrust coefficient
D	Rotor diameter
dl	Finite length of vortex filament
F_N, F_T	Normal and tangential force
F_{tip}, F_{root}	Prandtl tip and root correction factor
h	Absolute helix pitch
I_m, K_m	Modified Bessel function of first and second kind
K	Regularisation function
L_{wake}	Rotor wake length
l	Relative helix pitch
M_f	Flapwise moment
m	Order of Bessel functions
N_{annuli}	Number of annuli
N_b	Number of blades
R	Blade tip radius
r	Radial coordinate
r_c	Viscous core radius
r_{root}	Blade root radius
\mathbf{r}	Distance vector (Biot-Savart law)

Latin letters

...continued

U_∞	Freestream velocity
u	Axial induced velocity
\mathbf{V}	Velocity vector
x, y, z	Global cartesian coordinates
x_B, y_B, z_B	Local blade cartesian coordinates
y_P, z_P	Coordinates of evaluation point
y_{tip}	Tip displacement of swept blade
y_V, z_V	Coordinates of tip vortex starting point
y_Λ	Edgewise blade sweep
z_{start}	Sweep starting position

Greek letters

β_{pitch}	Blade pitch angle
Γ	Circulation
γ	Sweep exponent
δ	Helix lead angle
θ	Azimuthal angle
θ_1, θ_2	Angles between vortex filament and distance vector to evaluation point
Λ	Sweep angle
λ, λ_r	Rotor and local tip-speed ratio
ρ	Density of air
χ, χ_n	General and blade specific derived helical coordinate

Subscripts

BEM	BEM simulation
BS	Biot-Savart
ind	Induced velocity
LL	Lifting line simulation
ref	Straight reference blade geometry
VF	Vortex filament
Γ_b	Simulation modelling the bound vortex self-induction
Λ	Swept blade geometry
$\infty/2$	Semi-infinite helical vortex filament



BIBLIOGRAPHY

- [1] K. Suzuki, S. Schmitz, and J.-J. Chattot. “Analysis of a swept wind turbine blade using a hybrid Navier–Stokes/Vortex-Panel model”. In: *Computational Fluid Dynamics 2010*. Springer Berlin Heidelberg, 2011, pp. 213–218. DOI: [10.1007/978-3-642-17884-9_25](https://doi.org/10.1007/978-3-642-17884-9_25).
- [2] M. N. Kaya, F. Kose, D. Ingham, L. Ma, and M. Pourkashanian. “Aerodynamic performance of a horizontal axis wind turbine with forward and backward swept blades”. In: *Journal of Wind Engineering and Industrial Aerodynamics* 176 (May 2018), pp. 166–173. DOI: [10.1016/j.jweia.2018.03.023](https://doi.org/10.1016/j.jweia.2018.03.023).
- [3] J.-J. Chattot. “Effects of blade tip modifications on wind turbine performance using vortex model”. In: *Computers & Fluids* 38.7 (Aug. 2009), pp. 1405–1410. DOI: [10.1016/j.compfluid.2008.01.022](https://doi.org/10.1016/j.compfluid.2008.01.022).
- [4] N. Picot, D. Verelst, and T. Larsen. “Free yawing stall-controlled downwind wind turbine with swept blades and coned rotor”. In: *European Wind Energy Conference and Exhibition 2011, EWEC 2011* (Jan. 2011).
- [5] M. Sessarego, N. Ramos-García, and W. Z. Shen. “Analysis of winglets and sweep on wind turbine blades using a lifting line vortex particle method in complex inflow conditions”. In: *Journal of Physics: Conference Series* 1037 (June 2018), p. 022021. DOI: [10.1088/1742-6596/1037/2/022021](https://doi.org/10.1088/1742-6596/1037/2/022021).
- [6] S. Larwood, C. van Dam, and D. Schow. “Design studies of swept wind turbine blades”. In: *Renewable Energy* 71 (Nov. 2014), pp. 563–571. DOI: [10.1016/j.renene.2014.05.050](https://doi.org/10.1016/j.renene.2014.05.050).
- [7] D. R. Verelst and T. J. Larsen. *Load consequences when sweeping blades - A case study of a 5 MW pitch controlled wind turbine*. Tech. rep. RISO-R-1724(EN). Technical University of Denmark, Risø National Laboratory for Sustainable Energy. Wind Energy Division, Roskilde (Denmark), 2010.
- [8] F. Grasso, A. van Garrel, and G. Schepers. “Development and validation of generalized lifting line based code for wind turbine aerodynamics”. In: *49th AIAA aerospace sciences meeting including the new horizons forum and aerospace exposition*. American Institute of Aeronautics and Astronautics, Jan. 2011. DOI: [10.2514/6.2011-146](https://doi.org/10.2514/6.2011-146).
- [9] A. Li, G. Pirrung, H. A. Madsen, M. Gaunaa, and F. Zahle. “Fast trailed and bound vorticity modeling of swept wind turbine blades”. In: *Journal of Physics: Conference Series* 1037 (June 2018), p. 062012. DOI: [10.1088/1742-6596/1037/6/062012](https://doi.org/10.1088/1742-6596/1037/6/062012).
- [10] H. A. Madsen and F. Rasmussen. “A near wake model for trailing vorticity compared with the blade element momentum theory”. In: *Wind Energy* 7.4 (2004), pp. 325–341. DOI: [10.1002/we.131](https://doi.org/10.1002/we.131).



- [11] G. R. Pirrung, H. A. Madsen, T. Kim, and J. Heinz. “A coupled near and far wake model for wind turbine aerodynamics”. In: *Wind Energy* 19.11 (Mar. 2016), pp. 2053–2069. DOI: [10.1002/we.1969](https://doi.org/10.1002/we.1969).
- [12] A. Li, G. R. Pirrung, M. Gaunaa, H. A. Madsen, and S. G. Horcas. “A computationally efficient engineering aerodynamic model for swept wind turbine blades”. In: *Wind Energy Science* 7.1 (Aug. 2021), pp. 129–160. DOI: [10.5194/wes-2021-96](https://doi.org/10.5194/wes-2021-96).
- [13] M. Zuteck. *Adaptive blade concept assessment: Curved platform induced twist investigation*. Tech. rep. SAND2002-2996. Sandia National Laboratories, Oct. 2002. DOI: [10.2172/803289](https://doi.org/10.2172/803289).
- [14] M. Hansen. “Aeroelastic properties of backward swept blades”. In: *49th AIAA aerospace sciences meeting including the new horizons forum and aerospace exposition*. American Institute of Aeronautics and Astronautics, Jan. 2011. DOI: [10.2514/6.2011-260](https://doi.org/10.2514/6.2011-260).
- [15] T. Burton, D. Sharpe, N. Jenkins, and E. Bossanyi. *Wind Energy Handbook*. John Wiley & Sons, June 2011. ISBN: 978-1-119-99392-6.
- [16] A. van Garrel. *Development of a wind turbine aerodynamics simulation module*. Tech. rep. ECN-C-03-079. Petten, Netherlands: Energy Research Center of the Netherlands, 2003.
- [17] S. Kawada. “Induced velocity by helical vortices”. In: *Journal of the Aeronautical Sciences* 3.3 (Jan. 1936), pp. 86–87. DOI: [10.2514/8.141](https://doi.org/10.2514/8.141).
- [18] J. C. Hardin. “The velocity field induced by a helical vortex filament”. In: *Physics of Fluids* 25.11 (1982), p. 1949. DOI: [10.1063/1.863684](https://doi.org/10.1063/1.863684).
- [19] Y. Fukumoto, V. L. Okulov, and D. H. Wood. “The contribution of kawada to the analytical solution for the velocity induced by a helical vortex filament”. In: *Applied Mechanics Reviews* 67.6 (Nov. 2015). DOI: [10.1115/1.4031964](https://doi.org/10.1115/1.4031964).
- [20] V. L. Okulov. “On the stability of multiple helical vortices”. In: *Journal of Fluid Mechanics* 521 (Dec. 2004), pp. 319–342. DOI: [10.1017/s0022112004001934](https://doi.org/10.1017/s0022112004001934).
- [21] D. Wood, V. Okulov, and D. Bhattacharjee. “Direct calculation of wind turbine tip loss”. In: *Renewable Energy* 95 (Sept. 2016), pp. 269–276. DOI: [10.1016/j.renene.2016.04.017](https://doi.org/10.1016/j.renene.2016.04.017).
- [22] D. Wood, V. Okulov, and J. Vaz. “Calculation of the induced velocities in lifting line analyses of propellers and turbines”. In: *Ocean Engineering* 235 (Sept. 2021), p. 109337. DOI: [10.1016/j.oceaneng.2021.109337](https://doi.org/10.1016/j.oceaneng.2021.109337).
- [23] D. Wood. “Wake expansion and the finite blade functions for horizontal-axis wind turbines”. In: *Energies* 14.22 (Nov. 2021), p. 7653. DOI: [10.3390/en14227653](https://doi.org/10.3390/en14227653).
- [24] E. Branlard. *Wind turbine aerodynamics and vorticity-based methods*. Springer International Publishing, 2017. ISBN: 978-3-319-85583-7. DOI: [10.1007/978-3-319-55164-7](https://doi.org/10.1007/978-3-319-55164-7).
- [25] J. Katz and A. Plotkin. *Low-speed aerodynamics*. Cambridge University Press, Feb. 2001. ISBN: 978-0-511-81032-9. DOI: [10.1017/cbo9780511810329](https://doi.org/10.1017/cbo9780511810329).

- [26] E. Gaertner et al. *Definition of the IEA wind 15-megawatt offshore reference wind turbine*. Tech. rep. NREL/TP-5000-75698. Golden, CO, US: National Renewable Energy Laboratory, 2020.
- [27] E. Gaertner et al. *Definition of the IEA wind 15-megawatt offshore reference wind turbine, GitHub repository*.
- [28] J. Schepers, T. Lutz, K. Boorsma, S. Gomez-Iradi, I. Herraes, L. Oggiano, H. Rahimi, P. Schaffarczyk, G. Pirrung, H. A. Madsen, et al. *Final report of IEA Wind Task 29 Mexnext (phase 3)*. Tech. rep. ECN-E-18-003. Energy Research Center of the Netherlands, 2018.
- [29] J. Schepers et al. *IEA Wind TCP Task 29, phase IV: Detailed aerodynamics of wind turbines*. Tech. rep. Zenodo, 2021. DOI: [10.5281/ZENODO.4817875](https://doi.org/10.5281/ZENODO.4817875).



3

THE REFERENCE WIND TUNNEL EXPERIMENT WITH STRAIGHT BLADES

The previous chapter discusses the effect of blade sweep on blade aerodynamics in the context of numerical modelling. Chapters 3 and 4 examine blade aerodynamics from an experimental point of view. The present chapter formulates the basis for this discussion, i.e. it describes an experiment on a three-bladed HAWT with straight blades. As such, a baseline case is created and analysed. Chapter 4 builds upon the findings discussed here by presenting the results of a second experimental campaign on the same turbine but equipped with swept blades.

The experiment is conducted on a performance-scaled version of the IEA 15 MW reference wind turbine. Particle image velocimetry is used to measure the flow field around cross-sections at multiple radial locations. The blades are characterised aerodynamically in terms of circulation, induction terms, inflow angle, angle of attack and blade loads. As such, this chapter provides an extensive experimental database, that can be used to validate numerical models aiming to simulate a turbine whose non-dimensionalised thrust distribution resembles that of the IEA 15 MW reference wind turbine.

After an introduction in Section 3.1, Section 3.2 details the methodology. This includes a description of the scaled model geometry, the measurement setup, and the methods used to derive the blade aerodynamic quantities from the flow field data. Finally, the experimental results are presented in Section 3.3 and the main conclusions drawn from this experimental campaign are given in Section 3.4.

Parts of this chapter have been published in E. Fritz, A. Ribeiro, K. Boorsma, C. Ferreira, *Aerodynamic characterisation of a thrust-scaled IEA 15 MW wind turbine model: experimental insights using PIV data*, *Wind Energy Science* 9, 5 (2024).



3.1. INTRODUCTION

Wind tunnel experiments are vital in progressing horizontal axis wind turbine (HAWT) technology. They help in improving the understanding of, e.g. the turbine's aerodynamic, aeroelastic or acoustic characteristics. Equally important, the gathered data can be used to validate and improve numerical models that aim to simulate reality as closely as possible.

In light of these two goals, arguably, the two most relevant experiments on HAWTs are the Unsteady Aerodynamics Experiment (UAE) and the Model Rotor Experiment in Controlled Conditions (MEXICO). NREL executed the UAE in multiple phases. While Phases I - IV, conducted between 1989 and 1997, were field experiments [1, 2], Phase VI was a wind tunnel experiment conducted in 2000. A two-bladed rotor of 10 m diameter was heavily instrumented and placed in the NASA Ames wind tunnel [3]. The MEXICO experiment was conducted in 2006 in the German-Dutch Wind Tunnel (DNW). Detailed aerodynamic measurements, including pressure, loads and 3D flow field characteristics using particle image velocimetry (PIV) were taken on a three-bladed rotor with 4.5 m diameter [4, 5]. Its successor project "New Mexico" was conducted in 2014 to obtain additional data [6]. The results of these two experimental campaigns have been analysed in great detail and have been used for the validation and calibration of simulation tools of varying fidelity. For an extensive review of the literature related to these two experiments, the reader is referred to the work of Schepers and Schreck [7].

Given the success of these two experiments, the existing databases were extended by conducting further experiments on scaled versions of the two rotors. The wake of a 1:8 scaled version of the UAE Phase VI rotor was measured using PIV by Xiao et al. [8]. At the Korean Aerospace Research Institute (KARI), Cho and Kim tested the Reynolds number effect on torque and power on a 1:5 scaled model of the UAE Phase VI turbine [9]. Comparable experiments were done by the same researchers for a 2:4.5 scaled version of the MEXICO rotor [10]. The Spanish National Institute for Aerospace Technology (INTA) tested a 1:4 scaled MEXICO rotor and their results of the scaled models were compared against the original MEXICO data in IEA Task 29 [11].

Complementary to experimental investigations, HAWTs are studied extensively using numerical simulations. To enable numerical benchmarks between different simulation tools and to facilitate collaboration between academic and industrial research, multiple reference wind turbine (RWT) models have been developed in recent years, e.g. the NREL 5 MW RWT [12], the DTU 10 MW RWT [13] and the IEA 15 MW RWT [14]. While not representing existing wind turbines, these open-source reference models reflect current trends and developments of HAWT technology. Wind tunnel campaigns with scaled versions of these reference wind turbines have been conducted to provide experimental datasets that can be used to validate numerical simulations. Berger et al. developed a model turbine based on the NREL 5 MW RWT [15], which has since been used to study dynamic inflow phenomena due to pitch steps [16] and fluid-structure interaction by means of photogrammetry [17, 18]. Fontanella et al. ran experiments on a scaled DTU 10 MW wind turbine mimicking the motions of a floating offshore wind turbine (FOWT) [19]. In addition to load cell measurements on the turbine, the wake was characterised using PIV measurements. Similar experiments were conducted by Taruffi et al., extending the mimicked floater motions to six degrees of freedom and larger am-

plitudes and frequencies [20]. Fontanella et al. performed another set of experiments on a 1:100 scaled model of the IEA 15 MW RWT developed by Allen et al. [21, 22]. Here, rotor loads were measured using load cells, and the wake was characterised using hot-wire velocity measurements. A 1:70 scaled model of the IEA 15 MW RWT was tested by Kimball et al. with a focus on verifying thrust and torque curves and validating the utilised pitch controller [23]. While these studies on scaled-down versions of the RWTs provide valuable data regarding rotor-level aerodynamics, they lack more detailed data on the blade level.

Such blade-level data can be obtained using non-intrusive measurement techniques such as laser Doppler velocimetry (LDV) or stereoscopic particle image velocimetry (SPIV). Phengpom et al. studied the flow field in the direct vicinity of the blade using LDV [24, 25, 26]. Akay et al. researched the vortex structure around the blade root of a two-bladed wind turbine with a 2 m diameter based on SPIV measurements [27]. Similarly, Lignarolo et al. investigated the wake development of a smaller model (two blades, 0.6 m diameter) focusing on the tip vortices [28]. Continuing this line of research, the generation of the tip vortex was investigated in more detail on a different two-bladed wind turbine model of 2 m diameter by Micallef et al. [29, 30]. Furthermore, and most relevant to the present work, SPIV was employed to derive the spanwise blade load distribution of a HAWT in axial and yawed inflow by del Campo et al. [31, 32].

This chapter studies the spanwise aerodynamic characteristics of a 1:133 scaled model of the IEA 15 MW RWT, and thus of the most recent available reference wind turbine. SPIV is used to measure the flow field around various radial sections of the blade and, consequently to derive the spanwise aerodynamic properties of this model wind turbine. By characterising the blades in terms of induction values, inflow angle and angle of attack, circulation, and blade loads, this study provides a more complete dataset of blade-level aerodynamics than previous wind tunnel experiments. As such, this research aims to enable further multi-fidelity numerical benchmarking as well as to establish a reference dataset that can be used as a starting point for future experimental studies on this wind tunnel model turbine.

3.2. METHODOLOGY

3.2.1. SCALED WIND TURBINE MODEL

The model HAWT tested in this experiment is a scaled version of the IEA 15 MW RWT [14], preserving non-dimensional thrust. The main model characteristics are given in Table 3.1 alongside their full-scale equivalents.

Table 3.1: Specifications of the IEA 15 MW RWT and the scaled wind tunnel model

Parameter		IEA 15 MW RWT	Wind tunnel model
Rotor diameter	D	240 m	1.8 m
Blade root radius	r_{root}	3 m	0.06 m
Design tip-speed ratio	λ	9 -	9 -

The geometric scaling factor of 1:133 applied to the rotor diameter cannot be main-



tained at the blade root. Here, mechanical and electronic components necessitate a larger blade root radius leading to a scaling factor of 1:50. The ratio of root to tip radius is in close agreement with comparable wind tunnel models, see [21].

Multiple challenges occur when creating a scaled-down wind tunnel model of a wind turbine. Arguably, the largest challenge lies in the fact that the chord Reynolds number Re_c present on a full-scale wind turbine generally cannot be achieved in a wind tunnel. A difference in Re_c of multiple orders of magnitude necessitates the use of airfoils designed explicitly for low Reynolds numbers. One such airfoil is the *SD7032* airfoil, which has a maximum relative thickness of 10 % and was characterised experimentally by Fontanella et al. [33]. The lift and drag coefficient of the *SD7032* airfoil for different Reynolds numbers is given in Figure 3.1. A characteristic of this airfoil making it useful for small-scale wind turbines is the relative insensitivity of the lift polar to the Reynolds number over a large range of angles of attack. The well documented wind tunnel polars as well as the airfoil's application in comparable wind tunnel campaigns [23, 21] motivated the choice for the *SD7032* airfoil.

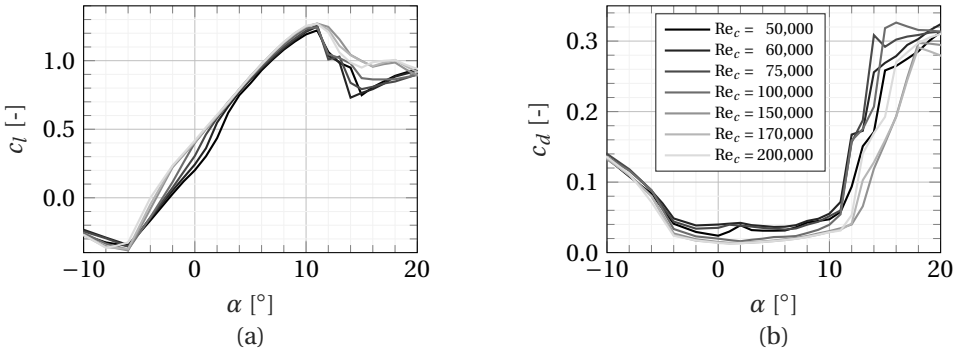


Figure 3.1: Lift coefficient c_l (a) and drag coefficient c_d (b) of the *SD7032* airfoil for varying Reynolds numbers [33]

Instead of using various airfoils along the span, the developed model blades are defined by this single airfoil, which transitions into a cylindrical section at the blade root. The polars of the wind tunnel model differ from those of the airfoils used on the full-scale turbine. Thus, even at identical angles of attack, the non-dimensionalised lift distribution will differ between the model and original. Bayati et al. detail a scaling approach designed to ensure comparable non-dimensionalised blade loads [34]. In this approach, the model chord distribution c_M is calculated as

$$c_M = \frac{c_O}{\lambda_L} \frac{Kl_O}{Kl_M}, \quad (3.1)$$

where c_O is the original chord distribution, λ_L is the geometric scaling factor, and Kl_O and Kl_M are the lift slopes in the linear region of the original and model airfoil polars, respectively. The model twist distribution β_M is calculated as

$$\beta_M = \beta_O - \frac{c_{l,O}^0}{Kl_O} + \frac{c_{l,M}^0}{Kl_M}, \quad (3.2)$$

where β_O is the original twist distribution and $c_{l,O}^0$ and $c_{l,M}^0$ are the lift coefficient values at zero angle of attack of the original and model airfoil polars, respectively.

Since the IEA 15 MW RWT's blade is very slender, applying this scaling approach leads to blades with very small chord values. Using the *SD7032* airfoil to create the geometry, such low chord values entail very thin blades. To avoid unnecessary challenges during the manufacturing process of the wind tunnel model blades, a constant factor is applied to the chord scaling so that

$$c_M = \frac{c_O}{\lambda_L} \frac{Kl_O}{Kl_M} C_c, \quad (3.3)$$

with $C_c = 1.5$. Furthermore, this factor ensures angles of attack well away from the stall margin of the *SD7032* airfoil. Inboard of $r/R = 0.25$, a cubic spline is used to reduce the chord to a cylindrical root section with $D_{root} = 4$ cm. This is a common practice for scaled wind tunnel models [34, 35] motivated by manufacturing and assembly constraints, and it is expected to have little impact on rotor aerodynamics due to the generally lower aerodynamic forces acting in the root region.

Rather than matching the lift force, a comparable thrust distribution along the blade is targeted. Therefore, equal thrust coefficient distributions $C_T = \frac{F_N dr}{\frac{1}{2}\rho U_\infty^2 2\pi r dr}$ are enforced.

$$\frac{F_{N,M}}{\rho U_{\infty,M}^2 \pi r_M} = \frac{F_{N,O}}{\rho U_{\infty,O}^2 \pi r_O} \quad (3.4a)$$

$$F_{N,M} = \frac{U_{\infty,M}^2}{U_{\infty,O}^2} \frac{r_M}{r_O} F_{N,O} \quad (3.4b)$$

F_N is the axial force per unit span, ρ is the density of air, U_∞ is the freestream velocity and r is the radial coordinate. The local axial force coefficient c_N can be expressed as

$$c_N = \frac{F_N}{\frac{1}{2}\rho V_{rel}^2 c} = c_l \cos(\phi) + c_d \sin(\phi), \quad (3.5)$$

with V_{rel} being the local relative inflow velocity, ϕ being the local inflow angle, and c_l and c_d the lift and drag coefficients, respectively. Substituting Equation 3.4b in Equation 3.5 yields a minimum function with β_M as variable.

$$\min_{\beta_M} = c_{N,M}(\alpha_M) - c_{N,O}(\alpha_O) \quad (3.6a)$$

$$\min_{\beta_M} = c_{l,M}(\phi_O - \beta_M) \cos(\phi_O) + c_{d,M}(\phi_O - \beta_M) \sin(\phi_O) - \frac{U_{\infty,M}^2}{U_{\infty,O}^2} \frac{r_M}{r_O} \frac{F_{N,O}}{\frac{1}{2}\rho V_{rel,M}^2 c_M} \quad (3.6b)$$

Here, $V_{rel,M} = \sqrt{(U_{\infty,M}(1 - a_O))^2 + (\omega_M r_M(1 + a'_O))^2}$, with a_O and a'_O being the axial and tangential induction factors, respectively, and ω the angular rotation frequency. Based on Equation 3.6b, the model twist distribution can be determined. The original flow properties ϕ_O , $F_{N,O}$, a_O and a'_O are taken from numerical simulations of the full-scale IEA 15 MW RWT based on blade element momentum theory (BEM). The underlying algorithm has been used for simulations of the IEA 15 MW RWT in Chapter 2, where it was



validated against the established lifting line algorithm AWSM [36]. For these simulations, an inflow velocity of $U_{\infty,O} = 10 \text{ m s}^{-1}$ is chosen, corresponding to operation just below rated. $U_{\infty,M}$ is set to match the targeted wind tunnel inflow velocity. The resulting chord and twist distributions of the wind tunnel model blade are given in Figure 3.2.

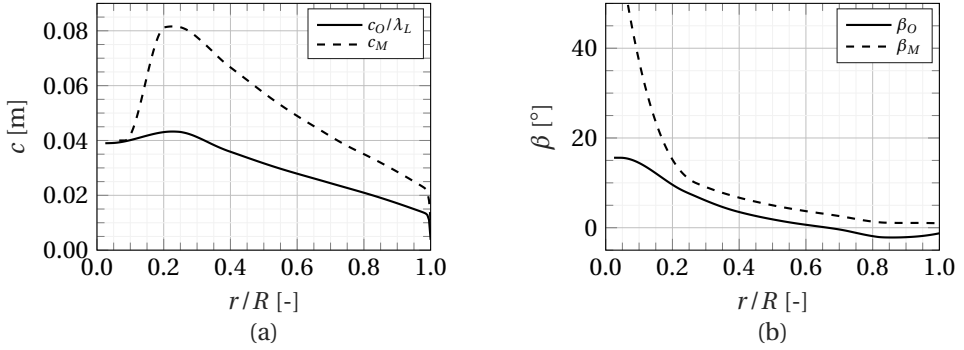


Figure 3.2: Chord (a) and twist (b) distribution of the geometrically scaled IEA 15 MW RWT and the wind tunnel model

The presented scaling approach ensures close resemblance of the model's non-dimensionalised thrust distribution to that of its reference. It should, however, be noted that other flow physics, such as flow transition or separation, can be fundamentally different due to the changes in airfoil and chord Reynolds number.

3.2.2. EXPERIMENTAL SETUP AND MEASUREMENT SYSTEM

The experiments were conducted in the Open Jet Facility at the TU Delft Faculty of Aerospace Engineering, which is a closed-circuit open jet wind tunnel. The jet exit is an octagon of $2.85 \text{ m} \times 2.85 \text{ m}$. A schematic of the OJF is given in Figure 3.3. The turbine was operated at an approximate tip-speed ratio of $\lambda = 9$ and an inflow velocity of $U_{\infty} = 3.75 \text{ m s}^{-1}$. To achieve the desired tip-speed ratio, the turbine is driven by a motor that closely maintains the set rotational speed. Inflow conditions of the wind tunnel were logged for each measurement point and showed no significant variation. The wind tunnel was kept at a constant temperature of 20°C .

In this campaign, SPIV was used to non-intrusively measure the flow around the blades. A Quantel EverGreen double-pulsed neodymium-doped yttrium aluminium garnet (Nd:YAG) laser provides the light source. Using laser optics, a thin vertical laser sheet was generated that illuminates the area around the targeted blade cross-section. To reduce reflections of the laser, the blades and most other turbine components were spray-painted matt black. A Safex smoke generator produced smoke particles with a median diameter of $1 \mu\text{m}$, which were used as tracers. The smoke generator was placed downstream of the tunnel test section, ensuring homogeneous mixing during the flow recirculation.

Two LaVision Imager sCMOS cameras with lenses of 105 mm focal length and an aperture of $f/8$ captured the illuminated particles during the two laser pulses. The laser and cameras were simultaneously triggered by an optical sensor that was activated by

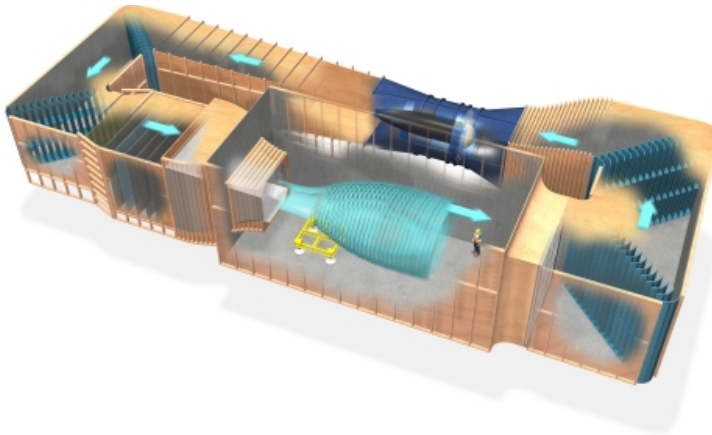


Figure 3.3: Schematic of the Open Jet Facility at TU Delft

a notch in the rotor shaft once per revolution. A time delay between the optical sensor's signal and the laser/camera trigger ensured the blade was in the horizontal position during its upward movement when taking the images. The image pairs were taken with a time separation of $150\ \mu\text{s}$, which allowed the tracing of the particles' movement. This time separation is equivalent to a particle movement of approximately 5 pixels and a turbine rotation of 0.3° . At each measurement location, 120 phase-locked images were taken, which are used in post-processing to obtain an average flow field and its standard deviation. The images are acquired and processed using the LaVision DaVis 8 software. The field of view (FOV) resulting from this measurement setup is approximately $FOV \approx 297\ \text{mm} \times 257\ \text{mm}$ and the final image resolution is $8.81\ \text{pixels mm}^{-1}$.

Both cameras and laser were mounted rigidly on a traversing system. This way, velocity measurements could be conducted at multiple radial stations without the need to refocus the cameras and calibrate the software. Figure 3.4 shows a schematic of the measurement setup.

A total of 22 measurement planes were placed along the blade span as follows:

- $\Delta r/R = 0.100$ for $0.10 \leq r/R \leq 0.40$
- $\Delta r/R = 0.050$ for $0.40 \leq r/R \leq 0.80$
- $\Delta r/R = 0.025$ for $0.80 \leq r/R \leq 1.05$

This selection aims at accurately representing the stronger gradients in blade aerodynamics typically present close to the tip. At four radial locations, namely at $r/R = [0.4, 0.6, 0.8, 0.9]$, measurements were taken for all three blades to evaluate how representative the main measurement blade is for the remaining two blades.

When illuminating a cross-section, the blade cast a shadow where no particles could be traced. Thus, the flow field was captured in two steps. In a first step, the blade's pressure side was evaluated by placing the laser upstream of the turbine and angling the laser sheet downstream. Following that, the laser was relocated downstream of the rotor



plane and its laser sheet was tilted upstream to capture the suction side (as shown in Figure 3.4). In a post-processing step, the two flow fields averaged individually over the phase-locked upstream and downstream images were stitched together, resulting in the entire flow field around a blade cross-section.

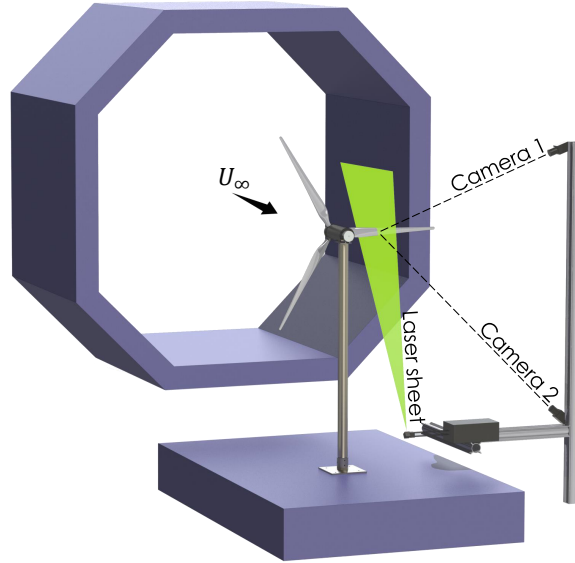


Figure 3.4: Experimental setup and measurement system

3.2.3. DERIVING BLADE-LEVEL AERODYNAMICS FROM PIV MEASUREMENTS

This section presents the equations used to derive the distributed blade aerodynamics regarding bound circulation, induction, inflow angle and angle of attack, and blade loads. Based on these quantities, it is possible to calculate the experimental lift polar, too. In this study, the equations presented below are applied under the assumption of local two-dimensional flow; i.e. only the velocity components in the measurement plane are considered.

DETERMINATION OF BOUND CIRCULATION

The bound circulation Γ at each measurement location can be calculated as the line integral of the measured velocity field \mathbf{u} along a curve S enclosing the blade cross-section [e.g. 37, p. 176].

$$\Gamma = - \oint_S \mathbf{u} \cdot d\mathbf{s} \quad (3.7)$$

A study of the sensitivity to the bounding curve's size is presented in Appendix 3.A. It revealed that the circulation, and also the forces calculated using Noca's method (see Section 3.2.3), do not exhibit perfect convergence with varying control volume size. As a consequence, the methods presented in this section are applied for multiple control

volumes with different sizes, from which a mean value and standard deviation are calculated.

DETERMINATION OF INDUCED VELOCITIES, INFLOW ANGLE AND ANGLE OF ATTACK

Several methods for determining the local inflow conditions exist. The inverse BEM approach [38, 39, 40] uses measured/simulated forces as input to the blade element momentum equations and iteratively solves for the inflow conditions. Other methods characterise the inflow based on the annulus average flow field [41, 42] or based on the wake induction at the plane exactly between two blades [43]. Other approaches use the bound circulation strength to estimate local induced velocity and consequently the inflow conditions [44, 45, 46]. Several benchmarks of these methods have been conducted based on CFD and/or experimental data [47, 43, 48].

The approach denoted as the Ferreira-Micallef method in [48] is used here. It relies on potential flow theory to estimate the induced velocities at each spanwise location. This theory states that the velocity at any point can be expressed by the sum of the relative velocity and the velocities induced by free and bound vorticity such that the measured velocity at a point p is given as

$$\mathbf{u}_p = \sum \mathbf{u}_{ind} + \mathbf{V}_{rel}. \quad (3.8)$$

The Biot-Savart law is employed to determine the sum of the induced velocities at a set of control points located along S so that

$$\sum \mathbf{u}_{ind} = \sum \frac{\Gamma}{2\pi} \frac{\mathbf{x}_p - \mathbf{x}}{|\mathbf{x}_p - \mathbf{x}|^2}, \quad (3.9)$$

where \mathbf{x}_p and \mathbf{x} are the position vectors of the control point and inducing vortex element, respectively. By minimising the error between \mathbf{u}_p and \mathbf{u}_{ind} using a least-squares approach, the relative inflow vector \mathbf{V}_{rel} is determined, yielding the local axial and tangential induction factors.

$$a = 1 - \frac{u_{rel}}{U_\infty} \quad (3.10)$$

$$a' = \frac{v_{rel}}{\omega r} \quad (3.11)$$

Knowing the induced velocities, the local inflow angle and angle of attack can then be calculated as

$$\phi = \tan^{-1} \left(\frac{U_\infty(1-a)}{\omega r(1+a')} \right) \quad (3.12)$$

$$\alpha = \phi - \beta. \quad (3.13)$$

DETERMINATION OF BLADE LOADS

Noca's method:

The forces exerted by an immersed body on the surrounding fluid can be evaluated by integrating the change of momentum over a finite control volume. Noca et al. presented an alternative formulation of the momentum conservation equation, solely relying on



surface integrals of flow quantities placed on the boundary of the control volume [49]. The forces can thus be derived from the measured velocity field and its spatial and time derivatives. This approach has been successfully applied to PIV data collected on a vertical-axis wind turbine by LeBlanc and Ferreira [50]. The force per density is given by

$$\frac{\mathbf{F}}{\rho} = \oint_S \mathbf{n} \cdot \boldsymbol{\gamma} ds - \oint_{S_B} \mathbf{n} \cdot (\mathbf{u} - \mathbf{u}_B) \mathbf{u} ds - \frac{d}{dt} \oint_{S_B} \mathbf{n} \cdot (\mathbf{u}\mathbf{x}) ds, \quad (3.14)$$

where \mathbf{n} is the normal vector of the bounding curve, $\boldsymbol{\gamma}$ is the flux term, S is the outer boundary curve of the control volume surrounding the immersed body, S_B is the control volume's inner boundary curve prescribed by the immersed body's surface, and \mathbf{u}_B is the velocity vector of the immersed body's surface.

The term $\oint_{S_B} \mathbf{n} \cdot (\mathbf{u} - \mathbf{u}_B) \mathbf{u} ds$ is related to the flow through the inner boundary curve S_B . Given the solid airfoil surface, this term is zero. The third term $\frac{d}{dt} \oint_{S_B} \mathbf{n} \cdot (\mathbf{u}\mathbf{x}) ds$ describes the force due to acceleration of the inner boundary surface. As the model wind turbine was running at a constant speed during the experiment, the velocity of the airfoil representing the inner boundary surface can be approximated as constant within the measurement plane. Therefore, this term is zero, too. The flux term $\boldsymbol{\gamma}$ can be determined as

$$\begin{aligned} \boldsymbol{\gamma} = & \frac{1}{2} u^2 \mathbf{I} - \mathbf{u}\mathbf{u} - \frac{1}{\mathcal{N}-1} \mathbf{u}(\mathbf{x} \times \boldsymbol{\omega}) + \frac{1}{\mathcal{N}-1} \boldsymbol{\omega}(\mathbf{x} \times \mathbf{u}) \\ & - \frac{1}{\mathcal{N}-1} \left(\mathbf{x} \cdot \frac{\partial \mathbf{u}}{\partial t} \right) \mathbf{I} + \frac{1}{\mathcal{N}-1} \mathbf{x} \frac{\partial \mathbf{u}}{\partial t} - \frac{\partial \mathbf{u}}{\partial t} \mathbf{x} \\ & + \frac{1}{\mathcal{N}-1} [\mathbf{x} \cdot (\nabla \cdot \boldsymbol{\tau})] \mathbf{I} - \frac{1}{\mathcal{N}-1} \mathbf{x} (\nabla \cdot \boldsymbol{\tau}) + \boldsymbol{\tau}, \end{aligned} \quad (3.15)$$

where \mathbf{I} is the identity matrix, \mathcal{N} is the dimensional constant, $\boldsymbol{\omega}$ is the vorticity vector and $\boldsymbol{\tau}$ is the Reynolds stress tensor.

There are two possible frames of reference in which to apply the equations given above. On the one hand, a stationary reference frame can be chosen, where the measured blade cross-section moves vertically through the control volume, see Figure 3.5 (a). On the other hand, a reference frame rotating with the investigated cross-section can be used, see Figure 3.5 (b). While the original PIV data are captured in a stationary reference frame, they can easily be converted to a rotating frame by adding the apparent rotational velocity $V_{rot} = -\omega r$ to the measured vertical velocity component v .

For the analysis performed in the present work, a rotating frame of reference is chosen. In this reference frame, the time derivatives of Equation 3.15 are zero.

Kutta-Joukowski theorem (KJ):

Alternatively to Noca's method, the forces can be derived from the bound circulation using the Kutta-Joukowski theorem [e.g. 37, p. 282], which states that the sectional lift force is given by $L = \rho V_{rel} \Gamma$. This formulation can be decomposed to yield the forces normal and tangential to the rotor plane.

$$F_N = \rho \omega r (1 + a') \Gamma \quad (3.16)$$

$$F_T = \rho U_\infty (1 - a) \Gamma \quad (3.17)$$

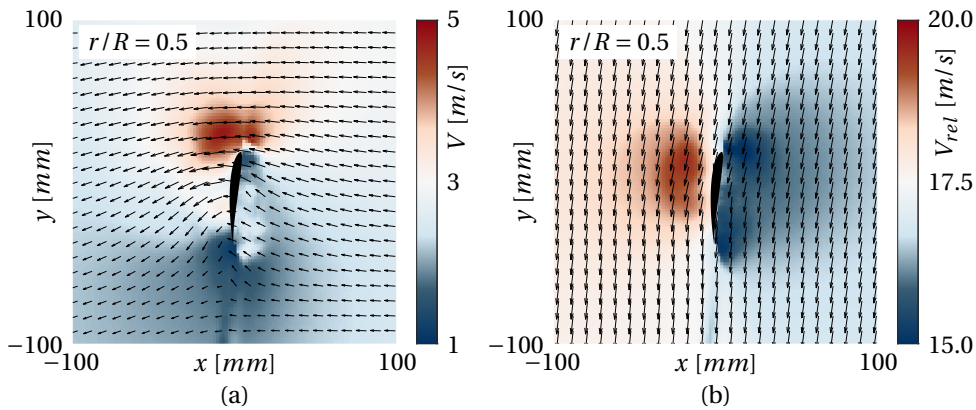


Figure 3.5: Velocity field in a stationary (a) and rotating (b) reference frame

It should be noted that the Kutta-Joukowski theorem is based on potential flow theory. Thus, e.g. the viscous drag contribution to the tangential force is neglected.

3.3. RESULTS

3.3.1. DETERMINATION OF THE COMBINED PITCH AND TWIST OFFSET

The blades used in this experiment are made of vacuum-infused carbon-fibre-reinforced material. This partially manual manufacturing approach led to minor differences between the three blades. Based on visual inspection, one blade was chosen on which the measurement campaign was mainly conducted, hereafter called blade 1. However, measurements were taken for blades 2 and 3 at $r/R = [0.4, 0.6, 0.8, 0.9]$ to estimate the main measurement blade's representation of the other two blades.

Early investigations into the gathered data indicated non-negligible differences in blade aerodynamics between the three blades. To explain this behaviour, the blade cross-sections visible in the raw images were visually inspected and compared against the original design of the blade. This approach is visualised in Figure 3.6 (a), where the blade cross-section is illuminated in white. The original design is overlaid as red airfoil shape. Then, the correct local twist is found by rotating this airfoil around the trailing edge until its pressure side approximately follows the same curve as the pressure side of the illuminated cross-section. This correction was determined with a precision of 0.1° . The corrected airfoil is shown in green. Based on this comparison, it became apparent that the blade cross-sections were positioned at different angles than designed, resulting in the offset in twist and pitch shown in Figure 3.6 (b).

For blade 1, where many data points are available along the span, a quadratic fit is used to describe the trend and balance out the fluctuations likely due to human error in the interpretation of the raw images. Blade 1 appears to have a pitch offset of approximately -1° and additionally shows slight twist deformation towards the tip. More extreme twist deformations can be observed for blades 2 and 3, with opposite directions.



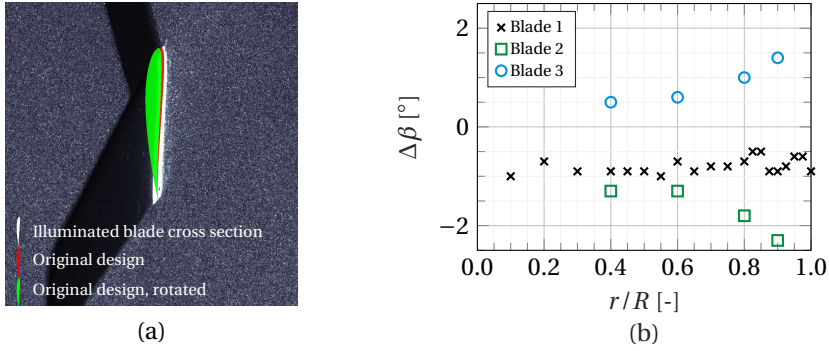


Figure 3.6: Approach of determining actual local airfoil orientation (a), twist and pitch offset determined by comparing experimentally captured blade cross-sections to the original design (b)

This shows how challenging the use of vacuum-infused carbon-fibre composite blades is. Despite having the same fibre lay-up, the manufacturing process is a highly manual task where minor differences can impact the structural properties of the blade. The pitch offset can be explained by the model turbine's connection between blade root and hub: the turbine is equipped with a manual pitch mechanism which is fixed in the desired position using set screws. Despite being used with care, this manual mechanism is likely the origin of the pitch deviations between the three blades. As these deviations from the intended design were only found in post-processing after the campaign had ended, no correction to the pitch angle could be made anymore.

3.3.2. FLOW FIELDS

The flow fields represent the primary data collected during this experiment using stereoscopic PIV. Figure 3.7 depicts the measured velocity magnitude fields at the four radial stations where data for all three blades are available. Overall, the general flow patterns are in good agreement. However, the twist and pitch offset described in the previous section leads to differences in the angle of attack, explaining minor discrepancies in velocity magnitudes. For example, blade 2, exhibiting twist deformations towards higher angles of attack, induces higher velocities, while the opposite holds for blade 3.

Notably, many measurement points have low-velocity regions close to the suction side surface. Here, laser reflections from the blade surface reduce the accuracy of the PIV processing. This is less the case on the pressure side, where the concave blade surface causes lower reflections.

3.3.3. BLADE AERODYNAMICS

All plots presented in this section contain error bars. These represent the 95% confidence interval and are based on variations in the measured velocity field during the capturing of the PIV images as well as in the processing with various control volume sizes, see Appendix 3.A. This uncertainty is a measure of both the quality of the phase lock and the unsteadiness of the flow. While almost all data points have very low uncertainty, the

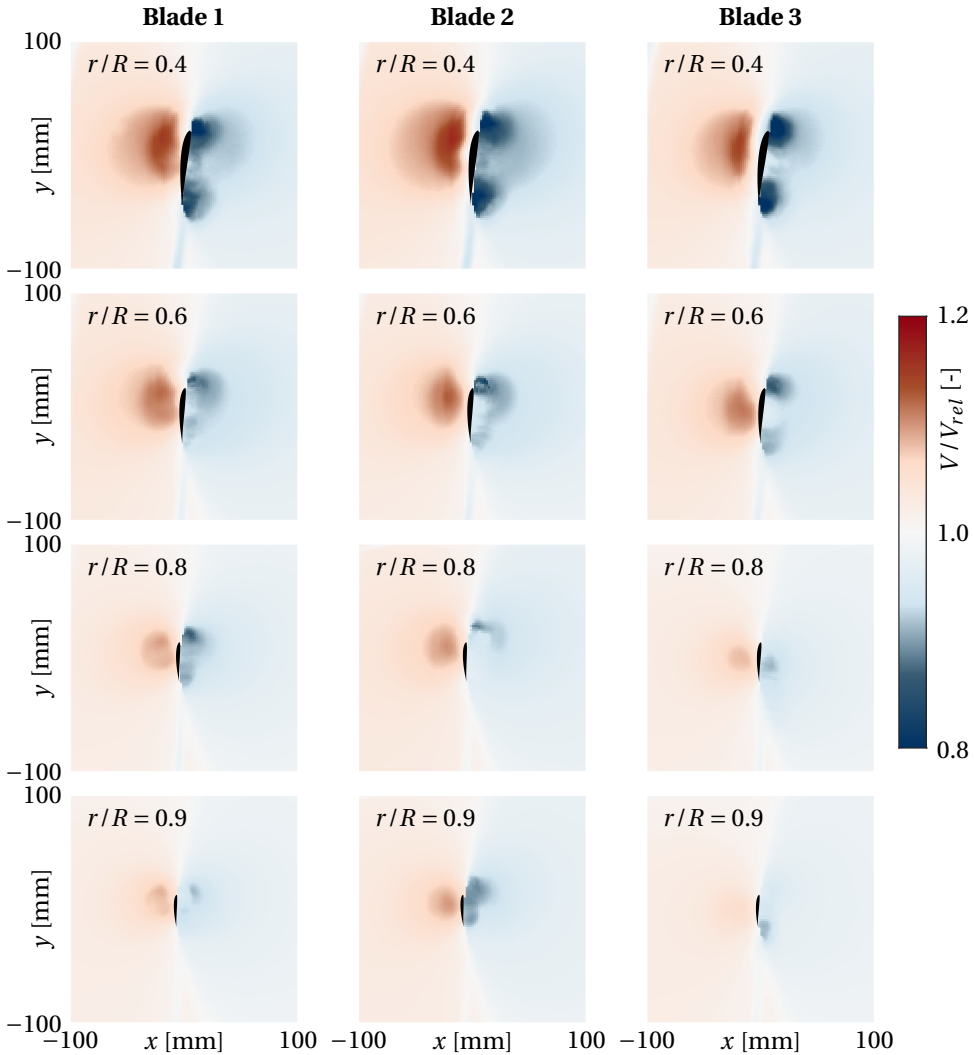


Figure 3.7: Non-dimensionalised velocity magnitudes at the radial stations measured for all three blades

measurement point closest to the root suffers from the laser reflecting off the nacelle and hub, increasing measurement uncertainty. This effect is visible to a varying degree in all derived aerodynamic quantities.

Figure 3.8 shows the circulation distribution of the three blades. The effect of varying pitch angles and twist deflection expresses itself in the different circulation levels of the three individual blades.

The axial and tangential induction factor distribution is shown in Figure 3.9. Compared to the circulation distribution, differences in induction are minor between the



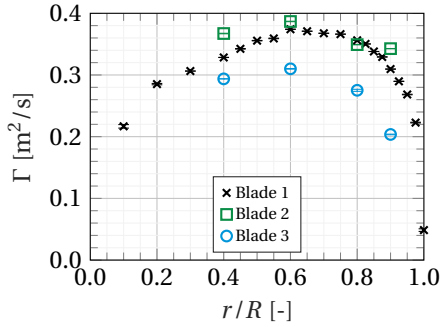


Figure 3.8: Spanwise distribution of bound circulation, error bars representing the 95% confidence interval

three blades. This is a significant finding in support of fundamental BEM theory, which uses a rotor-averaged induction factor.

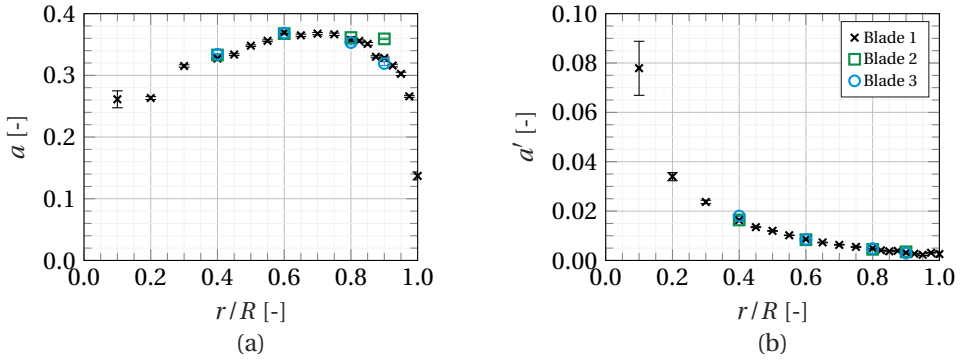


Figure 3.9: Spanwise distribution of axial (a) and tangential (b) induction factors, error bars representing the 95% confidence interval

Figure 3.10 depicts the local inflow angle and angle of attack distribution. Given that the blades have a cylindrical cross-section at $r/R = 0.1$, the value of the angle of attack at this location is meaningless and reported for completeness only. The angle of attack distribution is evidently influenced by the pitch and twist variations between the three blades. Despite these variations, all derived angles of attack are well within the linear region of the design airfoil's lift polar.

The axial and tangential force distributions are presented in Figure 3.11. Two methods are employed to derive the normal force distribution, namely Noca's method and the Kutta-Joukowski theorem (KJ). Both methods are in close agreement; a linear fit between the results of all three blades yields $F_{N,KJ} = 1.02 F_{N,Noca} - 0.39$ with $R^2 = 0.9965$. By integrating the normal force distribution, the rotor thrust can be calculated and non-dimensionalised to obtain the thrust coefficient. To this end, piecewise cubic curves are fit to the experimental results. Where no data are available at blade root and tip, zero loading is assumed. The resulting thrust coefficients are $C_{T,Noca} = 0.82$ and $C_{T,KJ} = 0.78$.

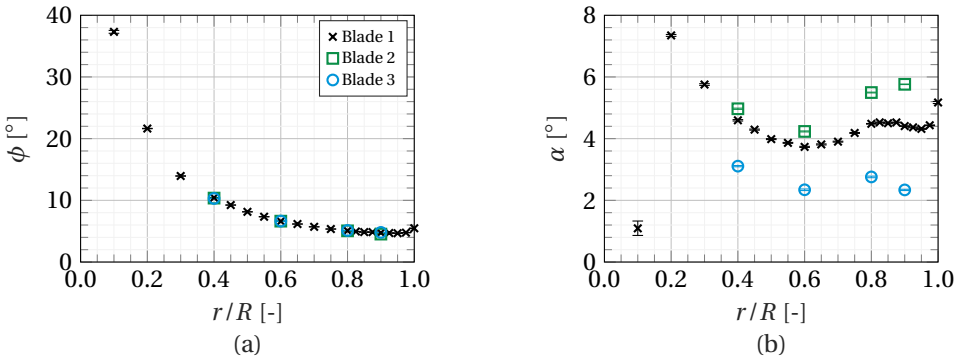


Figure 3.10: Spanwise distribution of inflow angle (a) and angle of attack (b), error bars representing the 95% confidence interval

For a tip-speed ratio of $\lambda = 9$, the IEA 15 MW RWT has a thrust coefficient of $C_T = 0.8$ [14]. Thus, the relative deviation of the thrust-scaled blades to their reference corresponds to $\Delta C_{T,Noca} = 2.1\%$ and $\Delta C_{T,KJ} = -2.2\%$, respectively.

As demonstrated in Appendix 3.A, Noca’s method is, however, unreliable when estimating the tangential force from this experimental dataset. Therefore, only the tangential force derived using the Kutta-Joukowski theorem is presented here. It is noteworthy, that this method neglects viscous effects and consequently misses the contribution of the viscous drag. Overall, the normal and tangential force trends are consistent between the three blades. However, the magnitude is fairly different, with blade 2 having, on average, slightly higher values than blade 1, while blade 3 exhibits lower values than the other two blades. These differences are in line with the pitch and twist offset discussed in Section 3.3.1.

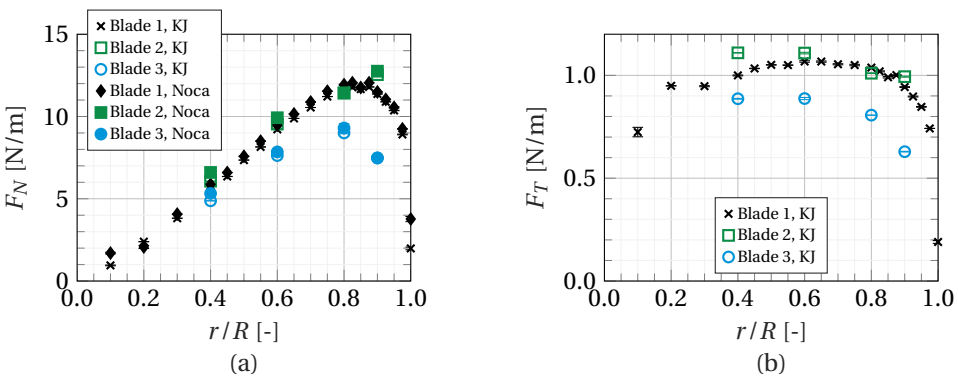


Figure 3.11: Spanwise distribution of normal (a) and tangential (b) force, error bars representing the 95% confidence interval



3.3.4. LIFT POLAR

Based on the aerodynamic quantities presented in the previous section, the lift coefficient is derived. The lift force is calculated using the force distributions based on the Kutta-Joukowski theorem.

$$c_l = \frac{F_{N,KJ} \cos(\phi) + F_{T,KJ} \sin(\phi)}{\frac{1}{2} \rho V_{rel}^2 c} \quad (3.18)$$

Figure 3.12 (a) shows the experimental lift polar compared to the *SD7032* airfoil [33], at Reynolds numbers resembling those present in this experiment, which varies between approximately 40,000 and 65,000 depending on the radial position. For clarity, only the mean values are reported. The two measurements closest to the root are omitted as these cross-sections are defined by a cylinder and a blend between a cylinder and the *SD7032* airfoil. Additionally, the two measurements closest to the tip are omitted because the tip vortex causes highly three-dimensional flow features, which should not be compared to two-dimensional airfoil polars. The remaining measurement points are in good agreement with the lift coefficient curve of the design airfoil.

While giving an indication of the experimentally derived lift polar, Figure 3.12 (a) does not represent the variable Reynolds number along the blade. Alternatively, the design airfoil polars can be interpolated for the experimentally derived Reynolds number and angle of attack to obtain a polar-based, expected lift coefficient $c_{l,pol}$. These values are plotted alongside the lift coefficient based on the measured forces and the spanwise distribution of the chord Reynolds number in Figure 3.12 (b). It demonstrates that, in the root and tip region, the blades used in this experiment produce less lift than would be expected. It can be hypothesised that this is a consequence of differences in surface finish between the used blades and the airfoil measured by [19], as well as minor inaccuracies in the manually produced geometry.

3.4. CONCLUSIONS

This chapter presents the results from an experimental campaign on a thrust-scaled version of the IEA 15 MW RWT. Particle image velocimetry is used to measure the flow field at multiple radial stations around the blade. Various aerodynamic blade properties are derived directly from the measured flow field along a closed curve around the blade cross-sections: the circulation is determined from the velocity integral, the inflow conditions by removing the blade induction from the measured flow field using elemental potential flow solutions, and the forces based on Noca's method and the Kutta-Joukowski theorem.

Early analyses revealed that the blades were mounted with minor deviations from the desired pitch angle and, on top of that, exhibited twist deformations. This leads to considerable differences in the angle of attack and consequently blade loads among the three blades, which is consistently reflected in their experimentally derived spanwise distributions. In contrast, the derived induction values remain nearly constant between the three blades, indicating that induction can be considered a rotor-averaged phenomenon. This is an experimental confirmation of one of the fundamental assumptions in blade element momentum theory.

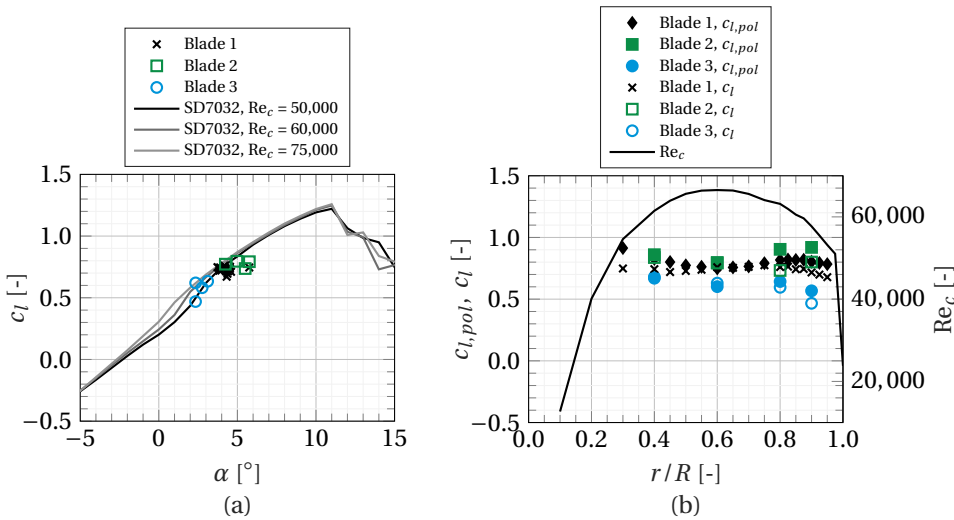


Figure 3.12: Experimental lift polar compared to the *SD7032* airfoil lift polar (a) and comparison between the lift coefficient derived from measured forces to that expected based on the design lift polars, alongside the chord Reynolds number distribution (b)

The dataset created in this wind tunnel experiment fully characterises the three blades in terms of the surrounding flow field, bound circulation, local inflow conditions and blade loads. The normal force distributions derived using Noca’s method and the Kutta-Joukowski theorem were found to be in good agreement. Knowing these aerodynamic parameters, it can be demonstrated that the lift coefficient measured along the span follows the trend of the lift polar used in the blade design. There are, however, slight deficits in lift production in the root and tip regions compared to the expected values based on the design airfoil’s lift polar.

The experimental data presented here can be used in future numeric model validation studies. It provides data relevant for validating low-fidelity models, such as algorithms based on blade element momentum theory or lifting line theory, and for mid-to high-fidelity models, such as panel codes and computational fluid dynamics. Since the model blade is based on the IEA 15 MW RWT, the non-dimensionalised loads resemble the current state of the art of real offshore wind turbines and numerical reference models.

3.A. SENSITIVITY TO CHOSEN CONTROL VOLUME

In this study, the blade’s aerodynamic quantities are determined by interrogating flow information along a closed curve enclosing the investigated blade cross-section. A circular curve is chosen with the blade cross-section positioned in its centre. To verify the methods presented in Section 3.2.3, a panel code developed by Ribeiro et al. [51] based on the work of Katz and Plotkin [52] is used to replicate the wind tunnel experiment numerically. The panel code simulates the three-dimensional surface of the blade and



can be used to derive flow fields at locations equivalent to the measurement planes of the experiment. Such results then offer the opportunity to derive circulation and loads based on the velocity field around the blade ("indirect") but also from the aerodynamic solution on the blade ("direct"). By comparing these two approaches, the methods for deriving aerodynamic quantities from the flow field can be verified before applying them to the experimental data.

Figure 3.13 shows the sensitivity of the calculated circulation and of the forces based on Noca's method to the control volume's size, given as the ratio of its radius r_{CV} to the local chord, at three radial locations. When calculating the forces based on the Kutta-Joukowski theorem, they are directly proportional to the circulation distribution and are thus not presented here.

The sensitivity is investigated for both the experimental data and the panel code results. Generally, there is a conflict of interest between the data points per control volume size, which favours a large control volume, and the approximation of two-dimensional flow in a flat measurement surface, which favours a small control volume.

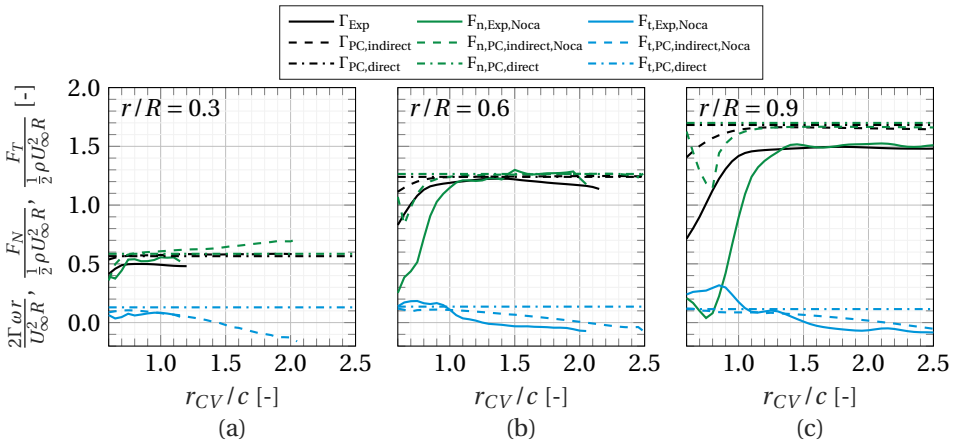


Figure 3.13: Sensitivity of determined blade loads and circulation to the chosen boundary curve size at various radial stations

For the panel code results (PC), it can be observed that the indirectly determined circulation converges against the directly determined value with increasing control volume size. For the normal force, this is only true for the two outboard sections shown in Figure 3.13 (b) and (c). The discrepancy between the direct and indirect approach at the inboard section can be attributed to the increasing flow curvature in this region, which stands in contrast to the two-dimensional control volume.

In contrast to circulation and normal force, the tangential force does not converge anywhere along the span but rather decreases with increasing control volume size. The high tip-speed ratio of the model turbine entails very low torque values and the tangential force is very small. As such, the momentum change corresponding to the tangential force is difficult to capture with the Noca method. Based on this finding, only the tangential force calculated via the Kutta-Joukowski theorem is presented in this chapter.

The circulation and forces determined based on the experimental data largely follow the same trends observed for the panel code results. However, given the less clean flow field, the convergence is not as steady and shows slight deviations even after the initial, clearly unconverged ramp. This is particularly true for the forces calculated using Noca's method, which relies on sensitive derivatives of the velocity field. To limit the influence of the control volume, the convergence is evaluated individually for each measurement plane and the endpoint of the initial convergence ramp is identified. The aerodynamic quantities are determined for multiple control volumes with sizes beyond the initial convergence ramp and then averaged over these. This approach yields the results presented in Section 3.3.3. It should further be noted, that for the experimental results, the largest possible control volume is dictated by the available field of view. Thus, the convergence of methods such as Noca's should be taken into consideration when defining the PIV setup and consequently the field of view.

3.B. NOMENCLATURE

Latin letters

a, a'	Axial and tangential induction factor
C_c	Chord scaling constant
C_T	Thrust coefficient
c	Chord
c_l, c_d	Lift and drag coefficient
c_l^0	Lift coefficient at zero angle of attack
D	Rotor diameter, drag force
D_{root}	Diameter of the blade root section
\mathbf{F}	Force vector
F_N, F_T	Normal and tangential force
\mathbf{I}	Identity matrix
Kl	Lift slope
L	Lift force
\mathcal{N}	Dimensional constant
\mathbf{n}	Normal vector
R	Blade tip radius
Re_c	Chord Reynolds number
r	Radial coordinate
r_{root}	Blade root radius
S, S_B	Outer and inner boundary curve of a control volume
t	Time
U_∞	Freestream velocity
\mathbf{u}	Velocity vector
u, v	Velocity components
V_{rel}	Relative inflow velocity
V_{rot}	Rotational velocity
\mathbf{x}	Position vector



Greek letters and other symbols

α	Angle of attack
β	Blade twist angle
Γ	Circulation
γ	Flux term
λ	Tip-speed ratio
λ_L	Geometric scaling factor
ρ	Density of air
τ	Reynolds stress tensor
ϕ	Inflow angle
ω	Angular velocity
$\boldsymbol{\omega}$	Vorticity vector
∇	Nabla operator

Subscripts

CV	Control volume
ind	Induced
KJ	Kutta-Joukowski
M	Model
O	Original
pol	Based on design polars

BIBLIOGRAPHY

- [1] C. Butterfield, W. Musial, and D. Simms. *Combined experiment phase I. Final report*. Tech. rep. NREL/TP-257-4655. National Renewable Energy Laboratory (NREL), Oct. 1992. DOI: [10.2172/10105837](https://doi.org/10.2172/10105837).
- [2] D. A. Simms, M. M. Hand, L. J. Fingersh, and D. W. Jager. *Unsteady aerodynamics experiment phases II-IV test configurations and available data campaigns*. Tech. rep. NREL/TP-500-25950. National Renewable Energy Laboratory, Aug. 1999. DOI: [10.2172/12144](https://doi.org/10.2172/12144).
- [3] M. M. Hand, D. A. Simms, L. J. Fingersh, D. W. Jager, J. R. Cotrell, S. Schreck, and S. M. Larwood. *Unsteady aerodynamics experiment phase VI: Wind tunnel test configurations and available data campaigns*. Tech. rep. NREL/TP-500-29955. National Renewable Energy Laboratory, Dec. 2001. DOI: [10.2172/15000240](https://doi.org/10.2172/15000240).
- [4] J. Schepers and H. Snel. *Model experiments in controlled conditions, final report*. Tech. rep. ECN-E-07-042. Energy Research Center of the Netherlands, 2007.
- [5] K. Boorsma and J. Schepers. *Description of experimental set-up. Mexico measurements*. Tech. rep. ECN-X-09-0XX. Energy Research Center of the Netherlands, 2009.
- [6] K. Boorsma and J. Schepers. *Description of experimental setup, New Mexico experiment*. Tech. rep. ECN-X15-093. Energy Research Center of the Netherlands, 2015.
- [7] J. G. Schepers and S. J. Schreck. “Aerodynamic measurements on wind turbines”. In: *Wiley Interdisciplinary Reviews: Energy and Environment* 8.1 (Aug. 2018), e320. DOI: [10.1002/wene.320](https://doi.org/10.1002/wene.320).
- [8] J.-p. Xiao, J. Wu, L. Chen, and Z.-y. Shi. “Particle image velocimetry (PIV) measurements of tip vortex wake structure of wind turbine”. In: *Applied Mathematics and Mechanics* 32.6 (June 2011), pp. 729–738. DOI: [10.1007/s10483-011-1452-x](https://doi.org/10.1007/s10483-011-1452-x).
- [9] T. Cho and C. Kim. “Wind tunnel test for the NREL phase VI rotor with 2 m diameter”. In: *Renewable Energy* 65 (May 2014), pp. 265–274. DOI: [10.1016/j.renene.2013.10.009](https://doi.org/10.1016/j.renene.2013.10.009).
- [10] T. Cho and C. Kim. “Wind tunnel test results for a 2/4.5 scale MEXICO rotor”. In: *Renewable Energy* 42 (June 2012), pp. 152–156. DOI: [10.1016/j.renene.2011.08.031](https://doi.org/10.1016/j.renene.2011.08.031).
- [11] J. Schepers, K. Boorsma, T. Cho, S. Gomez-Iradi, P. Schaffarczyk, W. Shen, T. Lutz, B. Stoevesandt, S. Schreck, D. Micallef, et al. *Analysis of mexico wind tunnel measurements. Final report of IEA task 29, mexnext (phase 1)*. Tech. rep. ECN-E-12-004. Energy Research Center of the Netherlands, 2012.



- [12] J. Jonkman, S. Butterfield, W. Musial, and G. Scott. *Definition of a 5-MW Reference Wind Turbine for Offshore System Development*. Tech. rep. NREL/TP-500-38060. National Renewable Energy Laboratory, Feb. 2009. DOI: [10.2172/947422](https://doi.org/10.2172/947422).
- [13] C. Bak, F. Zahle, R. Bitsche, T. Kim, A. Yde, L. C. Henriksen, M. H. Hansen, J. P. A. A. Blasques, M. Gaunaa, and A. Natarajan. “The DTU 10-MW Reference Wind Turbine”. In: *Danish Wind Power Research 2013*. 2013.
- [14] E. Gaertner et al. *Definition of the IEA wind 15-megawatt offshore reference wind turbine*. Tech. rep. NREL/TP-5000-75698. Golden, CO, US: National Renewable Energy Laboratory, 2020.
- [15] F. Berger, L. Kröger, D. Onnen, V. Petrović, and M. Kühn. “Scaled wind turbine setup in a turbulent wind tunnel”. In: *Journal of Physics: Conference Series* 1104 (Oct. 2018), p. 012026. ISSN: 1742-6588, 1742-6596. DOI: [10.1088/1742-6596/1104/1/012026](https://doi.org/10.1088/1742-6596/1104/1/012026).
- [16] F. Berger, D. Onnen, G. Schepers, and M. Kühn. “Experimental analysis of radially resolved dynamic inflow effects due to pitch steps”. In: *Wind Energy Science* 6.6 (Nov. 2021), pp. 1341–1361. ISSN: 2366-7451. DOI: [10.5194/wes-6-1341-2021](https://doi.org/10.5194/wes-6-1341-2021).
- [17] A. Langidis et al. “Design and evaluation of rotor blades for fluid structure interaction studies in wind tunnel conditions”. In: *Journal of Physics: Conference Series* 2265.2 (May 2022), p. 022079. ISSN: 1742-6588, 1742-6596. DOI: [10.1088/1742-6596/2265/2/022079](https://doi.org/10.1088/1742-6596/2265/2/022079).
- [18] S. Nietiedt, T. T. B. Wester, A. Langidis, L. Kröger, R. Rofallski, M. Göring, M. Kühn, G. Gülker, and T. Luhmann. “A Wind Tunnel Setup for Fluid-Structure Interaction Measurements Using Optical Methods”. In: *Sensors* 22.13 (July 2022), p. 5014. ISSN: 1424-8220. DOI: [10.3390/s22135014](https://doi.org/10.3390/s22135014).
- [19] A. Fontanella, I. Bayati, R. Mikkelsen, M. Belloli, and A. Zasso. “UNAFLOW: a holistic wind tunnel experiment about the aerodynamic response of floating wind turbines under imposed surge motion”. In: *Wind Energy Science* 6.5 (Sept. 2021), pp. 1169–1190. ISSN: 2366-7443. DOI: [10.5194/wes-6-1169-2021](https://doi.org/10.5194/wes-6-1169-2021).
- [20] F. Taruffi, F. Novais, and A. Viré. “An experimental study on the aerodynamic loads of a floating offshore wind turbine under imposed motions”. In: *Wind Energy Science* 9.2 (Feb. 2024), pp. 343–358. ISSN: 2366-7443. DOI: [10.5194/wes-9-343-2024](https://doi.org/10.5194/wes-9-343-2024).
- [21] A. Fontanella, A. Facchinetti, S. Di Carlo, and M. Belloli. “Wind tunnel investigation of the aerodynamic response of two 15 MW floating wind turbines”. In: *Wind Energy Science* 7.4 (Aug. 2022), pp. 1711–1729. ISSN: 2366-7443. DOI: [10.5194/wes-7-1711-2022](https://doi.org/10.5194/wes-7-1711-2022).
- [22] C. Allen, A. Viscelli, H. Dagher, A. Goupee, E. Gaertner, N. Abbas, M. Hall, and G. Barter. *Definition of the UMaine VoltturnUS-S Reference Platform Developed for the IEA Wind 15-Megawatt Offshore Reference Wind Turbine*. Tech. rep. NREL/TP-5000-76773. National Renewable Energy Lab. (NREL), Golden, CO (United States); Univ. of Maine, Orono, ME (United States), July 2020. DOI: [10.2172/1660012](https://doi.org/10.2172/1660012).

- [23] R. Kimball, A. Robertson, M. Fowler, N. Mendoza, A. Wright, A. Goupee, E. Lenfest, and A. Parker. “Results from the FOCAL experiment campaign 1: turbine control co-design”. In: *Journal of Physics: Conference Series* 2265.2 (May 2022), p. 022082. ISSN: 1742-6596. DOI: [10.1088/1742-6596/2265/2/022082](https://doi.org/10.1088/1742-6596/2265/2/022082).
- [24] T. Phengpom, Y. Kamada, T. Maeda, J. Murata, S. Nishimura, and T. Matsuno. “Study on blade surface flow around wind turbine by using LDV measurements”. In: *Journal of Thermal Science* 24.2 (Mar. 2015), pp. 131–139. DOI: [10.1007/s11630-015-0765-3](https://doi.org/10.1007/s11630-015-0765-3).
- [25] T. Phengpom, Y. Kamada, T. Maeda, J. Murata, S. Nishimura, and T. Matsuno. “Experimental investigation of the three-dimensional flow field in the vicinity of a rotating blade”. In: *Journal of Fluid Science and Technology* 10.2 (2015). DOI: [10.1299/jfst.2015jfst0013](https://doi.org/10.1299/jfst.2015jfst0013).
- [26] T. Phengpom, Y. Kamada, T. Maeda, T. Matsuno, and N. Sugimoto. “Analysis of wind turbine pressure distribution and 3D flows visualization on rotating condition”. In: *IOSR Journal of engineering* 6.02 (2016), pp. 18–30.
- [27] B. Akay, D. Ragni, C. S. Ferreira, and G. van Bussel. “Experimental investigation of the root flow in a horizontal axis wind turbine”. In: *Wind Energy* 17.7 (Apr. 2013), pp. 1093–1109. DOI: [10.1002/we.1620](https://doi.org/10.1002/we.1620).
- [28] L. Lignarolo, D. Ragni, C. Krishnaswami, Q. Chen, C. S. Ferreira, and G. van Bussel. “Experimental analysis of the wake of a horizontal-axis wind-turbine model”. In: *Renewable Energy* 70 (Oct. 2014), pp. 31–46. DOI: [10.1016/j.renene.2014.01.020](https://doi.org/10.1016/j.renene.2014.01.020).
- [29] D. Micallef, B. Akay, C. S. Ferreira, T. Sant, and G. van Bussel. “The origins of a wind turbine tip vortex”. In: *Journal of Physics: Conference Series* 555 (Nov. 2014), p. 012074. DOI: [10.1088/1742-6596/555/1/012074](https://doi.org/10.1088/1742-6596/555/1/012074).
- [30] D. Micallef, C. S. Ferreira, T. Sant, and G. van Bussel. “Experimental and numerical investigation of tip vortex generation and evolution on horizontal axis wind turbines”. In: *Wind Energy* 19.8 (Sept. 2015), pp. 1485–1501. DOI: [10.1002/we.1932](https://doi.org/10.1002/we.1932).
- [31] V. del Campo, D. Ragni, D. Micallef, B. Akay, F. J. Diez, and C. Simão Ferreira. “3D load estimation on a horizontal axis wind turbine using SPIV”. In: *Wind Energy* 17.11 (2014), pp. 1645–1657. ISSN: 1099-1824. DOI: [10.1002/we.1658](https://doi.org/10.1002/we.1658).
- [32] V. del Campo, D. Ragni, D. Micallef, F. J. Diez, and C. J. S. Ferreira. “Estimation of loads on a horizontal axis wind turbine operating in yawed flow conditions”. In: *Wind Energy* 18.11 (2015), pp. 1875–1891. ISSN: 1099-1824. DOI: [10.1002/we.1794](https://doi.org/10.1002/we.1794).
- [33] A. Fontanella, I. Bayati, R. Mikkelsen, M. Belloli, and A. Zasso. *UNAFLOW: Unsteady Aerodynamics of FLOating Wind turbines*. May 2021. DOI: [10.5281/zenodo.4740006](https://doi.org/10.5281/zenodo.4740006).
- [34] I. Bayati, M. Belloli, L. Bernini, and A. Zasso. “Aerodynamic design methodology for wind tunnel tests of wind turbine rotors”. In: *Journal of Wind Engineering and Industrial Aerodynamics* 167 (Aug. 2017), pp. 217–227. ISSN: 0167-6105. DOI: [10.1016/j.jweia.2017.05.004](https://doi.org/10.1016/j.jweia.2017.05.004).



- [35] S. Muggiasca, F. Taruffi, A. Fontanella, S. Di Carlo, and M. Belloli. “Aerodynamic and Structural Strategies for the Rotor Design of a Wind Turbine Scaled Model”. In: *Energies* 14.8 (Jan. 2021), p. 2119. ISSN: 1996-1073. DOI: [10.3390/en14082119](https://doi.org/10.3390/en14082119).
- [36] F. Grasso, A. van Garrel, and G. Schepers. “Development and validation of generalized lifting line based code for wind turbine aerodynamics”. In: *49th AIAA aerospace sciences meeting including the new horizons forum and aerospace exposition*. American Institute of Aeronautics and Astronautics, Jan. 2011. DOI: [10.2514/6.2011-146](https://doi.org/10.2514/6.2011-146).
- [37] J. D. Anderson. *Fundamentals of aerodynamics*. Sixth. McGraw-Hill series in aeronautical and aerospace engineering. New York, NY: McGraw-Hill Education, 2017. ISBN: 978-1-259-12991-9.
- [38] A. Bruining, G. Van Bussel, G. Corten, and W. Timmer. “Pressure distribution from a wind turbine blade; field measurements compared to 2-Dimensional wind tunnel data”. In: *Institute for Windenergy, Delft University of Technology* (1993).
- [39] H. Snel, R. Houwink, and T. Bosscher. *Sectional prediction of lift coefficients on rotating wind turbine blades in stall*. Tech. rep. ECN-C-93-052. Energy Research Center of the Netherlands, 1994.
- [40] C. Bak, J. Johansen, and P. B. Andersen. “Three-dimensional corrections of airfoil characteristics based on pressure distributions”. In: *Proceedings of the european wind energy conference*. 2006, pp. 1–10.
- [41] M. O. L. Hansen and J. Johansen. “Tip studies using CFD and comparison with tip loss models”. In: *Wind Energy* 7.4 (2004), pp. 343–356. DOI: [10.1002/we.126](https://doi.org/10.1002/we.126).
- [42] J. Johansen and N. N. Sørensen. “Aerofoil characteristics from 3D CFD rotor computations”. In: *Wind Energy* 7.4 (Oct. 2004), pp. 283–294. DOI: [10.1002/we.127](https://doi.org/10.1002/we.127).
- [43] I. Herráez, E. Daniele, and J. G. Schepers. “Extraction of the wake induction and angle of attack on rotating wind turbine blades from PIV and CFD results”. In: *Wind Energy Science* 3.1 (Jan. 2018), pp. 1–9. DOI: [10.5194/wes-3-1-2018](https://doi.org/10.5194/wes-3-1-2018).
- [44] W. Z. Shen, M. O. L. Hansen, and J. N. Sørensen. “Determination of angle of attack (AOA) for rotating blades”. In: *Wind energy*. Springer Berlin Heidelberg, 2007, pp. 205–209. DOI: [10.1007/978-3-540-33866-6_37](https://doi.org/10.1007/978-3-540-33866-6_37).
- [45] W. Z. Shen, M. O. L. Hansen, and J. N. Sørensen. “Determination of the angle of attack on rotor blades”. In: *Wind Energy* 12.1 (Jan. 2009), pp. 91–98. DOI: [10.1002/we.277](https://doi.org/10.1002/we.277).
- [46] E. Jost, L. Klein, H. Leipprand, T. Lutz, and E. Krämer. “Extracting the angle of attack on rotor blades from CFD simulations”. In: *Wind Energy* 21.10 (June 2018), pp. 807–822. DOI: [10.1002/we.2196](https://doi.org/10.1002/we.2196).
- [47] S. Guntur and N. N. Sørensen. “An evaluation of several methods of determining the local angle of attack on wind turbine blades”. In: *Journal of Physics: Conference Series* 555 (Dec. 2014), p. 012045. DOI: [10.1088/1742-6596/555/1/012045](https://doi.org/10.1088/1742-6596/555/1/012045).

- [48] H. Rahimi, J. Schepers, W. Shen, N. R. García, M. Schneider, D. Micallef, C. S. Ferreira, E. Jost, L. Klein, and I. Herráez. “Evaluation of different methods for determining the angle of attack on wind turbine blades with CFD results under axial inflow conditions”. In: *Renewable Energy* 125 (Sept. 2018), pp. 866–876. DOI: [10.1016/j.renene.2018.03.018](https://doi.org/10.1016/j.renene.2018.03.018).
- [49] F. Noca, D. Shiels, and D. Jeon. “A comparison of methods for evaluating time-dependant fluid dynamic forces on bodies, using only velocity fields and their derivatives”. In: *Journal of Fluids and Structures* 13.5 (July 1999), pp. 551–578. ISSN: 0889-9746. DOI: [10.1006/jf1s.1999.0219](https://doi.org/10.1006/jf1s.1999.0219).
- [50] B. LeBlanc and C. Ferreira. “Estimation of blade loads for a variable pitch vertical axis wind turbine from particle image velocimetry”. In: *Wind Energy* 25.2 (2022), pp. 313–332. ISSN: 1099-1824. DOI: [10.1002/we.2674](https://doi.org/10.1002/we.2674).
- [51] A. Ribeiro, D. Casalino, and C. Ferreira. “Surging wind turbine simulations with a free wake panel method”. In: *Journal of physics: Conference series* 2265.4 (2022), p. 042027. DOI: [10.1088/1742-6596/2265/4/042027](https://doi.org/10.1088/1742-6596/2265/4/042027).
- [52] J. Katz and A. Plotkin. *Low-speed aerodynamics*. Cambridge University Press, Feb. 2001. ISBN: 978-0-511-81032-9. DOI: [10.1017/cbo9780511810329](https://doi.org/10.1017/cbo9780511810329).



4

THE WIND TUNNEL EXPERIMENT WITH SWEEPED BLADES

Chapter 3 established an experimental reference case of the scaled IEA 15 MW reference wind turbine with straight blade geometries. In this chapter, the experimental analysis is repeated with swept blades.

Neither experimentally measured flow fields in the vicinity of the blades nor spanwise distributions of aerodynamic quantities were previously available in the scientific community for rotating swept wind turbine blades. Thus, a primary scientific contribution of this chapter lies in the creation of such an experimental dataset for swept blades based on PIV data. As with the straight-bladed case, this dataset can be used for the validation of numerical models of varying fidelity.

Following the introduction in Section 4.1, Section 4.2 of this chapter describes the swept blade geometry used in the experiment, the experimental setup in the wind tunnel, and the methods used to derive the blade aerodynamics from the measured flow fields. In Section 4.3, the experimental results are presented. Conclusions from this experiment with swept blades are presented in Section 4.4.

Parts of this chapter have been published in E. Fritz, K. Boorsma, C. Ferreira, *Experimental analysis of a horizontal-axis wind turbine with swept blades using PIV data*, *Wind Energy Science* **9**, 8 (2024).



4.1. INTRODUCTION

One obstacle in developing swept blades on a state-of-the-art scale is that wind turbine blade design optimisation still largely relies on simulation tools based on blade element momentum theory (BEM). As discussed in Chapter 2, BEM algorithms, in their basic form, however, cannot accurately represent the aerodynamics of swept blades as they inherently assume a straight blade geometry. The developed sweep correction model enables BEM algorithms to account for blade sweep more accurately.

To complement numerical developments, experiments dedicated to studying swept wind turbine blades have been conducted. Barlas et al. tested a non-rotating swept wind turbine tip in a wind tunnel [1] and later on a rotor test rig in the field, which allowed the testing of the tip on a "one-armed" turbine [2]. An experimental study of swept blades on a three-bladed rotor in controlled conditions is yet missing in the literature.

This chapter provides precisely that: A wind tunnel campaign on a HAWT equipped with swept blades. Particle image velocimetry (PIV) is used to measure detailed flow fields in the vicinity of the blades. Blade-level aerodynamics are derived from these flow fields, characterising the blades in terms of circulation, axial and tangential induction, inflow angle and angle of attack, and forces normal and tangential to the rotor plane. As such, the created dataset is suited for the validation of low- to high-fidelity numerical tools. By basing the scaled blade geometry on the aerodynamic characteristics of the IEA 15 MW reference wind turbine (RWT) [3], the relevance for current research interests of the wind energy community is ensured. For example, this reference turbine is being studied extensively in the ongoing IEA task 47 [4].

4.2. METHODOLOGY

4.2.1. SCALED WIND TURBINE MODEL

The wind tunnel model used for this study is a horizontal axis wind turbine with a rotor diameter of $D = 1.8 \text{ m}$. It is, with the exception of blade sweep, identical to that presented in Chapter 3. The swept blades are derived from the straight reference blade by gradually displacing the blade axis in the rotor plane as a function of the coordinate z defined along the blade pitch axis

$$y_{\Lambda} = \begin{cases} 0 & \text{for } z \leq z_{start} \\ y_{tip} \left(\frac{z - z_{start}}{R - z_{start}} \right)^{\gamma} & \text{for } z > z_{start} \end{cases}, \quad (4.1)$$

where R is the blade tip radius. The sweep starting position is chosen as $z_{start} = 0.5 R$, the tip displacement as $y_{tip} = 0.2 R$ and the sweep exponent as $\gamma = 2$. Such tip displacement values would likely be unrealistic on a full-scale, operational wind turbine. For example, the blades tested in the STAR project had a tip radius of 28 m and a tip displacement of 2.2 m, corresponding to $y_{tip} = 0.08 R$ [5]. Nevertheless, this tip sweep is chosen to exaggerate the effect of sweep on the blade's aerodynamic characteristics. This exaggeration is intended to ensure that the effect of sweep exceeds the uncertainties and noise otherwise present in experimental data and, thus, facilitate the validation of numerical models. The local sweep angle can be determined as $\Lambda = \tan^{-1}(\partial y / \partial z)$. The swept blade geometry is generated by locally orienting the airfoils perpendicular to the swept blade

axis. To maintain the same tip radius as the unswept reference blade, the swept-blade axis coordinates are scaled by $z/\sqrt{z^2 + y_\Lambda^2}$. If this were not done, the swept-blade tip radius would be $\sqrt{R^2 + y_{tip}^2}$, and the rotor area of the straight and swept blades would be unequal. The swept blade axis is depicted in Figure 4.1. Note that the blade root radius is $r_{root} = 0.06 \text{ m} = 0.0667R$.

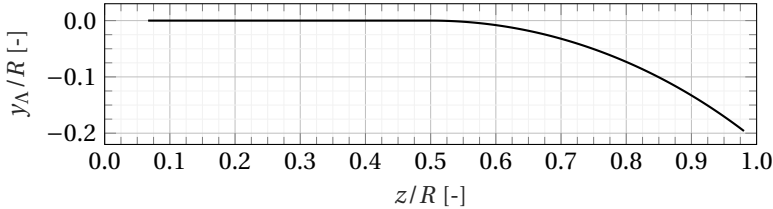


Figure 4.1: Swept blade axis

Chord and twist distributions of the straight reference blade, as shown in Figure 4.2, are kept identical for the swept blade. These distributions were derived to obtain a scaled version of the IEA 15 MW RWT as defined by Gaertner et al. [3]. The main objective of the scaling procedure was to maintain the IEA 15 MW RWT blade's non-dimensionalised thrust distribution. The blade geometry is defined by the *SD7032* airfoil, which blends into a cylinder close to the blade root. This airfoil has been used in multiple wind tunnel experiments on rotating wind turbines, e.g. by Fontanella et al. [6] or Kimball et al. [7], because of its good performance in low-Reynolds-number conditions. Details of the scaling approach can be found in Chapter 3.

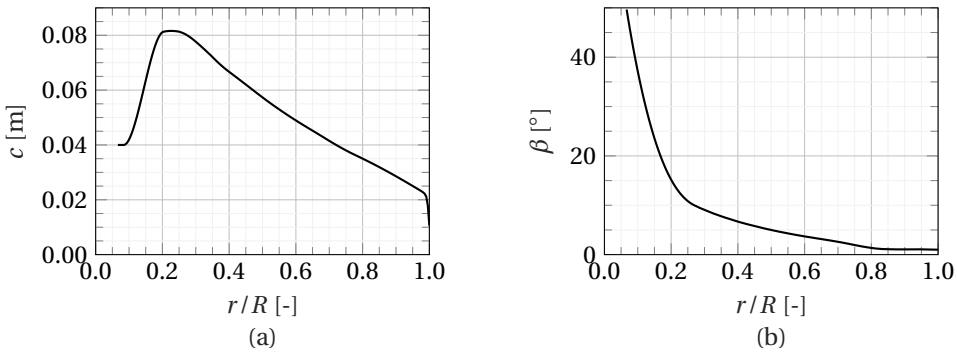


Figure 4.2: Chord (a) and twist (b) distribution of the wind tunnel model

4.2.2. EXPERIMENTAL SETUP AND MEASUREMENT SYSTEM

The experimental campaign was conducted in TU Delft's Open Jet Facility (OJF), which has an octagonal jet exit of $2.85 \text{ m} \times 2.85 \text{ m}$. The model turbine was operated at a constant tip-speed ratio of $\lambda = 9$ and an inflow velocity of $U_\infty = 3.95 \text{ m s}^{-1}$. To exclude external phenomena from impacting the measurements, the wind tunnel's operating conditions



were logged in terms of velocity, pressure, temperature and density for each measurement point and showed no significant variation (generally, less than 1 % maximum deviation from the mean value of the entire campaign).

The primary data gathered in this campaign are flow fields measured around various blade cross-sections along the span using stereoscopic particle image velocimetry (SPIV). Employing laser optics, a thin, uniform light sheet was created within a vertical measurement plane aligned with the inflow. Smoke particles were introduced into the wind tunnel downstream of the measurement section. The smoke, then, distributed homogeneously during the recirculation, enabling the airflow's visualisation. Two cameras captured the flow field from two angles, allowing the measurement of velocity components in three spatial directions. The entire flow field surrounding a blade cross-section was captured in two steps because the blade itself casts a shadow and covered part of the measurement plane from the cameras' perspective. Thus, the flow around the blade's pressure side was evaluated with the measurement setup placed upwind of the rotor and the laser sheet angled downstream. The suction side's flow was then captured by placing the apparatus downstream of the turbine and tilting the laser sheet upstream. By stitching the two measurements together in post-processing, the entire flow field was made available. This process was facilitated by the constant wind turbine operational conditions and environmental conditions of the wind tunnel.

Laser and cameras were triggered by a notch on the turbine's main shaft, activating an optical sensor once per revolution. Per measurement plane, 120 phase-locked images were recorded and post-processed into an average velocity field and its standard deviation using LaVision DaVis software. While Table 4.1 lists more specific information regarding the hardware used in this measurement campaign, Table 4.2 details the SPIV measurement specifications. Figure 4.3 (a) shows the swept blades and Figure 4.3 (b) shows the wind tunnel setup and measurement system.

Table 4.1: Hardware used in the SPIV setup

Illumination	Quantel EverGreen double-pulsed neodymium-doped yttrium aluminium garnet (Nd:YAG)
Seeding	Safex smoke generator, median particle diameter of 1 μm
Imaging	Two LaVision Imager sCMOS cameras with lenses of 105 mm focal length and an aperture of $f/8$
Trigger	Optical gate activated once per revolution
Computing	Acquisition PC with LaVision DaVis 8 software

The entire SPIV setup was mounted rigidly on a traverse system moving in radial direction, allowing for time-efficient measurements without the need to recalibrate the software at each new location. In total, measurements were taken at 22 planes along the blade span with the following spacing:

- $\Delta r/R = 0.100$ for $0.10 \leq r/R \leq 0.40$
- $\Delta r/R = 0.050$ for $0.40 \leq r/R \leq 0.80$
- $\Delta r/R = 0.025$ for $0.80 \leq r/R \leq 1.05$

Table 4.2: SPIV specifications

Laser pulse time separation	150 μ s
Equivalent change in turbine azimuth	0.3°
Approximate particle movement	5 pixels
No. of phase-locked image pairs	120
Field of view	297 mm \times 257 mm
Image resolution	8.81 pixels mm ⁻¹

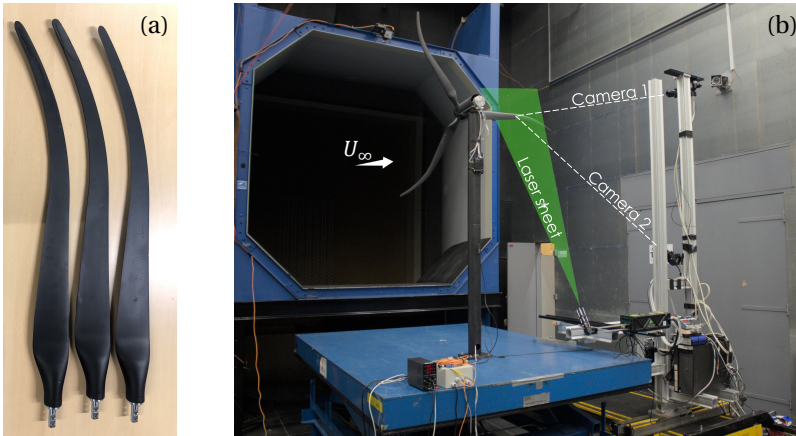


Figure 4.3: Swept model wind turbine blades (a) and experimental setup and measurement system (b). The laser sheet is oriented in the plane spanned by the vertical and the inflow direction

These planes were chosen to guarantee higher resolution in the tip region where higher gradients in aerodynamic quantities and the main impact of blade sweep are expected. To evaluate how representative the main measurement blade is for the remaining two blades, measurements were taken for all three blades at $r/R = [0.4, 0.6, 0.8, 0.9]$.

A time delay was set between the trigger signal and camera/laser activation for measurement planes in the swept part of the blade. This is to ensure that (1) the blade cross-section remains in the centre of the field of view and that (2) the radial position of the measurements is equivalent to the measurements on the straight reference blades as presented in Chapter 3. This increases the comparability of the two wind tunnel campaigns. Figure 4.4 shows a supporting schematic of this approach. Figure 4.4 (a) is representative of measurements in the unswept part of the blade. Here, the measurement plane is perpendicular to the blade axis. Figure 4.4 (b) is representative of measurements in the swept part of the blade, where the local blade axis is not perpendicular to the measurement plane. Two coordinate systems are introduced: one global coordinate system and one aligned with the local blade axis and airfoil orientation. In the unswept part of the blade, these two coordinate systems coincide.

The global sweep angle ζ of a given blade section and the required additional time



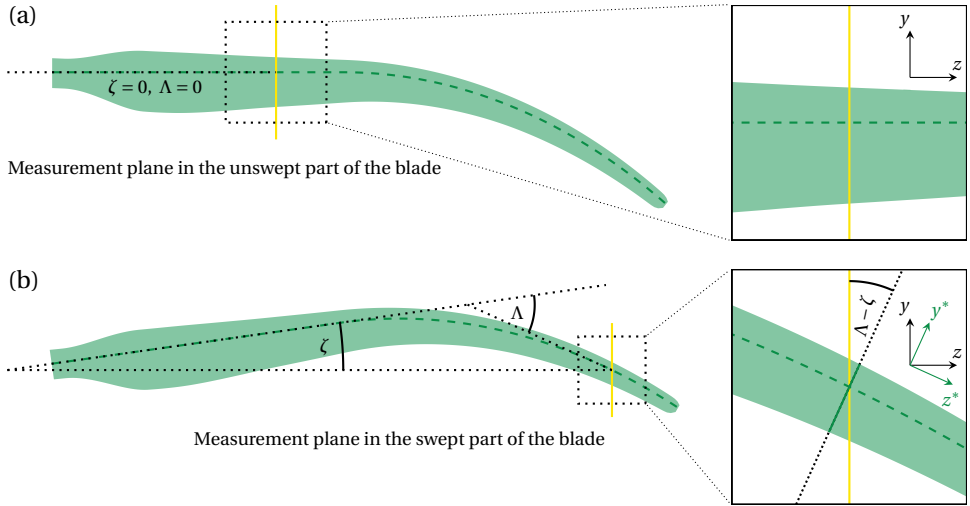


Figure 4.4: Schematic of measurement planes in the unswept (a) and swept (b) part of the blade

delay Δt_Λ are calculated as

$$\zeta = \tan^{-1} \left(\frac{y_\Lambda}{r} \right), \quad (4.2)$$

$$\Delta t_\Lambda = \frac{\zeta}{\omega}, \quad (4.3)$$

where ω is the angular velocity.

4.2.3. DERIVING BLADE-LEVEL AERODYNAMICS FROM PIV MEASUREMENTS

In this study, multiple aerodynamic quantities are derived from the measured flow fields. Only a brief summary of the methods employed is given here. For a detailed description and the mathematical formulation of these methods, the reader is referred to Chapter 3.

All methods rely on evaluating the velocity field on a closed curve encompassing the investigated blade cross-section. The bound circulation Γ is computed as the line integral of the measured velocity field along this control curve [e.g. 8, p. 176]. The inflow conditions are determined using the Ferreira-Micallef approach [9]. It aims to remove the regarded blade cross-section's induction from the measured flow field using elemental potential flow solutions. What is left after this removal is the sum of the freestream velocity and the velocities induced by the remainder of the blades and the wake, yielding the relative inflow vector. The inflow vector then allows the computation of induction values, inflow angle and angle of attack. The blade forces are calculated using two approaches, namely Noca's method [10], which calculates the forces using a momentum balance based on the velocity field along a control volume's bounding curve, and the Kutta-Joukowski theorem, which directly relates the forces to the bound circulation [e.g. 8, p. 282].

It was found that Noca's method is only reliable when determining the normal force. In contrast, the tangential force did not converge for varying control volume sizes. The developed wind tunnel model turbine has low torque and tangential force values. Consequently, accurately capturing the momentum change associated with the tangential force proves challenging when utilising the Noca method. The same challenge was observed in Chapter 3. Given this challenge, only the tangential force based on the Kutta-Joukowski theorem is presented in this article. It should be noted that the Kutta-Joukowski theorem is based on potential flow theory, thus it neglects the viscous drag contribution to the tangential force. While this might lead to some inaccuracies in the tangential force, the neglect of viscosity has limited impact on the normal force.

As discussed in Section 4.2.2, the airfoil orientation and measurement plane do not align in the swept part of the blade. Therefore, additional considerations are necessary. Firstly, the inflow angle in the measurement plane and the inflow angle in the plane perpendicular to the local blade axis differ. The rotational velocity needs to be decomposed, and only its component aligned with the airfoil orientation should be considered in calculating the inflow angle:

$$\phi = \tan^{-1} \left(\frac{U_{\infty}(1-a)}{\omega r (1+a') \cos(\Lambda - \zeta)} \right), \quad (4.4)$$

where a and a' are the axial and tangential induction factors, respectively. The angle of attack, which is a two-dimensional quantity defined in the direction of the airfoil orientation, is then given by

$$\alpha = \phi - \beta. \quad (4.5)$$

Secondly, when discussing blade loading, it is relevant to distinguish between forces per unit blade length and per unit radius. In contrast to a straight blade, there are non-negligible differences between the two for swept blades. The infinitesimal blade length dl , oriented along the local blade axis, is related to the infinitesimal radial coordinate dr by

$$dl \cos(\Lambda - \zeta) = dr. \quad (4.6)$$

4.3. RESULTS

4.3.1. DETERMINATION OF THE COMBINED PITCH AND TWIST OFFSET

The blades used in this experiment were manually manufactured out of vacuum-infused carbon-fibre-reinforced material. The manual manufacturing can lead to minor differences in the exact positioning of the carbon fibre layers for the individual blades. On top of that, the resin infusion can introduce changes to the layup, which are much more difficult to mitigate as the blade moulds are closed during this process. As a consequence, varying twist deformations occurred for the three blades during operation. Additionally, a manual pitch mechanism implemented between the blade root and hub led to minor pitch offsets.

To quantify the pitch and twist offsets, the blade cross-sections visible in the raw images were inspected and compared against the original blade design. This approach



is visualised in Figure 4.5 (a), showing a blade cross-section illuminated in white and the original design, i.e. the expected airfoil orientation, overlaid in red. In green, the corrected airfoil orientation is shown, generated by rotating the original design around the trailing edge until it approximately aligns with the pressure side of the illuminated cross-section.

It should be noted that for a measurement point in the unswept region of the blade, this orientation correction corresponds directly to a deviation from the original twist distribution and pitch angle. For measurement planes in the swept part of the blade, this correction is less trivial, as the visible cross-section corresponds approximately to the local airfoil elongated vertically by a factor of $1/\cos(\Lambda - \zeta)$, see Figure 4.4. Therefore, the deviation from the twist distribution, determined in the measurement plane, has to be multiplied by the same factor to correct the twist in the airfoil coordinate system. Figure 4.5 (b) shows the resulting offset in twist and pitch from the original design.

4

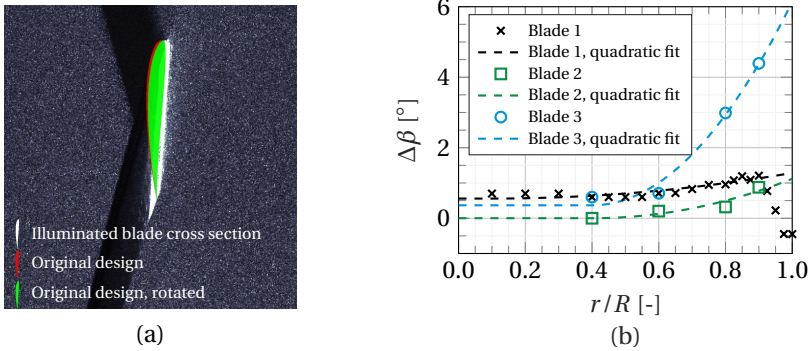


Figure 4.5: Approach of determining actual local airfoil orientation (a), twist and pitch offset determined by comparing experimentally captured blade cross-sections to the original design (b)

For all blades, a quadratic curve is fitted to the distribution of pitch and twist offset to balance out fluctuations, likely due to human error in interpreting the raw images. This is particularly evident in the tip measurements of blade 1: the very small chord makes the interpretation of the cross-section's orientation difficult. Thus, measurements with $r/R > 0.9$ were excluded in generating the curve fit. The mathematical descriptions of the quadratic curve fits are given in Equations (4.7a) – (4.7c). All three blades exhibit twisting behaviour as expected for aft-swept blades, namely twisting to lower angles of attack under aerodynamic loading. However, the three blades vary significantly in their twist extent. The tip twist deformation angle varies from $\Delta\beta(r=R) - \Delta\beta(r=0) = 0.7^\circ$ for blade 1 to $\Delta\beta(r=R) - \Delta\beta(r=0) = 1.1^\circ$ for blade 2 and $\Delta\beta(r=R) - \Delta\beta(r=0) = 5.8^\circ$ for blade 3. While the blade deformations and pitch offsets were unintentional, the method described here allows the determination of the actual blade geometries with reasonable accuracy. This bears significance for potential future numerical validation studies based on the experimental results presented in the following sections.

$$\Delta\beta_{Blade 1} = \begin{cases} 0.5580 & \text{for } r/R \leq 0.1 \\ 1.1090 (r - 0.1R)^2 + 0.5580 & \text{for } r/R > 0.1 \end{cases} \quad (4.7a)$$

$$\Delta\beta_{Blade 2} = \begin{cases} 0.0008 & \text{for } r/R \leq 0.4 \\ 3.8330 (r - 0.4R)^2 + 0.0008 & \text{for } r/R > 0.4 \end{cases} \quad (4.7b)$$

$$\Delta\beta_{Blade 3} = \begin{cases} 0.3662 & \text{for } r/R \leq 0.4 \\ 19.8100 (r - 0.4R)^2 + 0.3662 & \text{for } r/R > 0.4 \end{cases} \quad (4.7c)$$

4.3.2. FLOW FIELDS

The PIV-processed velocity fields are the primary data collected during this experiment. Velocity magnitudes from the measurement planes where data from all three blades are available are shown in Figure 4.6, non-dimensionalised by the local relative inflow velocity, which is defined as

$$V_{rel} = \sqrt{(U_\infty(1-a))^2 + (\omega r(1+a') \cos(\Lambda - \zeta))^2}. \quad (4.8)$$

The induction terms used in this equation are presented in the next section.

The general flow patterns are congruent between the three blades. Yet, differences caused by the varying pitch and twist offsets from the original blade design are evident from the flow fields; see e.g. the second row of subplots corresponding to $r/R = 0.6$. Blade 2, experiencing the highest angle of attack of all three blades, exhibits higher induced velocities and, thus, higher velocity magnitudes on the suction side. By contrast, blade 3 twists to lower angles of attack, entailing lower velocity magnitudes in the blade's vicinity.

Close to the suction side, low-velocity regions are observable for many measurement points. These are caused by laser reflection from the convex blade surface, complicating the PIV processing. They are much less prominent on the concave pressure side.

4.3.3. BLADE AERODYNAMICS

This section discusses the spanwise distributions of the derived aerodynamic quantities. In addition to the mean value, error bars indicate the 95 % confidence interval based on the standard deviation in the measured velocity fields as calculated during the PIV processing. This uncertainty covers both the accuracy of phase-locking and the variability in the flow field during the image acquisition. Noteworthy uncertainties are only present at the blade root. These can be attributed to reflections from the nacelle and hub, which lead to increased uncertainty in the PIV processing. In the outer regions, uncertainties are negligible, indicating very high accuracy in phase-locking and steady flow conditions. As a consequence, the error bars for these data points are smaller than the marker size of the mean value.

Figure 4.7 shows the circulation distribution of the three blades. Straight wind turbine blades are usually designed to have a constant circulation value over large parts of the blade in design conditions. This is also the case for the IEA 15 MW RWT, which served as a reference to develop the planform of the straight blades presented in Chapter 3. The



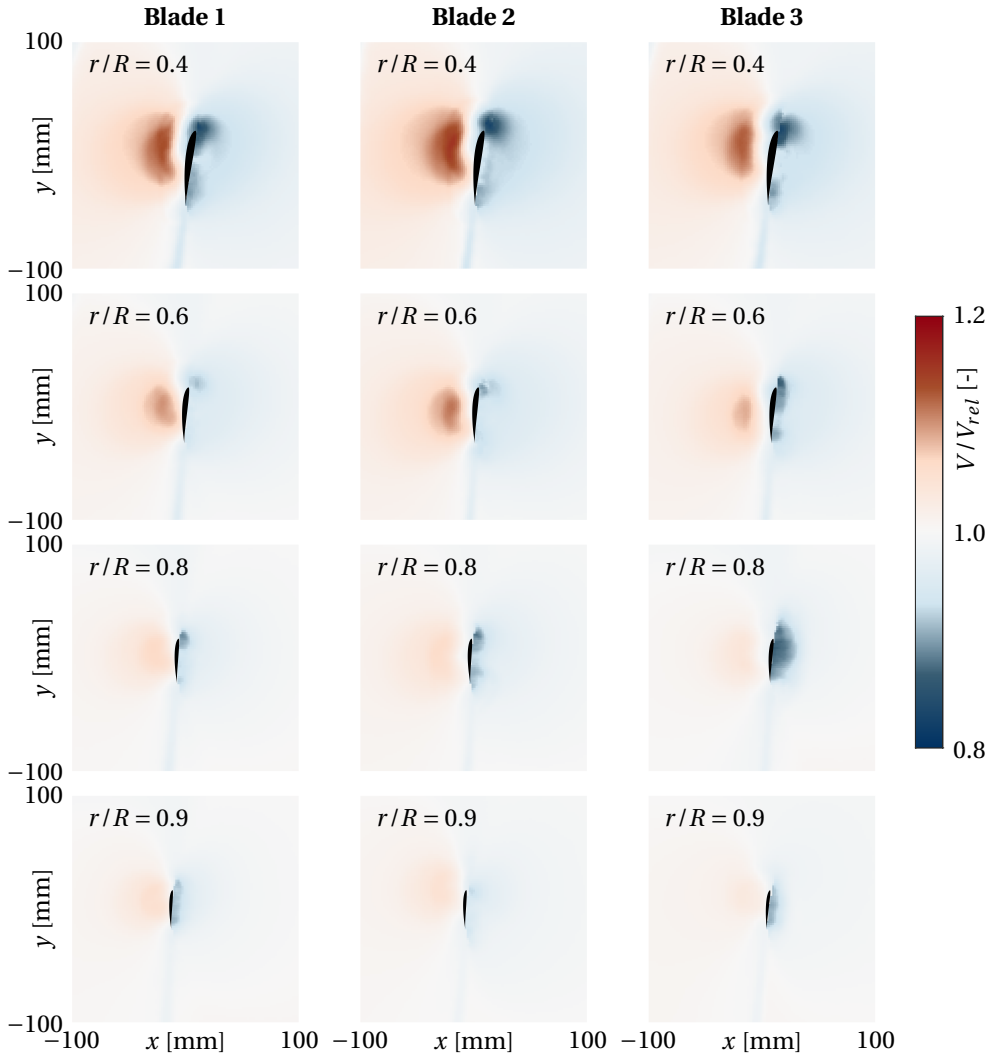


Figure 4.6: Non-dimensionalised velocity magnitudes at the radial stations measured for all three blades

presence of blade sweep leads to a slanted distribution with the circulation decreasing towards the tip. It is not clear how much of this can be attributed to the misalignment of airfoil orientation and inflow velocity and how much to the bend-twist coupling presented in Section 4.3.1. The differences in circulation distribution between the three blades align with the observed pitch and twist offset.

The axial and tangential induction factors are plotted in Figure 4.8. Both distributions exhibit relatively small differences between the three blades, with the only relevant deviations at $r/R = 0.9$ where the twist deformations vary strongly. A similar pattern

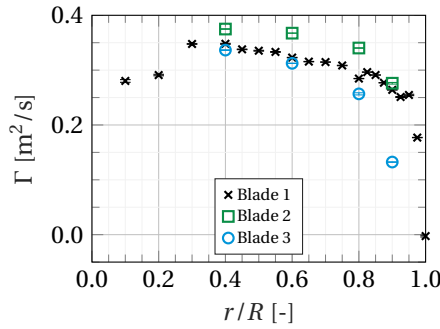


Figure 4.7: Spanwise distribution of bound circulation, error bars representing the 95% confidence interval

was observed for the experimental campaign with straight blades. It indicates that, at the rather high tip-speed ratio present in this experiment, induction is largely a rotor-averaged phenomenon, independent of whether the blades are swept or not. At the tip, the axial induction reaches negative values. It can be speculated that this is due to the tip vortex’s induction and that the three-dimensional nature of the flow in this region is also responsible for the slightly higher uncertainties present at this measurement location.

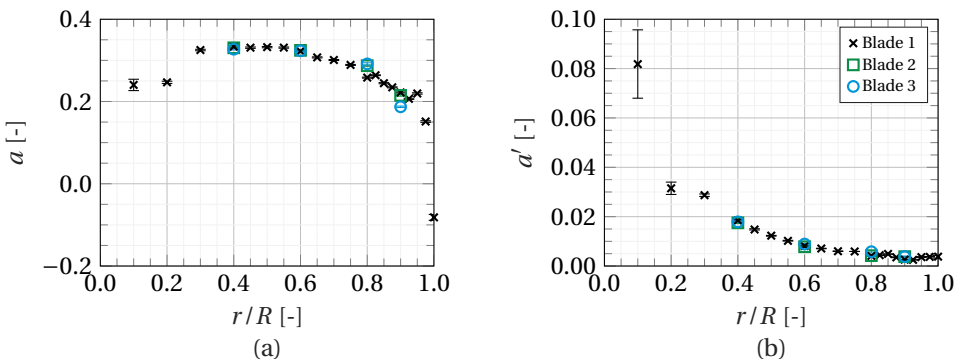


Figure 4.8: Spanwise distribution of axial (a) and tangential (b) induction factors, error bars representing the 95% confidence interval

Figure 4.9 shows the inflow angle and angle of attack distribution, both quantities defined perpendicular to the local blade axis. At $r/R = 0.1$, the blade geometry is defined by a cylindrical cross-section, rendering the angle of attack value presented at this location meaningless. In line with the derived induction values, the inflow angle varies very little between the three blades. The angle of attack, however, is evidently influenced by each blade’s pitch and twist offset. Particularly, blade 3, which has the highest twist deformations, experiences near-zero angles of attack at the tip. Given that the *SD7032* airfoil used in the blade design stalls at approximately $\alpha = 11^\circ$ [11], all angle of attack values derived from the PIV data suggest operation in the linear region of the airfoil.

The normal and tangential force distribution is depicted in Figure 4.10. It should



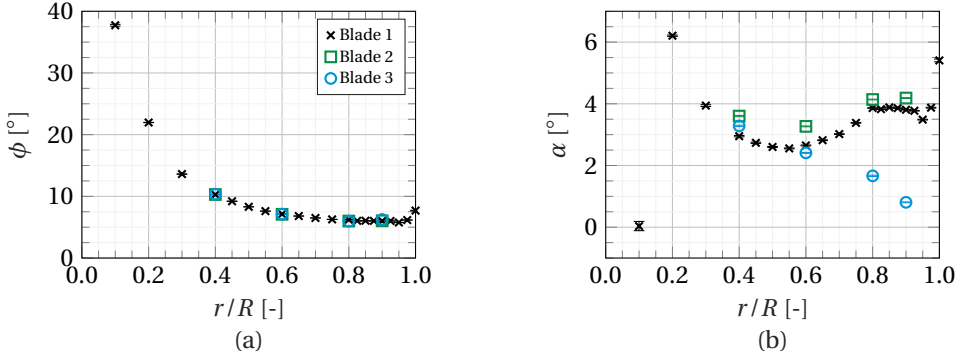


Figure 4.9: Spanwise distribution of inflow angle (a) and angle of attack (b), error bars representing the 95% confidence interval

4

be noted that the forces are given per unit radius and not per unit blade length. This corresponds to the forces in the coordinate system spanning the measurement planes and, thus, not in the plane of the airfoil definition (see Figure 4.4). The normal force is calculated using both Noca's method and the Kutta-Joukowski (KJ) theorem. The rotor thrust can be calculated by integrating the normal force along the blade radius. For this purpose, piecewise cubic curves are fit to the experimental data with zero loading prescribed at root and tip if no data are available there. The non-dimensionalisation of the rotor thrust yields the thrust coefficient $C_T = F_N / (0.5\rho U_\infty^2 \pi R^2)^{-1}$. Depending on the approach, the experimental thrust coefficients are $C_{T,Noca} = 0.75$ and $C_{T,KJ} = 0.70$, respectively.

Chapter 3 demonstrated for a comparable dataset that Noca's method does not converge with varying control volume size for the tangential force; the same holds for the data presented in this study, which is why only the tangential force calculated using the Kutta-Joukowski theorem is presented here. With the exception of the measurements at $r/R = 0.2$, Noca's method consistently results in slightly higher normal force values than the Kutta-Joukowski theorem. Variations in the calculated forces are, again, aligned with the pitch and twist offset discussed above.

4.3.4. LIFT POLAR

Given the aerodynamic characteristics presented in the previous section, the experimental lift coefficient c_l can be calculated for each measurement point. Being an airfoil-level quantity, the lift coefficient has to be calculated using quantities aligned with the airfoil orientation. Using Equation 4.6, the forces measured per unit radius can be converted to forces per unit blade length so that

$$c_l = \frac{F_{N,KJ} \cos(\Lambda - \zeta) \cos(\phi) + F_{T,KJ} \cos(\Lambda - \zeta) \sin(\phi)}{\frac{1}{2} \rho V_{rel}^2 c}, \quad (4.9)$$

where ρ is the density of air. The resulting values are plotted in Figure 4.11 (a) alongside the SD7032 lift polar [11] at Reynolds numbers resembling the experimental conditions

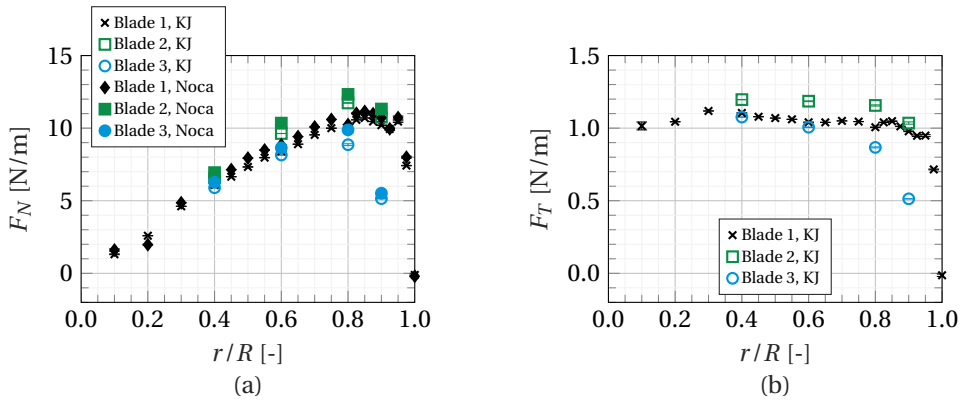


Figure 4.10: Spanwise distribution of normal (a) and tangential (b) force, error bars representing the 95% confidence interval

varying between approximately 40,000 and 70,000 along the blade span. The two measurement points closest to the root and the two closest to the tip are omitted. At the root, the blade is defined not by the design airfoil but rather by a cylinder and a blend between cylinder and airfoil. At the tip, the tip vortex increases the flow's three-dimensionality and thus, measurements cannot be compared to two-dimensional wind tunnel data. For all other measurement points, the agreement between the design airfoil's lift polar and the experimental values is good.

While Figure 4.11 (a) provides insight into the experimentally obtained lift polar, it lacks representation of the varying Reynolds numbers across the blade. Alternatively, the experimentally derived lift coefficient c_l is plotted as a function of the radial position alongside the chord Reynolds number distribution in Figure 4.11 (b). Additionally, the design airfoil polars can be evaluated for the experimentally derived angle of attack and Reynolds number to obtain the expected polar-based lift coefficient $c_{l,pol}$. Comparing c_l and $c_{l,pol}$ reveals that blades 1 and 2 utilised in this experiment generate less lift than anticipated in the outboard regions. The experimentally derived lift coefficient of blade 3 agrees well with the expected polar-based one. It can be hypothesised that this discrepancy can be attributed to differences in surface finish between the model blades and the airfoil studied by [12] and minor inaccuracies in the manually manufactured geometry. The latter have a more significant impact towards the tip where the chord values are very low.

4.4. CONCLUSIONS

This chapter presents results from a wind tunnel experiment where a three-bladed model turbine equipped with swept blades was tested. The velocity fields around multiple radial stations were measured using a particle image velocimetry setup. From the measured velocity fields, blade-level aerodynamic quantities are derived, namely bound circulation, induction values, inflow angle and angle of attack, and forces normal and tangential to the rotor plane. The normal force distributions, determined with both Noca's



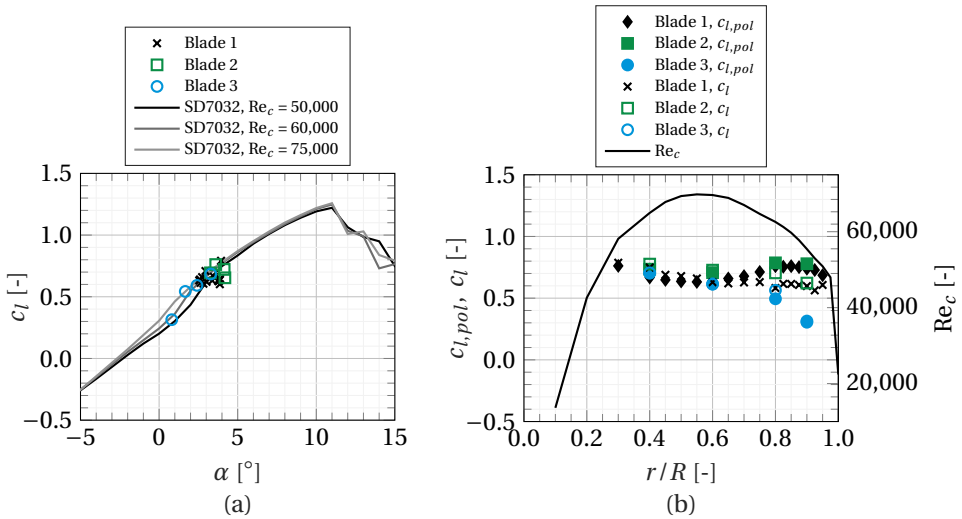


Figure 4.11: Experimental lift polar compared to the *SD7032* airfoil lift polar (a) and the lift coefficient derived from measured forces to that expected based on the design lift polars, alongside the chord Reynolds number distribution (b)

method and the Kutta-Joukowski theorem, agree reasonably well. Furthermore, the deviations in the aerodynamic response between the three blades are consistent with the determined offsets in blade pitch and twist deformations from the original design. Knowing the aerodynamic blade characteristics, the local lift coefficient can be calculated, which shows good agreement with the lift polar of the design airfoil.

The created dataset characterises the three swept blades aerodynamically in rotating and controlled conditions. Such data, rarely available even for more conventional straight blades, were absent in the current literature. It provides a baseline for future experimental research on the same model turbine as well as a valuable validation dataset for numerical tools of varying fidelity aiming at simulating swept wind turbine blades. While the flow fields can serve for the validation of higher-fidelity models, such as panel codes and computational fluid dynamics, the blade-level aerodynamics are also relevant to lower-fidelity models, such as BEM and lifting line algorithms.

4.A. NOMENCLATURE

Latin letters	continues on next page...
a, a'	Axial and tangential induction factor
C_T	Thrust coefficient
c	Chord
c_l	Lift coefficient
D	Rotor diameter
F_N, F_T	Normal and tangential force

Latin letters

...continued

l	Coordinate along blade axis
R	Blade tip radius
Re_c	Chord Reynolds number
r	Radial coordinate
t	Time
U_∞	Freestream velocity
V_{rel}	Relative inflow velocity
y_Λ	Blade sweep
y_{tip}	Tip sweep extent
z_{start}	Sweep starting position

Greek letters

α	Angle of attack
β	Combined blade pitch and twist angle
γ	Sweep exponent
Γ	Circulation
ζ	Global sweep angle
Λ	Local sweep angle
λ	Tip-speed ratio
ρ	Density of air
ϕ	Inflow angle
ω	Angular velocity

Subscripts

KJ	Kutta-Joukowski
pol	Based on design polars



BIBLIOGRAPHY

- [1] T. Barlas, G. R. Pirrung, N. Ramos-García, S. G. Horcas, R. F. Mikkelsen, A. S. Olsen, and M. Gaunaa. “Wind tunnel testing of a swept tip shape and comparison with multi-fidelity aerodynamic simulations”. In: *Wind Energy Science* 6.5 (Oct. 2021), pp. 1311–1324. DOI: [10.5194/wes-6-1311-2021](https://doi.org/10.5194/wes-6-1311-2021).
- [2] T. Barlas, G. R. Pirrung, N. Ramos-García, S. González Horcas, A. Li, and H. A. Madсен. “Atmospheric rotating rig testing of a swept blade tip and comparison with multi-fidelity aeroelastic simulations”. In: *Wind Energy Science* 7.5 (Oct. 2022), pp. 1957–1973. ISSN: 2366-7443. DOI: [10.5194/wes-7-1957-2022](https://doi.org/10.5194/wes-7-1957-2022).
- [3] E. Gaertner et al. *Definition of the IEA wind 15-megawatt offshore reference wind turbine*. Tech. rep. NREL/TP-5000-75698. Golden, CO, US: National Renewable Energy Laboratory, 2020.
- [4] G. Schepers. *IEA Task 47 Innovative aerodynamic experiment technologies and simulations on wind turbines in turbulent inflow*. Feb. 2021.
- [5] T. Ashwill, G. Kanaby, K. Jackson, and M. Zuteck. “Development of the sweep-twist adaptive rotor (STAR) blade”. In: *48th AIAA aerospace sciences meeting including the new horizons forum and aerospace exposition*. American Institute of Aeronautics and Astronautics, Jan. 2010. DOI: [10.2514/6.2010-1582](https://doi.org/10.2514/6.2010-1582).
- [6] A. Fontanella, A. Facchinetti, S. Di Carlo, and M. Belloli. “Wind tunnel investigation of the aerodynamic response of two 15 MW floating wind turbines”. In: *Wind Energy Science* 7.4 (Aug. 2022), pp. 1711–1729. ISSN: 2366-7443. DOI: [10.5194/wes-7-1711-2022](https://doi.org/10.5194/wes-7-1711-2022).
- [7] R. Kimball, A. Robertson, M. Fowler, N. Mendoza, A. Wright, A. Goupee, E. Lenfest, and A. Parker. “Results from the FOCAL experiment campaign 1: turbine control co-design”. In: *Journal of Physics: Conference Series* 2265.2 (May 2022), p. 022082. ISSN: 1742-6596. DOI: [10.1088/1742-6596/2265/2/022082](https://doi.org/10.1088/1742-6596/2265/2/022082).
- [8] J. D. Anderson. *Fundamentals of aerodynamics*. Sixth. McGraw-Hill series in aeronautical and aerospace engineering. New York, NY: McGraw-Hill Education, 2017. ISBN: 978-1-259-12991-9.
- [9] H. Rahimi, J. Schepers, W. Shen, N. R. García, M. Schneider, D. Micallef, C. S. Ferreira, E. Jost, L. Klein, and I. Herráez. “Evaluation of different methods for determining the angle of attack on wind turbine blades with CFD results under axial inflow conditions”. In: *Renewable Energy* 125 (Sept. 2018), pp. 866–876. DOI: [10.1016/j.renene.2018.03.018](https://doi.org/10.1016/j.renene.2018.03.018).
- [10] F. Noca, D. Shiels, and D. Jeon. “A comparison of methods for evaluating time-dependant fluid dynamic forces on bodies, using only velocity fields and their derivatives”. In: *Journal of Fluids and Structures* 13.5 (July 1999), pp. 551–578. ISSN: 0889-9746. DOI: [10.1006/jfls.1999.0219](https://doi.org/10.1006/jfls.1999.0219).



- [11] A. Fontanella, I. Bayati, R. Mikkelsen, M. Belloli, and A. Zasso. *UNAFLOW: Unsteady Aerodynamics of Floating Wind turbines*. May 2021. DOI: [10 . 5281 / zenodo . 4740006](https://doi.org/10.5281/zenodo.4740006).
- [12] A. Fontanella, I. Bayati, R. Mikkelsen, M. Belloli, and A. Zasso. “UNAFLOW: a holistic wind tunnel experiment about the aerodynamic response of floating wind turbines under imposed surge motion”. In: *Wind Energy Science* 6.5 (Sept. 2021), pp. 1169–1190. ISSN: 2366-7443. DOI: [10 . 5194/wes-6-1169-2021](https://doi.org/10.5194/wes-6-1169-2021).

5

VALIDATING THE BEM CORRECTION MODEL FOR SWEEPED BLADES

This chapter utilises the experimental results presented in the previous two chapters with the ultimate goal of validating the BEM correction model presented in Chapter 2. To establish a baseline, the original blade geometries, i.e. without the deformations and pitch offsets encountered during the experiment, are simulated using BEM and lifting line algorithms. Then, inverse versions of the BEM and lifting line algorithms accounting for these deviations from the original geometry are used to validate the proposed BEM correction model. These inverse approaches use the experimentally determined forces and circulation as input and iteratively solve their respective equations until the induction values converge. These methods are applied to the straight blade experiment first to evaluate the achievable agreement before transferring the analysis to the swept blade experimental data yielding the final validation.

A brief introduction and an overview of the employed numerical models are given in Sections 5.1 and 5.2, respectively. The results of the numerical model validation are presented in Section 5.3. Finally, conclusions are drawn in Section 5.4.

Parts of this chapter have been published in E. Fritz, K. Boorsma, C. Ferreira, *Validation of a BEM correction model for swept blades using experimental data*, *Journal of Physics: Conference Series* **2767**, 022035 (2024). Due to changes in the validation approach, the results presented here differ from those in the original publication.



5.1. INTRODUCTION

Wind turbine blade sweep has potential as a passive load alleviation mechanism [1, 2], achieved by coupling the bending and torsional deformations. To harvest the full potential of blade sweep, the aerodynamic properties of swept blades need to be accurately modelled by low-fidelity simulation tools on which the design and optimisation processes of modern wind turbine blades rely. In recent years, research has been conducted regarding the correct numerical modelling of swept blades [3, 4, 5]. The model proposed in Chapter 2 corrects blade element momentum theory (BEM) so that it can account for swept blade shapes while retaining BEM's streamtube-independent approach as well as its computational efficiency. The model currently lacks experimental validation, an issue the present Chapter aims to resolve.

To this end, the data from the wind tunnel campaign with straight blades, presented in Chapter 3, and with swept blades, presented in Chapter 4, are compared to the results of the corrected BEM algorithm. The experimental datasets consist of flow fields which are measured at the blade level of a rotating, scaled horizontal axis wind turbine (HAWT) using a stereoscopic particle image velocimetry (PIV) setup. These flow fields were post-processed to obtain the spanwise distribution of several aerodynamic quantities, which can be directly compared against numerical simulation results.

5

5.2. METHODOLOGY

The reader is referred to Chapters 3 and 4 for a detailed description of the scaled wind tunnel model and its blade geometries, of the PIV measurement setup used to acquire the experimental data, and of the post-processing methods for deriving the blade aerodynamics. The remainder of this section explains the numerical modelling used for this validation study.

A simple BEM algorithm is implemented, following the standard equations given, e.g. by Burton et al. [6]. Prandtl's tip and root loss corrections and Glauert's correction model for highly loaded rotors are implemented. In this basic form, blade element momentum theory assumes a straight blade geometry. When sweeping a wind turbine blade, however, multiple aspects regarding the blade aerodynamics change with respect to a straight reference blade. The first aspect is commonly known as crossflow principle [7]. It states that only a part of the local inflow velocity effectively contributes to the lift and drag forces, while the spanwise flow component has a negligible influence. Most BEM-based algorithms account for this to some degree. Two further aspects of blade sweep are usually not accounted for in BEM algorithms, namely, the induction of the curved bound vortex on itself and the displacement of the wake vorticity, including the dominant tip vortex. Both affect the local induced velocity and, consequently, the blade loads. Figure 5.1 gives a schematic representation of the sweep-induced changes in blade aerodynamics as discussed in this section. Chapter 2 proposed a correction model that accounts for these effects. For a more detailed rundown of the BEM algorithm, including the derivation of the equations on which the correction model is built, the reader is referred to that chapter.

Additionally, lifting line (LL) simulations are run. The lifting line algorithm employs a semi-free wake approach where the trailed vorticity is represented by helical vortex

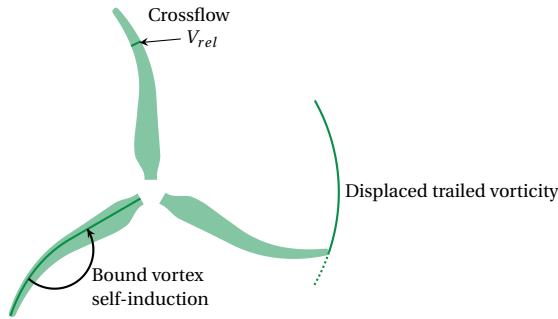


Figure 5.1: Schematic representation of the sweep-induced changes in blade aerodynamics

filaments, whose helix pitch angle is adjusted iteratively based on the calculated axial induction factor.

For the validation of the numerical model, inverse versions of the aforementioned BEM and lifting line algorithm are applied. The inverse BEM approach, developed by Bruining et al. [8] and Snel et al. [9], uses the measured forces as input and then solves the momentum equation to obtain the inflow conditions, i.e. induced velocities, inflow angle and angle of attack. For swept blades, the sweep correction model is also applied in the inverse BEM method. As it requires local circulation values to calculate the bound vortex's self-induction, the experimentally derived circulation values are fed as input in addition to the forces.

Inverse vortex wake methods have previously been applied using measurements from the Unsteady Aerodynamic Experiment Phase VI [10, 11, 12, 13] and from the MEXICO experiment [14]. In the present study, the inverse lifting line method uses the same semi-free wake approach as the direct lifting line simulation. The inverse algorithm uses the experimentally derived circulation distribution as input and then solves the induction system of bound and trailed vorticity in an iterative manner. Similar to the inverse BEM method, this allows the determination of the inflow conditions.

Both inverse approaches underwent a sanity check, in which directly simulated force/circulation distributions were used as input, and the inflow conditions calculated by the direct and inverse approaches were compared. Both methods yielded identical inflow conditions between the direct and inverse approaches.

5.3. RESULTS

5.3.1. AERODYNAMIC CHARACTERISTICS OF THE ORIGINAL BLADE DESIGN

To establish a baseline for the analyses presented in the coming sections, the original straight and swept blade designs are simulated using BEM-based and lifting line algorithms.

STRAIGHT WIND TUNNEL MODEL BLADE DESIGN

The straight blades used in the wind tunnel campaign were designed to match the non-dimensionalised thrust distribution of the IEA 15 MW reference wind turbine (RWT).



Thus, the simulation results of the wind tunnel model blade are compared against those of its reference blade in this section. For this purpose, the pre-bending of the IEA 15 MW RWT is neglected. Simulations of the two rotors are run with an identical tip-speed ratio $\lambda = 9$, where the wind tunnel model is simulated with an inflow velocity of $U_\infty = 4 \text{ m s}^{-1}$ and the reference turbine with $U_\infty = 10 \text{ m s}^{-1}$. These conditions were also used during the scaling process of the wind tunnel model blade.

The respective circulation distributions, simulated with BEM and lifting line algorithm, are shown in Figure 5.2. Due to the chosen scaling procedure, the circulation distributions of the reference turbine and the wind tunnel model show comparable magnitudes and shapes. Additionally, there is a good agreement between the BEM and lifting line simulations.

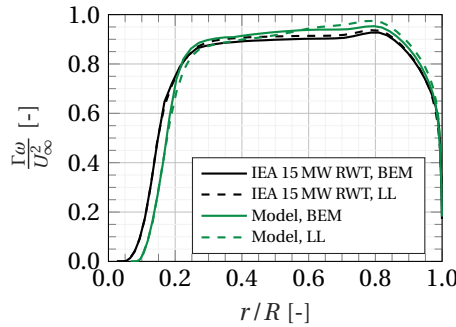


Figure 5.2: Spanwise distribution of the original straight blade design's circulation; BEM and lifting line simulations

The same holds for the axial induction distribution, shown in Figure 5.3 (a). In contrast to that, the spanwise distributions of the angle of attack show a considerable offset between the model and reference, see Figure 5.6 (b). This is a consequence of different airfoils used to generate the respective blade geometries. While the IEA 15 MW RWT's blade is generated using various FFA airfoils, the wind tunnel model is created using a single SD7032 airfoil. These differences in sectional blade geometry are motivated by the vastly different Reynolds numbers. Given the varying airfoil polars, the model blade reaches non-dimensionalised load levels comparable to those of the reference turbine at considerably lower angles of attack.

The design driving non-dimensionalised normal force distribution is shown in Figure 5.4 (a). As intended, close agreement between the normal loads of the IEA 15 MW RWT and the wind tunnel model is achieved. Unfortunately, it is not possible to maintain comparable non-dimensional load distributions in both normal and tangential directions. Therefore, the tangential force distributions of model and reference turbine, shown in Figure 5.4 (b), do not align. These expected deviations aside, the scaling process yields the desired resemblance of non-dimensionalised blade aerodynamic distributions.

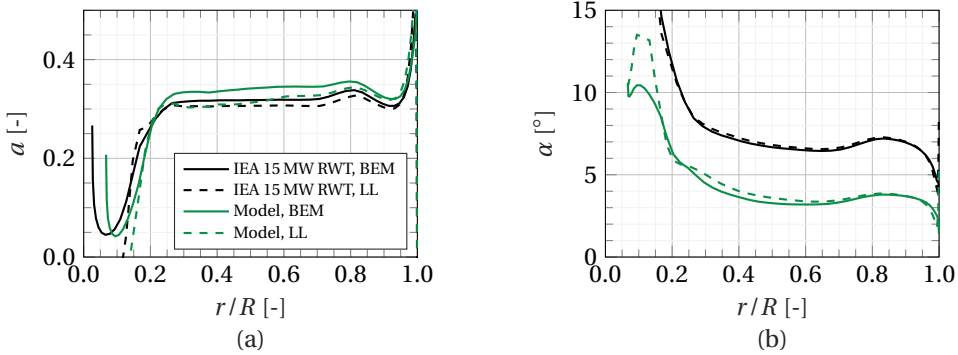


Figure 5.3: Spanwise distribution of the original straight blade design's axial induction (a) and angle of attack (b); BEM and lifting line simulations

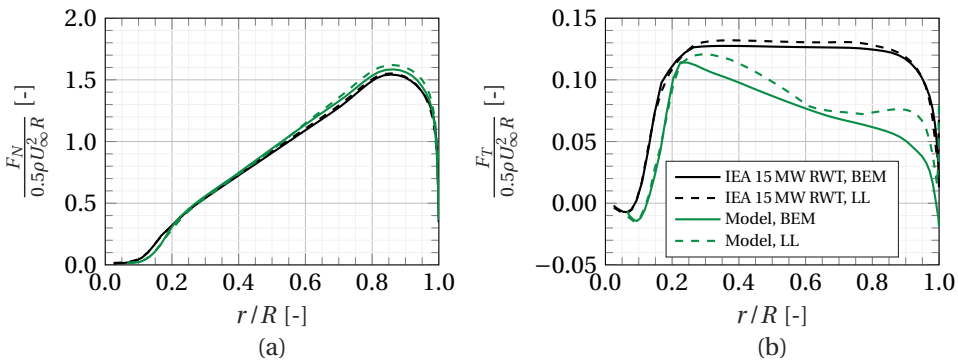


Figure 5.4: Spanwise distribution of the original straight blade design's normal (a) and tangential (b) force; BEM and lifting line simulations

SWEPT WIND TUNNEL MODEL BLADE DESIGN

Three BEM implementations are used to simulate the swept blade design: BEM_0 , not correcting for blade sweep effects, BEM_{cf} , correcting for crossflow, and BEM_Λ , fully correcting for sweep. While all three implementations yield identical results for straight blades (since none of the effects shown in Figure 5.1 occur), this is not the case for swept blades. Therefore, the results from these three BEM implementations are compared to each other and to lifting line simulation results in terms of circulation, axial induction, angle of attack and load distributions in this section. For a more detailed breakdown of where exactly differences between the three codes are introduced, the reader is referred to Appendix 5.A.

The spanwise circulation distribution is shown in Figure 5.5. Minor differences between the three BEM implementations can be observed in the outer 20% of the blade. The lifting line simulation yields a circulation distribution very similar to that of the BEM simulations. In the outboard part of the blade, the BEM_Λ simulation results is closest to that of the lifting line simulation.



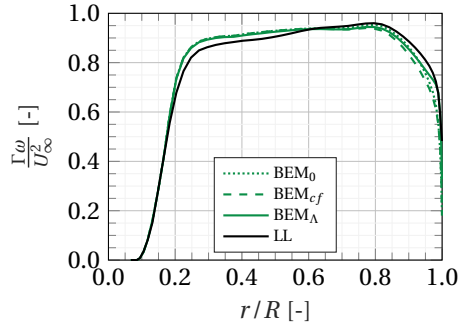


Figure 5.5: Spanwise distribution of the original swept blade design's circulation; BEM and lifting line simulations

5

The spanwise distribution of the axial induction factor shows larger relative differences between the three BEM implementations, see Figure 5.6 (a). The BEM_{cf} result, accounting for the misalignment of airfoil orientation and inflow velocity, deviates from the uncorrected BEM_0 simulation result by a small margin. The BEM_Λ simulation, additionally accounting for bound vortex self-induction and the displacement of the trailed vorticity, yields a notable decrease of axial induction towards the tip. In contrast to the other two BEM algorithms, the fully-corrected one lacks the sharp increase of induction at the very tip associated with the application of the Prandtl correction factor. Here, the implemented BEM correction model counteracts the Prandtl correction, and the algorithm converges at a lower induction value. The lifting line simulation exhibits the same drop-off in induction as the BEM_Λ , but it does result in a steep increase at the very tip due to the tip vortex induction.

The spanwise distribution of the angle of attack is given in Figure 5.6 (b). This is a quantity defined in the plane aligned with the airfoil orientation. In the swept part of the blade, only the component of the rotational velocity vector aligned with the airfoil orientation contributes to the calculation of the inflow vector and, consequently, of the angle of attack. Thus, both the crossflow-corrected and the fully-corrected simulations result in a relatively strong increase in angle of attack in the swept part of the blade. On top of that, the fully-corrected simulation sees an additional increase in angle of attack due to the reduced induction of the azimuthally displaced tip vortex. Again, the lifting line agrees best with the fully-corrected BEM simulation, particularly in the outer 40% of the blade.

The non-dimensionalised normal and tangential load distributions are presented in Figure 5.7. The forces are plotted per unit radius rather than per unit blade length. If the latter were done, both the crossflow-corrected and fully-corrected algorithms would exhibit a drop in section loading due to the misalignment of the inflow velocity and airfoil plane. This is balanced out by the fact that in the swept part of the blade, the blade length included in an annulus is larger than the annulus' radial extent. Therefore, the total force of each annulus is similar to that of a straight blade, and variations in normal loading between the three BEM implementations are limited. In the tangential direction, the relative difference in blade load between the BEM algorithms is more pronounced. Here,

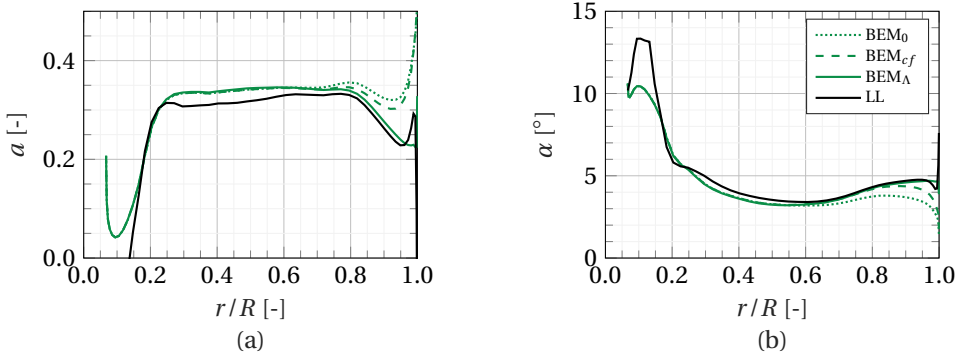


Figure 5.6: Spanwise distribution of the original swept blade design's axial induction (a) and angle of attack (b); BEM and lifting line simulations

the fully-corrected code results in the highest loads, while the uncorrected code yields the lowest loads. As a logical consequence of the discussion so far, the overall agreement between lifting line and BEM simulations is good for the non-dimensional force distributions, too. The trends observed in the lifting line results are best reproduced by the fully-corrected BEM algorithm.

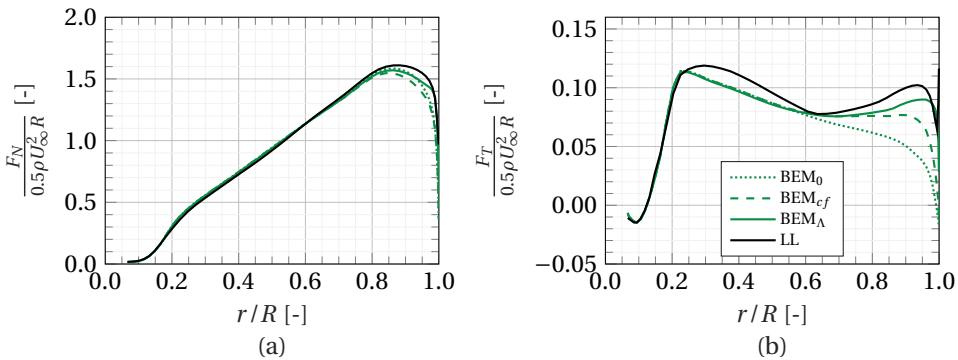


Figure 5.7: Spanwise distribution of the original swept blade design's normal (a) and tangential (b) force; BEM and lifting line simulations

5.3.2. COMBINED PITCH AND TWIST OFFSET

Both experimental campaigns faced the challenge of large variations in blade-level aerodynamics between the three blades. This was due to a combination of errors in the pitch angle and twist deformations, leading to varying angle of attack distributions and, consequently, different blade loading. While the pitch offset was attributed to a manually fixed pitch mechanism, the varying twist deformation was due to different stiffness properties of the vacuum-infused carbon fibre composite blades. The combined offsets in pitch/twist $\Delta\beta$ were quantified by comparing the cross-sections visible in the raw PIV



images with the original blade design and applying a rotational correction until a better match was achieved. The resulting offsets to the original twist distribution are shown in Figure 5.8 together with quadratic curve fits that balance out unrealistic fluctuations likely due to visual misinterpretation of the images. Notable are the tip measurements of swept blade 1, where the extremely small chord complicated the interpretation of the cross-section's orientation. Consequently, measurements with $r/R > 0.9$ were omitted in this curve fit. The curve fits are used to individually adjust each blade's twist distribution in the numerical simulations.

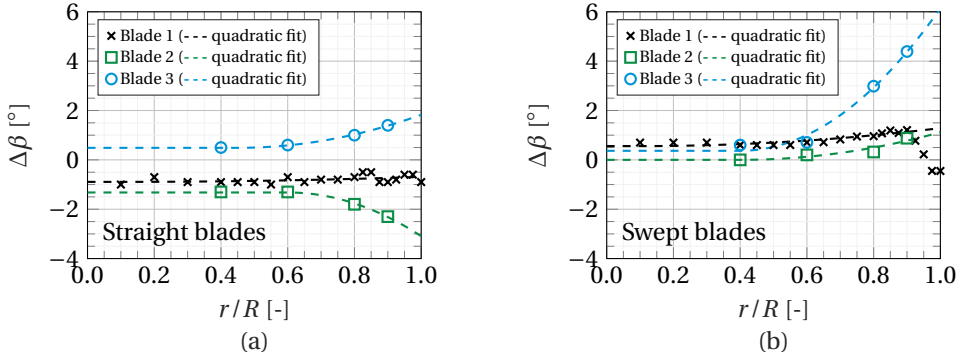


Figure 5.8: Combined pitch/twist offset $\Delta\beta$ from the original design twist distribution for the straight blades (a) and swept blades (b)

The quadratic curves used to fit the pitch and twist offset of the straight blades are given by

$$\Delta\beta_{Blade\ 1,\ straight} = \begin{cases} -0.8918 & \text{for } r/R \leq 0.1 \\ 0.3081(r - 0.1R)^2 - 0.8918 & \text{for } r/R > 0.1 \end{cases} \quad (5.1a)$$

$$\Delta\beta_{Blade\ 2,\ straight} = \begin{cases} -1.3200 & \text{for } r/R \leq 0.6 \\ -13.6600(r - 0.6R)^2 - 1.3200 & \text{for } r/R > 0.6 \end{cases} \quad (5.1b)$$

$$\Delta\beta_{Blade\ 3,\ straight} = \begin{cases} 0.4873 & \text{for } r/R \leq 0.45 \\ 5.4640(r - 0.45R)^2 + 0.4873 & \text{for } r/R > 0.45, \end{cases} \quad (5.1c)$$

while those of the swept blades are defined by

$$\Delta\beta_{Blade\ 1,\ swept} = \begin{cases} 0.5580 & \text{for } r/R \leq 0.1 \\ 1.1090(r - 0.1R)^2 + 0.5580 & \text{for } r/R > 0.1 \end{cases} \quad (5.2a)$$

$$\Delta\beta_{Blade\ 2,\ swept} = \begin{cases} 0.0008 & \text{for } r/R \leq 0.4 \\ 3.8330(r - 0.4R)^2 + 0.0008 & \text{for } r/R > 0.4 \end{cases} \quad (5.2b)$$

$$\Delta\beta_{Blade\ 3,\ swept} = \begin{cases} 0.3662 & \text{for } r/R \leq 0.4 \\ 19.8100(r - 0.4R)^2 + 0.3662 & \text{for } r/R > 0.4. \end{cases} \quad (5.2c)$$

Originally, measurements on blades 2 and 3 were intended to demonstrate replicability. Thus, only a few selected radial positions were measured. Differences in the twist deformations were only noticed in post-processing, and additional planes could not be measured anymore.

5.3.3. VALIDATION USING AN INVERSE BEM APPROACH

In this section, inverse BEM and lifting line approaches are used to derive the axial induction factor and angle of attack along the blade span. While the inverse BEM approach uses the experimentally derived blade loads as input, the inverse lifting line approach relies on the experimentally derived circulation distribution. Given that measurements of blades 2 and 3 were only conducted at four radial positions, their load and circulation distributions are assumed to be identical to that of blade 1. In several plots, only the line corresponding to blade 3 is visible. In such cases, the results for all three blades are close to identical and collapse to one line.

STRAIGHT BLADE EXPERIMENT

To establish a baseline, the measurements from the straight-bladed wind tunnel campaign are used in the inverse BEM and lifting line approaches. Figure 5.9 shows the spanwise distributions of the axial induction factor a and the angle of attack α . Both methods align well with the axial induction derived directly from the PIV-processed flow fields, particularly for $0.4 \leq r/R \leq 0.8$. Towards the blade tip, both inverse algorithms predict an increase in axial induction. For the inverse BEM method, this is due to the application of the Prandtl correction factor, which aims to replicate the induction of the tip vortex and to reduce blade loads to zero at the tip. By contrast, the inverse lifting line method models the tip vortex, and thus, the induction increases close to the tip. At the very tip, a viscous core model reduces the tip vortex induction to avoid singularities otherwise inherent to vortex models. Despite using the loads and circulation of blade 1 as input for all blades, the induction level is captured well. This can be explained by the fact that, in terms of pitch and twist offset, blades 2 and 3 had approximately symmetric deviations from blade 1, see Figure 5.8 (a).

Similar to the axial induction distribution, the angle of attack distribution derived from the flow fields and those calculated using the inverse algorithms match well. Again, deviations are mainly found at the tip, where the values derived from the flow field increase while the inverse methods predict an adverse trend.

The contrary trends of inverse BEM and lifting line on the one hand and values derived from the flow field on the other regarding axial induction at the tip require further investigation. This reduction in axial induction at the tip is in line with research by Rahimi et al. [15] and Bangsa [16], who attempted to derive induction values from 3D CFD simulation data. Rahimi et al. argue that the methods applied to determine the induction (among which is the Ferreira-Micallef method) treat the cross-sections in a two-dimensional sense and, thus, fail to capture the highly three-dimensional flow features close to the tip. Additionally, they emphasise that the proximity to the tip vortex with which the velocity field is interrogated impacts the accuracy with which the induction can be determined. Following this logic, the tip vortex measured in this experiment is investigated. Figure 5.10 (a) shows the out-of-plane velocity field measured at the blade



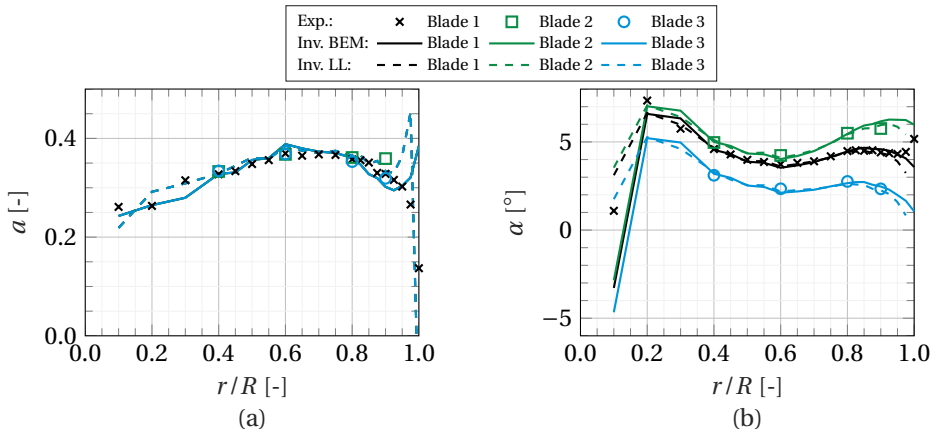


Figure 5.9: Spanwise distribution of the straight blades' axial induction (a) and angle of attack (b); Inverse BEM and lifting line simulations

5

tip of the straight blade. Figure 5.10 (b) show the out-of-plane velocity evaluated along the black line plotted in Figure 5.10 (a). Based on this velocity profile, the viscous vortex core, defined as the distance between the minimum and maximum velocity locations, can be determined to be approximately 15 mm in diameter. The measurement plane second closest to the tip is located 22.5 mm (i.e. 2.5% R) from the tip, which corresponds to three times the viscous core radius. Therefore, it is unsurprising that the increase in axial induction due to the tip vortex is not captured by the experimental data.

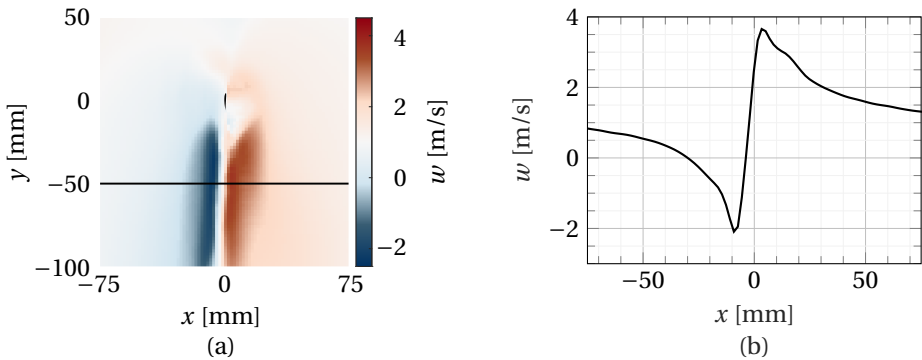


Figure 5.10: Out-of-plane velocity field measured at the blade tip (with evaluation line shown in black) (a) and out-of-plane velocity along the evaluation line (b)

SWEEPED BLADE EXPERIMENT

Figure 5.11 shows the distribution of axial induction and angle of attack for the swept blade configuration. The induction factor calculated using the inverse lifting line method generally matches the values derived directly from the flow fields well. Between 40% and

80 % span, the lifting line results predict slightly lower values. The inverse BEM algorithm predicts rather unrealistic fluctuations of axial induction for $r/R \leq 0.4$. Moving further outboard, there is good agreement with the directly derived induction values. Similar to the inverse lifting line method, the inverse BEM algorithm also predicts slightly lower values than those directly derived from the PIV data in the outer part of the blade. Acknowledging these minor offsets, the shape of the induction distribution, particularly the continuous reduction in axial induction in the swept part of the blade, is well-captured. Close to the tip, the inverse lifting line algorithm again predicts a sharp increase in induction due to the tip vortex, which then subsides at the tip as a consequence of the viscous core modelling.

The angle of attack distributions are highly influenced by the varying blade deformations and pitch offsets. The values directly derived from the flow fields, the inverse BEM method and the inverse lifting line all exhibit similar trends for the individual blades and there is an overall good agreement between the three methods.

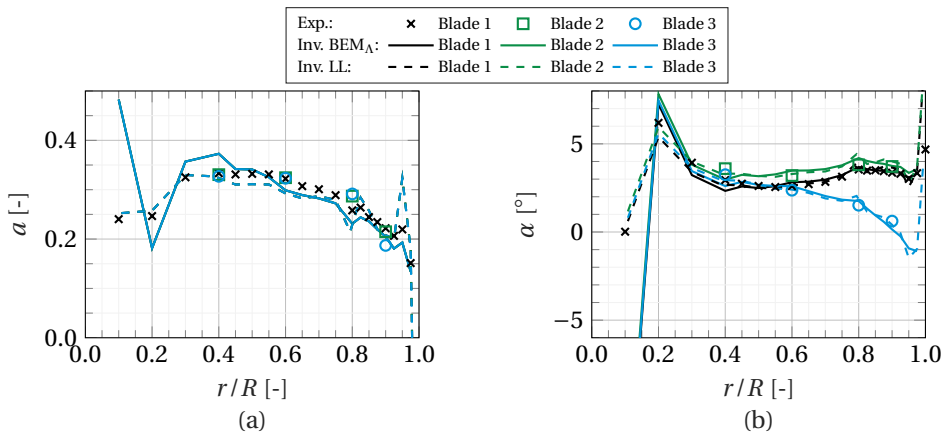


Figure 5.11: Spanwise distribution of the swept blades' axial induction (a) and angle of attack (b); Inverse BEM and lifting line simulations

Next to the comparison between the inverse BEM and inverse lifting line results, it is of interest to compare inverse BEM algorithms with and without the sweep correction model enabled. This comparison is presented in Figure 5.12. While resulting in very similar induction values up to 80 % R , the modelling of the tip vortex' displacement dominates the difference between the two implementations towards the tip. The uncorrected inverse BEM approach predicts an increase in the induction due to the application of the Prandtl tip correction. As explained in Section 5.3.1, the sweep correction model accounts for the decrease in axial induction towards the tip due to the azimuthal tip vortex displacement and, consequently, counteracts the Prandtl correction for aft-swept blades. Comparing the trends of the two inverse BEM approaches with that of the directly derived induction values, it can be concluded that the corrected inverse BEM approach yields much better agreement.

It should be noted that there is no distinction between an uncorrected and crossflow-corrected inverse BEM algorithm as in Section 5.3.1. The crossflow correction is applied



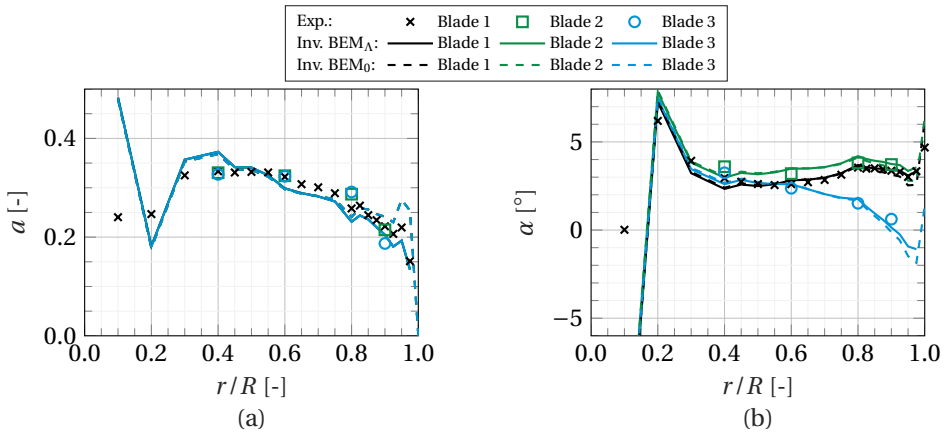


Figure 5.12: Spanwise distribution of the swept blades' axial induction (a) and angle of attack (b); Inverse BEM simulation with and without sweep correction model applied

on the blade element side of a BEM algorithm. While the determination of the blade element forces is replaced by the measured forces in the inverse BEM, the momentum part is identical for uncorrected and crossflow-corrected methods, and thus, only the uncorrected inverse BEM algorithm is considered.

5.4. CONCLUSIONS

This chapter presents an effort to validate a correction model developed to extend blade element momentum theory to swept blades. BEM-based algorithms usually assume a straight blade geometry and can account for the added complexity of a swept blade only to a certain extent. This model aims to improve the representation of swept blades in BEM codes by accounting for the effects of an azimuthally displaced tip vortex and for the curved bound vortex's self-induction.

The BEM algorithm with sweep correction model is validated using results from wind tunnel campaigns in which a model HAWT was equipped with straight and swept blades. PIV-based flow field measurements were processed to obtain a blade-level aerodynamic description of the blades, which can be compared against the numerical results.

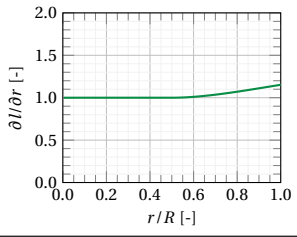
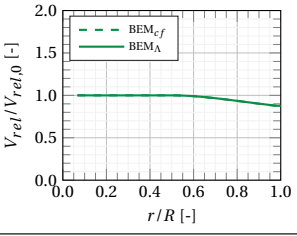
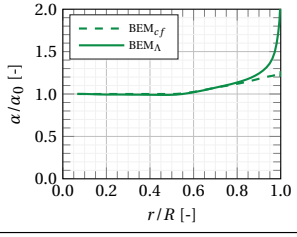
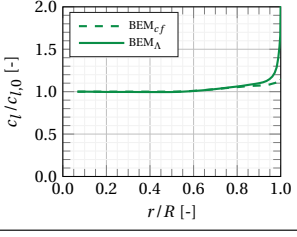
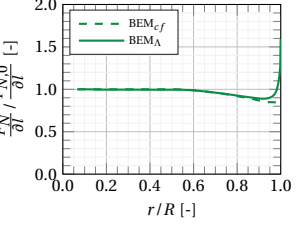
To establish a baseline validation, inverse BEM and lifting line simulation results are compared against the experimental data from the campaign with straight blades. For this case, no correction model is needed, and as such, the accuracy of the basic BEM implementation can be evaluated. Overall, good agreement is found despite the fact that the three blades used in the experiment were found to have non-negligible deviations from the design twist distribution during operation.

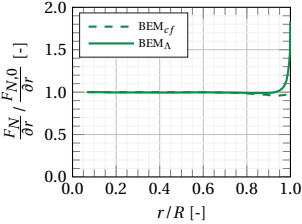
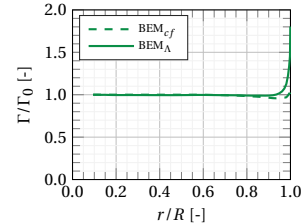
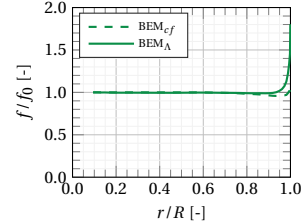
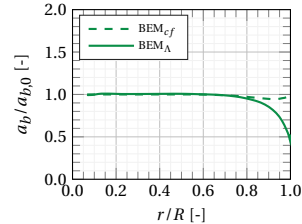
Building on this, the inverse algorithms are employed to numerically replicate the experiment with swept blade configuration. Both inverse BEM, including the sweep correction model and the inverse lifting line algorithm, slightly underpredict the induction values directly derived from the measured flow fields in the mid- to outboard region. However, the general trend is captured well. In contrast, the inverse BEM algorithm with-

out sweep correction model follows this trend much less. This indicates that the sweep correction model indeed improves the accuracy of BEM simulations for swept blades and, thus, validates the proposed model.



5.A. STEP-BY-STEP DISCUSSION OF THE IMPACT OF BLADE SWEEP DURING THE BEM SOLUTION PROCESS

Comparison to BEM ₀	BEM _{cf}	BEM _Λ
	<p>↑</p> <p>In the swept part of the blade the blade length δl contained in an annulus of radial extent δr are not identical: $\frac{\delta l}{\delta r} = \frac{1}{\cos(\Lambda - \zeta)}$</p>	<p>↑</p> <p>Same as BEM_{cf}.</p>
	<p>↓</p> <p>Due to the misalignment of airfoil orientation and rotational velocity, the tangential velocity component acting on the airfoil reduces by $\cos(\Lambda - \zeta)$. Closely related to the reduction of V_t, also V_{rel} reduces due to the misalignment of airfoil and inflow.</p>	<p>↓</p> <p>Same as BEM_{cf}.</p>
	<p>↑</p> <p>Due to the decomposition of the relative inflow velocity into the airfoil plane, the angle of attack increases.</p>	<p>↑</p> <p>The same reasoning as for BEM_{cf} applies here, too. However, the modelling of the bound vortex self-induction and the displacement of the trailed vorticity leads to a further increase in angle of attack.</p>
	<p>↑</p> <p>The force coefficients are determined by interpolating the airfoil polars based on the angle of attack. Assuming operation within the attached flow regime, an increase in angle of attack yields a (close to proportional) increase in lift coefficient.</p>	<p>↑</p> <p>The same reasoning as for BEM_{cf} applies here, too. However, given the additional increase in angle of attack discussed above, the lift coefficient increases slightly more, too.</p>
	<p>↓</p> <p>The forces per unit blade length (L, D, F_N, F_T) are calculated from the force coefficients as $F_x = 0.5\rho V_{rel}^2 c_x c$. Due to the misalignment of airfoil orientation and inflow, the forces per unit blade length reduce. Exemplarily shown on the left for F_N.</p>	<p>↘</p> <p>For the largest part of the blade, the force per unit blade length behaves similarly to that of BEM_{cf}. In the outermost part, the additional increase in angle of attack and, consequently, lift outweighs the decrease due to the velocity decomposition. Here, the fully-corrected load is higher than the one of BEM₀.</p>

Comparison to BEM ₀	BEM _{cf}	BEM _Λ
	<p style="text-align: center;">→</p> <p>The forces per unit radius are $\frac{F_x}{dr} = \frac{F_x}{dl} \frac{dl}{dr} = \frac{F_x}{dl} \frac{1}{\cos(\Lambda-\zeta)}$. Then, the force per unit radius is approximately the same as for BEM₀. Exemplarily shown on the left for F_N.</p> <p>Being proportional to the radial integration of $\frac{F_N}{dr}$, the annulus thrust coefficient is approximately the same as for BEM₀.</p> <p>Being a function of the annulus thrust coefficient, the annulus induction factor is approximately the same as for BEM₀.</p> <p>Minor differences prevail as the airfoil polars are not perfectly proportional to the angle of attack.</p>	<p style="text-align: center;">↑</p> <p>Similar reasoning as for BEM_{cf} applies here, too. However, towards the blade tip, the forces per unit radius exceed those of BEM₀ and BEM_{cf} for reasons explained above.</p> <p>Consequently, the annulus thrust coefficient and induction factor are higher as well.</p>
	<p style="text-align: center;">→</p> <p>The circulation can be calculated from the lift coefficient as $\Gamma = 0.5 V_{rel} c_l c$. Thus, it is approximately the same as for BEM₀.</p> <p>Minor differences prevail, see explanation above.</p>	<p style="text-align: center;">↑</p> <p>Similar reasoning as for BEM_{cf} applies here, too. Like the forces per unit radius the circulation exceeds those of BEM₀ and BEM_{cf} towards the blade tip, too, for reasons explained above.</p>
	<p style="text-align: center;">→</p> <p>f corrects the annulus induction factor to the blade induction factor, such that $a_b = a/f$. For BEM₀ and BEM_{cf}, this is the Prandtl correction factor, which is, among others, a function of the axial induction factor. The axial induction is, in turn, a function of the thrust coefficient. Therefore, the difference in Prandtl correction factor follows a similar trend.</p> <p>Minor differences prevail, see explanation above.</p>	<p style="text-align: center;">↑</p> <p>In contrast to BEM₀ and BEM_{cf}, f accounts for the Prandtl correction as well as the BEM correction model for swept blades in the BEM_Λ implementation. For an aft-swept blade, the displacement of the tip vortex leads to a reduction of the axial induction compared to a straight reference case. To achieve this change in axial induction, f tends towards values larger than one at the tip. This stands in contrast to the Prandtl correction factor, which tends towards zero at the tip to approximate the tip vortex induction. The difference in f is the reason why other quantities presented here, starting with the angle of attack, show variations from the BEM_{cf} implementation.</p>
	<p style="text-align: center;">→</p> <p>As a consequence of the discussion above, the axial blade induction factor is approximately the same as for BEM₀.</p> <p>Minor differences prevail, see explanation above.</p>	<p style="text-align: center;">↓</p> <p>As a consequence of the discussion above, the axial blade induction factor reduces at the blade tip when compared to the BEM₀ and BEM_{cf} implementations.</p>



5.B. NOMENCLATURE

Latin letters

a	Axial induction factor
c_l	Lift coefficient
F_N, F_T	Normal and tangential force
f	Ratio of annulus-averaged to blade induction factor
l	Spanwise coordinate
R	Blade tip radius
r	Radial coordinate
U_∞	Freestream velocity
V_{rel}	Relative inflow velocity
w	Out-of-plane velocity component
x, y	Cartesian coordinates

Greek letters

α	Angle of attack
β	Combined blade pitch and twist angle
Γ	Circulation
λ	Tip-speed ratio
ρ	Density of air
ω	Angular velocity

Subscripts

0	Uncorrected simulations
cf	Crossflow-corrected simulations
Λ	Fully corrected simulations

BIBLIOGRAPHY

- [1] D. R. Verelst and T. J. Larsen. *Load consequences when sweeping blades - A case study of a 5 MW pitch controlled wind turbine*. Tech. rep. RISO-R-1724(EN). Technical University of Denmark, Risø National Laboratory for Sustainable Energy, Wind Energy Division, Roskilde (Denmark), 2010.
- [2] S. Larwood, C. van Dam, and D. Schow. “Design studies of swept wind turbine blades”. In: *Renewable Energy* 71 (Nov. 2014), pp. 563–571. DOI: [10.1016/j.renene.2014.05.050](https://doi.org/10.1016/j.renene.2014.05.050).
- [3] A. Li, G. R. Pirrung, M. Gaunaa, H. A. Madsen, and S. G. Horcas. “A computationally efficient engineering aerodynamic model for swept wind turbine blades”. In: *Wind Energy Science* 7.1 (Aug. 2021), pp. 129–160. DOI: [10.5194/wes-2021-96](https://doi.org/10.5194/wes-2021-96).
- [4] E. K. Fritz, C. Ferreira, and K. Boorsma. “An efficient blade sweep correction model for blade element momentum theory”. In: *Wind Energy* 25.12 (2022), pp. 1977–1994. ISSN: 1099-1824. DOI: [10.1002/we.2778](https://doi.org/10.1002/we.2778).
- [5] S. G. Horcas, N. Ramos-García, A. Li, G. Pirrung, and T. Barlas. “Comparison of aerodynamic models for horizontal axis wind turbine blades accounting for curved tip shapes”. In: *Wind Energy* 26.1 (2023), pp. 5–22. ISSN: 1099-1824. DOI: [10.1002/we.2780](https://doi.org/10.1002/we.2780).
- [6] T. Burton, D. Sharpe, N. Jenkins, and E. Bossanyi. *Wind Energy Handbook*. John Wiley & Sons, June 2011. ISBN: 978-1-119-99392-6.
- [7] S. F. Hoerner. *Fluid-dynamic lift*. Published by Liselotte A. Hoerner, 1985.
- [8] A. Bruining, G. Van Bussel, G. Corten, and W. Timmer. “Pressure distribution from a wind turbine blade; field measurements compared to 2-Dimensional wind tunnel data”. In: *Institute for Windenergy, Delft University of Technology* (1993).
- [9] H. Snel, R. Houwink, and T. Bosscher. *Sectional prediction of lift coefficients on rotating wind turbine blades in stall*. Tech. rep. ECN-C-93-052. Energy Research Center of the Netherlands, 1994.
- [10] J. L. Tangler. “The nebulous art of using wind-tunnel airfoil data for predicting rotor performance”. In: *ASME 2002 wind energy symposium*. ASMEDC, Jan. 2002. DOI: [10.1115/wind2002-40](https://doi.org/10.1115/wind2002-40).
- [11] J. L. Tangler. “Insight into wind turbine stall and post-stall aerodynamics”. In: *Wind Energy* 7.3 (July 2004), pp. 247–260. DOI: [10.1002/we.122](https://doi.org/10.1002/we.122).
- [12] T. Sant, G. van Kuik, and G. J. W. van Bussel. “Estimating the angle of attack from blade pressure measurements on the NREL Phase VI rotor using a free wake vortex model: Axial conditions”. In: *Wind Energy* 9.6 (2006), pp. 549–577. DOI: [10.1002/we.201](https://doi.org/10.1002/we.201).



- [13] T. Sant, G. van Kuik, and G. J. W. van Bussel. “Estimating the angle of attack from blade pressure measurements on the National Renewable Energy Laboratory phase VI rotor using a free wake vortex model: yawed conditions”. In: *Wind Energy* 12.1 (Jan. 2009), pp. 1–32. DOI: [10.1002/we.280](https://doi.org/10.1002/we.280).
- [14] D. Micallef, M. Kloosterman, C. Ferreira, T. Sant, and G. van Bussel. “Validating BEM, direct and inverse free wake models with the MEXICO experiment.” In: *48th AIAA aerospace sciences meeting including the new horizons forum and aerospace exposition*. American Institute of Aeronautics and Astronautics, Jan. 2010. DOI: [10.2514/6.2010-462](https://doi.org/10.2514/6.2010-462).
- [15] H. Rahimi, J. Schepers, W. Shen, N. R. García, M. Schneider, D. Micallef, C. S. Ferreira, E. Jost, L. Klein, and I. Herráez. “Evaluation of different methods for determining the angle of attack on wind turbine blades with CFD results under axial inflow conditions”. In: *Renewable Energy* 125 (Sept. 2018), pp. 866–876. DOI: [10.1016/j.renene.2018.03.018](https://doi.org/10.1016/j.renene.2018.03.018).
- [16] G. Bangga. “Comparison of Blade Element Method and CFD Simulations of a 10 MW Wind Turbine”. In: *Fluids* 3.4 (Dec. 2018), p. 73. ISSN: 2311-5521. DOI: [10.3390/fluids3040073](https://doi.org/10.3390/fluids3040073).



III

TOWARDS SWEEP BLADE TIPS IN THE FIELD



THE TIADE PROJECT

The PhD research presented in this dissertation is part of the activities of the TIADE (Turbine Improvements for ADDitional Energy) project, a collaborative research project by TNO, GE Renewable Energy and LM Wind Power. In this project, innovative wind turbine blade improvements (a.o. innovative tips) and blade add-ons (a.o. spoilers, vortex generators) are developed and validated.

In an initial campaign, a set of conventional blades was mounted on the 3.8 MW research turbine shown in Figure 5.13. Among many other measurements, pressure measurements were conducted at 25 % blade radius. The layout of these pressure sensors was chosen based on the optimisation routines that will be presented in Chapter 6. The measurement campaign resulted in multiple months of pressure data, which are used to validate aeroelastic simulations in Chapter 7.

The original project planning included a second phase, in which the conventional blades used in the first phase would be replaced by blades featuring a tip joint. This tip joint would have allowed the exchange and testing of various tip geometries. In this second phase of the project, it was also intended to conduct pressure measurements at four radial stations. The idea was to gather data for both a conventional tip shape and an aeroelastically tailored tip allowing the validation of aeroelastic models and providing a proof of concept of this tailoring in a field environment. The numerical design study for this aeroelastically tailored tip is presented in Chapter 8.

Delays due to the COVID-19 pandemic and financial challenges in the project consortium prevented the second phase from being executed. This also means that the research presented in this dissertation ends with the numerical design study of an aeroelastically tailored tip. The task of validating swept wind turbine blade tips on a multi-megawatt turbine scale remains for future research.



Figure 5.13: The TIADE research turbine in Wieringermeer, North Holland, Netherlands

A public summary of the TIADE project can be found on the website of [Topsector Energie](#).



6

OPTIMISING THE PRESSURE SENSOR LAYOUT ON WIND TURBINE AIRFOILS

In the pursuit of validating numerical simulations using data from field experiments, a major challenge lies in the generation of high-quality measurements. Pressure measurements are commonly employed to characterise airfoil aerodynamics and to derive sectional loads. In field experiments, the number of pressure sensors can be limited due to access, structural or financial restrictions. Therefore, the layout of these sensors has to be chosen carefully to enable deriving the aerodynamic properties with high accuracy over a wide range of operating conditions.

This chapter presents a robust approach to optimising the sensor layout, aiming at an accurate estimation of the airfoil's lift. Two fundamentally different optimisation algorithms are employed. Given that they arrive at almost identical results, it can be concluded that an optimal solution to this problem exists. The benefit of the proposed approach is demonstrated by comparing results against a simple cosine sensor spacing. Optimising the sensor layout, one can either drastically reduce the number of sensors without losing accuracy or, conversely, increase the accuracy for the same number of sensors.

After an introduction in Section 6.1, Section 6.2 presents the use case on which the sensor layout optimisation is demonstrated as well as the methodology of the optimisation itself. The results are given in Section 6.3 before conclusions are drawn in Section 6.4.

Parts of this chapter have been published in E. Fritz, C. Kelley, K. Brown, *On optimizing the sensor spacing for pressure measurements on wind turbine airfoils*, [Wind Energy Science](#) **9**, 8 (2024).



6.1. INTRODUCTION

Pressure measurements are an essential technique in analysing the flow over aerodynamic bodies. By having knowledge of the pressure field distributed over an airfoil surface, flow characteristics can be determined, and aerodynamic forces can be derived. Pressure measurements are, therefore, well established throughout different research communities, such as aircraft engineering [1] and wind turbine engineering [2].

Most commonly, they are used to derive airfoil polars, i.e. the non-dimensionalised aerodynamic forces and moments as a function of inflow angle of attack [3, 4, 5, 6, 7, 8, 9]. Of particular interest to the wind energy sector, where airfoils rotate and experience different inflow conditions throughout one rotation, is the determination of unsteady airfoil polars [10, 11, 12, 13, 14].

Modern wind turbines make use of a variety of blade add-ons to improve local blade aerodynamics. Surface pressure measurements can be used to study the changes in local airfoil aerodynamics imposed by add-ons such as Gurney flaps [15, 16], vortex generators [17] and trailing edge flaps [18, 19]. In the latter case, pressure measurements have also been used as input for actuation control of trailing edge flaps [20, 21, 22]. Other application areas include investigations into boundary layer transition behaviour [23, 24] or the use of surface pressure spectra for noise modelling [25].

In larger experimental setups on rotating blades, blade aerodynamics can be characterised by measuring pressure distributions at multiple radial locations [26, 27, 28, 29, 30, 31, 32, 33, 18, 34, 35, 36].

Finally, a critical application of such measurements lies in creating reference datasets that can be used for numerical model validation [37, 38, 39, 33, 36].

Irrespective of the application, the number of sensors and their placement on the airfoil's surface impact the accuracy with which the aerodynamic properties of the airfoil can be characterised. A logical consensus is that the pressure sensors should be more densely placed towards the airfoil's leading edge to capture the higher gradients in the pressure distribution commonly present in this region. While some authors mention this explicitly [26, 29, 30, 32, 11], the same can be derived for most other studies mentioned above based on the published graphs and/or schematics. Very few authors go beyond this level of detail regarding the thought process that went into the sensor layout. Brunner et al. gave a mathematical formulation to derive the sensor spacing, which ensures higher resolution at the leading edge [9]. Bak et al. state that "the distribution of the pressure taps was decided from the theoretical target pressure distributions to reflect the expected pressure gradients" [18]. While indicating a more strategic approach to determining the layout, unfortunately, no further details are given.

The lack of detail regarding the selected pressure sensor layout shows that, in most cases, this issue is tackled by simply using a very high number of pressure taps, resulting in an apparently high enough resolution of the pressure distribution. There exist, however, many situations where this is not possible. Limitations on the number of available sensors could be imposed by geometrical considerations, such as small-scale experimental geometries or the use of airfoils with internal structures, structural concerns where too many sensors endanger safe operation, or simply the sensor price. The latter is becoming especially relevant as new sensor technologies such as fibre-optic pressure sensors pose an alternative to the historically most common arrangement of pres-

sure taps leading to transducers. Furthermore, it can be desirable to limit the number of sensors to minimise flow disturbances that could trip the boundary layer or alter measurements further downstream. For such situations, wherein the number of available/allowable sensors is limited, there is a need for a robust approach to finding an optimal sensor spacing which represents the airfoil's pressure distribution and, thus, aerodynamic characteristics as accurately as possible.

In this chapter, two optimisation routines (genetic algorithm and sequential quadratic programming) are used to derive the optimal pressure sensor layout for various airfoils. While applied to the case of rotating wind turbine airfoils, the approach is suited just as well for aerospace applications or wind tunnel experiments. In this study, the sensor layout is optimised for a range of angles of attack, where each angle is weighted based on its probability of occurrence. Results of the optimised pressure sensor layouts are compared against a simple cosine sensor spacing, which is closer to the sensor layouts used in current experiments. Based on the accuracy of lift prediction and the ability to closely represent the expected pressure distribution, the potential to reduce the number of sensors is studied.

6.2. METHODOLOGY

6.2.1. SELECTED AIRFOILS AND THEIR OPERATING CONDITIONS

For the present study, the IEA 15 MW reference wind turbine (RWT) is chosen. All relevant information is taken from the report by Gaertner et al. [40] and the complementary GitHub repository [41]. The IEA 15 MW RWT's blade is defined using the FFA airfoil family. A schematic of the blade geometry, along with the starting positions of the respective airfoils, is shown in Figure 6.1. This study focuses on the four most outboard, non-blended airfoils, which are part of the original FFA-W3 airfoil family and are well-documented [42, 43]: FFA-W3-360, FFA-W3-301, FFA-W3-241 and FFA-W3-211.

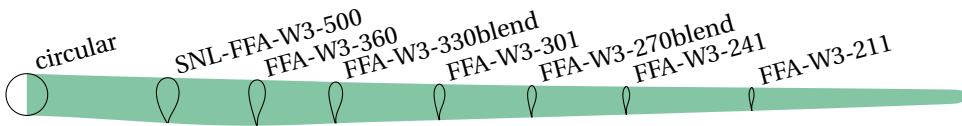


Figure 6.1: IEA 15 MW RWT blade and the starting locations of the airfoils used in the blade definition

The information included in the IEA 15 MW documentation is used to estimate the operating conditions of the respective airfoils in a simplified approach. The turbine is categorised as turbine class IB as defined in IEC standard 61400-1 [44]. According to this standard, the normal wind conditions experienced by a wind turbine are given by a Rayleigh distribution with the cumulative distribution function

$$CDF(U_\infty) = 1 - \exp\left(-\pi\left(\frac{U_\infty}{2U_{ave}}\right)^2\right) \quad (6.1)$$

and probability density function

$$PDF(U_\infty) = \frac{\pi U_\infty}{2U_{ave}^2} \exp\left(-\pi\left(\frac{U_\infty}{2U_{ave}}\right)^2\right), \quad (6.2)$$



where U_∞ is the wind speed at hub height and U_{ave} is defined as $U_{ave} = 0.2 U_{ref}$. The reference wind speed U_{ref} is defined per turbine class, in the case of IEC class IB $U_{ref} = 50 \text{ m s}^{-1}$. Figure 6.2 shows the Rayleigh probability density function between the cut-in and cut-out wind speed of the IEA 15 MW RWT.

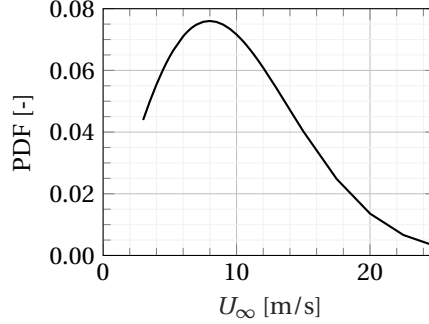


Figure 6.2: Rayleigh wind distribution according to IEC 61400-1 for turbine class IB

Now, the documented rotor performance data [41] are used to estimate the operating regime of the blade cross-sections under investigation. Applying 1D momentum theory with Glauert correction for heavily loaded rotors [see, e.g., 45], the rotor-averaged induction factor a is calculated as a function of the thrust coefficient C_T , which is given in the turbine documentation for the operating range of wind speeds.

$$a = \begin{cases} \frac{1}{2} - \frac{\sqrt{1-C_T}}{2}, & \text{for } C_T < C_{T_2} \\ 1 + \frac{C_T - C_{T_1}}{4\sqrt{C_{T_1} - 4}}, & \text{for } C_T \geq C_{T_2} \end{cases}, \quad (6.3)$$

where $C_{T_1} = 1.816$ and $C_{T_2} = 2\sqrt{C_{T_1}} - C_{T_1} = 0.879$. By applying the Prandtl root and tip corrections

$$f_{tip} = \frac{2}{\pi} \cos^{-1} \left(e^{-\frac{N_b}{2} \left(\frac{R}{r} - 1 \right) \sqrt{1 + \left(\frac{\lambda_r}{1-a} \right)^2}} \right) \quad (6.4)$$

$$f_{root} = \frac{2}{\pi} \cos^{-1} \left(e^{\frac{N_b}{2} \left(\frac{r_{root}}{r} - 1 \right) \sqrt{1 + \left(\frac{\lambda_r}{1-a} \right)^2}} \right), \quad (6.5)$$

where r_{root} and R are the root and tip radius and λ_r is the local tip-speed ratio, the rotor-averaged induction factor can be converted to a local blade induction factor $a_B = \frac{a}{f_{tip} f_{root}}$. Now, the local inflow angle can be calculated as

$$\phi = \tan^{-1} \left(\frac{U_\infty (1 - a_B)}{\omega r (1 + a'_B)} \right), \quad (6.6)$$

where ω is the angular velocity. To simplify the analysis for the current study, the tangential induction factor is assumed to be $a'_B = 0$. It should be noted that this assumption

becomes less valid closer to the blade root but is deemed accurate enough for the proof of concept presented here. For the application of sensor layout optimisation on a real turbine, it should be aimed to obtain realistic tangential induction values, e.g., through numerical simulations. Based on the inflow angle, the angle of attack is calculated as

$$\alpha = \phi - \beta_{twist} - \beta_{pitch}, \quad (6.7)$$

where β_{twist} is the local blade twist angle, and β_{pitch} is the global blade pitch angle. Equation 6.7 neglects elastic twist deformations that should be considered if reliable data or simulation results are available. The angles of attack estimated through this simplified approach are shown for the investigated airfoils as a function of the wind speed in Figure 6.3. Realistic environmental and operational conditions, such as turbulence or shear, would lead to a range of angles of attack present for each wind speed.

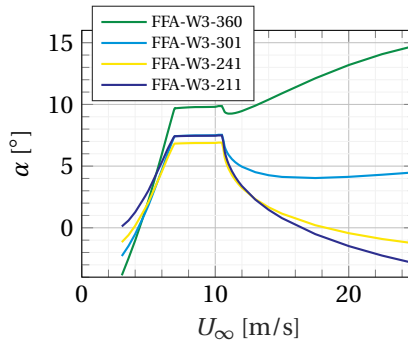


Figure 6.3: Angle of attack as a function of wind speed

6.2.2. GENERATING AIRFOIL POLARS USING XFOIL

Airfoil polars and corresponding pressure distributions are prerequisites for the sensor layout optimisation approaches presented in Sections 6.2.4 and 6.2.4. In this study, the 2D viscous/inviscid code XFOIL, developed by Drela, is used to generate these polars [46]. When simulating viscous airfoil polars, this code requires the chord Reynolds number Re_c as input. It is defined as

$$Re_c = \frac{\rho V_{eff} c}{\mu}, \quad (6.8)$$

where ρ and μ are the density and dynamic viscosity of air, respectively. The local effective velocity can be calculated as

$$V_{eff} = \sqrt{(U_\infty (1 - a_B))^2 + (\omega r (1 + a'_B))^2}. \quad (6.9)$$

At the IEA 15 MW RWT's rated wind speed $U_\infty = 10.59 \text{ m s}^{-1}$, the thrust coefficient is $C_T = 0.769$ and the rotor speed is $\omega = 7.56 \text{ rpm}$, resulting in a tip-speed ratio of $\lambda = 8.97$, see [41]. Using the approach detailed in Section 6.2.1, the rotor-averaged axial induction factor and, consequently, the local blade axial induction are determined. Again, tangential induction is assumed to be negligible. The approximated chord Reynolds numbers



are listed alongside geometric information of the airfoils in Table 6.1. Here, the properties of air are assumed as $\rho = 1.204 \text{ kg m}^{-3}$ and $\mu = 1.825 e^{-5} \text{ kg (m s)}^{-1}$, corresponding to 20°C and standard atmospheric pressure.

Table 6.1: FFA airfoils as used in the definition of the IEA 15 MW RWT and their approximated chord Reynolds number

Airfoil	r [m]	r/R [-]	c [m]	t/c [-]	$Re_{c,approx}$ [-]
FFA-W3-360	31.68	0.26	5.70	0.360	9.86 e6
FFA-W3-301	54.38	0.45	4.48	0.301	12.93 e6
FFA-W3-241	77.67	0.65	3.50	0.241	14.31 e6
FFA-W3-211	93.29	0.78	2.90	0.211	14.20 e6

Based on the approximated chord Reynolds numbers, the airfoil polars are simulated. The results generated with XFOIL are depicted in Figure 6.4. Given the expected angles of attack as shown in Figure 6.3, the polars are determined between $\alpha = -5^\circ$ and $\alpha = 15^\circ$ with a step size of $\Delta\alpha = 0.25^\circ$. To mimic turbulent inflow conditions likely to occur for a wind turbine in the field, boundary layer transition is enforced at $x/c = 0.05$ on the suction side and at $x/c = 0.1$ on the pressure side. The XFOIL simulations were run using 160 panels to discretise the airfoils, with the exception of the FFA-W3-211 airfoil, which was simulated using 195 panels to avoid convergence issues.

6

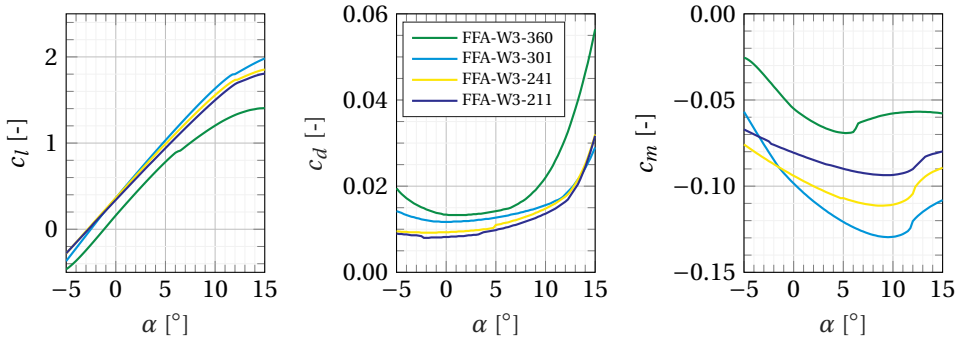


Figure 6.4: Airfoil polars as simulated by XFOIL

It should be noted that XFOIL is one way of generating the polars and pressure distributions later used as inputs for the optimisation routine. This code was chosen for its widespread use and open access. Its applicability to high Reynolds number flows as present in this study has been demonstrated by [47, 48]. Alternatively to XFOIL, the required data could be obtained using other approaches, e.g., RFOIL, which is an adaptation of XFOIL developed for rotating airfoils [49, 50], or higher-fidelity tools such as computational fluid dynamics (CFD).

6.2.3. ESTIMATING LIFT BASED ON A DISCRETE NUMBER OF PRESSURE SENSORS

The polar curves presented in the previous section correspond to the forces distributed over the airfoil surface. Based on the surface pressure coefficient distribution c_p , the chord normal force coefficient c_n and chord tangential force coefficient c_t are calculated as

$$\begin{bmatrix} c_t \\ c_n \end{bmatrix} = \int_S c_p(s) \mathbf{n}(s) ds, \quad (6.10)$$

where \mathbf{n} is the surface normal vector and s is the surface coordinate. It should be considered that these forces do not account for forces due to skin friction. Skin friction forces typically represent a negligible contribution to the lift and pitching moment.

The lift coefficient can be determined by decomposing the normal and tangential force coefficients.

$$c_l = c_n \cos(\alpha) - c_t \sin(\alpha) \quad (6.11)$$

In an experimental setup, information regarding the surface pressure is only available at the discrete points on the airfoil surface where pressure sensors are placed. These discrete points can then be interpolated to derive a pressure distribution spanning the entire airfoil surface. How accurate this interpolation and, thus, the integrated airfoil loads are depends on the number and placement of sensors used. Additionally, a chosen sensor layout might not be equally suitable for all angles of attack. Therefore, one should consider whether priority is given to optimally resolving the pressure distribution for

1. a single angle of attack,
2. a range of angles of attack given equal priority, or
3. a range of angles of attack weighted based on their likelihood to occur during operation/testing.

In the first case, the error between the lift coefficient determined based on the pressure distribution interpolated between sensor locations $c_{l,int}$ and the expected true value of the airfoil coefficient $c_{l,exp}$ is simply their difference

$$E(c_l) = c_{l,int}(\alpha) - c_{l,exp}(\alpha). \quad (6.12)$$

When giving equal priority to several angles of attack N_α , the error between interpolated and expected lift coefficient can be expressed as the mean error

$$\bar{E}(c_l) = \frac{1}{N_\alpha} \sum_{\alpha=\alpha_{min}}^{\alpha_{max}} |c_{l,int}(\alpha) - c_{l,exp}(\alpha)|. \quad (6.13)$$

To avoid cancellation of errors from the different angles of attack, the absolute error values are used in the calculation of the mean error.

In the present study, the third variant is used. Combining the wind speed distribution shown in Figure 6.2 with the expected angle of attack shown in Figure 6.3, the probability of the occurrence of an angle of attack can be calculated. For this purpose, the expected angles of attack are binned using the angle of attack discretisation used in the XFOIL



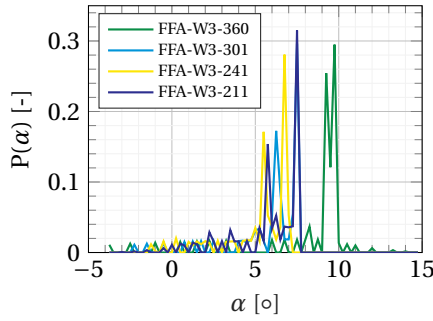


Figure 6.5: Probability of occurrence of an angle of attack for the investigated airfoils

simulations. The resulting probabilities are given in Figure 6.5, where the spikes are due to the binning of the angles of attack.

Now, the probability-weighted error in the prediction of the lift coefficient based on the measurements of a discrete number of pressure sensors can be calculated as

$$E_{prob}(c_l) = \frac{1}{C_{PDF}} \sum_{\alpha=\alpha_{min}}^{\alpha_{max}} P(\alpha) |c_{l,int}(\alpha) - c_{l,exp}(\alpha)|, \quad (6.14)$$

where $P(\alpha)$ is the probability of an angle of attack to occur. Because the integral of the probability density function shown in Figure 6.2 is not equal to unity between the cut-in and cut-out speed, a scaling factor $C_{PDF} = \int_{U_{cut-in}}^{U_{cut-out}} PDF(U_{\infty}) dU_{\infty}$ is applied to the weights. This ensures that the scaled sum of probabilities equals unity and the weighted error is representative of an actual deviation in lift coefficient.

6.2.4. APPROACHES TO DEFINING THE PRESSURE SENSOR LAYOUT

COSINE SPACING

There is a consensus in the literature that the pressure sensor layout should be most dense where high gradients in the pressure distribution need to be resolved. Most commonly, this entails the highest sensor density at the airfoil's leading edge, where pressure gradients are the largest of any location on the airfoil, and trailing edge, where the onset of trailing-edge flow separation similarly can produce relatively large local gradients. An easy way to create such a sensor layout is by applying a cosine distribution as shown in Figure 6.6 for $N_s = 15$ sensors on the FFA-W3-241 airfoil.

GENETIC ALGORITHM (GA) LAYOUT OPTIMISATION

Genetic algorithms imitate biological evolutionary behaviour, and their functionality is only briefly summarised here in a simplified manner: in the initial iteration, a population of random design variable sets is generated. Based on a rating of their fitness and, thus, their ability to minimise the objective function, "parent variable sets" are chosen from which "children variable sets" are generated that form the population of the next iteration. This evolutionary process is repeated until a convergence criterion is met. Genetic algorithms do not require any derivative information and have a good chance of

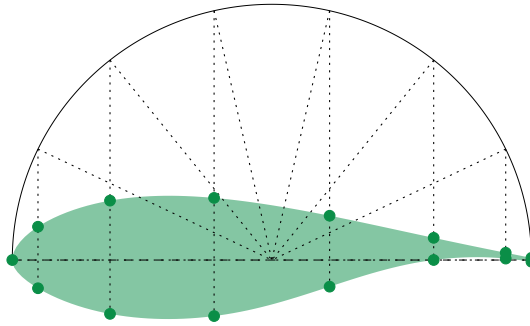


Figure 6.6: Sensor layout using a cosine spacing approach on the FFA-W3-241 airfoil, $N_s = 15$

converging towards the global optimum due to searching the entire design space. As such, they are well-suited for a relatively complex optimisation problem as posed in this study. For a more detailed description of genetic algorithms, the reader is referred to dedicated textbooks such as Kramer [51].

In this study, the design variables are the sensor positions of N_s pressure sensors p_i with $i \in [1, 2, \dots, N_s]$. Each design variable is bounded by $0 \leq p \leq 2$, where p is the coordinate along the chord line moving from the trailing edge of the suction side ($p = 0$) to the leading edge ($p = 1$) and back via the chord line to the trailing edge of the pressure side ($p = 2$). Each population generation consists of 5000 sets of N_s sensor positions, and the convergence criterion is met when 15 consecutive generations do not result in an improvement of fitness. The objective function is chosen as

$$\min E_{prob}(c_p) = \min_{C_{PDF}} \frac{1}{\sum_{\alpha=\alpha_{min}}^{\alpha_{max}} P(\alpha)} \int_S |c_{p,int}(\alpha, s) - c_{p,exp}(\alpha, s)| ds, \quad (6.15)$$

which targets an optimal match between the expected and interpolated pressure distribution. Note that the objective function is an integral of the difference between expected and interpolated pressure distribution rather than the difference at the discrete sensor locations, where this difference is, by definition, zero. The absolute values of their local difference are used to avoid the cancellation of errors, e.g. an equivalent shaving of the negative suction peak and the positive stagnation peak. For the same reason of error cancellation, it is not advisable to directly optimise for a minimal error in lift coefficient prediction $E(c_l)$. Early investigations showed that doing so can yield a very high agreement between the expected airfoil coefficient and the one based on interpolation from the sensor positions. However, when looking at the resulting sensor positions themselves, it appeared that the optimisation routine had merely found a sensor layout which resulted in a close fit in lift prediction while the pressure distribution was not at all captured well. It should be noted that $c_{p,int}(\alpha, s)$ is derived using linear interpolation and extrapolation. Using higher-order interpolation schemes could potentially increase the accuracy with which the pressure distribution is approximated, but it could also introduce numerical artifacts undesired in the proof of concept provided by this study.



This study analyses the effect of sensor placement on the lift prediction, specifically, though the technique could alternatively be applied to improve the measurement of the pitching moment or the pressure component of the drag force. Potential other objectives, such as the accurate determination of the angle of attack or the separation point, would necessitate alternative formulations of the objective function considered outside of this chapter's scope.

SEQUENTIAL QUADRATIC PROGRAMMING (SQP) LAYOUT OPTIMISATION

Another optimisation algorithm, sequential quadratic programming, was implemented to ensure the robustness of solution for the GA described in the previous section. Kelley et al. showed the benefits of an SQP optimised port layout including lift coefficient error reduction compared to cosine spacing [52]. The number of pressure ports was reduced from 48 to 30 to measure lift coefficient with less than 5% error across a broad range of angles of attack for a NACA 64₃ – 618 airfoil by using the SQP optimised layout instead of cosine spacing.

The SQP optimisation algorithm is suited for constrained and non-linear problems. Details of SQP are well documented in [53, 54]. It is a gradient-based, deterministic and computationally efficient optimisation routine. Its working principle entails a risk of converging to local minima rather than the global optimum. As such, a comparison between the results of GA and SQP can be indicative of whether the optimisation problem has a clear optimum or whether multiple minima exist. Design variables and the objective function of the SQP optimisation are identical to the GA optimisation approach in Section 6.2.4. This ensured any differences in the port location solutions were limited to the two optimisation algorithms described. The SQP algorithm was directly swapped within the minimisation function call implemented for the GA approach. The GA and SQP layout optimisation were both implemented in MATLAB's Global optimisation Toolbox.

LIMITING THE OPTIMISATION ALGORITHM

For the generic optimisation problem presented in this study, a design variable space of $0 \leq p \leq 2$ is chosen. In an experiment, however, many practical reasons might limit the spacing of the sensors, a couple of which are discussed below:

- *Fixed sensor position.* If it is desired to fix one sensor at a specific location on the airfoil surface, say at the leading edge of an airfoil, the upper and lower bound of a design variable can be altered such that $p_1 = 1$, while the other design variables are free to be optimised in $0 \leq p \leq 2$.
- *Sensor size.* A real sensor has a finite size (e.g., the diameter of the pressure tap) and therefore, a minimum distance between sensors has to be ensured, which allows for their installation.
- *"No-go" zones.* If certain areas of the tested airfoil are inaccessible, the placement of a sensor in such a "no-go" zone can be avoided. This could be relevant for, for example, a region at the trailing edge too thin to allow for the internal guidance of pressure tubes, the existence of trailing edge adhesive or the presence of internal structures such as a shear web.

The above constraints can be readily applied in the SQP and GA optimisation algorithms. While the first is related to input settings, the latter two can be enforced by outputting an unrealistically high value from the objective function if the desired criteria are not met. The optimisation routine then does not converge towards layouts which violate the minimum sensor spacing or "no-go" zones.

6.3. RESULTS

This section presents the results of applying cosine spacing and optimisation routines to obtain the pressure sensor layout. For all approaches, a number of sensors of $5 \leq N_s \leq 40$ is considered for the four FFA airfoils under investigation.

6.3.1. COSINE SPACING

As mentioned in Section 6.2.4, the optimisation routines do not optimise for lift prediction accuracy but instead for an accurate representation of the pressure distribution. While this ensures that no cancellation of errors occurs, the accuracy of lift prediction is a direct consequence of a well-represented pressure distribution.

The quality of representation of the pressure distribution as a function of the number of sensors is shown in Figure 6.7 (a) for cosine-spaced sensors. Irrespective of the investigated airfoil, this error initially falls sharply before entering a region in which the increase in the number of sensors barely affects the prediction quality. Figure 6.7 (b) depicts the resulting error in lift prediction. As with the error in the representation of the pressure distribution, an increase in sensors leads to a strong initial decrease of error before more gently decreasing for higher N_s . For $N_s \gtrsim 25$, the error of the predicted lift is $E_{prob}(c_l) \leq 0.01$.

For both the accuracy of pressure distribution and lift estimation, it becomes apparent that even numbers of sensors perform considerably better than odd numbers of sensors. This indicates that the steep pressure gradient at the leading edge can be captured accurately without a sensor placed exactly at the leading edge. Having two sensors close to (but not exactly at) the leading edge instead is beneficial for capturing the suction peak and stagnation point. This is the case for even numbers of sensors. This trend is lost upwards of $N_s \approx 30$ where the prediction error behaves more randomly.

6.3.2. OPTIMISED SENSOR LAYOUT

Based on their expected operating conditions, each investigated airfoil has a different range of expected angles of attack and, thus, an individual objective function. Additionally, the airfoil's pressure distributions differ significantly due to their range of relative thickness. Therefore, the optimisation routines arrive at a sensor layout tailored to the individual airfoil. Figure 6.8 shows the optimised sensor layout for the four airfoils using $N_s = 15$ sensors. The individual plots contain the pressure distribution at the angle of attack with the highest probability of occurrence, see also Figure 6.5. Both optimisation routines converge to almost identical sensor layouts. Furthermore, the optimised layouts capture individual features of the pressure distributions very well, such as the flow separation on the suction side of the FFA-W3-360 airfoil or the sharp suction and stagnation peaks of the FFA-W3-211 airfoil.



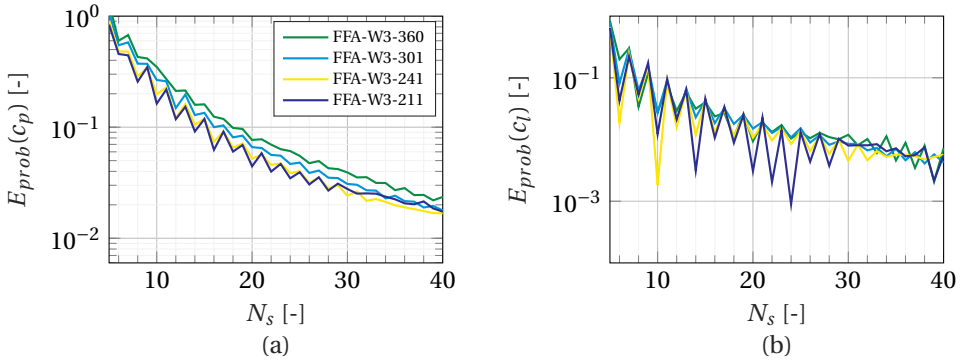


Figure 6.7: Error in the representation of the c_p distribution (a) and c_l determination (b) as a function of the number of sensors using a cosine sensor spacing

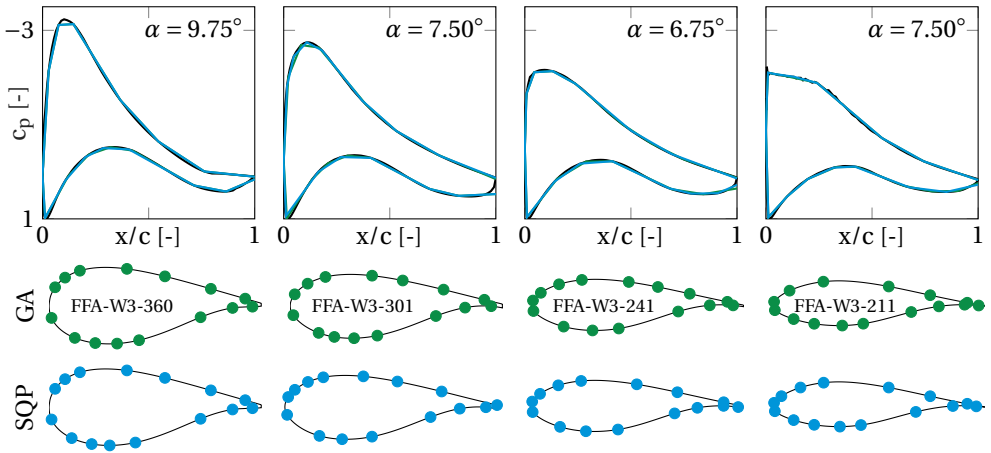


Figure 6.8: Optimised pressure sensor layouts for $N_s = 15$ along with the expected (black) and interpolated (green and light blue) pressure distributions at the angle of attack with the highest probability of occurrence per airfoil

To further underline the advantage of sensor layout optimisation, Figure 6.9 shows both optimised layouts as well as the cosine-spaced counterpart for an increasing number of sensors on the FFA-W3-241. Again, the GA and SQP optimisers converge to almost identical results. It is evident that for lower N_s , the optimised layouts yield a much higher fidelity to the actual pressure distribution at the angle of attack with the highest probability of occurrence. While the optimised layouts achieve an almost perfect match for $N_s = 20$, there are still apparent deviations between the expected pressure distribution and that interpolated from a cosine spacing.

Given the similar convergence behaviour of the two optimisation routines, only the results created using the genetic algorithm are considered from here on. The optimised

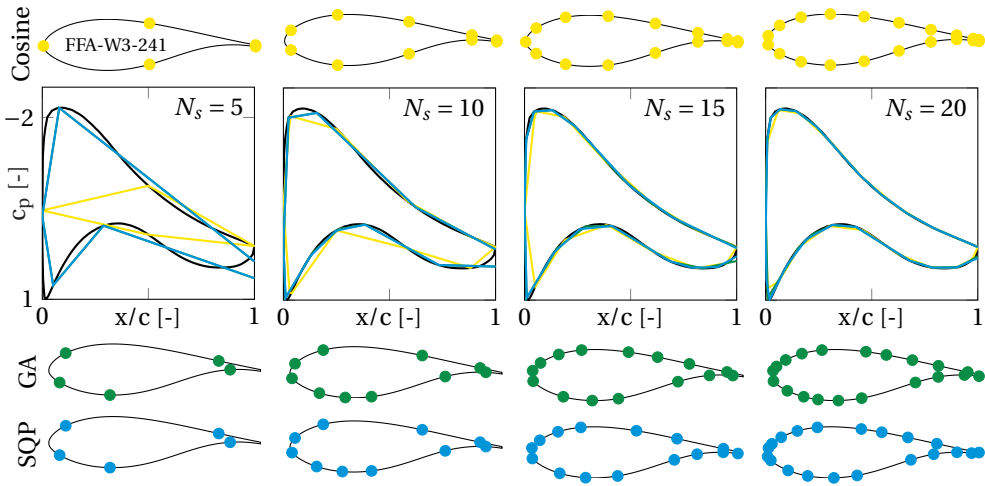


Figure 6.9: Accuracy in representing the expected (black) pressure distribution when using a cosine sensor spacing (yellow) and optimised layouts (green and light blue) for a varying number of sensors, shown for the FFA-W3-241 airfoil and $\alpha = 6.75^\circ$

layout’s accuracy in predicting the pressure distribution and the lift coefficient as a function of the number of sensors is shown in Figure 6.10. Comparing these results to the ones achieved using cosine spacing (see Figure 6.7), the optimised layout exhibits a higher accuracy for the same number of sensors.

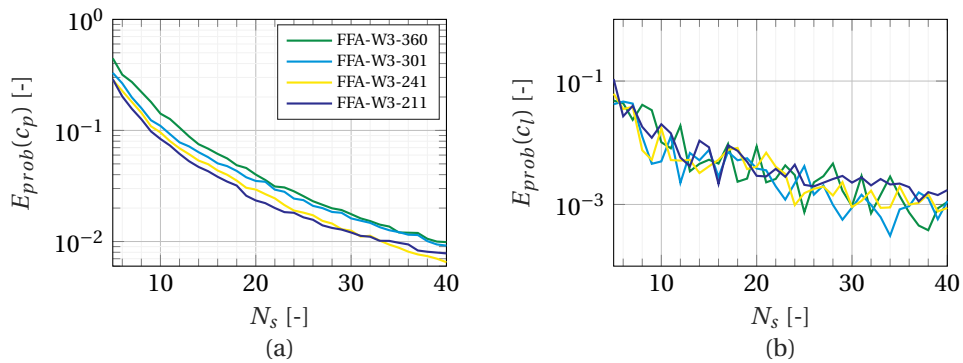


Figure 6.10: Error in the representation of the c_p distribution (a) and c_l determination (b) as a function of the number of sensors using a GA-optimised sensor layout

The probability of specific angles of attack to occur drives the optimiser towards layouts allowing an accurate representation of the pressure distribution in the expected conditions. To further evaluate the benefit of layout optimisation, the difference in errors between the optimised and cosine layout can be calculated for all individual angles of attack, thus also including those expected to occur less often. Figure 6.11 exemplarily



shows this difference of errors for the FFA-W3-241 airfoil and a varying number of sensors. The pressure distribution is clearly represented better when using an optimised layout. While there is an overall large improvement for a very low number of sensors ($N_s = 5$), the largest reductions in error are found around the main expected angle of attack ($\alpha = 6.75^\circ$ for the FFA-W3-241 airfoil) for higher numbers of sensors. With an increasing number of sensors, the error of optimised and cosine layout reduces and, consequently, their difference, too.

For positive angles of attack, the optimised layouts generally also outperform the cosine-spaced layout in predicting the lift coefficient. The exception is the cosine sensor layout with $N_s = 10$ sensors, which gives a very good approximation of the lift coefficient. Similar cases, where the cosine spacing yields very good lift predictions by means of error cancellation in the pressure distribution representation, also occur for the FFA-W3-211 airfoil for $N_s = 14, 20, 22, 24$. These cases are also visible in Figure 6.7 (b) and should be interpreted as outliers.

This analysis of accuracy differences in lift prediction and pressure distribution representation shows that even though the optimisation is driven by the angles of attack expected to occur most often, it has a positive impact throughout large ranges of angles.

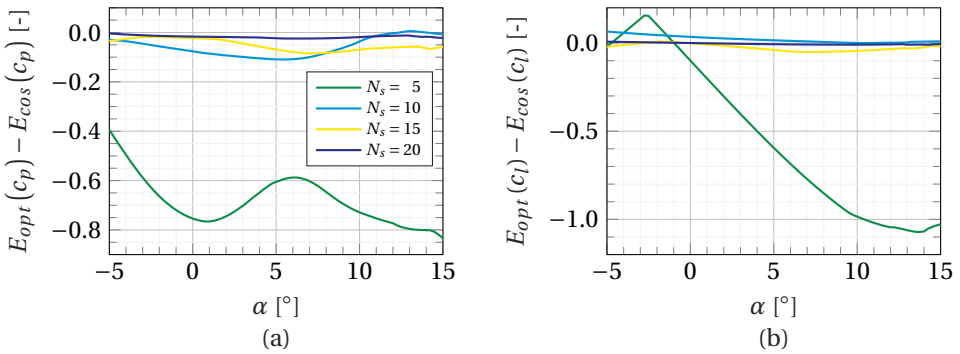


Figure 6.11: Difference of error in the representation of the c_p distribution (a) and c_l determination (b) between an optimised and cosine-spaced sensor layout as a function of angle of attack, shown for the FFA-W3-241 airfoil

While not the focus of this study, the effect of sensor layout optimisation on the determination of the pressure drag coefficient $c_{d,p}$ will briefly be discussed, too. Since pressure measurements cannot capture the viscous contribution to the drag force, results of the drag coefficient c_d are not presented here. Figure 6.12 shows the difference in pressure drag estimation error between the optimised and cosine layout. Similar to the results shown in Figure 6.11, the largest improvements in accuracy occur for very low sensor numbers ($N_s = 5$). For higher numbers of sensors, the added value of sensor layout optimisation reduces. Again, the case with $N_s = 10$ sensors yields an exception, where the cosine spacing outperforms the optimized layout for $\alpha > 2^\circ$. As mentioned in Section 6.2.4, the objective function of the optimisation routines could be tailored to put more emphasis on drag prediction, which would likely lead to a more pronounced increase in accuracy compared to the cosine spacing.

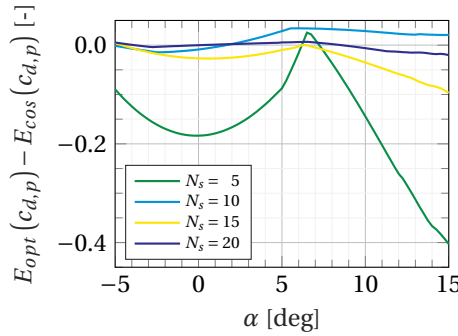


Figure 6.12: Difference of error in the $c_{d,p}$ determination between an optimised and cosine-spaced sensor layout as a function of angle of attack, shown for the FFA-W3-241 airfoil

6.3.3. POTENTIAL FOR REDUCING THE NUMBER OF SENSORS

To estimate the potential for reducing the number of sensors, power law curve fits are applied to all graphs shown in Figures 6.7 and 6.10. This serves the purpose of capturing the general trends of how many sensors are required for a specific level of accuracy without the local maxima and minima present in the underlying curves. The parameters used in the individual curve fits following equation

$$N_s(E_{prob}) = AE_{prob}^{-B} \tag{6.16}$$

are listed in Table 6.2.

Table 6.2: Parameters for curve fits

FFA-W3-		Cosine spacing				Optimised layout			
		360	301	241	211	360	301	241	211
$E_{prob}(c_p)$	A	5.474	5.098	4.616	4.296	3.570	2.820	2.852	2.441
	B	0.522	0.512	0.516	0.540	0.527	0.575	0.536	0.570
$E_{prob}(c_l)$	A	3.612	3.381	4.443	5.097	2.075	1.710	1.378	1.255
	B	0.428	0.441	0.350	0.312	0.399	0.415	0.463	0.509

Based on these curve fits, a ratio of optimised to cosine-spaced sensors $N_{s,opt}/N_{s,cos}$ can be calculated as a function of a specified error in lift prediction or representation of the pressure distribution. Figure 6.13 shows this ratio of required sensors for targeted errors of $0.001 \leq E_{prob} \leq 1$.

As expected, the number of sensors required to achieve a certain accuracy is always lower for the optimised layout than for the cosine-spaced layout. Exemplary, for a lift accuracy of $E_{prob}(c_l) = 0.01$, the ratio of required sensors lies between $N_{s,opt}/N_{s,cos} = 0.45$ and $N_{s,opt}/N_{s,cos} = 0.61$ depending on the airfoil, see Figure 6.13 (b). Assuming that $N_s = 25$ sensors are required to achieve an accuracy of $E_{prob}(c_l) = 0.01$ with a cosine spacing, approximately 10 - 14 fewer sensors yield the same accuracy when placed in an optimised layout.



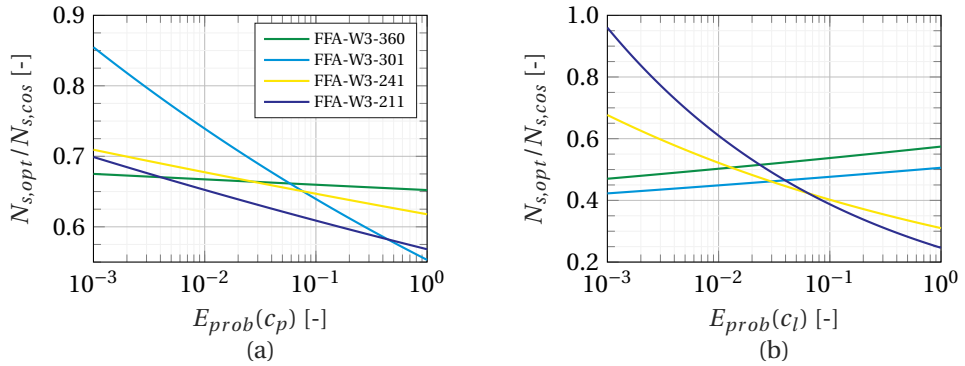


Figure 6.13: Ratio of required number of sensors between an optimised and cosine-spaced sensor layout to represent the pressure distribution (a) and the lift coefficient (b) with a specified accuracy

Historically, experimental testing has been performed predominantly on thin airfoils and with many sensors. The analysis presented here demonstrates that the thinner airfoils are special beneficiaries of the optimisation approach when fewer sensors are available but exhibit less of an advantage over the conventional cosine spacing for a higher number of sensors. For thicker airfoils, sensor layout optimisation has a more constant positive impact on lift prediction throughout the range of desired accuracies.

6

6.4. CONCLUSIONS

Pressure measurements are a commonly used measurement technique to aerodynamically characterise airfoils, in particular, to derive their aerodynamic loading. In most experiments, the accuracy of predicting aerodynamic properties is ensured by placing a large number of pressure sensors on the investigated geometry. There are, however, situations which do not allow for the placement of such a large number of sensors, e.g. due to geometrical, structural or financial restrictions. For these situations, the present work details a robust approach to optimising the pressure sensor layout for fidelity to the expected aerodynamic conditions. To this end, precalculated pressure distributions are input to two optimisation routines, a genetic algorithm and a sequential quadratic programming algorithm, with the sensor locations as design variables. The pressure distributions are weighted based on the expected occurrence of angles of attack. The sensor layout optimisation is applied to the generic case of the IEA 15 MW reference wind turbine, whose blades are defined by the FFA airfoil family. It is expected that the optimisation approach is suited for other airfoil families as well.

The fact that two algorithms using fundamentally different optimisation routines converge on almost identical sensor layouts suggests that an optimal solution exists for this problem. The optimised layouts show a clear advantage over a simpler layout using cosine spacing. They capture the expected pressure distribution more accurately and, consequently, allow a better approximation of the lift coefficient. Even though the optimisation is driven by those angles of attack most likely to occur, the positive impact of sensor layout optimisation is present for large ranges of angles of attack. Based on these

benefits, fewer sensors are required in an optimised layout than in a cosine-spaced layout with the same accuracy. Depending on the targeted error in lift prediction as well as the regarded airfoil geometry, a 39-55 % reduction in the number of sensors compared to cosine spacing is achievable. As such, the presented optimisation approach can contribute significantly to improving the data quality, reducing unnecessary equipment and saving costs in experimental setups. The port savings come mainly from the chordwise regions where the pressure coefficient is linear. This is usually located at the maximum thickness location on the suction surface of the airfoil, and the inflection point of airfoil shape on the pressure surface.

Cost savings are particularly relevant in full-scale wind turbine blade aerodynamics measurements using pressure ports. A low number of pressure ports and transducers may be a low-cost solution. The present work demonstrates the potential of using as few as 5-10 pressure ports to still achieve lift coefficient errors less than 10 % to 2 %, respectively, with an optimised port layout. Further reduction of lift coefficient error with a very low number of pressure ports may be possible by adjusting the optimiser's objective function. The analysis in [52] minimised lift coefficient error as the objective function instead of the sum of pressure coefficient errors. The shape of the pressure coefficient curve was not well represented in the optimal solution because no ports were placed near the suction peak. However, the integration of pressure to lift coefficient was surprisingly accurate with less than 10 % lift coefficient error using only eight ports for a large range of angles of attack. The potential of such minimalistic sensor layouts optimised for lift coefficient accuracy should be investigated in future research.

To further increase the robustness of the optimisation approach presented here, future investigations should aim to incorporate aspects critical to experiments into the optimisation routine, such as sensor failure, measurement uncertainty and a change of the airfoil's pressure distribution due to roughness development. Furthermore, the probability of specific angles of attack to occur is calculated based on the assumption that a single angle of attack occurs per wind speed. In realistic conditions, many characteristics, such as rotor tilt, yaw misalignment, wind shear and turbulence, cause the angle of attack to vary dynamically. These conditions could also lead to dynamic stall. These unsteady effects on optimal port placement are not part of the existing work. But it would be interesting to observe whether the optimised sensor layouts change when adding more realistic inflow and operating conditions to the methodology presented in this study.

6.A. NOMENCLATURE

Latin letters	continues on next page...
A, B	Curve fitting parameters
a, a'	Rotor-averaged axial and tangential induction factor
a_B, a'_B	Local axial and tangential induction factor at blade
CDF	Cumulative distribution function
C_{PDF}	Scaling factor
C_T	Thrust coefficient



Latin letters	...continued
c	Chord
$c_l, c_d, c_{d,p}, c_m$	Lift, drag, pressure drag, and moment coefficient
c_n, c_t	Chord normal and tangential force coefficient
c_p	Pressure coefficient
E	Error function
f_{root}, f_{tip}	Prandtl root and tip correction factors
GA	Genetic algorithm
N_b	Number of blades
N_s	Number of pressure sensors
N_α	Number of investigated angles of attack
\mathbf{n}	Normal vector
P	Probability
PDF	Probability density function
p	Optimisation design variable (chordwise sensor position)
R	Blade tip radius
Re_c	Chord Reynolds number
r	Radial coordinate
r_{root}	Blade root radius
SQP	Sequential quadratic programming
s	Airfoil surface coordinate
t	Airfoil thickness
U_{ave}	Average freestream velocity according to IEC standard 61400-1
U_{ref}	Reference wind speed average over 10 min according to IEC standard 61400-1
U_∞	Freestream velocity
V_{eff}	Local inflow velocity
x	Chordwise coordinate

Greek letters	
α	Angle of attack
β_{pitch}	Blade pitch angle
β_{twist}	Blade twist angle
λ	Tip-speed ratio
λ_r	Local tip-speed ratio
μ	Dynamic viscosity of air
ρ	Density of air
ϕ	Inflow angle
ω	Angular velocity

Subscripts

<i>cos</i>	Cosine sensor layout
<i>exp</i>	Expected true value
<i>int</i>	Interpolated
<i>opt</i>	Optimised sensor layout
<i>prob</i>	Weighted by each angle of attack's probability of occurrence



BIBLIOGRAPHY

- [1] J. B. Barlow, W. H. Rae, and A. Pope. *Low-speed wind tunnel testing*. John Wiley & Sons, 1999. ISBN: 978-0-471-55774-6.
- [2] S. Schreck. “Surface Pressure Measurements”. In: *Handbook of Wind Energy Aerodynamics*. Ed. by B. Stoevesandt, G. Schepers, P. Fuglsang, and Y. Sun. Cham: Springer International Publishing, 2022, pp. 763–801. ISBN: 978-3-030-31306-7. DOI: [10.1007/978-3-030-31307-4_37](https://doi.org/10.1007/978-3-030-31307-4_37).
- [3] W. Timmer and R. Rooij. “Summary of the Delft University Wind Turbine Dedicated Airfoils”. In: *41st Aerospace Sciences Meeting and Exhibit*. Reno, Nevada: American Institute of Aeronautics and Astronautics, Jan. 2003. ISBN: 978-1-62410-099-4. DOI: [10.2514/6.2003-352](https://doi.org/10.2514/6.2003-352).
- [4] M. Post, R. Jones, A. Denton, and R. Millard. “Characterization of a Flatback Airfoil for Use in Wind Power Generation”. In: *46th AIAA Aerospace Sciences Meeting and Exhibit*. Reno, Nevada: American Institute of Aeronautics and Astronautics, Jan. 2008. ISBN: 978-1-62410-128-1. DOI: [10.2514/6.2008-1330](https://doi.org/10.2514/6.2008-1330).
- [5] J. G. Coder and M. D. Maughmer. “Comparisons of Theoretical Methods for Predicting Airfoil Aerodynamic Characteristics”. In: *Journal of Aircraft* 51.1 (2014), pp. 183–191. ISSN: 0021-8669. DOI: [10.2514/1.C032232](https://doi.org/10.2514/1.C032232).
- [6] O. Pires, X. Munduate, O. Ceyhan, M. Jacobs, J. Madsen, and J. G. Schepers. “Analysis of the high Reynolds number 2D tests on a wind turbine airfoil performed at two different wind tunnels”. In: *Journal of Physics: Conference Series* 749.1 (Sept. 2016), p. 012014. ISSN: 1742-6596. DOI: [10.1088/1742-6596/749/1/012014](https://doi.org/10.1088/1742-6596/749/1/012014).
- [7] J. Bartl, K. F. Sagmo, T. Bracchi, and L. Sætran. “Performance of the NREL S826 airfoil at low to moderate Reynolds numbers—A reference experiment for CFD models”. In: *European Journal of Mechanics - B/Fluids* 75 (May 2019), pp. 180–192. ISSN: 0997-7546. DOI: [10.1016/j.euromechflu.2018.10.002](https://doi.org/10.1016/j.euromechflu.2018.10.002).
- [8] D. Holst, B. Church, G. Pechlivanoglou, E. Tüzüner, J. Saverin, C. N. Nayeri, and C. O. Paschereit. “Experimental Analysis of a NACA 0021 Airfoil Section Through 180-Deg Angle of Attack at Low Reynolds Numbers for Use in Wind Turbine Analysis”. In: *Journal of Engineering for Gas Turbines and Power* 141.4 (Apr. 2019), p. 041012. ISSN: 0742-4795, 1528-8919. DOI: [10.1115/1.4041651](https://doi.org/10.1115/1.4041651).
- [9] C. E. Brunner, J. Kiefer, M. O. L. Hansen, and M. Hultmark. “Study of Reynolds number effects on the aerodynamics of a moderately thick airfoil using a high-pressure wind tunnel”. In: *Experiments in Fluids* 62.8 (Aug. 2021), p. 178. ISSN: 0723-4864, 1432-1114. DOI: [10.1007/s00348-021-03267-8](https://doi.org/10.1007/s00348-021-03267-8).
- [10] T. Lee and P. Gerontakos. “Investigation of flow over an oscillating airfoil”. In: *Journal of Fluid Mechanics* 512 (Aug. 2004), pp. 313–341. ISSN: 1469-7645, 0022-1120. DOI: [10.1017/S0022112004009851](https://doi.org/10.1017/S0022112004009851).



- [11] D. Holst, B. Church, F. Wegner, G. Pechlivanoglou, C. N. Nayeri, and C. O. Paschereit. “Experimental Analysis of a NACA 0021 Airfoil Under Dynamic Angle of Attack Variation and Low Reynolds Numbers”. In: *Volume 9: Oil and Gas Applications; Supercritical CO2 Power Cycles; Wind Energy*. Oslo, Norway: American Society of Mechanical Engineers, June 2018, V009T48A010. ISBN: 978-0-7918-5118-0. DOI: [10.1115/GT2018-76514](https://doi.org/10.1115/GT2018-76514).
- [12] D. Holst, F. Balduzzi, A. Bianchini, B. Church, F. Wegner, G. Pechlivanoglou, L. Ferrari, G. Ferrara, C. N. Nayeri, and C. O. Paschereit. “Static and Dynamic Analysis of a NACA 0021 Airfoil Section at Low Reynolds Numbers Based on Experiments and Computational Fluid Dynamics”. In: *Journal of Engineering for Gas Turbines and Power* 141.5 (May 2019), p. 051015. ISSN: 0742-4795, 1528-8919. DOI: [10.1115/1.4041150](https://doi.org/10.1115/1.4041150).
- [13] Y. D. Mayer, B. Zang, and M. Azarpeyvand. “Aeroacoustic investigation of an oscillating airfoil in the pre- and post-stall regime”. In: *Aerospace Science and Technology* 103 (Aug. 2020), p. 105880. ISSN: 1270-9638. DOI: [10.1016/j.ast.2020.105880](https://doi.org/10.1016/j.ast.2020.105880).
- [14] D. De Tavernier, C. Ferreira, A. Viré, B. LeBlanc, and S. Bernardy. “Controlling dynamic stall using vortex generators on a wind turbine airfoil”. In: *Renewable Energy* 172 (July 2021), pp. 1194–1211. ISSN: 0960-1481. DOI: [10.1016/j.renene.2021.03.019](https://doi.org/10.1016/j.renene.2021.03.019).
- [15] J. A. Cole, B. A. O. Vieira, J. G. Coder, A. Premi, and M. D. Maughmer. “Experimental Investigation into the Effect of Gurney Flaps on Various Airfoils”. In: *Journal of Aircraft* 50.4 (2013), pp. 1287–1294. ISSN: 0021-8669. DOI: [10.2514/1.C032203](https://doi.org/10.2514/1.C032203).
- [16] F. Balduzzi, D. Holst, P. F. Melani, F. Wegner, C. N. Nayeri, G. Ferrara, C. O. Paschereit, and A. Bianchini. “Combined Numerical and Experimental Study on the Use of Gurney Flaps for the Performance Enhancement of NACA0021 Airfoil in Static and Dynamic Conditions”. In: *Journal of Engineering for Gas Turbines and Power* 143.2 (Feb. 2021), p. 021004. ISSN: 0742-4795, 1528-8919. DOI: [10.1115/1.4048908](https://doi.org/10.1115/1.4048908).
- [17] D. Baldacchino, C. Ferreira, D. D. Tavernier, W. Timmer, and G. J. W. van Bussel. “Experimental parameter study for passive vortex generators on a 30% thick airfoil”. In: *Wind Energy* 21.9 (2018), pp. 745–765. ISSN: 1099-1824. DOI: [10.1002/we.2191](https://doi.org/10.1002/we.2191).
- [18] C. Bak, H. A. Madsen, U. S. Paulsen, M. Gaunaa, N. N. Sørensen, P. Fuglsang, J. Romblad, N. A. Olsen, P. Enevoldsen, J. Laursen, et al. “DAN-AERO MW: Detailed aerodynamic measurements on a full scale MW wind turbine”. In: *European wind energy conference and exhibition (EWEC)*. 2010, pp. 20–23.
- [19] H. A. Madsen, T. Barlas, A. Fischer, A. S. Olsen, and A. G. Gonzalez. “Inflow and pressure measurements on a full scale turbine with a pressure belt and a five hole pitot tube”. In: *Journal of Physics: Conference Series* 2265.2 (May 2022), p. 022096. ISSN: 1742-6596. DOI: [10.1088/1742-6596/2265/2/022096](https://doi.org/10.1088/1742-6596/2265/2/022096).
- [20] M. Gaunaa and P. B. Andersen. “Load reduction using pressure difference on airfoil for control of trailing edge flaps”. In: *EWEC 2009 proceedings online*. EWEC, 2009.

- [21] C. M. Velte, R. F. Mikkelsen, J. N. Sørensen, T. Kaloyanov, and M. Gaunaa. “Closed loop control of a flap exposed to harmonic aerodynamic actuation”. In: *Proceedings of Torque 2012, The science of making torque from wind*. 2012.
- [22] S. Bartholomay et al. “Pressure-based lift estimation and its application to feed-forward load control employing trailing-edge flaps”. In: *Wind Energy Science* 6.1 (Feb. 2021), pp. 221–245. ISSN: 2366-7443. DOI: [10.5194/wes-6-221-2021](https://doi.org/10.5194/wes-6-221-2021).
- [23] G. v. Groenewoud, L. Boermans, and J. v. Ingen. *Investigation of laminar-turbulent transition of the boundary layer on the 25m HAT wind turbine*. Tech. rep. LR-390. Faculty of Aerospace Engineering, TU Delft, 1983.
- [24] A. P. Schaffarczyk, D. Schwab, and M. Breuer. “Experimental detection of laminar-turbulent transition on a rotating wind turbine blade in the free atmosphere”. In: *Wind Energy* 20.2 (June 2016), pp. 211–220. DOI: [10.1002/we.2001](https://doi.org/10.1002/we.2001).
- [25] F. Bertagnolio, H. A. Madsen, A. Fischer, and C. Bak. “A semi-empirical airfoil stall noise model based on surface pressure measurements”. In: *Journal of Sound and Vibration* 387 (Jan. 2017), pp. 127–162. ISSN: 0022-460X. DOI: [10.1016/j.jsv.2016.09.033](https://doi.org/10.1016/j.jsv.2016.09.033).
- [26] C. Butterfield, W. Musial, and D. Simms. *Combined experiment phase 1. Final report*. Tech. rep. NREL/TP-257-4655. National Renewable Energy Laboratory (NREL), Oct. 1992. DOI: [10.2172/10105837](https://doi.org/10.2172/10105837).
- [27] A. Brand, J. Dekker, C. de Groot, and M. Späth. *Overview of aerodynamic measurements on an Aerpac 25 WPX wind turbine blade at the HAT 25 experimental wind turbine*. Tech. rep. ECN-DE-Memo-96-014. Energy Research Center of the Netherlands, 1996.
- [28] A. Bruining. *Aerodynamic characteristics of a 10m diameter rotating wind turbine blade*. Tech. rep. IW95-084R. Delft, 1997.
- [29] D. A. Simms, M. M. Hand, L. J. Fingersh, and D. W. Jager. *Unsteady aerodynamics experiment phases II-IV test configurations and available data campaigns*. Tech. rep. NREL/TP-500-25950. National Renewable Energy Laboratory, Aug. 1999. DOI: [10.2172/12144](https://doi.org/10.2172/12144).
- [30] M. M. Hand, D. A. Simms, L. J. Fingersh, D. W. Jager, J. R. Cotrell, S. Schreck, and S. M. Larwood. *Unsteady aerodynamics experiment phase VI: Wind tunnel test configurations and available data campaigns*. Tech. rep. NREL/TP-500-29955. National Renewable Energy Laboratory, Dec. 2001. DOI: [10.2172/15000240](https://doi.org/10.2172/15000240).
- [31] J. Schepers, A. Brand, A. Bruining, M. Hand, D. Infield, H. Madsen, T. Maeda, J. Paynter, R. van Rooij, Y. Shimizu, et al. *Final report of IEA Annex XVIII: enhanced field rotor aerodynamics database*. Tech. rep. ECN-C-02-016. Energy Research Center of the Netherlands, 2002.
- [32] T. Maeda and H. Kawabuchi. “Surface pressure measurement on a rotating blade of field horizontal axis wind turbine in yawed condition”. In: *JSME International Journal Series B* 48.1 (2005), pp. 156–163. DOI: [10.1299/jsmeb.48.156](https://doi.org/10.1299/jsmeb.48.156).
- [33] J. Schepers and H. Snel. *Model experiments in controlled conditions, final report*. Tech. rep. ECN-E-07-042. Energy Research Center of the Netherlands, 2007.



- [34] C. Bak, N. Troldborg, and H. A. Madsen. “DAN-AERO MW: Measured airfoil characteristics for a MW rotor in atmospheric conditions”. In: *Scientific Proceedings, European Wind Energy Association (EWEA)* (2011).
- [35] P. Medina, M. Singh, J. Johansen, A. Jove, L. J. Fingersh, and S. Schreck. “Inflow characterization and aerodynamic measurements on a SWT-2.3-101 wind turbine”. In: *50th AIAA aerospace sciences meeting including the new horizons forum and aerospace exposition*. 2012, p. 230.
- [36] K. Boorsma and J. Schepers. *Description of experimental setup, New Mexico experiment*. Tech. rep. ECN-X15-093. Energy Research Center of the Netherlands, 2015.
- [37] R. K. Singh, M. R. Ahmed, M. A. Zullah, and Y.-H. Lee. “Design of a low Reynolds number airfoil for small horizontal axis wind turbines”. In: *Renewable Energy. International Symposium on Low Carbon and Renewable Energy Technology 2010 (ISLCT 2010)* 42 (June 2012), pp. 66–76. ISSN: 0960-1481. DOI: [10.1016/j.renene.2011.09.014](https://doi.org/10.1016/j.renene.2011.09.014).
- [38] H. Sarlak, R. Mikkelsen, S. Sarmast, and J. N. Sørensen. “Aerodynamic behaviour of NREL S826 airfoil at Re=100,000”. In: *Journal of Physics: Conference Series* 524.1 (June 2014), p. 012027. ISSN: 1742-6596. DOI: [10.1088/1742-6596/524/1/012027](https://doi.org/10.1088/1742-6596/524/1/012027).
- [39] H. Heißelmann, J. Peinke, and M. Hölling. “Experimental airfoil characterization under tailored turbulent conditions”. In: *Journal of Physics: Conference Series* 753.7 (Sept. 2016), p. 072020. ISSN: 1742-6596. DOI: [10.1088/1742-6596/753/7/072020](https://doi.org/10.1088/1742-6596/753/7/072020).
- [40] E. Gaertner et al. *Definition of the IEA wind 15-megawatt offshore reference wind turbine*. Tech. rep. NREL/TP-5000-75698. Golden, CO, US: National Renewable Energy Laboratory, 2020.
- [41] E. Gaertner et al. *Definition of the IEA wind 15-megawatt offshore reference wind turbine, GitHub repository*.
- [42] A. Björck. *Coordinates and Calculations for the FFA-W1-xxx, FFA-W2-xxx and FFA-W3-xxx Series of Airfoils for Horizontal Axis Wind Turbines*. Tech. rep. FFA TN 1990-15. Stockholm: Flygtekniska Försöksanstalten, 1990.
- [43] F. Bertagnolio, N. N. Sorensen, J. Johansen, and P. Fuglsang. *Wind turbine airfoil catalogue*. Risø-R-1280(EN). Forskingscenter Risø, Aug. 2001.
- [44] International Electrotechnical Commission. *Wind turbines – part 1: Design requirements (IEC 61400-1:2005(E))*. Tech. rep. 2005.
- [45] T. Burton, D. Sharpe, N. Jenkins, and E. Bossanyi. *Wind Energy Handbook*. John Wiley & Sons, June 2011. ISBN: 978-1-119-99392-6.
- [46] M. Drela. “XFOIL: An analysis and design system for low reynolds number airfoils”. In: *Lecture notes in engineering*. Springer Berlin Heidelberg, 1989, pp. 1–12. DOI: [10.1007/978-3-642-84010-4_1](https://doi.org/10.1007/978-3-642-84010-4_1).

- [47] O. Ceyhan et al. “Summary of the Blind Test Campaign to predict the High Reynolds number performance of DU00-W-210 airfoil”. In: *35th Wind Energy Symposium*. AIAA SciTech Forum. American Institute of Aeronautics and Astronautics, Jan. 2017. DOI: <https://doi.org/10.2514/6.2017-0915>.
- [48] M. Caboni. *Validation of high Reynolds number, free-transition, RANS-based CFD simulations using the DNW-HDG’s airfoil experiment*. Tech. rep. TNO 2021 R12123. TNO, July 2021.
- [49] R. Van Rooij. *Modification of the boundary layer calculation in RFOIL for improved airfoil stall prediction*. Tech. rep. IW-96087R. Netherlands, Sept. 1996.
- [50] G. Ramanujam, H. Özdemir, and H. W. M. Hoeijmakers. “Improving Airfoil Drag Prediction”. In: *Journal of Aircraft* 53.6 (2016), pp. 1844–1852. ISSN: 0021-8669. DOI: [10.2514/1.C033788](https://doi.org/10.2514/1.C033788).
- [51] O. Kramer. *Genetic algorithm essentials*. 1st ed. New York, NY: Springer Berlin Heidelberg, 2017. ISBN: 978-3-319-52155-8.
- [52] C. Kelley, J. Cutler, and K. Brown. “Optimum pressure port layout with minimum sensors for wind turbine aerodynamics measurements”. In: *Wind energy science conference glasgow*. 2023.
- [53] M. C. Biggs. *Constrained minimization using recursive quadratic programming*. North-Holland, 1975.
- [54] P. Boggs and J. Tolle. “Sequential quadratic programming for large-scale nonlinear optimization”. In: *Journal of Computational and Applied Mathematics* 124.1 (2000), pp. 123–137. DOI: [10.1016/S0377-0427\(00\)00429-5](https://doi.org/10.1016/S0377-0427(00)00429-5).



7

AEROELASTIC MODEL VALIDATION USING FIELD MEASUREMENTS

In this chapter, low-fidelity numerical models are validated using experimental data from the TIADE field experiment. Central to this validation exercise are several months of pressure measurements obtained at 25 % of the blade radius. These are analysed on a ten-minute average and on a time-resolved time scale. The ten-minute average data are used to validate aerodynamic simulations based on both integrated sectional loads as well as on the underlying pressure distributions. The time-resolved data are used to investigate the relative error of numerical simulations regarding the unsteady sectional blade loads and its relation to various environmental and operational conditions.

A brief introduction is given in Section 7.1. Section 7.2 details the measurement setup, the data reduction, the numerical simulation tools, and the approach of estimating the angle of attack from the pressure measurements. The results from analysing the field data and validating the numerical models are presented in Section 7.3. The conclusions from this study are given in Section 7.4.

Parts of this chapter have been published in E. Fritz, K. Boorsma, M. Caboni, A. Herrig *Blade surface pressure measurements in the field and their usage for aerodynamic model validation*, [Wind Energy](#) (2024).



7.1. INTRODUCTION

Historically, the wind energy community has conducted multiple experiments on field turbines, many of which included pressure measurements. At the TNO Wind Energy (formerly ECN) facilities, a two-bladed research turbine of 25 m diameter was operated. Pressure measurements at three radial locations were used to, among others, study the boundary layer's transition behaviour [1]. NREL conducted the Unsteady Aerodynamics Experiment (UAE) in multiple phases. Phases I - IV, executed between 1989 and 1997, were field experiments on a three-bladed rotor of 10 m diameter where both pressure distributions and blade loads were measured [2, 3]. Imperial College and Rutherford Appleton Laboratory measured pressures at six radial locations of a three-bladed turbine with 17 m diameter. Between 1989 and 1993, the Technical University of Denmark (DTU) ran several measurement campaigns on a three-bladed rotor of 19 m, investigating 3D flow effects on a rotating blade and studying its effect on airfoil characteristics [4, 5]. At the Technical University of Delft (TUD), experiments on a two-bladed rotor of 10 m diameter with pressure taps at four radial stations were conducted [6]. At Mie University, pressure distributions at midspan of a three-bladed with 10 m diameter were measured and compared alongside with the integrated forces for different yaw angles [7]. A more detailed summary of the field experiments described so far is given in the final report of IEA Annex XVIII [8]. Falling into the same range of rotor size, an Enercon E30 research turbine with 29.6 m diameter is operated on the campus of Flensburg University. Employing pressure and hot-film sensors, the airfoil boundary layer was characterised [9].

While all experiments mentioned so far undoubtedly contribute to the scientific progress in wind turbine aerodynamics, they were all conducted on turbines of smaller than current state-of-the-art size and power rating. One example of a field experiment close to modern wind turbine scales is the DAN-AERO MW project conducted by DTU in collaboration with LM Glasfiber (nowadays LM Wind Power), Siemens Wind Power (nowadays Siemens Gamesa), Vestas and DONG Energy (nowadays Ørsted) [10, 11]. Here, inflow characteristics were measured on a Siemens 3.6 MW turbine using five-hole pitot tubes and on an NM80 2 MW wind turbine using a meteorological mast. Additionally, the NM80 turbine was equipped with pressure sensors at four radial stations and microphones for high-frequency measurements at the outermost station. These field pressure measurements were compared to 2D wind tunnel experiments of corresponding airfoils [12] and 3D computational fluid dynamics (CFD) [13]. The DAN-AERO database has further been used for the validation of CFD regarding spanwise blade loading [14], rotor induction [15] and aerodynamics in sheared and yawed conditions [16] as well as for the validation of engineering correction models commonly used in blade element momentum theory (BEM) [17]. A validation benchmark comparing simulation results from a wide range of numerical tools suggested that it is still challenging to obtain a good match with field measurements [18]. Furthermore, DTU and Siemens Gamesa investigated the impact of an active trailing edge flap using measurements obtained with a pressure belt on a 4.3 MW wind turbine [19] and measurements were used to validate aeroelastic simulations [20]. Another example of large-scale field experiments is the ongoing RAAW experiment conducted on a 2.8 MW research wind turbine by GE Vernova, NREL and Sandia National Laboratories [21]. This experiment aims to provide an exhaustive validation dataset by measuring the flow field upstream and downstream of the

turbine [22] and the turbine's loads and performance. The measurements have been used to inform wind field reconstruction methods based on large-eddy simulations [23] and to validate load and performance predictions by aeroservoelastic simulations [24]. It should be noted, that research conducted on state-of-the-art wind turbines is often done in collaboration with industrial partners. As a consequence, results can only partly be disseminated to protect commercial interests.

As outlined in Chapter 1, a central development in the field of wind turbine technology is the ever-growing size of the rotor. Modern wind turbine blades surpass lengths of 100 m and are becoming increasingly slender and flexible structures. The scalability of research results obtained in previous field experiments has to be questioned, leading to two important challenges: Firstly, field research needs to be conducted to understand the aerodynamic and aeroelastic behaviour of these larger wind turbines. Secondly, in contrast to the turbines themselves, the numerical tools used to design them remain largely unchanged. It is thus of utmost importance to continuously validate the simulation algorithms' capability to accurately predict the aerodynamic and aeroelastic behaviour of wind turbines. As discussed above, few extensive measurement campaigns that capture a vast range of operating and environmental conditions are available for such validation exercises.

This chapter presents results from a long-term measurement campaign conducted on a 3.8 MW research wind turbine with a rotor diameter of 130 m. Complimenting recent available literature, this research wind turbine size enables the acquisition of data more representative of state-of-the-art wind turbines. Pressure measurements are performed at 25 % of the blade radius, where the blade is defined by a 38 % thick airfoil, and a ground-based LiDAR system provides inflow measurements. Limited experimental data exists for airfoils of comparable thickness, particularly not in rotating conditions in the field. Measurements are logged over several months, resulting in an extensive field experiment database. In this study, the pressure measurements are used to validate aerodynamic models on the physical scale of rotor and airfoil and on the time scale of ten-minute averages and fully time-resolved data.

7.2. METHODOLOGY

7.2.1. EXPERIMENTAL SETUP

TEST SITE

A long-term validation campaign is performed on a 130 m diameter, three-bladed 3.8 MW wind turbine featuring variable speed and active blade pitch (to vane) control at 110 m hub height. As of spring 2021, this turbine has become operational at the test site of ECN Wind Energy Facilities (EWEF) in Wieringerwerf, The Netherlands [25, 26]. An overview of the test site is given in Figure 7.1.

The test site and its surroundings are characterised as flat terrain, consisting of mainly agricultural areas, with single farmhouses and rows of trees. The EWEF farm is very well suited for an investigation into effects at full scale because of its state-of-the-art turbines and the comprehensive and reliable measurement infrastructure for turbine and meteorological data. The TIADE turbine is located at the most westerly spot within a row of prototypes that are positioned on a line that is roughly oriented West to East,



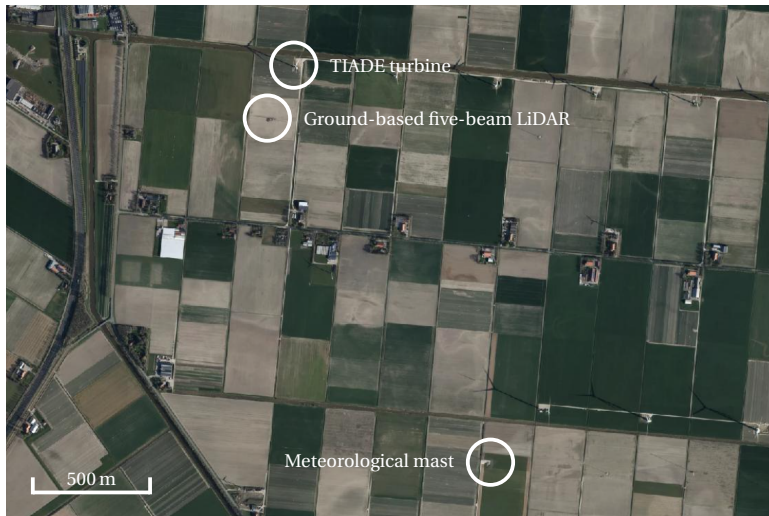


Figure 7.1: Overview of the test site, map derived from data provided by PDOK (Publieke Dienstverlening op de Kaart), licensed under the CC-BY-4.0 license [27]

hence resulting in a relatively large undisturbed sector which includes the prevailing southwesterly wind direction.

The turbine has been instrumented in accordance with IEC measurement campaigns for power and loads [28]. Wind speed measurements have been taken from a ground-based LiDAR located 280 m in southwesterly direction, which measures at eleven different heights from 42 to 188 m. Also, air pressure and temperature are measured at a nearby meteorological mast. In addition to the ground-based LiDAR, two forward-looking nacelle-based LiDARs are operational on the turbine, plus a scanning LiDAR positioned 912 m in southwesterly direction to measure wake characteristics.

PRESSURE MEASUREMENTS

At 25 % of the blade radius, 31 pressure taps are used to measure the pressure distribution around the blade cross-section. The pressure taps on the blade surface are connected to two Scanivalve DSA3218-PTP pressure scanners through pressure tubes. Each pressure scanner can accommodate 16 signals and typically has a 0.05 % full-scale long-term accuracy. The reference pressure, measured in the turbine hub, is connected to the pressure scanners by a tube of approximately 15 m length.

At the measurement location, the blade geometry is defined by a 38 % thick airfoil closely resembling the DU-00-W-401 airfoil. Its geometry is a blend between the DU-00-W-401 airfoil and a proprietary airfoil by LM Wind Power, which is why limited information regarding its characteristics can be made publicly available. The pressure sensor layout is designed using a genetic algorithm optimisation routine (see Chapter 6) to represent the pressure distribution as accurately as possible throughout the operational range of the turbine. A schematic of the measurement system, the optimised sensor layout and the inflow conditions are shown in Figure 7.2.

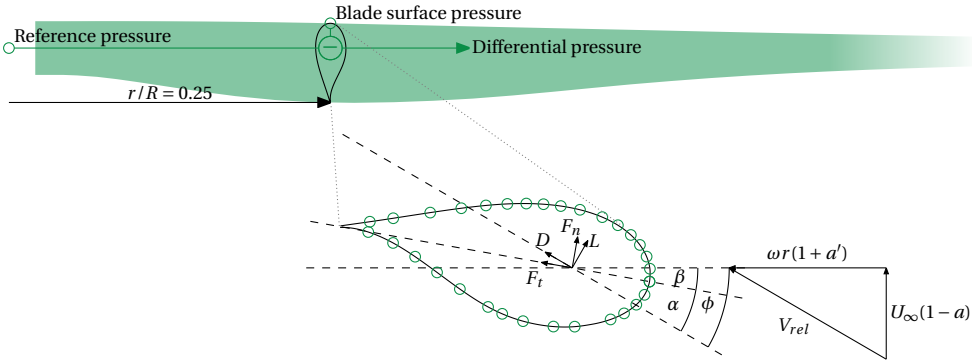


Figure 7.2: Schematic of the measurement setup and DU-00-W-401 airfoil with pressure taps and inflow conditions

Spanwise sensor staggering is applied to avoid any turbulence created by the upstream sensors interfering with measurements of the sensors further downstream. On top of that, the streamlines on the blade surface at 25% radius will be curved due to the circular motion of the blade. Therefore, an additional arc is added to the spanwise staggered sensor positions. The resulting differences in the individual sensors' spanwise location entail a negligible change in the local airfoil shape.

7.2.2. DATA REDUCTION

CORRECTION FOR CENTRIFUGAL FORCES

For each tap, the pressure is measured as the differential pressure Δp between the blade surface pressure and a reference pressure. To derive the blade surface pressure, Bernoulli's equation is employed, which in differential form reads

$$\frac{dp}{\rho} + VdV + g dz = 0, \quad (7.1)$$

where p is the static pressure, ρ is the density of air, V is a velocity, g is the gravitational constant and z is the height. The height of a blade cross-section can be expressed as

$$z(r, \theta) = z_{hub} + r (\cos \zeta \cos \tau \cos \theta - \sin \zeta \sin \tau), \quad (7.2)$$

where z_{hub} is the hub height, r is the radial position, ζ is the cone angle, τ is the tilt angle and θ is the azimuthal angle ($\theta = 0$ refers to the vertical upward blade position). Here, straight blades without prebend, sweep or deformation are assumed. Applying partial derivatives with respect to the variable quantities r and θ , dz becomes

$$dz = \frac{\partial z}{\partial r} dr + \frac{\partial z}{\partial \theta} d\theta, \quad (7.3)$$

where

$$\frac{\partial z}{\partial r} = \cos \zeta \cos \tau \cos \theta - \sin \zeta \sin \tau \quad (7.4)$$



and

$$\frac{\partial z}{\partial \theta} = -r \cos \zeta \cos \tau \sin \theta . \quad (7.5)$$

Substituting Equations 7.3 - 7.5 into Equation 7.1, Bernoulli's equation now reads

$$\frac{dp}{\rho} + VdV + g(\cos \zeta \cos \tau \cos \theta - \sin \zeta \sin \tau) dr - g r \cos \zeta \cos \tau \sin \theta d\theta = 0 . \quad (7.6)$$

Assuming two points with p_1, V_1, r_1, θ_1 and p_2, V_2, r_2, θ_2 , Bernoulli's equation yields

$$\begin{aligned} \frac{p_2 - p_1}{\rho} + \frac{V_2^2 - V_1^2}{2} + g(\cos \zeta \cos \tau \cos \theta - \sin \zeta \sin \tau) (r_2 - r_1) \\ + g r \cos \zeta \cos \tau (\cos \theta_2 - \cos \theta_1) = 0 . \end{aligned} \quad (7.7)$$

Assuming further that $p_1 = p_\infty, V_1 = U_\infty, r_1 = 0, p_2 = p_{surf}, V_2 = V, r_2 = r_{PS}$ and $\theta_1 = \theta_2$, then the pressure on the blade surface p_{surf} can be expressed as

$$p_{surf} = p_\infty + \frac{\rho}{2} (U_\infty - V)^2 - \rho g r_{PS} (\cos \zeta \cos \tau \cos \theta - \sin \zeta \sin \tau) . \quad (7.8)$$

Here, p_∞ and U_∞ are the freestream static pressure and velocity, respectively, at hub height, V is the velocity over the airfoil and r_{PS} is the radial position of the pressure sensors.

Bernoulli's equation is employed again to derive the pressure on the reference side of the pressure sensor. The air in the reference tube experiences an additional radial acceleration field so that

$$\frac{dp}{\rho} + VdV + g dz + \omega^2 r dr = 0 , \quad (7.9)$$

where ω is the angular velocity of the turbine. Similar to the blade surface side, this leads to

$$\begin{aligned} \frac{p_2 - p_1}{\rho} + \frac{V_2^2 - V_1^2}{2} + g(\cos \zeta \cos \tau \cos \theta - \sin \zeta \sin \tau) (r_2 - r_1) \\ + g r \cos \zeta \cos \tau (\cos \theta_2 - \cos \theta_1) + \frac{\omega^2}{2} (r_2^2 - r_1^2) = 0 . \end{aligned} \quad (7.10)$$

Assuming $p_1 = p_{hub}, V_1 = 0, r_1 = 0, p_2 = p_{ref}, V_2 = 0, r_2 = r_{PS}$ and $\theta_1 = \theta_2$, then the pressure on the sensor's reference side p_{ref} can be expressed as

$$p_{ref} = p_{hub} - \rho g r_{PS} (\cos \zeta \cos \tau \cos \theta - \sin \zeta \sin \tau) - \frac{\rho}{2} \omega^2 r_{PS}^2 , \quad (7.11)$$

where p_{hub} is the static pressure in the hub. The measured difference between blade surface pressure p_{surf} and reference pressure p_{ref} is then

$$\Delta p = p_\infty + \frac{\rho}{2} (U_\infty - V)^2 - p_{hub} + \frac{\rho}{2} \omega^2 r_{PS}^2 . \quad (7.12)$$

As can be seen from Equation 7.12, the hydrostatic pressure changes experienced on the blade surface are equal to those on the reference side of the pressure sensors and thus cancel each other out. In contrast to that, the measured data has to be corrected for centrifugal effects. The ratio of the centrifugal pressure to the dynamic pressure $p_{dyn} = \frac{\rho}{2} V_{rel}^2$ is

$$\frac{\Delta p_{cent}}{p_{dyn}} = \frac{\frac{\rho}{2} \omega^2 r_{PS}^2}{\frac{\rho}{2} V_{rel}^2}. \quad (7.13)$$

The relative velocity can be expressed as $V_{rel} = \omega r \sqrt{\frac{1}{\lambda^2} \frac{R^2}{r^2} (1-a)^2 + (1+a')^2}$. With $r/R = 0.25$, assuming axial and tangential induction factors of $a = 0.3$ and $a' = 0$, respectively, and a tip-speed ratio of $\lambda = 9$, then $\frac{\Delta p_{cent}}{p_{dyn}} = 0.91$, showcasing the importance of the correction for centrifugal loads. To eliminate centrifugal effects from the measurements, the measured differential pressure is corrected so that

$$\Delta p_{cor} = \Delta p + \frac{\rho}{2} \omega^2 r_{PS}^2. \quad (7.14)$$

ESTIMATION OF THE LOCAL INFLOW VELOCITY

The wind profile is provided by a ground-based LiDAR system. Mathematically, the wind profile including shear can be described by a power law curve

$$V_{hor}(z) = V_{hor}(z_{ref}) \left(\frac{z}{z_{ref}} \right)^{\alpha_s}, \quad (7.15)$$

where V_{hor} is the horizontal wind velocity, z_{ref} is a reference height often taken to be the hub height, and α_s is the shear exponent. The shape of the wind profile is time-dependent, thus inducing time-dependent loads on the turbine. To estimate the change of loading with time, a good approximation of the instantaneous wind profile is desirable. For time-resolved analyses, a shear exponent $\alpha_s(t)$ is fit to the instantaneous wind profile for each time stamp and the time-varying wind profile is calculated as

$$V_{hor}(z, t) = V_{hor}(z_{hub}, t) \left(\frac{z(t)}{z_{hub}} \right)^{\alpha_s(t)}. \quad (7.16)$$

This approach enables the estimation of the horizontal wind speed $V_{hor,est}$ at a given time and height. As such, it can be used to estimate the inflow conditions at the blade location where the pressure sensors are located. The velocity components normal and tangential to the rotor plane/cone are given by

$$V_N = V_{hor} \cos \psi \cos \tau \quad (7.17)$$

$$V_T = \omega r \cos \zeta + V_{hor} (\sin \tau \sin \theta - \sin \psi \cos \theta), \quad (7.18)$$

where ψ is the yaw misalignment angle. Neglecting axial and tangential induction, the relative velocity at the blade is

$$V_{rel} = \sqrt{V_N^2 + V_T^2}. \quad (7.19)$$



PROCESSING OF TEN-MINUTE STATISTICS

The power, loads, pressures and turbine operational measurement signals of the research turbine, together with the wind speed measurements of the ground-based LiDAR and atmospheric measurements of the meteorological mast, have been used for the analysis in this chapter. Ten-minute statistics in the form of mean $\bar{\xi}_{10}$, standard deviation $\sigma_{10}(\xi)$, minimum $\xi_{10,min}$ and maximum $\xi_{10,max}$ have been retrieved from the database, resulting in a large number of ten-minute samples. Here, the arbitrary variable ξ represents the measurement signals. After retrieving the statistics from the database, a second data reduction step is performed to filter out erroneous samples, outliers, and complex inflow instances that are too hard to replicate with aeroelastic simulations. The underlying ten-minute samples are excluded from the dataset for selected signals

- when a measurement signal is not recorded, for example, due to a malfunction, resulting in a non-numeric value (NaN),
- when the wind direction falls outside the undisturbed wind sector, leading to wake effects from neighbouring turbines,
- when the turbine is not in normal operation conditions in power production, discarding parked and idling cases, or
- when large yaw misalignment, extreme turbulence and shear occur.

Starting with about 48,000 ten-minute samples from the database for a nine-month period featuring a constant blade configuration, about 4,000 samples remained after application of the above-specified filtering. These ten-minute samples and their statistics are used for the analyses presented in Sections 7.3.1 and 7.3.2. The distribution of these samples as a function of wind speed and turbulence intensity TI is illustrated in Figure 7.3 (a).

Aerodynamic forces and pressures are influenced by atmospheric conditions linearly through the air density. The variation of the air density can be shown to lie between 1.2 and 1.3 kg m⁻³ for the selected samples. To account for these changes, the measured aerodynamic pressures are corrected to a reference air density of 1.225 kg m⁻³ using the ideal gas law.

To characterise trends in the data, the ten-minute samples are binned. Bin averaging is applied to the resulting data set both in wind speed and turbulence intensity. The standard error S of the mean within each bin is calculated using

$$S(\bar{\xi}) = \frac{\sigma_{bin}(\bar{\xi})}{\sqrt{N}}, \quad (7.20)$$

where $\sigma_{bin}(\bar{\xi})$ is the standard deviation of the bin data samples and N is the number of samples per bin. This standard error is a measure of the ten-minute mean's repeatability over the various samples within one bin. Additionally, the mean value of the ten-minute standard deviations of the samples in one bin $\bar{\sigma}_{10}(\xi)$ is a measure of the variability of the regarded signal in a particular bin. A minimum of six samples is chosen as requirement for a bin to have a valid average value. The measured data is binned for inflow velocities

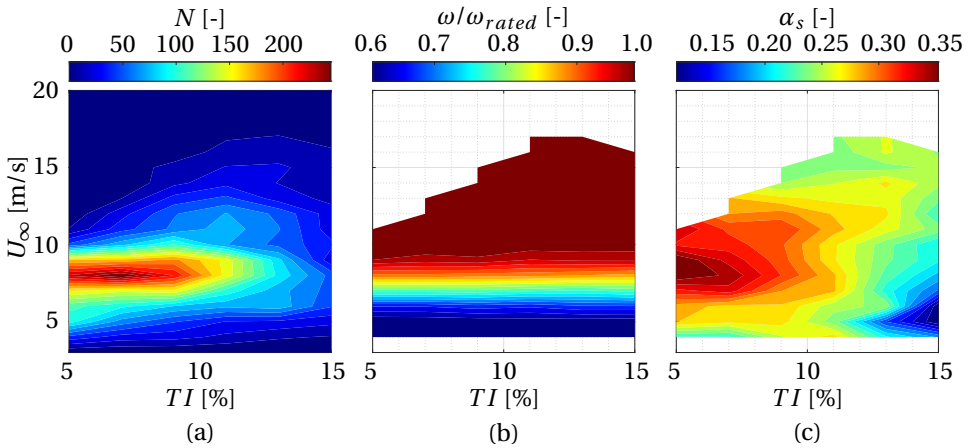


Figure 7.3: Distribution of number of ten-minute samples (a), non-dimensionalised rotor speed (b) and vertical wind shear exponent (c) as function of binned wind speed and TI for the current data set.

between 3 m s^{-1} and 20 m s^{-1} with an increment of 1 m s^{-1} , and for turbulence intensity values between 5 % and 15 % with an increment of 2 %.

Figure 7.3 (b) shows the binned rotor speed non-dimensionalised by the rated rotor speed. It can be observed, that the rotor speed is a function of the wind speed rather than of the turbulence intensity. Combining the data from Figure 7.3 (a) and (b), it becomes clear that the majority of the available data is located close to where the rated rotor speed is reached.

Unsteady loads are highly influenced by turbulence and its intensity as well as other wind non-uniformities such as vertical shear. If bin-averaged load results are compared, it is important to also consider these to prevent bias. It is known that TI and vertical wind shear are correlated, in the sense that nighttime features high shear and low TI , while daytime features higher TI and lower shear. This relationship is once more illustrated in Figure 7.3 (c) for the current dataset. It is acknowledged that this relationship makes it difficult to distinguish between the effects of shear and turbulence intensity in the bin-averaged dataset.

PROCESSING FOR THE TIME-RESOLVED ANALYSIS

In the second step of the analysis presented here, measurements and simulations are compared on a time-resolved basis. The pressure measurements are sampled at a frequency of 256 Hz. Considering multiple months of measurements, the amount of data rapidly outgrows sizes manageable in standard data processing software. Thus, several steps are taken in addition to the filtering for time period, rotational speed, turbine state, wind direction and invalid data described in the previous section:

1. On and after rainy days, water accumulates in the pressure tubes, which expresses itself in "spiky" pressure measurements, where sensors containing water in their



connecting tube exhibit a different mean pressure level due to the density of water. Either centrifugal forces drive the water out of the tubes again or the tubes can be purged to return to undisturbed data acquisition. While this can average out to an extent in the ten-minute average values, it is clearly visible in the time-resolved data. Thus, a filter for the smoothness of the pressure distribution is applied. Any ten-minute time series containing too many time stamps that fail that filter is discarded. This filter leads to a strong cut in available data but ensures that only measurement periods with very clean data are used.

2. The data undisturbed by rain are downsampled to a frequency of 8 Hz to make the amount of data more manageable. At rated rotor speed, this sampling increment corresponds to about ten-degree rotor rotation, which is deemed sufficient to capture most unsteady effects.
3. Even during ten minutes, the environmental and operating conditions can vary significantly, making a comparison to simulations on a time-resolved level difficult. Therefore, the ten-minute time series are further broken down into two-minute intervals. The average environmental (ρ , U_∞ , α_s) and operating (ω , β , ψ) conditions are then used as input to steady aeroelastic simulations.

After this filtering, approximately 1,300 two-minute time series remain, which will be compared against an equal number of aeroelastic simulations. This comparison is presented in Section 7.3.3.

7

7.2.3. NUMERICAL MODELLING

In the present study, multiple simulation tools are employed. Rotor-level aerodynamics are solved using tools based on blade element momentum theory. Phatas is a time-domain aeroelastic simulation software currently developed and maintained by LM Wind Power [29] (with last publicly available documentation by Lindenburg [30]). It solves the dynamic response of wind turbines by coupling the aerodynamic loads calculated by a BEM algorithm with a non-linear structural solver. To make use of more advanced aerodynamic models, the TNO-inhouse aerodynamic simulation suite Aero-Module [31] is coupled to the structural solver of Phatas. This coupled tool is referred to as Phataero. Unsteady aerodynamic effects are accounted for by the first-order model by Snel [32] and Prandtl root and tip corrections are active.

Airfoil level aerodynamics are solved using the 2D panel code RFOIL which couples the potential flow solution of an airfoil to a boundary layer solver [33]. The tool is based on the widely known XFOIL code developed by Drela [34], but tailored specifically to the simulation of rotating airfoils as used among others on wind turbines. Previous research has shown RFOIL to be a valid tool for the analysis of airfoils with a relative thickness comparable to the one under investigation here [35].

7.2.4. ESTIMATION OF THE ANGLE OF ATTACK

Based on the pressure measurement setup described in Section 7.2.1, local aerodynamic quantities can be measured directly or estimated from the measurements. The local

chord normal force F_n and chord tangential force F_t can be derived by integrating the measured pressure distribution p along the surface of the blade cross-section S_B

$$\begin{bmatrix} F_t \\ F_n \end{bmatrix} = \oint_{S_B} \mathbf{n} p ds, \quad (7.21)$$

where \mathbf{n} is the surface normal vector.

Another aerodynamic quantity of interest is the angle of attack. The determination of the angle of attack in rotating systems is a recognised challenge; it is a subquestion of IEA Task 47, which aims at scientific cooperation in the field of detailed aerodynamic measurements on MW-scale wind turbines. Multiple methods for estimating the angle of attack on rotating wind turbine blade sections have been applied in the past.

When detailed information on the flow around an investigated blade cross-section is available, for example, in the form of particle image velocimetry data or numerical simulation results, the angle of attack can be estimated by calculating the axial induction, either as annulus average axial induction [36, 37], as the induced axial velocity at the blade location [38] or as the wake induction at the plane exactly between two blades [39]. Other approaches use the velocity field in the vicinity of the blade to estimate the bound circulation strength, which, in turn, can be used to estimate local induced velocity and consequently the angle of attack [40, 41, 42]. Furthermore, these two approaches can be combined, initially calculating the vorticity distributed over the blade surface and then calculating the axial induction based on the velocity field around the blade from which the induction of the bound vortex has been subtracted [43]. Several of the methods described here were applied to computational fluid dynamics (CFD) simulations of a 10 MW reference wind turbine in axial flow by Rahimi et al. [44] and of the MEXICO rotor in yawed inflow by Vimalakanthan et al. [45].

In many experimental setups, the available data is limited to pressure distributions and the resulting sectional forces. The above-mentioned methodologies are, therefore, often not suitable to determine the angle of attack based on experimental data [46]. For such cases, several other methods have been developed.

The **inverse BEM method**, developed by Bruining et al. [47] and Snel et al. [48] uses measured sectional forces and inflow velocities to determine the axial and tangential induction factors based on blade element momentum theory. Once the induction is known, the inflow angle and, consequently, the angle of attack can be calculated. Laino et al. [49] and Bak et al. [50] used the inverse BEM method to derive the angle of attack and 3D airfoil characteristics using the measurements of the UAE Phase VI experiment. Potentier et al. developed an unsteady inverse BEM method and applied it to the field measurements of the DAN-AERO MW project [17].

When aerodynamic forces are measured at multiple radial stations, an **inverse vortex wake method** can be applied. Tangler used this approach with prescribed wake to determine the 3D airfoil characteristics based on the UAE Phase VI measurements [51, 52]. This analysis was extended by Sant et al. using a lifting line algorithm with a free wake formulation [53, 54] and Micallef et al. applied the inverse free wake approach to data from the MEXICO experiment [55].

Alternatively to these "inverse" approaches, the angle of attack can be estimated by applying **pattern-matching**, that is, by finding the minimum deviation between the



measured pressure distribution and known combinations of pressure distribution and angle of attack. These known pressure distributions can be obtained from wind tunnel measurements [56, 57, 12] or using numerical simulations [46, 58].

In the present work, a pattern-matching algorithm is chosen to estimate the angle of attack. To this end, the measured pressure distributions are compared to RFOIL simulation results. Within the estimated range of operational angles of attack, pressure distributions are simulated with an increment of $\Delta\alpha = 0.1^\circ$. It should be noted, that these simulation results are given as non-dimensionalised pressures, whereas the measured pressures are absolute pressure values. Since the given measurement setup does not allow for an accurate estimation of both axial and tangential induction, the relative inflow velocity at the measurement blade section cannot be derived, and consequently, the pressure measurements cannot be non-dimensionalised. To make simulated and measured values comparable, the pressure distributions are scaled to an arbitrary scale (here, zero to one is used), and the pattern matching hence becomes a matching of the shapes of pressure distributions.

The pattern-matching algorithm's accuracy could potentially be increased by allowing scaling and shifting of the measured pressure distribution instead of using a fixed arbitrary scale. These additional degrees of freedom would make a brute force approach, as used in the current implementation, computationally extremely expensive, because the angle of attack is determined on a time-resolved basis for a large number of time series. An actual optimisation scheme might then be better suited to find the closest match. The development of such an algorithm is considered outside the scope of this work.

7

7.3. RESULTS

The results presented in this section were obtained in a research project in collaboration with GE Renewable Energy and LM Wind Power. To respect their intellectual property, the tick values on most axes are omitted, and arrows indicating ranges of the presented values are shown instead.

7.3.1. HOW REPRESENTATIVE IS A TEN-MINUTE AVERAGE PRESSURE DISTRIBUTION?

In later parts of the presented study, ten-minute statistics are used as input for numerical simulations. These numerical simulations yield aerodynamic characteristics along the blade span. One of these characteristics is the local angle of attack. The angle of attack can, in turn, be used as input for RFOIL calculations that result in pressure distributions which can be compared against the measured data. By using measured data both as input to the numeric simulations and as comparison to the simulation output, the combined workflow of numerical simulations on a turbine and airfoil level can be validated. This validation procedure, however, relies on the assumption that a ten-minute average pressure distribution is representative of the mean operating conditions of the same period.

To test this assumption the following approach is chosen. For each time step, the time-resolved pressure distribution is used to estimate the time-resolved angle of at-

tack $\alpha_{est,TS}$ according to the approach described in Section 7.2.4. Averaging these time-resolved values, one mean angle of attack of the time-resolved data $\bar{\alpha}_{est,TS}$ is calculated per ten-minute time series. Additionally, the ten-minute average pressure distribution is used to estimate the angle of attack $\bar{\alpha}_{est,10}$. The correlation of these two angle of attack estimates is shown in Figure 7.4 (a) coloured based on the mean measured inflow velocity. A linear correlation exists for lower angles of attack, corresponding to wind speeds up to approximately 15 m s^{-1} . For higher wind speeds and, consequently, higher angles of attack, non-linear aerodynamic phenomena, such as flow separation, occur more frequently. This leads to the ten-minute average angle of attack $\bar{\alpha}_{est,10}$ overestimating the mean time-resolved angle of attack $\bar{\alpha}_{est,TS}$. This indicates that ten-minute averaged pressure data is likely less representative of the underlying time-resolved data when obtained at higher wind speeds and should, thus, be interpreted with additional care.

Contrary to the estimated angle of attack, the mean time-resolved blade forces and the ten-minute average blade forces are identical. Using the estimated angle of attack, the chord normal and tangential forces resulting from the integrated pressure distribution can be decomposed into the estimated lift force

$$L_{est} = F_n \cos(\alpha_{est}) - F_t \sin(\alpha_{est}) \quad (7.22)$$

and an estimate of the lift coefficient can be obtained

$$c_{l,est} = \frac{L_{est}}{\frac{\rho}{2} V_{rel}^2 c} \quad (7.23)$$

where c is the local chord length.

The lift coefficient curves based on the ten-minute average angle of attack estimate and based on the average time-resolved angle of attack estimate are shown in Figure 7.4 (b) and (c), respectively. For comparison, the DU-00-W-401 airfoil polars obtained in a wind tunnel for a chord Reynolds number of $Re_c = 3 \cdot 10^6$ and clean conditions are shown. It should be noted that, on average, the chord Reynolds number in the field is approximately twice as high. Since the measurement location is close to the root, the flow is expected to be three-dimensional. Next to the two-dimensional wind tunnel polars, two lift curves corrected for three-dimensional flow effects are shown. Both corrected lift polars are derived from the wind tunnel lift coefficient $c_{l,2D}$ using the correction model by Snel et al. [48]:

$$c_{l,3D} = c_{l,2D} + 3.1 \left(\frac{c}{r} \right)^2 (c_{l,inv} - c_{l,2D}) \quad (7.24)$$

where $c/r = 0.2454$ and $c_{l,inv}$ is the inviscid lift coefficient. It was recommended by Montgomerie et al. to use an inviscid simulation tool such as RFOIL to generate these polars [59]. However, many BEM-based tools, including Phataero, are built to only receive viscous polars as input. In Phataero's case, the inviscid lift polar is approximated by linearly extrapolating the linear region of the viscous lift curve such that

$$c_{l,inv} = \frac{c_l(\alpha_{lin,max}) - c_l(\alpha_{lin,min})}{\alpha_{lin,max} - \alpha_{lin,min}} (\alpha - \alpha_0) \quad (7.25)$$



where $\alpha_{lin,min}$ and $\alpha_{lin,max}$ define the start and end point of the lift polar's linear region, respectively, and α_0 is the angle of attack resulting in zero lift. The results of both approaches are given in Figures 7.4 (b) and (c).

It should be noted that the lift force measured in the field is non-dimensionalised by a velocity not accounting for induction values since these cannot accurately be determined. Therefore, the field-measured lift curves should be interpreted in terms of trends rather than absolute values when comparing them to wind tunnel data.

Pre-stall, the trend of the field data matches well with that of the wind tunnel lift polar, particularly the 3D-corrected polar using inviscid polars based on RFOIL. In the field, stall occurs approximately 2° of angle of attack earlier than in the wind tunnel. Post-stall, the field data undershoots the 3D-corrected wind tunnel data and aligns better with the trend of the uncorrected 2D wind tunnel lift polar.

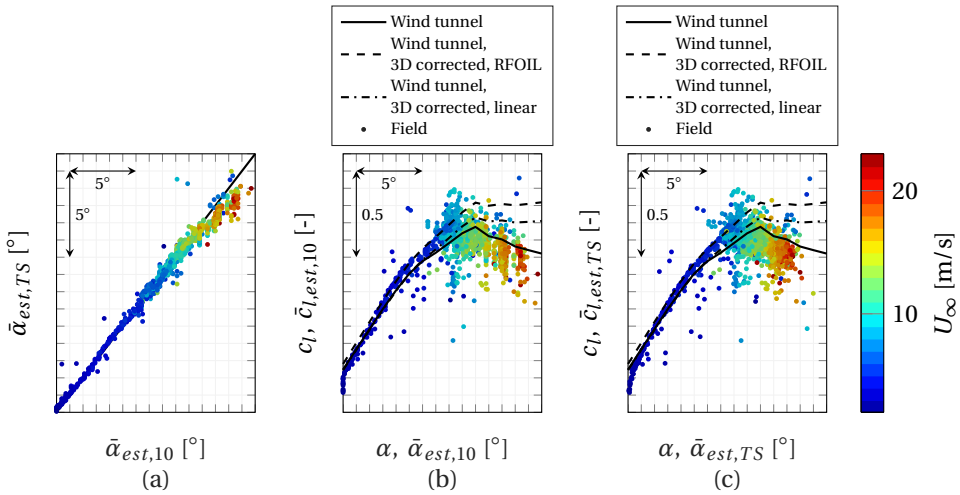


Figure 7.4: Comparison of angle of attack estimates based on ten-minute average and time-resolved pressure distributions (a), resulting estimates of the lift coefficient vs angle of attack curves based on ten-minute average data (b) and time-resolved data (c). α and c_l refer to the values of the wind tunnel experiments while α_{est} and $c_{l,est}$ refer to the values estimated based on the field pressure data

7.3.2. MODEL VALIDATION BASED ON LONG-TERM TEN-MINUTE AVERAGED EXPERIMENTAL DATA

After the data reduction using ten-minute statistics as described in Section 7.2.2, trends in pressure distribution for normal operating conditions can be obtained as a function of wind speed and turbulence intensity. Figure 7.5 (a) displays for an identical mean inflow speed the effect of a larger turbulence intensity, which clearly increases the unsteadiness as illustrated by the larger uncertainty band in the plot. Besides the varying inflow conditions, it is acknowledged that these lead to larger rotor speed variations, which affect the measured pressure distribution as well. Also note the standard error, resulting from the bin average process, is indicated in the plots, demonstrating satisfactory repeatability. Figure 7.5 (b) illustrates the effect of a varying wind speed, clearly changing dynamic

pressure levels but also the shape of the pressure distribution indicating a difference in local angle of attack. It is noteworthy that for some measurements, for example, the suction side sensor at $x/c = 0.18$ for $U_\infty = 10 \text{ m s}^{-1}$ and $TI = 5\%$, an elevated standard error can be observed compared to neighbouring sensors while the standard deviation does not show this behaviour. It can be hypothesised that this is due to a ten-minute sample with a clogged sensor (e.g., by rainwater). This would have an influence on the mean measured pressure level, and thus the standard error of that bin, while affecting the dynamic pressure variation less.

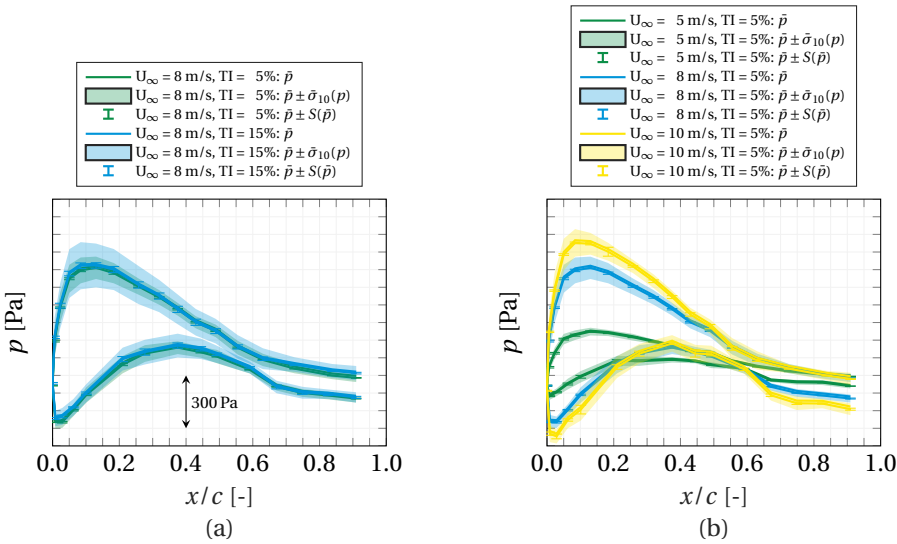


Figure 7.5: Mean pressure distributions, 95% confidence interval and standard error, subfigure (a) showing results for $U_\infty = 10 \text{ m s}^{-1}$ with varying TI , subfigure (b) showing results for $TI = 5\%$ and varying U_∞ ; subfigures with identical ordinates

Integration of the pressure distribution with respect to chord and thickness yields chord normal and tangential sectional forces, respectively, at the designated radial position. Figure 7.6 then illustrates the resulting chord normal and tangential force coefficient variation with wind speed, compared to Phataero simulations with both clean and rough wind tunnel measured airfoil polars used as input. Here, it is noted that the airfoil data is corrected for rotational augmentation in situ using the method of Snel [48] as explained in Section 7.3.1. The bin-averaged measurement values of pitch angle and rotational speed have been utilised as input for the operational conditions of the simulations. To ensure comparability, both measured and simulated forces are non-dimensionalised under neglect of induced velocities.

For the normal force variation, a good agreement in absolute level and trend is observed, provided the clean airfoil polar dataset is used. It is evident that for small wind speeds, the 3D correction of the polars ensures a slightly better match between measurements and simulation, while for wind speeds above $U_\infty = 9 \text{ m s}^{-1}$, the use of uncorrected polars yields better agreement. This observation aligns with findings from Section 7.3.1,



where the 3D-corrected wind tunnel lift polar exceeds the field measurements for higher wind speeds.

The measured and simulated tangential force coefficients show even better agreement, again under the condition that clean polars are input to the simulation. Detectable deviations occur above $U_\infty = 9 \text{ m s}^{-1}$, where the simulations predict higher tangential loading than was measured. As expected, the 3D correction has a negligible effect on the simulated tangential force coefficient. The good match between simulation and experiment is somewhat surprising given that the experimentally determined tangential force is lacking a non-negligible contribution of viscous forces. It was checked that the finite number of available pressure sensors causes a negligible error with which the inviscid tangential force coefficient is determined. Thus, it is expected that a comparison of tangential forces accounting for viscosity would result in less congruence.

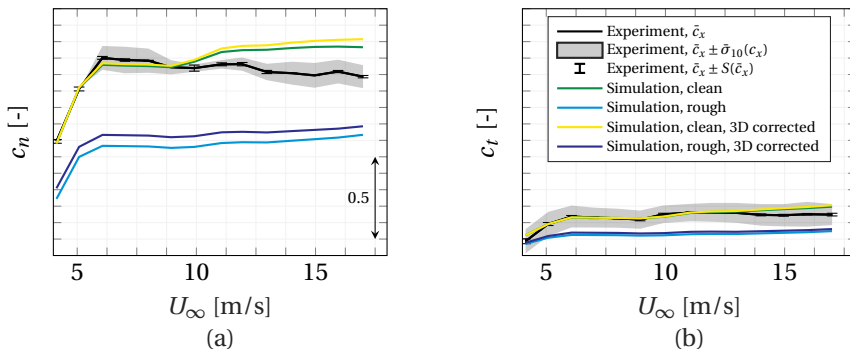


Figure 7.6: Chord normal (a) and tangential (b) force coefficient based on measured pressure distributions and numerical simulations, legend entry c_x represents c_n and c_t in their respective subfigures; subfigures with identical ordinates

The Phataero simulation results can further be used to provide RFOIL simulations with input, that is, angle of attack and chord Reynolds number. Additionally, RFOIL requires an estimate of the critical amplification factor N_{crit} , a parameter related to the boundary layer transition behaviour. The N_{crit} value is determined using a modified version of Mack's model [60], which relates N_{crit} to the local turbulence intensity. Several modifications to Mack's model exist, which improve the N_{crit} prediction for higher TI values [61, 62]. Here, the modification by Drela and Youngren [61] is applied, which ensures positive N_{crit} values even at high turbulence intensity values as are present in this field campaign.

The combination of Phataero and RFOIL enables a model validation on the airfoil level by comparing the simulated pressure distributions against those measured in the field. Results are shown exemplarily for one low and one high wind speed in Figure 7.7. RFOIL is run both with and without 3D correction model, which is one of the points of distinction from Drela's XFOIL code.

For lower wind speeds, there is a very good agreement between the 3D-corrected simulation and the field measurements. Deviations are largely found on the suction side towards the trailing edge, where RFOIL predicts separation from around 80% chord. In

the binned ten-minute averaged pressure distribution, the separation point is smeared out due to variations in the underlying, time-resolved operating conditions. The two-dimensional RFOIL simulations exhibit less congruence with the measurements.

For higher wind speeds, the use of RFOIL's 3D correction model is disadvantageous, leading to a significant overprediction of the suction peak and an underprediction of the flow separation. Contrarily, the two-dimensional simulation shows good agreement in terms of the separation point location. It can be observed that there is a discrepancy between measured and simulated stagnation pressure, preventing a better agreement between field measurements and 2D simulation for this wind speed. This stagnation pressure offset was found to increase with increasing wind speed. It is hypothesised that this is related to changes in the reference pressure, for example, due to deformations of the long reference tubing when the blade pitch angle increases.

The airfoil level comparison further corroborates findings from the blade level, namely that 3D corrections improve the match with simulations only until a certain wind speed, after which the use of such correction models yields lower agreement with the field experiment. This aligns with findings by Montgomerie et al. and Chaviaropoulos and Hansen, who link the decrease of three-dimensional flow effects with increasing wind speed to an increase in blade pitch angle [59, 63]. On the blade level, it was observed that the congruence between simulations and experiment reduces from $U_\infty = 9 \text{ m s}^{-1}$. Referring back to the experimentally derived lift polar presented in Figure 7.4, this is also the wind speed around which the airfoil stalls in the field. This suggests that the use of 3D correction models for airfoil polars should be linked to the occurrence of flow separation.

Remaining deviations between simulation and field might be attributed to the presence of roughness. The RFOIL simulations were run in clean conditions, whereas the surface roughness of the blade in the field is difficult to assess. While simulations with actively tripped boundary layer clearly worsened the agreement of results, the inclusion of minor levels of roughness could potentially improve the comparison. Investigating this further is, however, considered outside of this study's scope.

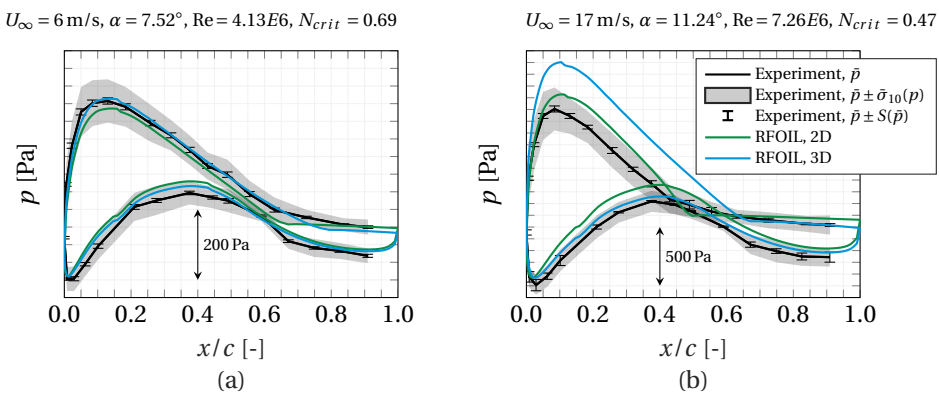


Figure 7.7: Pressure distribution measured in the field compared to RFOIL simulation results for a low (a) and high (b) wind speed



7.3.3. MODEL VALIDATION BASED ON LONG-TERM TIME-RESOLVED EXPERIMENTAL DATA

Next to the analysis based on ten-minute average data, an attempt is made to validate the numerical simulation model on a time-resolved scale. As described in Section 7.2.2, average operating and environmental conditions of two-minute time series are used as input to aeroelastic simulations. The simulation results are then compared to time-resolved field measurements in terms of normal and tangential force, and angle of attack. The majority of the two-minute samples have an average wind speed below or around rated conditions. Results from the previous section indicate that 3D flow corrections should be applied for these lower wind speeds. Therefore, the angle of attack estimation for the two-minute time series is done by pattern-matching the pressure measurements against RFOIL simulations with 3D correction.

Figure 7.8 shows the relative deviation of the simulated quantities from their measured/estimated counterpart as a function of both environmental and operational parameters. The relative deviation values are calculated for each of the approximately 1300 two-minute time series as the mean deviation between simulated and experimental values of 36 ten-degree azimuthal bins.

$$E(\xi) = \frac{1}{36} \sum_{i=1}^{36} \left| \frac{\xi_{i,sim} - \xi_{i,exp,bin}}{\xi_{i,exp,bin}} \right|, \quad (7.26)$$

where ξ is an arbitrary variable. The modulus is calculated to avoid the cancellation of errors.

Three data points are marked separately in colour. These correspond to the cases with the lowest (green), average (blue) and highest (red) sum of deviations between simulation and experiment regarding normal and tangential force, and angle of attack, weighted by their individual mean over the approximately 1300 two-minute time series

$$E_{sum} = \frac{E(F_n)}{\bar{E}(F_n)} + \frac{E(F_t)}{\bar{E}(F_t)} + \frac{E(\alpha)}{\bar{E}(\alpha)}. \quad (7.27)$$

Overall, there appears to be very little correlation between operating and environmental conditions and the error between simulation and experiment. The highest errors are found where the highest data counts are available, indicating a certain random appearance of such outliers with a growing number of data points. The only observable correlation exists for the turbulence intensity. Since the simulations use steady wind conditions, the better congruence at low turbulence intensity is not surprising. It was further investigated whether the accuracy with which the wind shear profile was approximated affected the deviations between simulation and experimental results. While no clear correlation could be observed, it should be noted that fitting a shear profile to the LiDAR measurements can be a source of error for all regarded time series. It is expected that the congruence of simulations and field experiment can be improved by using either the average measured wind profile or even the time-resolved wind profile data (ideally measured upstream of the turbine using, for example, a forward-facing nacelle-based LiDAR) as input to the simulations.

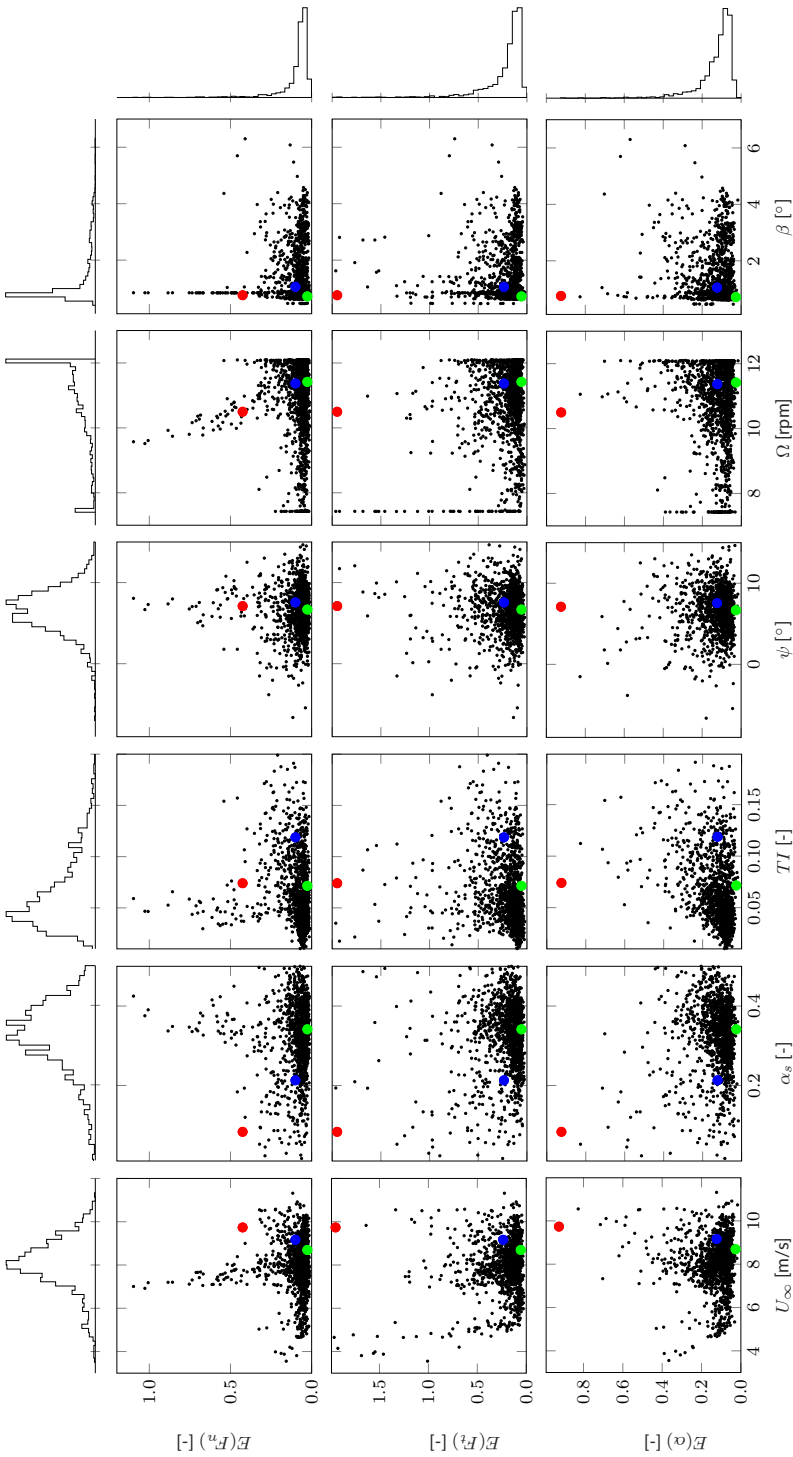


Figure 7.8: Relative deviation of the simulated normal force, tangential force and angle of attack from their measured/estimated counterpart as a function of environmental and operational parameters; The green •, blue • and red • mark correspond to the time series with lowest, average and highest deviation between field data and simulation results, respectively



Positively, the error distributions peak at relatively low values and quickly decay towards higher errors. The mean overall deviation between simulated and measured normal force is 10 % and for the tangential force 22 %. The higher value of the tangential force error can be explained by the fact that the simulations are based on viscous polars while the viscous drag, which largely contributes to the tangential force, cannot be measured using pressure taps. The mean overall relative deviation between the simulated and estimated angle of attack is 13 %, which corresponds to a mean absolute deviation of 0.97° .

To illustrate in more detail what the aforementioned cases with lowest (●), average (●) and highest (●) deviation between simulation and experimental data look like, the normal force and angle of attack values are plotted as function of azimuth in Figures 7.9 and 7.10. Both simulated and experimental data clearly show the dip in axial force due to the tower passage. Figures 7.9 (a) and 7.10 (a) demonstrate that in the lowest deviation case, near-perfect agreement between averaged field data and simulation can be achieved. While for the average deviation case (Figures 7.9 (b) and 7.10 (b)), the general shape and magnitude of force and angle of attack values are still approximated reasonably well, this is not the case anymore for the highest deviation case (Figures 7.9 (c) and 7.10 (c)). Independent of the regarded case, the variations in the time-resolved field data cannot be captured by the steady aeroelastic simulations.

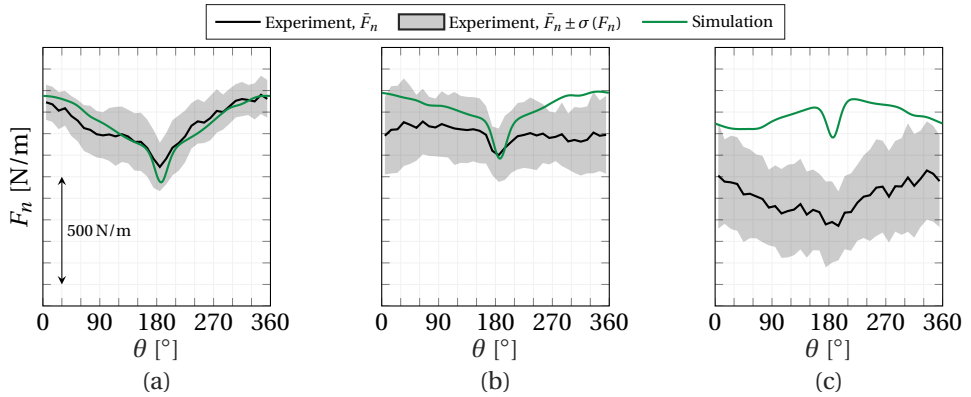


Figure 7.9: Measured and simulated normal force as a function of azimuth for the time series with lowest (a), average (b) and highest (c) deviation between field data and simulation results (see ●, ●, ● in Figure 7.8); subfigures with identical ordinates

Finally, the unsteady normal force to angle of attack curves are investigated. Figure 7.11 shows the experimental data coloured by the azimuthal position together with the numerical results. As visible in Figure 7.11 (a), the experimental data exhibits a hysteresis, which the simulation replicates accurately. In Figures 7.11 (b) and (c), this hysteresis is decreasingly detectable as the experimental data scatters more randomly. Consequently, the numerical tool's ability to accurately simulate reality decreases.

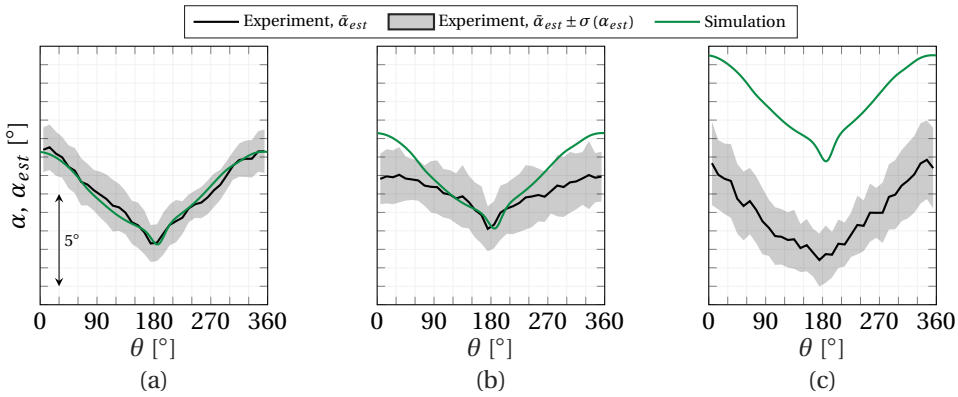


Figure 7.10: Estimated and simulated angle of attack as a function of azimuth for the time series with lowest (a), average (b) and highest (c) deviation between field data and simulation results (see ●●● in Figure 7.8), α refers to the simulated angle of attack while α_{est} refers to the values estimated based on the field pressure data; subfigures with identical ordinates

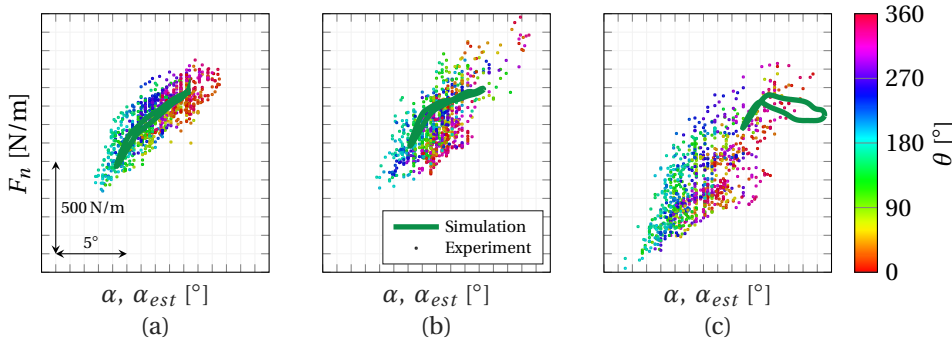


Figure 7.11: Measured/simulated normal force as a function of the estimated/simulated angle of attack for the time series with lowest (a), average (b) and highest (c) deviation between field data and simulation results (see ●●● in Figure 7.8), α refers to the simulated angle of attack while α_{est} refers to the values estimated based on the field pressure data; subfigures with identical abscissae and ordinates

7.4. CONCLUSIONS

This chapter presents measurements obtained on a 3.8 MW field research wind turbine located in the north of the Netherlands. Pressure measurements were logged continuously over multiple months. Simultaneously, a ground-based LiDAR system provided detailed wind speed measurements across the entire turbine height.

These measurements are used for the validation of numerical models aiming at simulating reality as closely as possible. As part of this validation exercise relies on ten-minute averaged pressure distributions, it is first investigated how representative such averaged measurements are of the underlying unsteady aerodynamics. It can be shown, that only for post-stall angles of attack, generally occurring for rather high wind speeds, the ten-minute average data loses its fidelity to the time-resolved aerodynamics.

Following this analysis, the ten-minute statistics are binned by wind speed and tur-



bulence intensity. The bin average values are used as input to BEM-based aeroelastic simulations. The simulated normal and tangential force coefficients are compared to the values determined from the measured pressure distributions. Furthermore, the simulated angle of attack and Reynolds number are used as input for RFOIL simulations which generate pressure distributions that can directly be compared against measurements. The best match is found when clean airfoil polars are used in the aeroelastic simulations. Furthermore, it is demonstrated that the use of 3D flow correction models largely influences the agreement between simulations and field measurements. For low wind speeds, employing such a correction leads to higher congruence, while for higher wind speeds, simulations match the field measurements better without 3D flow correction. Combined with the experimental lift polar derived from the field measurements, these findings suggest that 3D flow correction models should be switched on and off as a function of the amount of flow separation occurring.

This study closes by comparing measurements and aeroelastic simulations on a time-resolved scale. On average, the measured and simulated normal force deviate by 10%. A 13% average deviation is found between the simulated angle of attack and the one estimated from the measured pressure data. The simulations' accuracy seems generally unaffected by most operating and environmental conditions, but better agreement is found for low turbulence, which more closely resembles the steady nature of the aeroelastic simulations. Depending on the individual time series, large differences between simulation and field measurements are found regarding the unsteady normal force over angle of attack curves in terms of their mean force and angle of attack level as well as the curves' shape.

In conclusion, an extensive validation campaign has been performed based on multiple months of field measurements. Results confirm that BEM-based aeroelastic tools and 2D viscous-inviscid coupled panel methods like RFOIL are still viable for the simulation of modern multi-megawatt wind turbines when provided with accurate input. Furthermore, this study corroborates the value of pressure measurements on field turbines, both regarding the analysis of blade and airfoil aerodynamics and for the validation of numerical models on these scales.

7.A. NOMENCLATURE

Latin letters	
a, a'	Axial and tangential induction factor
c	Chord
D	Drag force
E	Relative deviation
F	Force
g	Gravitational constant
L	Lift force
N	Number of samples per bin
\mathbf{n}	Normal vector
p	Pressure

continues on next page...

Latin letters	...continued
R	Blade tip radius
Re_c	Chord Reynolds number
r	Radial coordinate
S	Standard error of bin averaged mean
TI	Turbulence intensity
t	Time
U_∞	Freestream velocity
V	Velocity
x	Chordwise coordinate
z	Height above ground

Greek letters	
α	Angle of attack
α_s	Shear exponent
β	Blade pitch angle
ζ	Cone angle
θ	Azimuthal angle
λ	Tip-speed ratio
ξ	Arbitrary variable
ρ	Density of air
σ	Standard deviation of the bin data samples
τ	Tilt angle
ϕ	Inflow angle
ψ	Yaw angle
Ω	Rotational speed
ω	Angular velocity

Subscripts	continues on next page...
$2D$	Two-dimensional
$3D$	Three-dimensional
10	Related to ten-minute average data
bin	Bin
$cent$	Centrifugal
cor	Corrected
dyn	Dynamic
est	Estimated
hor	Horizontal
hub	Hub
inv	Inviscid
N	Rotor plane-normal



Subscripts		...continued
<i>n</i>	Chord-normal	
<i>PS</i>	Pressure sensor	
<i>rated</i>	Rated conditions	
<i>ref</i>	Reference	
<i>rel</i>	Relative	
<i>sum</i>	Sum	
<i>TS</i>	Related to time-resolved data	
<i>T</i>	Rotor plane-tangential	
<i>t</i>	Chord-tangential	

BIBLIOGRAPHY

- [1] G. v. Groenewoud, L. Boermans, and J. v. Ingen. *Investigation of laminar-turbulent transition of the boundary layer on the 25m HAT wind turbine*. Tech. rep. LR-390. Faculty of Aerospace Engineering, TU Delft, 1983.
- [2] C. Butterfield, W. Musial, and D. Simms. *Combined experiment phase 1. Final report*. Tech. rep. NREL/TP-257-4655. National Renewable Energy Laboratory (NREL), Oct. 1992. DOI: [10.2172/10105837](https://doi.org/10.2172/10105837).
- [3] D. A. Simms, M. M. Hand, L. J. Fingersh, and D. W. Jager. *Unsteady aerodynamics experiment phases II-IV test configurations and available data campaigns*. Tech. rep. NREL/TP-500-25950. National Renewable Energy Laboratory, Aug. 1999. DOI: [10.2172/12144](https://doi.org/10.2172/12144).
- [4] H. A. Madsen. *Aerodynamics of a horizontal-axis wind turbine in natural conditions*. Tech. rep. Risø-M-2903. Risø, Sept. 1991.
- [5] H. A. Madsen. *Structural dynamics of a 100 kW HAWT*. Risø National Laboratory, 1991.
- [6] A. Bruining. *Aerodynamic characteristics of a 10m diameter rotating wind turbine blade*. Tech. rep. IW95-084R. Delft, 1997.
- [7] T. Maeda and H. Kawabuchi. “Surface pressure measurement on a rotating blade of field horizontal axis wind turbine in yawed condition”. In: *JSME International Journal Series B* 48.1 (2005), pp. 156–163. DOI: [10.1299/jsmeb.48.156](https://doi.org/10.1299/jsmeb.48.156).
- [8] J. Schepers, A. Brand, A. Bruining, M. Hand, D. Infield, H. Madsen, T. Maeda, J. Paynter, R. van Rooij, Y. Shimizu, et al. *Final report of IEA Annex XVIII: enhanced field rotor aerodynamics database*. Tech. rep. ECN-C-02-016. Energy Research Center of the Netherlands, 2002.
- [9] A. P. Schaffarczyk, D. Schwab, and M. Breuer. “Experimental detection of laminar-turbulent transition on a rotating wind turbine blade in the free atmosphere”. In: *Wind Energy* 20.2 (June 2016), pp. 211–220. DOI: [10.1002/we.2001](https://doi.org/10.1002/we.2001).
- [10] C. Bak, H. A. Madsen, U. S. Paulsen, M. Gaunaa, N. N. Sørensen, P. Fuglsang, J. Romblad, N. A. Olsen, P. Enevoldsen, J. Laursen, et al. “DAN-AERO MW: Detailed aerodynamic measurements on a full scale MW wind turbine”. In: *European wind energy conference and exhibition (EWEC)*. 2010, pp. 20–23.
- [11] H. Madsen, P. Fuglsang, J. Romblad, P. Enevoldsen, J. Laursen, L. Jensen, C. Bak, U. S. Paulsen, M. Gaunaa, and N. N. Sørensen. “The DAN-AERO MW Experiments”. In: *48th AIAA aerospace sciences meeting including the new horizons forum and aerospace exposition*. American Institute of Aeronautics and Astronautics, Jan. 2010. DOI: [10.2514/6.2010-645](https://doi.org/10.2514/6.2010-645).



- [12] C. Bak, N. Troldborg, and H. A. Madsen. “DAN-AERO MW: Measured airfoil characteristics for a MW rotor in atmospheric conditions”. In: *Scientific Proceedings, European Wind Energy Association (EWEA)* (2011).
- [13] N. Troldborg, C. Bak, N. N. Sørensen, H. Aagaard Madsen, P.-E. Réthoré, F. Zahle, and S. Guntur. “Experimental and numerical investigation of 3D aerofoil characteristics on a MW wind turbine”. In: *Proceedings - european wind energy conference & exhibition 2013*. European Wind Energy Association (EWEA), 2013.
- [14] H. A. Madsen, N. N. Sørensen, C. Bak, N. Troldborg, and G. Pirrung. “Measured aerodynamic forces on a full scale 2MW turbine in comparison with EllipSys3D and HAWC2 simulations”. In: *Journal of Physics: Conference Series* 1037 (June 2018), p. 022011. DOI: [10.1088/1742-6596/1037/2/022011](https://doi.org/10.1088/1742-6596/1037/2/022011).
- [15] A. Ghadirian, G. C. Larsen, and N. Troldborg. “Comparing rotor plane induction determined from full-scale measurements and CFD simulations”. In: *Wind Energy* 22.1 (Sept. 2018). Publisher: Wiley, pp. 109–123. DOI: [10.1002/we.2274](https://doi.org/10.1002/we.2274).
- [16] C. Grinderslev, G. Vijayakumar, S. Ananthan, N. N. Sørensen, F. Zahle, and M. A. Sprague. “Validation of blade-resolved computational fluid dynamics for a MW-scale turbine rotor in atmospheric flow”. In: *Journal of Physics: Conference Series* 1618.5 (Sept. 2020), p. 052049. DOI: [10.1088/1742-6596/1618/5/052049](https://doi.org/10.1088/1742-6596/1618/5/052049).
- [17] T. Potentier, C. Braud, E. Guilmineau, A. Finez, and C. L. Bourdat. “Analysis of the DANAERO wind turbine field database to assess the importance of different state-of-the-art blade element momentum (BEM) correction models”. In: *Energy Science & Engineering* 9.9 (June 2021), pp. 1477–1500. DOI: [10.1002/ese3.908](https://doi.org/10.1002/ese3.908).
- [18] K. Boorsma et al. “Progress in the validation of rotor aerodynamic codes using field data”. In: *Wind Energy Science* 8.2 (Feb. 2023), pp. 211–230. ISSN: 2366-7443. DOI: [10.5194/wes-8-211-2023](https://doi.org/10.5194/wes-8-211-2023).
- [19] H. A. Madsen, T. Barlas, A. Fischer, A. S. Olsen, and A. G. Gonzalez. “Inflow and pressure measurements on a full scale turbine with a pressure belt and a five hole pitot tube”. In: *Journal of Physics: Conference Series* 2265.2 (May 2022), p. 022096. ISSN: 1742-6596. DOI: [10.1088/1742-6596/2265/2/022096](https://doi.org/10.1088/1742-6596/2265/2/022096).
- [20] A. Gamberini, T. Barlas, A. Gomez Gonzalez, and H. A. Madsen. “Validation of aeroelastic dynamic model of active trailing edge flap system tested on a 4.3 MW wind turbine”. In: *Wind Energy Science* 9.5 (May 2024), pp. 1229–1249. ISSN: 2366-7451. DOI: [10.5194/wes-9-1229-2024](https://doi.org/10.5194/wes-9-1229-2024).
- [21] P. Doubrawa, C. Kelley, and J. Naughton. *RAAW*. 2023. DOI: [10.21947/RAAW/1984650](https://doi.org/10.21947/RAAW/1984650).
- [22] S. Letizia, N. Bodini, P. Brugger, A. Scholbrock, N. Hamilton, F. Porté-Agel, P. Doubrawa, and P. Moriarty. “Holistic scan optimization of nacelle-mounted lidars for inflow and wake characterization at the RAAW and AWAKEN field campaigns”. In: *Journal of Physics: Conference Series* 2505.1 (May 2023), p. 012048. ISSN: 1742-6588, 1742-6596. DOI: [10.1088/1742-6596/2505/1/012048](https://doi.org/10.1088/1742-6596/2505/1/012048).

- [23] A. Rybchuk, L. A. Martínez-Tossas, N. Hamilton, P. Doubrawa, G. Vijayakumar, M. Hassanaly, M. B. Kuhn, and D. S. Zalkind. “A baseline for ensemble-based, time-resolved inflow reconstruction for a single turbine using large-eddy simulations and latent diffusion models”. In: *Journal of Physics: Conference Series* 2505.1 (May 2023), p. 012018. ISSN: 1742-6588, 1742-6596. DOI: [10.1088/1742-6596/2505/1/012018](https://doi.org/10.1088/1742-6596/2505/1/012018).
- [24] K. Brown et al. “One-to-one aeroservoelastic validation of operational loads and performance of a 2.8 MW wind turbine model in OpenFAST”. In: *Wind Energy Science* 9.8 (Aug. 2024), pp. 1791–1810. ISSN: 2366-7451. DOI: [10.5194/wes-9-1791-2024](https://doi.org/10.5194/wes-9-1791-2024).
- [25] P. Eecen et al. *Measurements at the ECN wind turbine test station Wieringermeer*. Tech. rep. ECN-RX-06-055. Energy Research Center of the Netherlands, 2006.
- [26] Machiels, L.A.H. *Validatiemetingen EWTW, eindrapport*. Tech. rep. ECN-E-06-062. Energy Research Center of the Netherlands, 2006.
- [27] PDOK. *Map of EWEF test site, derived from data provided by PDOK (Publieke Dienstverlening op de Kaart), licensed under the CC-BY-4.0 license, accessed on 20/03/2024*. 2024.
- [28] C. van Diggelen, F. Danzl, and W. Castricum. *Instrumentation report TIADÉ research turbine*. Tech. rep. TNO 2022 R10475. TNO, 2022.
- [29] C. Lindenburg. *PHATAS User's manual version 11737*. Tech. rep. WMC-2016-005. (Confidential). LM Wind Power, 2020.
- [30] C. Lindenburg. *PHATAS Release "NOV-2003" and "APR-2005" User's Manual*. Tech. rep. ECN-I-05-005. Energy Research Centre of the Netherlands, 2005.
- [31] K. Boorsma, F. Grasso, and J. Holierhoek. “Enhanced approach for simulation of rotor aerodynamic loads”. In: *Proceedings of EWEA Offshore*. Proceedings of EWEA Offshore, 2011.
- [32] H. Snel. “Heuristic modelling of dynamic stall characteristics”. In: *EWEC-CONFERENCE*. Bookshop for Scientific Publications, 1997, pp. 429–433.
- [33] R. Van Rooij. *Modification of the boundary layer calculation in RFOIL for improved airfoil stall prediction*. Tech. rep. IW-96087R. Netherlands, Sept. 1996.
- [34] M. Drela. “XFOIL: An analysis and design system for low reynolds number airfoils”. In: *Lecture notes in engineering*. Springer Berlin Heidelberg, 1989, pp. 1–12. DOI: [10.1007/978-3-642-84010-4_1](https://doi.org/10.1007/978-3-642-84010-4_1).
- [35] G. Ramanujam, H. Özdemir, and H. W. M. Hoeijmakers. “Improving Airfoil Drag Prediction”. In: *Journal of Aircraft* 53.6 (2016), pp. 1844–1852. ISSN: 0021-8669. DOI: [10.2514/1.C033788](https://doi.org/10.2514/1.C033788).
- [36] M. O. L. Hansen and J. Johansen. “Tip studies using CFD and comparison with tip loss models”. In: *Wind Energy* 7.4 (2004), pp. 343–356. DOI: [10.1002/we.126](https://doi.org/10.1002/we.126).
- [37] J. Johansen and N. N. Sørensen. “Aerofoil characteristics from 3D CFD rotor computations”. In: *Wind Energy* 7.4 (Oct. 2004), pp. 283–294. DOI: [10.1002/we.127](https://doi.org/10.1002/we.127).



- [38] H. Rahimi, M. Hartvelt, J. Peinke, and J. Schepers. “Investigation of the current yaw engineering models for simulation of wind turbines in BEM and comparison with CFD and experiment”. In: *Journal of Physics: Conference Series* 753 (Sept. 2016), p. 022016. DOI: [10.1088/1742-6596/753/2/022016](https://doi.org/10.1088/1742-6596/753/2/022016).
- [39] I. Herráez, E. Daniele, and J. G. Schepers. “Extraction of the wake induction and angle of attack on rotating wind turbine blades from PIV and CFD results”. In: *Wind Energy Science* 3.1 (Jan. 2018), pp. 1–9. DOI: [10.5194/wes-3-1-2018](https://doi.org/10.5194/wes-3-1-2018).
- [40] W. Z. Shen, M. O. L. Hansen, and J. N. Sørensen. “Determination of angle of attack (AOA) for rotating blades”. In: *Wind energy*. Springer Berlin Heidelberg, 2007, pp. 205–209. DOI: [10.1007/978-3-540-33866-6_37](https://doi.org/10.1007/978-3-540-33866-6_37).
- [41] W. Z. Shen, M. O. L. Hansen, and J. N. Sørensen. “Determination of the angle of attack on rotor blades”. In: *Wind Energy* 12.1 (Jan. 2009), pp. 91–98. DOI: [10.1002/we.277](https://doi.org/10.1002/we.277).
- [42] E. Jost, L. Klein, H. Leipprand, T. Lutz, and E. Krämer. “Extracting the angle of attack on rotor blades from CFD simulations”. In: *Wind Energy* 21.10 (June 2018), pp. 807–822. DOI: [10.1002/we.2196](https://doi.org/10.1002/we.2196).
- [43] W. Zhong, W. Z. Shen, T. G. Wang, and W. J. Zhu. “A new method of determination of the angle of attack on rotating wind turbine blades”. In: *Energies* 12.20 (Oct. 2019), p. 4012. DOI: [10.3390/en12204012](https://doi.org/10.3390/en12204012).
- [44] H. Rahimi, J. Schepers, W. Shen, N. R. García, M. Schneider, D. Micallef, C. S. Ferreira, E. Jost, L. Klein, and I. Herráez. “Evaluation of different methods for determining the angle of attack on wind turbine blades with CFD results under axial inflow conditions”. In: *Renewable Energy* 125 (Sept. 2018), pp. 866–876. DOI: [10.1016/j.renene.2018.03.018](https://doi.org/10.1016/j.renene.2018.03.018).
- [45] K. Vimalakanthan, J. Schepers, W. Shen, H. Rahimi, D. Micallef, C. S. Ferreira, E. Jost, and L. Klein. “Evaluation of different methods of determining the angle of attack on wind turbine blades under yawed inflow conditions”. In: *Journal of Physics: Conference Series* 1037 (June 2018), p. 022028. DOI: [10.1088/1742-6596/1037/2/022028](https://doi.org/10.1088/1742-6596/1037/2/022028).
- [46] S. Guntur and N. N. Sørensen. “An evaluation of several methods of determining the local angle of attack on wind turbine blades”. In: *Journal of Physics: Conference Series* 555 (Dec. 2014), p. 012045. DOI: [10.1088/1742-6596/555/1/012045](https://doi.org/10.1088/1742-6596/555/1/012045).
- [47] A. Bruining, G. Van Bussel, G. Corten, and W. Timmer. “Pressure distribution from a wind turbine blade; field measurements compared to 2-Dimensional wind tunnel data”. In: *Institute for Windenergy, Delft University of Technology* (1993).
- [48] H. Snel, R. Houwink, and T. Bosscher. *Sectional prediction of lift coefficients on rotating wind turbine blades in stall*. Tech. rep. ECN-C-93-052. Energy Research Center of the Netherlands, 1994.
- [49] D. J. Laino, A. C. Hansen, and J. E. Minnema. “Validation of the AeroDyn subroutines using NREL unsteady aerodynamics experiment data”. In: *Wind Energy* 5.2-3 (2002), pp. 227–244. DOI: [10.1002/we.69](https://doi.org/10.1002/we.69).

- [50] C. Bak, J. Johansen, and P. B. Andersen. “Three-dimensional corrections of airfoil characteristics based on pressure distributions”. In: *Proceedings of the european wind energy conference*. 2006, pp. 1–10.
- [51] J. L. Tangler. “The nebulous art of using wind-tunnel airfoil data for predicting rotor performance”. In: *ASME 2002 wind energy symposium*. ASMEDC, Jan. 2002. DOI: [10.1115/wind2002-40](https://doi.org/10.1115/wind2002-40).
- [52] J. L. Tangler. “Insight into wind turbine stall and post-stall aerodynamics”. In: *Wind Energy* 7.3 (July 2004), pp. 247–260. DOI: [10.1002/we.122](https://doi.org/10.1002/we.122).
- [53] T. Sant, G. van Kuik, and G. J. W. van Bussel. “Estimating the angle of attack from blade pressure measurements on the NREL Phase VI rotor using a free wake vortex model: Axial conditions”. In: *Wind Energy* 9.6 (2006), pp. 549–577. DOI: [10.1002/we.201](https://doi.org/10.1002/we.201).
- [54] T. Sant, G. van Kuik, and G. J. W. van Bussel. “Estimating the angle of attack from blade pressure measurements on the National Renewable Energy Laboratory phase VI rotor using a free wake vortex model: yawed conditions”. In: *Wind Energy* 12.1 (Jan. 2009), pp. 1–32. DOI: [10.1002/we.280](https://doi.org/10.1002/we.280).
- [55] D. Micallef, M. Kloosterman, C. Ferreira, T. Sant, and G. van Bussel. “Validating BEM, direct and inverse free wake models with the MEXICO experiment.” In: *48th AIAA aerospace sciences meeting including the new horizons forum and aerospace exposition*. American Institute of Aeronautics and Astronautics, Jan. 2010. DOI: [10.2514/6.2010-462](https://doi.org/10.2514/6.2010-462).
- [56] A. Bruining and W. Timmer. “Airfoil characteristics of rotating wind turbine blades”. In: *Journal of Wind Engineering and Industrial Aerodynamics* 39.1-3 (Jan. 1992), pp. 35–39. DOI: [10.1016/0167-6105\(92\)90530-n](https://doi.org/10.1016/0167-6105(92)90530-n).
- [57] D. E. Shipley, M. S. Miller, M. C. Robinson, M. W. Luttges, and D. A. Simms. *Techniques for the determination of local dynamic pressure and angle of attack on a horizontal axis wind turbine*. Tech. rep. NREL/TP-442-7393. National Renewable Energy Laboratory, May 1995. DOI: [10.2172/61151](https://doi.org/10.2172/61151).
- [58] A. Saini and A. Gopalathnam. “Leading-edge flow sensing for aerodynamic parameter estimation”. In: *AIAA Journal* 56.12 (Dec. 2018), pp. 4706–4718. DOI: [10.2514/1.j057327](https://doi.org/10.2514/1.j057327).
- [59] B. Montgomerie, A. Brand, J. Bosschers, and R. Van Rooij. *Three-dimensional effects in stall*. Tech. rep. ECN-C-96-079. Energy Research Center of the Netherlands, 1996.
- [60] L. M. Mack. *Transition and laminar instability*. Tech. rep. JPL-PUBL-77-15. May 1977.
- [61] M. Drela and H. Youngren. “A user’s guide to MISES 2.53”. In: *Massachusetts Institute of Technology, Cambridge, MA* (1998).
- [62] T. Coelho Leite Fava, B. A. Lobo, A. Schaffarczyk, M. Breuer, D. S. Henningson, and A. Hanifi. *Numerical investigation of transition on a wind turbine blade under free-stream turbulence at $Re_c = 1,000,000$* . preprint. 2023.



- [63] P. K. Chaviaropoulos and M. O. L. Hansen. “Investigating Three-Dimensional and Rotational Effects on Wind Turbine Blades by Means of a Quasi-3D Navier-Stokes Solver”. In: *Journal of Fluids Engineering* 122.2 (June 2000), pp. 330–336. ISSN: 0098-2202, 1528-901X. DOI: [10.1115/1.483261](https://doi.org/10.1115/1.483261).

8

DESIGN OF A SWEEP WIND TURBINE BLADE TIP FOR FIELD EXPERIMENTS

Previous chapters discussed swept wind turbine blades in terms of fundamental numerical simulations and wind tunnel experiments. In pursuit of isolating the aerodynamic effects of blade sweep, several simplifications were applied, namely steady inflow conditions and a (in the case of the wind tunnel experiments at least intended) purely aerodynamic analysis. Furthermore, the sweep extent was exaggerated to decouple sweep-induced changes in aerodynamics from other aerodynamic phenomena.

This chapter describes the numerical conceptualisation of a swept blade tip that was intended to be tested on the full-scale TIADE research wind turbine. Therefore, the designed tip adheres to more realistic geometrical and load constraints imposed by the project framework. The conducted aeroelastic simulations demonstrate where sweep-induced reductions of the blade and tower extreme and fatigue loads are possible, as well as the penalties these load reductions come at. The complete analysis highlights the potential benefits swept wind turbine blades could have in realistic, full-scale scenarios.

Following a brief introduction in Section 8.1, Section 8.2 gives insight into design and operation limitations imposed by the project framework and the numerical tools used in this study. The results of the numerical design investigation are given in Section 8.3. Finally, the implications of the conducted numerical simulations are summarised in Section 8.4.

Parts of this chapter are currently under review in E. Fritz, K. Boorsma, A. Herrig, *Design of an aeroelastically tailored wind turbine blade tip for field experiments*, [Renewable Energy](#) (2024).



8.1. INTRODUCTION

In the past, swept blades were experimentally tested in the STAR (Sweep Twist Adaptive Rotor) project. Initial investigations by Zuteck [1] and Larwood and Zuteck [2] demonstrated the possibility for a sweep-induced increase in torsional deformation and a decrease in flapwise deformation, respectively. The swept blades eventually implemented in the field had a slightly extended blade length compared to their straight baseline. They showed an improved annual energy production of 10 – 12 % while maintaining the load envelope of the 750 kW reference wind turbine with straight blades [3]. More recently, the aerodynamic and aeroelastic characteristics of a swept wind turbine blade tip were investigated experimentally in a wind tunnel [4] and on a rotating test rig in the field [5]. Chapter 4 studied the aerodynamics of a rotating model HAWT equipped with swept blades in a wind tunnel.

Given that blade sweep is motivated by its coupling of aerodynamic and structural effects, aeroelastic simulations are required to fully evaluate the benefits of blade sweep numerically. Based on such simulations, Verelst and Larsen demonstrated that the flapwise extreme and fatigue loads at the blade root of the NREL 5 MW reference wind turbine could be reduced by up to 15 % and 10 %, respectively, by sweeping the blade [6]. In contrast to that, the torsional extreme and fatigue loads increased up to 400 % at the blade root. This increase in torsional moment is a major drawback of swept blades and presumably a reason why manufacturers have not adopted this concept. The potential for lowering blade root flapwise fatigue loads was also found by Larwood et al. [7].

A possible conclusion of the above studies is that swept blade tips have significant potential as alternatives to straight blade tips for modular blades and/or as a conscious design choice in developing novel blades. There is, however, a lack of field research data confirming this potential on modern, multi-megawatt wind turbines. As discussed at the beginning of Part III, the TIADE project aimed, among others, at the development of an aeroelastically tailored wind turbine blade tip for field application. As part of the research project's plan, unique jointed blades were developed that would allow the exchange of the blade tip. The work presented in this chapter embodies the first step towards a field test of a swept blade tip on a wind turbine representative of the state-of-the-art. It details the numerical investigations conducted in the design phase of the aeroelastically tailored tip. The simulations give insight into sweep-induced changes in extreme and fatigue loading as well as annual energy production.

8.2. METHODOLOGY

8.2.1. LIMITATIONS IMPOSED BY THE PROJECT

In this research project, the tip design space is primarily limited by the location of the pin joint, which connects the blade tip with the inboard part of the blade and is located at 80 % of the blade tip radius R . Thus, 20 % R remain on which aeroelastic tailoring techniques can be applied. During the concept phase for the tip design, it was decided to tailor the blades' properties through bend-twist coupling. Bend-twist coupling achieved through off-axis fibre orientation, as discussed by Karaolis et al. [8] and Capellaro [9], was dismissed early on, as aeroelastic simulations indicated limited additional torsion deformation due to the insufficient blade length of the interchangeable tip. As an alter-

native to off-axis fibre orientation, bend-twist coupling can be achieved geometrically by sweeping the blade. Despite the limited design space, blade sweep can significantly impact the blades' aeroelastic behaviour, as will be shown in this article.

Another design limitation imposed by the pin joint is that it is designed for the load envelope of a conventional, straight blade tip. A swept blade tip, however, inevitably leads to an increase in torsional loads in some parts of the blade, particularly in the proximity of the swept region itself. A swept tip would, thus, likely exceed the pin joint's torsional load envelope. To solve this, the project partners proposed lowering the turbine's rated rotational speed. Consequently, a margin to the torsional load limit is opened, which can be filled up by the sweep-induced torsional loads. This will be discussed in more detail in Section 8.3.3. For potential future application of blade sweep to wind turbine blades, the locally increased torsional loads have to be considered in the design process, and the structural properties should be adjusted accordingly to withstand them. The numerical analyses presented in Sections 8.3.4 to 8.3.6 compare blade loading for a straight and swept blade, both operating at the reduced rated rotational speed. This allows the direct evaluation of the impact of blade sweep on wind turbine blade loads.

8.2.2. NUMERICAL MODELLING

The simulations run for this study are based on two aerodynamic/aeroelastic tools, both based on blade element momentum theory (BEM):

1. A simple BEM algorithm based on the standard equations as presented e.g. in Burton et al. [10]. This code is purely aerodynamic and, thus, does not include blade deformations. For this study, a version of this code only accounting for crossflow and one additionally including the BEM correction model for swept blades proposed in Chapter 2 are implemented. In the remainder of this article, these two versions are denoted as crossflow-corrected and fully-corrected. Chapter 2 validated the baseline version of this BEM algorithm against the established aerodynamic solver *AWSM* [11]. This tool is only used for a preliminary study presented in Section 8.3.1.
2. The BEM-based aeroelastic simulation tool *Phatas* [12]. In the current *Phatas* release '*JAN-2014a SuperV*', the aforementioned BEM correction model is not included. This is shown to be of limited concern for the swept blade geometries considered in this study, see Section 8.3.1. Snel's first order dynamic stall model and correction model for three-dimensional flow are applied [13]. The aerodynamic solver is coupled to a non-linear structural dynamics solver, to take blade deformations into account while solving each time step. This tool allows the simulation of wind turbine design load cases (DLC) in accordance with IEC standard 61400-1 [14]. This tool is used for all simulations presented in Sections 8.3.2 to 8.3.6.

8.3. RESULTS

Due to confidentiality agreements with the project partners GE Renewable Energy and LM Wind Power, the y-axes of the plots presented in this section are redacted or nor-



malised. Nonetheless, they give clear indications regarding the influence of blade sweep on blade aerodynamics and aeroelasticity.

8.3.1. CROSSFLOW-CORRECTED VERSUS FULLY-CORRECTED BEM SIMULATIONS

In an initial step, the influence of the BEM correction model for swept blades proposed in Chapter 2 is evaluated. Chapter 5 aimed to validate the model using wind tunnel experimental data of blades with exaggerated sweep. Despite the improved modelling of the occurring flow physics, the added benefit of this correction model was difficult to demonstrate. Simulations corrected only for crossflow matched the experimental results similarly well as simulations fully corrected for sweep effects on blade aerodynamics.

To shed light on the relevance of this correction in the present study, the research turbine's blades are simulated both with only a crossflow correction (subscript cf) and fully corrected (subscript Λ). These simulations are run for swept blade tips with varying sweep extent y_{tip} , i.e. the maximum displacement of the blade axis in the rotor plane. All investigated tips follow a circular curve defined by the spanwise location of the tip joint (z_{start}) and the sweep extent at the tip (y_{tip}). The relative difference in the spanwise distributions of the axial induction factor and the normal force are shown in Figure 8.1.

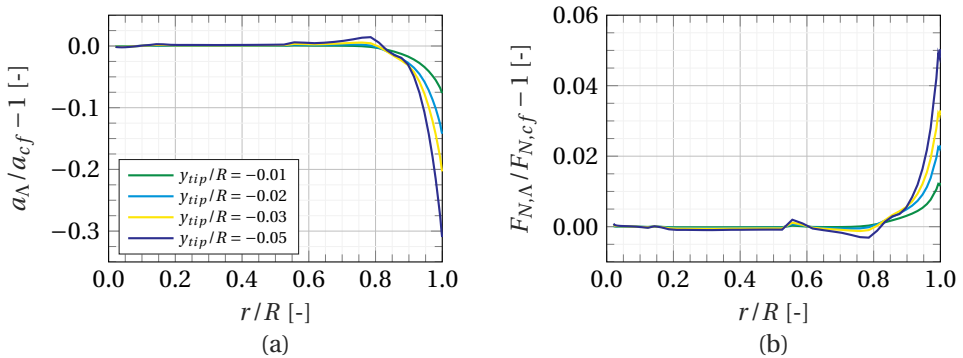


Figure 8.1: Relative difference in axial induction factor (a) and normal force (b) between simulations fully corrected for blade sweep (subscript Λ) and those corrected for crossflow only (subscript cf)

A seemingly significant relative difference in axial induction can be observed in the swept part of the blade ($r/R > 0.8$). Given that the local inflow velocity in this region is dominated by its in-plane component V_{rot} , this difference in axial induction causes a much smaller relative difference in the local blade loading. This can be seen in Figure 8.1 (b), showing a slight increase in axial load at the tip when simulating with full sweep correction. It should be noted that outboard of approximately $r/R = 0.85$, the normal force decreases rapidly so that relative differences in loading appear more prominent due to the diminishing denominator.

These differences in axial loading due to using the BEM correction model for swept blades are considered within reasonable limits, further supported by the relative difference in the rotor thrust coefficient C_T . For all simulated swept tips, the relative differ-

ence in thrust coefficient between the crossflow corrected and fully-corrected BEM simulations is below 0.25 %, see Table 8.1. Based on this observation, the BEM algorithm *Phatas*, which only corrects for crossflow, is deemed suitable for simulations of swept blades within the design space explored in this section.

Table 8.1: Relative difference in C_T between the fully sweep-corrected and crossflow-corrected simulations

Tip sweep y_{tip}	$-0.01 R$	$-0.02 R$	$-0.03 R$	$-0.05 R$
Relative difference in C_T	+0.12 %	+0.19 %	+0.23 %	+0.23 %

8.3.2. APPLICATION OF STEADY TWIST COMPENSATION

Wind turbine blades have a twist distribution tailored to the expected aerodynamic inflow conditions. Additionally, the twist distribution accounts for the steady aeroelastic twist induced by the sectional moment coefficient during operation. Next to the airfoil pitching moment, blade sweep induces an additional elastic twist to the wind turbine blade. Two states can be distinguished: Elastic twist due to aerodynamic loading in steady wind conditions and twisting due to unsteady aerodynamic events such as a gust. Considering an aft swept blade, it is clear that the steady aerodynamic loading of the swept part of the blade will induce a twist to lower angles of attack. Consequently, if one were to apply the same twist distribution to a swept blade as to a straight blade, the swept blade would experience lower aerodynamic forces and produce less power. Thus, a twist compensation should be applied, which corrects the operational angle of attack of the swept blade so that it more closely resembles that of the straight blade.

To determine the required twist compensation, aeroelastic simulations in steady wind are run for the straight and swept blade at approximately 1 – 2 m/s below the rated wind speed. This ensures that the twist compensation covers the larger twist deformations at rated conditions and the lower twist deformations for lower wind speeds equally well. Then, the difference in twist deformation between the swept and straight blade is added to the original blade's twist distribution as compensation. However, this could only be done in the region of the modular tip since the inboard blade geometry already existed. To ensure a smooth transition of the blade surface across the tip joint, the additional twist is faded out towards its location. Figure 8.2 depicts the original and amended twist distributions.

8.3.3. DETERMINATION OF THE ALLOWABLE SWEEP EXTENT

As described in Section 8.2.1, a reduction in rated rotor speed is used to accommodate additional torsional loads at the tip joint caused by blade sweep. This reduction is enforced by changing the rated rotor speed in the simulation settings of the turbine controller, which adjusts the blade pitch angle accordingly. By comparing extreme torsional loads of the straight blade with the original rated rotor speed Ω^0 to those of the swept tip with reduced rated rotor speed Ω^* , it can be determined whether the tip joint's original load envelope is exceeded. Simulations with stepwise increasing wind speed were run to determine the relevant loads. Figure 8.3 shows the ratio of extreme torsional moments at the tip joint for blade tips with varying sweep extent. It can be observed that the tor-



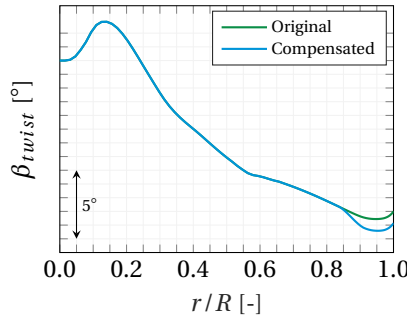


Figure 8.2: Twist distribution compensated for sweep-induced elastic deformations compared to the original twist distribution

sional load limit is exceeded for a sweep extent larger than approximately two per cent of the blade radius.

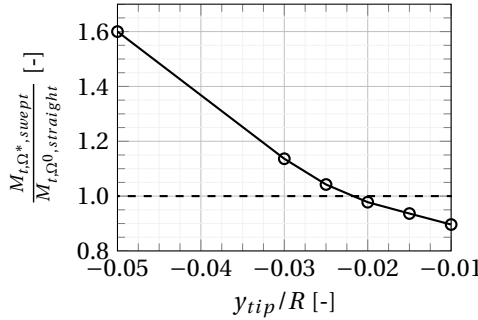


Figure 8.3: Ratio of the extreme torsional moment at the tip joint for blade tips of varying sweep extent operating with reduced rated rotor speed Ω^* and the straight reference tip operating with original rated rotor speed Ω^0

Combining this insight with the desire to maximise the impact of the swept blade tip, a design decision for a tip with a tip sweep of $y_{tip}/R = -0.02$ is made. Figure 8.4 gives a graphical representation of this swept tip defined by a sweep starting position of $z_{start}/R = 0.8$ and a tip sweep of $y_{tip}/R = -0.02$.



Figure 8.4: Schematic representation of a wind turbine blade with a swept tip defined by $z_{start}/R = 0.8$ and $y_{tip}/R = -0.02$, blade planform based on the IEA 15 MW reference wind turbine [15]

8.3.4. EFFECT OF BLADE SWEEP ON EXTREME LOADS

The effect of sweep on the extreme blade loads is determined by simulating operating conditions as defined by DLC 1.3 for turbine class IIB in IEC standard 61400-1 [14]. This

DLC reflects the turbine in power production under extreme turbulence. Given that extreme loads are expected either around the rated conditions or around the cut-out wind speed, wind speeds between 8 m s^{-1} and 25 m s^{-1} are simulated. This assumption is supported by the results presented in this section. For each wind speed, twenty random wind seeds are simulated, and each simulation is 640 s long, of which the final 600 s are considered for this analysis to avoid the influence of start-up phenomena. The blade moments are investigated at two spanwise locations, namely at the blade root and tip joint. The blade root is commonly equipped with strain gauges in field experiments, which would offer data for validation. Furthermore, the tip joint is of interest both because it is the structurally most critical part of the research wind turbine blade and because it represents the starting position of the applied sweep. Next to the aerodynamic moments on the blade, the moments acting on the base of the turbine tower are investigated.

For each random seed, the maximum flapwise, edgewise and torsional moments are determined and then averaged per wind speed. Figure 8.5 (a) – (c) shows the mean flapwise, edgewise and torsional blade root moment of both the straight and swept blade per wind speed. The general trends of all three moments agree well between the straight and swept blade simulations. The flapwise moment is closely related to the rotor thrust, which is typically highest at rated conditions before reducing for higher wind speeds. The edgewise and torsional blade root moments exhibit an approximately linear relation to the wind speed. With increasing wind speed, the occurring gust wind speeds also rise, leading to increased maximum loading in edgewise and torsional direction. Given that only the outer 20 % of the blade is swept, limited changes in blade root moments are observed. For most wind speeds, the flapwise and torsional loads of the straight blade slightly exceed those of the swept blade. The edgewise loads of the two blades almost coincide.

Figure 8.5 (d) – (f) demonstrates the strong coupling effect of sweep at the tip joint. The swept blade exhibits lower flapwise loads throughout the operating range, with the highest reduction for lower wind speeds. At the same time, the torsional loads are increased considerably compared to the straight blade. While the torsional loads of the straight blade are close to proportional to the wind speed, the swept blade follows this trend only at the inboard location. At the tip joint, the torsional moment follows a trend more closely related to that of the flapwise moment, namely with a peak around rated and then a slight reduction with higher wind speeds. Again, the edgewise moment has little sensitivity to blade sweep.

To further demonstrate the coupling of flapwise bending and torsion, the correlation between the two output signals is calculated using the Pearson correlation coefficient. For two arbitrary signals s_a and s_b , this correlation coefficient is defined as

$$r_P = \frac{\sum (s_{a,i} - \bar{s}_a)(s_{b,i} - \bar{s}_b)}{\sqrt{\sum (s_{a,i} - \bar{s}_a)^2 \sum (s_{b,i} - \bar{s}_b)^2}}. \quad (8.1)$$

Figure 8.6 shows the correlation of torsional and flapwise blade moments at the blade root and tip joint as a function of wind speed. At the blade root, the torsional and flapwise moment correlation is approximately equal for the straight and swept blade config-



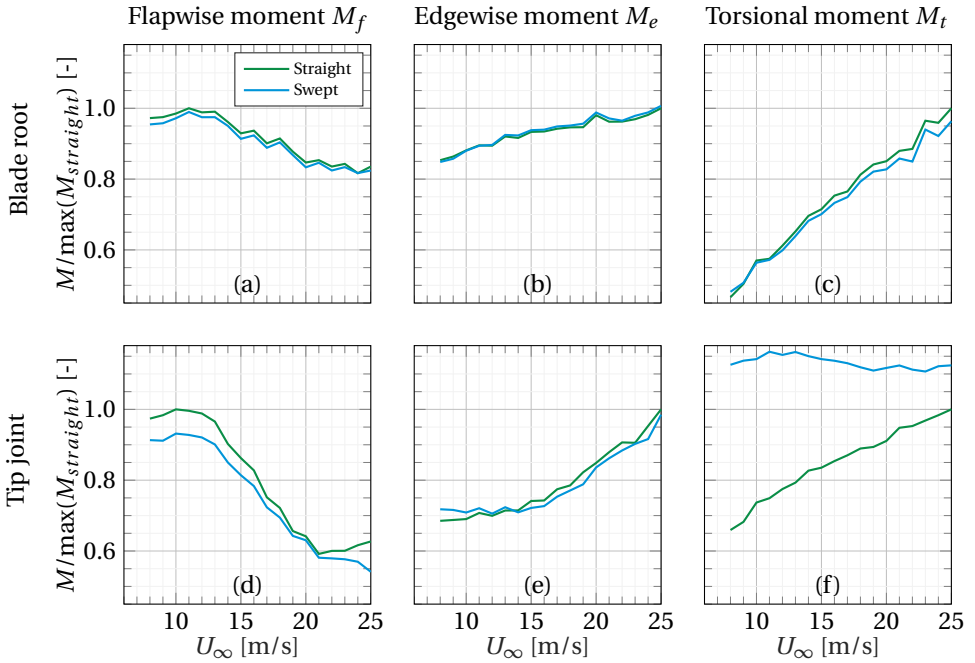


Figure 8.5: Normalised flapwise, edgewise and torsional extreme loads at the blade root and tip joint as a function of wind speed for the straight and swept case

urations. In contrast, the two moments are evidently more correlated at the tip joint for the swept blade than for the straight blade.

8

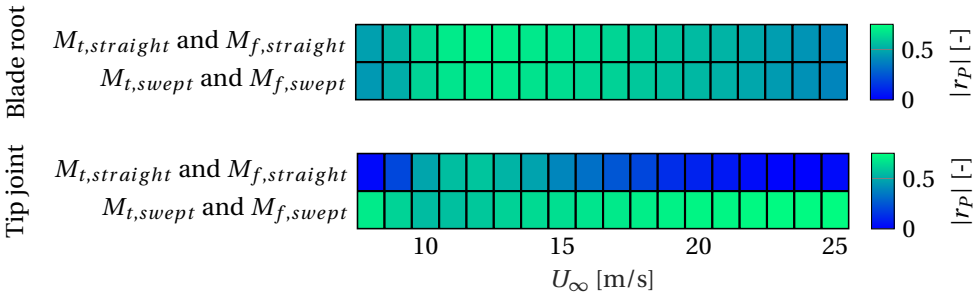


Figure 8.6: Correlation of torsional and flapwise blade moments at blade root and tip joint for the straight and swept-bladed configuration

The extreme tower bottom moments are shown in Figure 8.7. The fore-aft moment is closely related to the rotor thrust and flapwise blade moment and, thus, follows a comparable trend. Blade sweep reduces the tower fore-aft moment with a stronger decrease for low wind speeds. The side-side and yawing moments follow an approximately linear trend with increasing wind speed. Similar to the blade root edgewise and torsional

moments, this can be explained by the existence of higher wind speed extrema with increasing wind speed. A slight sweep-induced decrease in the yawing moment can be observed, while the side-side moment barely changes.

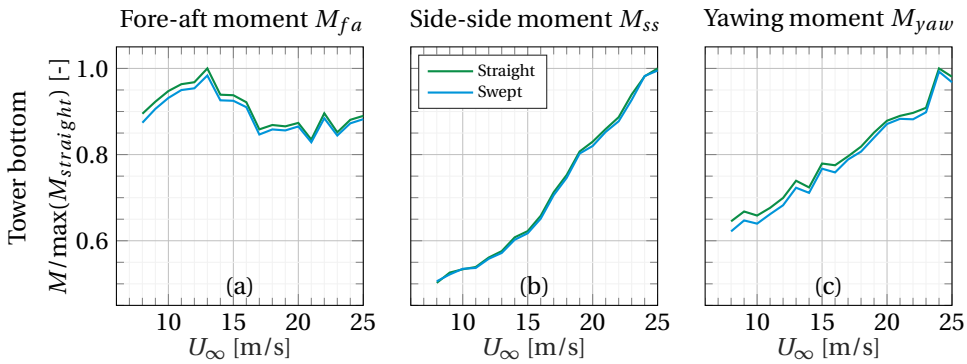


Figure 8.7: Normalised fore-aft, side-side and yaw extreme loads at the tower bottom as a function of wind speed for the straight and swept case

To summarise and quantify the effect of sweep on the blade and tower extreme loads, the relative difference in maximum moments experienced by the swept and straight blade configuration throughout DLC 1.3 are summed up in Table 8.2. Flapwise extreme loads reduce for both regarded spanwise locations. An even more substantial relative reduction can be observed for the torsional moment at the blade root, which comes with the penalty of a strong increase in torsion loads at the tip. In contrast to that, edgewise loads are barely affected, corroborating that blade sweep mostly couples flapwise and torsion deformations. All moments at the tower bottom are reduced when blade sweep is applied, with the largest decrease occurring in the fore-aft direction.

Table 8.2: Relative changes in extreme loads at blade root and tip joint, as well as tower bottom

Location	ΔM_f	ΔM_e	ΔM_t
Blade root	-1.0%	+0.7%	-3.7%
Tip joint	-6.8%	-1.5%	+16.3%

Location	ΔM_{fa}	ΔM_{ss}	ΔM_{yaw}
Tower bottom	-1.6%	-0.5%	-0.7%

8.3.5. EFFECT OF BLADE SWEEP ON FATIGUE LOADS

Similar to the analysis presented in Section 8.3.4, the influence of blade sweep on the fatigue loads can be investigated. For this purpose, simulations are run according to DLC 1.2 defined by the IEC standard [14]. This DLC represents the turbine in power production under normal turbulence. Again, multiple random wind seeds are run per



wind speed, and each simulation lasts 600 s plus an initial 40 s start-up period omitted in the final processing. Per wind speed and random seed, a damage-equivalent load (DEL) is calculated using a rainflow counting algorithm [16] on the flapwise, edgewise and torsional moment signals at blade root and tip joint as well as the fore-aft, side-side and yawing moments at the tower bottom. A Wöhler exponent of $m = 10$ for the blade loads, $m = 4$ for the tower loads [17], and a number of reference cycles $N_{ref} = 10^7$ are used.

Figure 8.8 (a) – (c) shows the flapwise, edgewise and torsional DEL at the blade root averaged per wind speed over the random wind seeds. The flapwise DEL generally increase with increasing wind speed, except for a saddle area around the rated wind speed. Leading up to the saddle, the turbine's rotor speed is driven by the wind velocity. With increasing wind speed, the magnitude of wind speed variations also increases. This entails changes in rotor speed and flapwise loading, leading to the initial steep rise in flapwise DEL. Around rated, the controller regulates the rotor speed to be more constant, thus reducing the fatigue loading. Beyond the saddle, the ever-larger variations in wind speed outweigh the controller's ability to reduce rotor speed variations so that the DEL rise again. The edgewise blade root DEL are dominated by the gravitational loads and, thus, by the rotor speed. This explains why the DEL curve flattens beyond rated conditions. For very high wind speeds, the pitch angle is also high so that the edgewise loads are more aligned with the wind direction. This leads to a slight increase in edgewise DEL for very high wind speeds. The torsional fatigue loads exhibit a minimum around rated conditions. The negative slope leading up to the rated wind speed is a consequence of flapwise blade prebend. This prebend entails a strong correlation of the torsional blade loads and the rotor azimuth due to gravity. With increasing wind speed, the rotor loading causes the blades to straighten out, and the gravitational contribution to the torsional blade root moment diminishes. Beyond rated conditions, the pitching rate increases. This, in combination with gravitational loads due to the blade bending towards the tower, causes the positive DEL slope for higher wind speeds. The DEL of the straight and swept blade configuration exhibit very similar trends. However, both flapwise and torsional blade root DEL reduce slightly when sweeping the blade tip. The edgewise DEL are practically identical.

Figure 8.8 (d) – (f) shows the DEL at the tip joint. In flapwise direction, the same trend as at the blade root can be observed. In edgewise direction, the DEL rise monotonously with increasing wind speed rather than plateauing as at the blade root. At the tip joint, gravitational loads are less dominant than at the root and aerodynamic loads contribute relatively more to the fatigue loading. Therefore, the edgewise DEL are driven by the increasing magnitude of velocity variations with increasing wind speed. The same holds for the torsional tip joint DEL of the straight blade. While the blade root experiences dominant gravitational loads due to blade prebend, their influence is relatively lower than that of the variable aerodynamic loads due to changes in wind speed. The torsional DEL of the swept blade differ significantly from the straight blade. The fatigue loads increase and follow a pattern closely related to the flapwise DEL, further corroborating the coupling of flapwise bending and torsional deformations. The increased torsional DEL are a sign that the blade passively twists due to unsteady inflow conditions, leading to the relatively substantial reduction of flapwise fatigue loads as seen in Figure 8.8 (d).

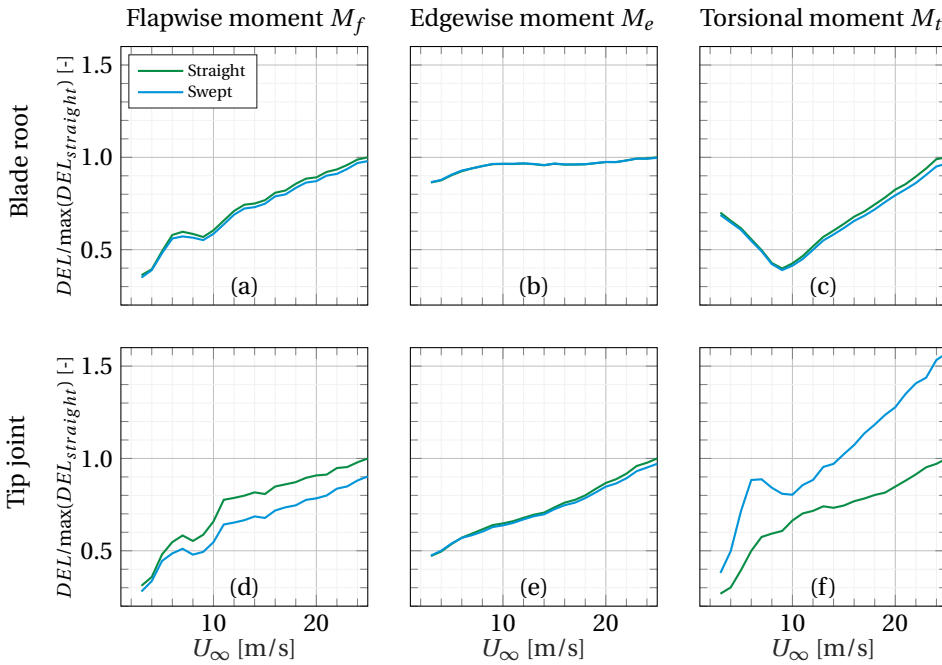


Figure 8.8: Normalised flapwise, edgewise and torsional DEL at the blade root and tip joint as a function of wind speed for the straight and swept case

In edgewise direction, a minor sweep-induced decrease of DEL can be seen for very high wind speeds.

The DEL of the fore-aft, side-side and yawing moment at the tower bottom are given in Figure 8.9. The fore-aft DEL are closely related to rotor thrust and, thus, exhibit a pattern very similar to the blade root flapwise DEL. The side-side and yawing DEL are dominated by the increasing magnitude of wind speed variations with increasing wind speed. However, just below rated conditions, there is an apparent tower excitation in the side-side direction by the rotational frequency. This leads to a local maximum before returning to the approximately linear relation to the wind speed. In terms of sweep-induced relative change, the tower bottom DEL show minor reductions in the fore-aft and yawing direction and negligible differences in the side-side direction.

By multiplying the DEL per wind speed with the expected wind speed probability distribution, a lifetime DEL is determined. The wind speed probability distribution is a Rayleigh distribution defined by

$$F(U_\infty) = 1 - \exp\left(-\pi \left(\frac{U_\infty}{2U_{ave}}\right)^2\right), \quad (8.2)$$

with an annual average wind speed $U_{ave} = 8.5$ m/s and the characteristic turbulence intensity is $TI = 14\%$ in accordance with IEC standard 61400-1 for turbine class IIB.

A summary of the relative changes in lifetime DEL is presented in Table 8.3. Flapwise DEL decrease throughout the blade. The relative decrease is higher at the tip joint than



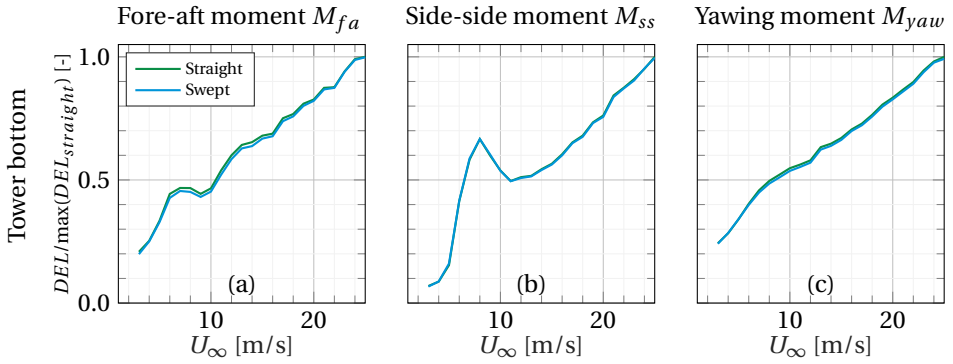


Figure 8.9: Normalised fore-aft, side-side and yawing DEL at the tower bottom as a function of wind speed for the straight and swept case

at the blade root, which can be explained by the overall decreasing load level with increasing spanwise position. The torsional DEL follow this trend at the blade root, where considerable load reductions are achieved. However, a strong increase of torsional DEL occurs at the tip joint. This is expected, as the objective of sweep is to passively twist the blade as a reaction to changing inflow conditions. This effect is felt most in the region where sweep is applied. Edgewise DEL are hardly sensitive to the application of blade sweep. The tower bottom fore-aft and yawing DEL decrease while there is a negligible increase in the side-side direction.

Table 8.3: Relative changes in lifetime DEL at blade root and tip joint, as well as tower bottom

Location	$\Delta\text{DEL}(M_f)$	$\Delta\text{DEL}(M_e)$	$\Delta\text{DEL}(M_t)$
Blade root	-2.6%	+0.1%	-3.0%
Tip joint	-15.0%	-1.9%	+43.2%

Location	$\Delta\text{DEL}(M_{fa})$	$\Delta\text{DEL}(M_{ss})$	$\Delta\text{DEL}(M_{yaw})$
Tower bottom	-2.1%	+0.1%	-1.4%

8.3.6. EFFECT OF BLADE SWEEP ON ENERGY PRODUCTION

The simulation results of DLC 1.2 also yield the rotational speed, pitch angle and generated power as a function of wind speed. As such, it can be evaluated how the swept blade tip affects the turbine performance. For each wind speed, these quantities are averaged over the simulation duration and the random seeds. Figure 8.10 shows the resulting normalised curves.

It is evident that the introduction of blade sweep does not lead to changes in the rotational speed. This is expected as both blade configurations are simulated with the same controller and, thus, also identical targeted rotor speeds. While the pitch angle is in

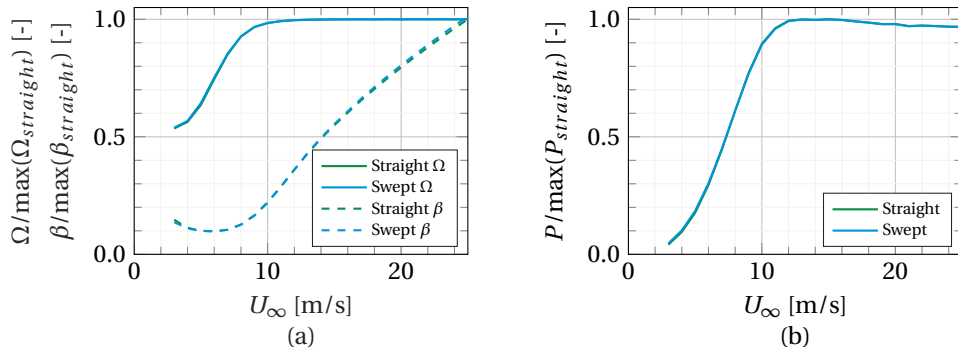


Figure 8.10: Normalised rotational speed and pitch angle curves (a) and power curves (b) of the straight and swept blade configuration

close agreement for most wind speeds, minor deviations can be seen for very high wind speeds. Here, the rotor loading and, consequently, the effect of bend-twist coupling are small. Therefore, the twist pre-compensation described in Section 8.3.2 is too large in these conditions, and the controller increases the pitch angle slightly to compensate.

As a logical consequence, changes in power output due to blade sweep are negligible, too. This is confirmed further when calculating the annual energy production (AEP) by multiplying the power curves with the wind speed probability distribution given in Equation 8.2 and the hours per year. The sweep-induced relative change in AEP is $\Delta AEP = +0.26\%$.

8.4. CONCLUSIONS

This chapter presents results from numerical investigations aimed at evaluating swept wind turbine blade tip designs and their impact on extreme and fatigue blade loading. By conducting this research within the framework of a field experiment, practical implications such as a realistic design space, the accommodation of increased torsional loading and the need for a steady twist compensation to maintain turbine performance could be highlighted.

The maximally swept tip geometry fulfilling the load restrictions was defined by a sweep starting position of $z_{start} = 0.8R$ and a tip sweep of $y_{tip} = -0.02R$. By simulating DLC 1.2 and DLC 1.3 as defined by IEC standard 61400-1, the impact of the swept tip on fatigue and extreme loads during power production was evaluated. Flapwise extreme loads were shown to reduce throughout the blade, with higher relative reductions with increasing radial position, where the absolute blade loading is smaller. Torsional extreme loads are reduced at the blade root but increased at the tip joint location where the bend-twist coupling is strongest. Edgewise extreme loads remained largely unaffected by the application of blade sweep. The extreme fore-aft, side-side and yawing moments at the tower bottom all reduce, with the most significant reduction in the fore-aft direction.

The sweep-induced changes in damage-equivalent loads followed a similar pattern



as the extreme loads. Again, flapwise DEL reduced throughout the blade with a higher relative impact in the outboard region. Torsional DEL also reduced at the blade root but increased at the tip joint. Edgewise DEL were hardly sensitive to the swept blade tip. The tower bottom DEL exhibited reductions in the fore-aft and torsional direction, while a negligible increase occurred in the side-side direction.

Finally, it was demonstrated that the power curve and, consequently, the annual energy production were unaffected by the swept blade geometry. This indicates that rotor loads can be reduced even within limited blade sweep design space without sacrificing rotor performance. As such, the potential of swept tips as a retrofit option for segmented blades is highlighted.

8.A. NOMENCLATURE

Latin letters

AEP	Annual energy production
a	Axial induction factor
C_T	Thrust coefficient
DEL	Damage-equivalent load
DLC	Design load case
F	Probability of wind speeds
F_N	Rotor plane normal force
M_f, M_e, M_t	Flapwise, edgewise and torsional blade moment
M_{fa}, M_{ss}, M_{yaw}	Fore-aft, side-side and yawing tower moment
m	Wöhler exponent
N_{ref}	Number of reference cycles
P	Power
R	Blade tip radius
r	Radial coordinate
r_p	Pearson correlation coefficient
s_a, s_b	Arbitrary signals
TI	Turbulence intensity
U_{ave}	Average freestream velocity according to IEC standard 61400-1
U_∞	Freestream velocity
V_{rot}	Rotational velocity
y_{tip}	Tip sweep
z_{start}	Sweep starting position

Greek letters

continues on next page...

β	Pitch angle
β_{twist}	Twist angle
Ω^0	Original rated rotor speed

Greek letters

...continued

 Ω^* Reduced rated rotor speed

Subscripts cf Corrected for crossflow Λ Corrected for crossflow, trailed vorticity displacement and bound vortex self-induction



BIBLIOGRAPHY

- [1] M. Zuteck. *Adaptive blade concept assessment: Curved platform induced twist investigation*. Tech. rep. SAND2002-2996. Sandia National Laboratories, Oct. 2002. DOI: [10.2172/803289](https://doi.org/10.2172/803289).
- [2] S. Larwood and M. Zuteck. “Swept wind turbine blade aeroelastic modeling for loads and dynamic behavior”. In: *AWEA Windpower*. AWEA Windpower, Jan. 2006.
- [3] T. Ashwill, G. Kanaby, K. Jackson, and M. Zuteck. “Development of the sweep-twist adaptive rotor (STAR) blade”. In: *48th AIAA aerospace sciences meeting including the new horizons forum and aerospace exposition*. American Institute of Aeronautics and Astronautics, Jan. 2010. DOI: [10.2514/6.2010-1582](https://doi.org/10.2514/6.2010-1582).
- [4] T. Barlas, G. R. Pirrung, N. Ramos-García, S. G. Horcas, R. F. Mikkelsen, A. S. Olsen, and M. Gaunaa. “Wind tunnel testing of a swept tip shape and comparison with multi-fidelity aerodynamic simulations”. In: *Wind Energy Science* 6.5 (Oct. 2021), pp. 1311–1324. DOI: [10.5194/wes-6-1311-2021](https://doi.org/10.5194/wes-6-1311-2021).
- [5] T. Barlas, G. R. Pirrung, N. Ramos-García, S. González Horcas, A. Li, and H. A. Madsen. “Atmospheric rotating rig testing of a swept blade tip and comparison with multi-fidelity aeroelastic simulations”. In: *Wind Energy Science* 7.5 (Oct. 2022), pp. 1957–1973. ISSN: 2366-7443. DOI: [10.5194/wes-7-1957-2022](https://doi.org/10.5194/wes-7-1957-2022).
- [6] D. R. Verelst and T. J. Larsen. *Load consequences when sweeping blades - A case study of a 5 MW pitch controlled wind turbine*. Tech. rep. RISO-R-1724(EN). Technical University of Denmark, Risø National Laboratory for Sustainable Energy. Wind Energy Division, Roskilde (Denmark), 2010.
- [7] S. Larwood, C. van Dam, and D. Schow. “Design studies of swept wind turbine blades”. In: *Renewable Energy* 71 (Nov. 2014), pp. 563–571. DOI: [10.1016/j.renene.2014.05.050](https://doi.org/10.1016/j.renene.2014.05.050).
- [8] N. M. Karaolis, P. J. Musgrove, and G. Jeronimidis. “Passive aerodynamic control using composite blades”. In: *Use of composite materials for wind turbines workshop, Harwell, UK*. Jan. 1988.
- [9] M. Capellaro. “Design Limits of Bend Twist Coupled Wind Turbine Blades”. In: *53rd AIAA/ASME/ASCE/AHS/ASC Structures, Structural Dynamics and Materials Conference & 20th AIAA/ASME/AHS Adaptive Structures Conference & 14th AIAA*. Honolulu, Hawaii: American Institute of Aeronautics and Astronautics, Apr. 2012. ISBN: 978-1-60086-937-2. DOI: [10.2514/6.2012-1501](https://doi.org/10.2514/6.2012-1501).
- [10] T. Burton, D. Sharpe, N. Jenkins, and E. Bossanyi. *Wind Energy Handbook*. John Wiley & Sons, June 2011. ISBN: 978-1-119-99392-6.

- [11] F. Grasso, A. van Garrel, and G. Schepers. “Development and validation of generalized lifting line based code for wind turbine aerodynamics”. In: *49th AIAA aerospace sciences meeting including the new horizons forum and aerospace exposition*. American Institute of Aeronautics and Astronautics, Jan. 2011. DOI: [10.2514/6.2011-146](https://doi.org/10.2514/6.2011-146).
- [12] C. Lindenburg. *PHATAS User’s manual version 11737*. Tech. rep. WMC-2016-005. (Confidential). LM Wind Power, 2020.
- [13] H. Snel, R. Houwink, and T. Bosscher. *Sectional prediction of lift coefficients on rotating wind turbine blades in stall*. Tech. rep. ECN-C-93-052. Energy Research Center of the Netherlands, 1994.
- [14] International Electrotechnical Commission. *Wind turbines – part 1: Design requirements (IEC 61400-1:2005(E))*. Tech. rep. 2005.
- [15] E. Gaertner et al. *Definition of the IEA wind 15-megawatt offshore reference wind turbine*. Tech. rep. NREL/TP-5000-75698. Golden, CO, US: National Renewable Energy Laboratory, 2020.
- [16] H. Hendriks and B. Bulder. *Fatigue Equivalent Load Cycle Method. A General Method to Compare the Fatigue Loading of Different Load Spectrums*. Tech. rep. ECN-C-95-074. Energy Research Center of the Netherlands, 1995.
- [17] N. Dimitrov, A. Natarajan, and J. Mann. “Effects of normal and extreme turbulence spectral parameters on wind turbine loads”. In: *Renewable Energy* 101 (Feb. 2017), pp. 1180–1193. ISSN: 0960-1481. DOI: [10.1016/j.renene.2016.10.001](https://doi.org/10.1016/j.renene.2016.10.001).

IV

CONCLUSION



9

CONCLUSIONS AND FUTURE RESEARCH

The research presented in this thesis was motivated by the following research questions:

- 1. How does blade sweep influence the aerodynamics of wind turbine blades?*
- 2. How can swept blade aerodynamics be modelled more accurately with low-fidelity simulation tools?*
- 3. How can field data be used for model validation beyond average integral values?*
- 4. Can a blade's aeroelastic performance be tailored through a swept tip design?*

In this chapter, key findings of the conducted research are presented and placed in the context of these research questions. Finally, recommendations for future research on the path towards swept wind turbine blades are given.

9.1. KEY FINDINGS OF THE CONDUCTED RESEARCH

How does blade sweep influence the aerodynamics of wind turbine blades?

The application of sweep to wind turbine blades introduces additional flow complexity. Several changes to the blade aerodynamics were identified and discussed in this thesis.

In the swept part of the blade, the relative inflow velocity and the airfoil orientation are not aligned. The inflow vector can then be decomposed into a velocity component aligned with the local blade axis and a component aligned with the airfoil orientation. Assuming that the spanwise velocity component is equally large on the pressure and suction side of an airfoil, its influence on the pressure forces is negligible. The decomposition of the inflow vector into the airfoil plane leads to changes in the inflow conditions when compared to a straight reference, namely a reduction in relative velocity and an increase in inflow angle and consequently in angle of attack. The existence of cross-flow is well-established in aircraft aerodynamics, where swept back wings are common practice. An important distinction between an aircraft wing and a wind turbine blade is that the former generally performs a straight flight while the latter performs a rotational movement. As a consequence, the velocity decomposition on an aircraft wing is a function of only one angle, while for a wind turbine blade, two angles need to be considered, referred to as global and local sweep angles.

Next to the misalignment between inflow and airfoil orientation, the curved blade shape leads to an elongation of the blade span when comparing it to a straight blade with identical blade tip radius. This holds particular relevance for the numerical modelling of wind turbines, where the blade is often discretised by a number of spanwise elements. In the swept part of a blade, the radial extent of such a blade segment and its spanwise length are not equal. This has to be considered in the determination of blade forces which are often calculated based on force coefficients defined per unit blade length.

Additional deviations from straight blade aerodynamics occur in the bound and wake vorticity system of the blades. The added curvature of the blade in the rotor plane displaces the blade's wake in the azimuthal direction. The wake can be expressed as a combination of trailed and shed vorticity, which induces a velocity in the rotor plane and at the blade itself. The change in wake shape and release point, when compared to a straight reference case, brings about a change in the induction system of the rotor.

Similar to the wake vorticity system, also the bound vorticity system is altered by blade sweep. Simplifying this problem to lifting line terms, where the bound vorticity is collapsed into a vortex filament running through the quarter chord location of each spanwise blade segment, a straight blade's bound vorticity approximately forms a straight vortex filament. By definition, this filament does not induce a velocity on itself. This changes when blade sweep is introduced, and the bound vorticity follows a curved shape. Then, an additional induction term is introduced to the overall induction system.

How can swept blade aerodynamics be modelled more accurately with low-fidelity simulation tools?

Having determined the major sweep-induced changes in blade aerodynamics, the following step is to ensure accurate modelling of these. While mid- to high-fidelity models

such as CFD and vorticity-based methods intrinsically model the changes to blade and wake geometry, blade element momentum theory could not reliably capture the aerodynamics of swept blades so far.

This dissertation presents a novel correction model that enables BEM algorithms to model swept blades. The model consists of two corrections, one accounting for the displacement of the trailed vorticity in azimuthal direction and one for the bound vortex's self-induction. A major advantage of this model is that it retains BEM's streamtube-independent approach, which facilitates its incorporation into existing BEM algorithms employing this approach, and adds negligible additional computational effort.

In the correction model, the displacement of the trailed vorticity is approximated by modelling the displacement of the dominant tip vortex. In practice, this is done by adding or subtracting (depending on the direction of sweep) the induction of a straight vortex filament corresponding to the tip displacement to/from the induction of a semi-infinite helical vortex filament corresponding to the tip vortex evolution. This procedure can be incorporated inside the iterative BEM solution loop. Only geometric parameters of the blade need to be passed on to each streamtube while solving the BEM equations.

The curved vortex self-induction is approximated by evaluating the induction of all blade elements on each other based on unit circulation. It is assumed that neighbouring blade elements have the highest influence on each other and, furthermore, that moderate gradients in circulation are present. Then, the local induction of the bound vortex on itself can be estimated by multiplying the induction based on unit circulation calculated prior to the simulation with the local circulation of the regarded blade element during the solution process. In the a priori calculation of the induction based on unit strength, a vortex cut-off radius of 25 % of the local chord is deemed representative of a realistic vorticity distribution on a blade surface.

The correction model was initially validated against lifting line simulations for a wide range of both fore- and aft-swept blades. The changes in loading and induction were captured well by the BEM algorithm including the sweep correction model. Aiming at further validation, two wind tunnel campaigns on a newly developed model HAWT were conducted. One campaign was conducted using a straight baseline blade geometry, which is a thrust-scaled version of the IEA 15 MW RWT. The second campaign was run on swept versions of these blades. Particle image velocimetry was used to capture detailed flow fields around the blades at multiple radial locations. In post-processing, the spanwise distributions of circulation, induction values, inflow angle, angle of attack, normal and tangential forces, and lift coefficient were derived from the PIV data, thereby precisely characterising the blade aerodynamics.

The data gathered during the straight-bladed campaign form an extensive dataset previously unavailable for a thrust-scaled version of the IEA 15 MW RWT. The experiment on the swept blades is the first conducted wind tunnel experiment on a rotating HAWT with swept wind turbine blades, and thus, represents a significant contribution to the scientific community.

Next to their standalone value, the collected data are used to validate numerical simulations and, in particular, the developed BEM correction model. To this end, the experimentally derived loads and circulation are used as input to inverse BEM and lifting line algorithms. Both methods yield the induction terms, which can then be compared

against those derived directly from the PIV flow fields. There is a good agreement between directly derived values and those resulting from the inverse numerical approaches for both the straight and swept blades. For the latter, it is additionally shown that inverse BEM simulations without sweep correction match the directly derived induction values less than the corrected implementation. This further supports the value of the developed BEM correction model.

How can field data be used for model validation beyond average integral values?

This question was taken directly from the long-term research challenges in wind energy as presented by van Kuik et al. [1]. This context already suggests that a single dissertation cannot fully answer this question by itself. Nonetheless, the research presented in Chapters 6 and 7 contributes to answering this rather broad research question.

To be of any use in a validation exercise, field data needs to be as accurate as possible, especially when it comes to more complex measurements, such as local pressure distributions, rather than integrated values, such as e.g. blade root bending moments. This dissertation presents a robust approach to optimise the placement of pressure sensors around an airfoil to capture its pressure distribution accurately for a range of expected operating conditions. Two optimisation approaches working on fundamentally different principles arrive at nearly identical solutions, indicating that an optimal solution for the placement of pressure sensors exists (for a given objective function). Sensor layout optimisation shows great potential to increase measurement accuracy and/or reduce the number of required sensors, allowing for material cost savings. While developed in the context of wind turbine aerodynamics, the approach can equally benefit other aerodynamic applications relying on pressure measurements.

Utilising an optimised sensor layout, pressure measurements were captured on a research turbine in the field over several months. Combined with detailed inflow measurements from a LiDAR system, these measurements form an extensive database that enables a wide range of analyses. In the context of this dissertation, these measurements were used to validate BEM-based aeroelastic simulations both on a ten-minute average time scale as well as time-resolved. On the ten-minute average time scale, simulated local blade aerodynamics were validated regarding integrated sectional forces, but also regarding airfoil aerodynamics in terms of the pressure distribution. The pressure measurements were conducted at approximately 25% blade radius, where three-dimensional flow effects can occur. Overall, good agreement between the simulated and measured quantities was found. However, it was demonstrated that for higher wind speeds and, thus, higher pitch angles, the 3D corrections often applied in BEM simulations and 2D panel codes are less accurate and uncorrected two-dimensional aerodynamics yield a better match with the field data.

It was further demonstrated that a ten-minute average pressure distribution is in good approximation representative of the underlying time-resolved data for low wind speeds. However, at higher wind speeds, this representativeness worsens due to the onset of non-linear aerodynamic phenomena such as stall, and ten-minute statistical pressure data should be interpreted more carefully.

On the time-resolved scale, it was shown that the accuracy of aeroelastic simulations

has a large dependency on individual time series without clear correlations to operational or environmental conditions. While the congruence of simulated and measured hysteresis loops of unsteady airfoil forces can be extremely good in some cases, it might be rather bad in other cases. This indicates that there is still high uncertainty in the modelling of unsteady airfoil aerodynamics, but likely also in the transfer of measured operational and environmental conditions in the field to simulation inputs on the numerical side. On average, the error between simulated and measured forces and angle of attack was shown to be on an acceptable level. This suggests that BEM-based aeroelastic simulation tools are still relevant when it comes to simulating wind turbines comparable in size to industry standards for onshore wind turbines.

Can a blade's aeroelastic performance be tailored through a swept tip design?

As indicated at the beginning of Part III of this dissertation, the original plan was to be able to answer this question based on the TIADE field experiment conducted on a full-scale research turbine. Due to obstacles encountered in the project execution, the planned field campaign with a swept tip was not realised. Thus, the posed research question is answered based on the numerical results presented in Chapter 8 without experimental corroboration.

Working within the TIADE project framework, the design study is closely guided by considerations necessary to make a swept blade design feasible in realistic conditions. The design space in terms of both sweep starting position and sweep extent was limited by the location and structural strength of the tip joint to which a swept blade tip would have been attached. The sweep-induced increase in the torsional moment was the largest concern. Therefore, a load margin was first opened up by reducing the rated rotor speed, which could then be filled with the increased sweep-induced torsional loads without exceeding the baseline tip joint loads. The maximum allowable tip sweep within this load restriction was shown to be two per cent of the blade tip radius. Furthermore, it is shown that the twist induced by blade sweep in steady wind conditions requires a correction of the blade's twist distribution.

By simulating IEC design load cases 1.2 and 1.3, a detailed analysis of sweep-induced changes to the extreme and fatigue loads is conducted. Both extreme and fatigue loads in flapwise direction are shown to reduce at the blade root and at the tip joint. The torsional fatigue loads decrease at the blade root while clearly increasing at the tip joint, as expected. Edgewise loading remains largely unaffected by the swept tip since blade sweep mostly couples the torsional deformation with the flapwise bending deformation. It is further demonstrated that the swept blade tip leads to a reduction in tower fore-aft and yawing loads compared to a straight reference blade. Simultaneously, the turbine's energy production remained unchanged. These simulation results highlight the potential benefit of swept blade tips as an alternative for modular blades or as a conscious design choice in new blade developments.

The presented numerical simulations were conducted within the context of the TIADE project. By working in this framework rather than on a virtual reference turbine, realistic complications that can be a side effect of blade sweep were highlighted. The positive findings can likely be transferred to wind turbine blade designs not subjected

to the project-specific design restrictions. It is expected that a less limited design space would enable even higher load reductions while maintaining the desired turbine performance.

9.2. RECOMMENDATIONS FOR FUTURE RESEARCH

This dissertation presents research efforts on the path towards making swept wind turbine blades a realistic design choice. Several areas remain where additional research could support the development of such blades. In this section, suggestions for future research are given, some of which concern improvements to existing setups and approaches while others concern completely new lines of research.

9.2.1. NUMERICAL MODELLING

- Currently, the correct numerical modelling of swept blades is researched by individual researchers with limited interaction. Should swept blade geometries become a viable option for wind turbine manufacturers, the wind energy community should have a clear understanding and consensus on what is required to accurately model swept blades. In the context of numerical modelling of wind turbine aerodynamics and aeroelasticity, benchmarks have been of immense value in creating a common ground for discussion and identifying research areas requiring additional attention [2, 3, 4]. A comparable benchmark, ideally including purely aerodynamic as well as aeroelastic simulations, would be crucial in further developing the accuracy of swept blade numerical modelling. The experimental data presented in Chapter 4, which is publicly available on the 4TU.ResearchData repository [5], could serve as starting point for such a benchmark.
- One aspect that such a benchmark could support is the investigation of spanwise flow effects in the swept part of the blade. 3D flow correction models exist for the blade root, and it could be relevant to establish whether comparable models are required to accurately model the aerodynamics of swept blades, too. In particular, high-fidelity CFD simulations would be valuable in such an investigation.
- Swept blades have been demonstrated to have the potential for reducing blade loads. Future research could investigate whether there is also a potential for reducing turbine noise, which would be particularly relevant for onshore applications. This idea is motivated by the parallels between blade sweep and serrations, where the trailing edge is angled to the flow over the airfoil to reduce trailing edge noise.

9.2.2. EXPERIMENTAL TESTING

WIND TUNNEL EXPERIMENTS

The wind tunnel campaigns conducted in this PhD project suffered from unintended blade deformations and deviations from the desired pitch angle. Thus, some improvements to the experimental setup are recommended:

- To reduce uncertainty in the pitch angle, it is recommended to upgrade the model turbine to an electrical pitch mechanism that allows precise pitch angle setting after an initial calibration.

- The model turbine has been designed to accommodate a six-axis load cell between the tower top and the nacelle and a torque sensor on the drive train. Data acquisition interfaces were not available at the time of the experiments. Given that these sensors would provide valuable additional data, efforts should be made to create the data acquisition interfaces.
- To obtain more coherent material properties between the individual blades used in experiments, either new blades could be manufactured with an improved vacuum infusion process or the manufacturing process could be outsourced to professionals. In either case, testing the structural properties prior to an experiment is recommended.

Next to improvements to the setup, additional recommendations are given regarding potential lines of research.

- To enable a more exhaustive validation of numerical simulations of swept blades, including the BEM correction model proposed in this dissertation, a wider range of operating points, realised e.g. by sweeping through different tip-speed ratios and pitch angles, should be investigated experimentally.
- Blade sweep targets the coupling of bending and twisting deformations, which was observed in the presented wind tunnel experiment. Improved deformation tracking [6, 7, 8] could help characterise the aeroelastic response of the blade and even enable running experiments designed to be of aeroelastic rather than purely aerodynamic nature.

FIELD EXPERIMENTS

- The most relevant recommendation for future research is an experimental campaign testing blade sweep, whether applied to a modular tip as intended in the TIADE project or applied to a larger part of the blade geometry, on a multi-megawatt scale. Using pressure and strain gauge measurements, changes to local and integrated blade loads can be determined. Such efforts will enable a true evaluation of the potential of swept blades in reducing turbine loads while maintaining rotor performance.
- In field conditions, it could be additionally interesting to investigate whether the curved shape of a swept blade has an effect on leading edge erosion.

9.2.3. SWEEPED BLADE DESIGN FOR STATE-OF-THE-ART TURBINES

Benefits of swept blades in terms of load reduction have been demonstrated repeatedly. Nonetheless, wind turbine blade manufacturers have not adopted this concept. It is expected that this is in part due to practical and logistical questions and in part due to concerns about the business case of swept blades when going beyond the aeroelastic analysis.

- Conventional blades are convenient in manufacturing as straight shear webs and spar caps can be applied, and the fibre layup follows a straight primary orientation. It is recommended to investigate how much conventional manufacturing

approaches would need to be altered to accommodate swept blades. Does the introduction of blade sweep necessitate curved shear webs and spar caps, or can they be piecewise linear? Can the fibre layup approach be adjusted to follow the curved blade shape?

- An important factor for swept wind turbine blades is the increased torsional moment when compared to a straight reference blade. Does this imply that an increase in pitch motor size is required to withstand these loads?
- The aforementioned practical implications of blade sweep make it a challenging design choice. To establish whether or not swept blades have a business case, the aeroelastic design of such blades needs to be coupled with appropriate cost modelling. Such cost modelling could include advantages and disadvantages like the increased cost due to more complex manufacturing and transport, the increased lifetime and associated income due to less fatigue loading, and adjusted material choices due to different loading (more material to compensate torsional loads, less material because of reduced flapwise loads).

With improved numerical modelling, a large-scale proof-of-concept in the field, and integrated cost and load analyses, a clearer vision for swept blades as a realistic design choice can be established. Blade sweep's evident potential for aeroelastic blade tailoring makes it a relevant design path for state-of-the-art and future blades, which are extremely slender and flexible.

BIBLIOGRAPHY

- [1] G. A. M. van Kuik et al. “Long-term research challenges in wind energy – a research agenda by the European Academy of Wind Energy”. In: *Wind Energy Science* 1.1 (Feb. 2016), pp. 1–39. ISSN: 2366-7451. DOI: [10.5194/wes-1-1-2016](https://doi.org/10.5194/wes-1-1-2016).
- [2] P. Passon, M. Kühn, S. Butterfield, J. Jonkman, T. Camp, and T. J. Larsen. “OC3—Benchmark exercise of aero-elastic offshore wind turbine codes”. In: *Journal of Physics: Conference Series* 75 (July 2007), p. 012071. DOI: [10.1088/1742-6596/75/1/012071](https://doi.org/10.1088/1742-6596/75/1/012071).
- [3] J. Schepers et al. “Final results from the EU project AVATAR: Aerodynamic modelling of 10 MW wind turbines”. In: *Journal of Physics: Conference Series* 1037 (June 2018), p. 022013. ISSN: 1742-6588, 1742-6596. DOI: [10.1088/1742-6596/1037/2/022013](https://doi.org/10.1088/1742-6596/1037/2/022013).
- [4] R. Bergua et al. “OC6 project Phase III: validation of the aerodynamic loading on a wind turbine rotor undergoing large motion caused by a floating support structure”. In: *Wind Energy Science* 8.4 (Apr. 2023), pp. 465–485. ISSN: 2366-7443. DOI: [10.5194/wes-8-465-2023](https://doi.org/10.5194/wes-8-465-2023).
- [5] E. Fritz, K. Boorsma, and C. Ferreira. *Supporting data belonging to the publication Experimental analysis of a horizontal axis wind turbine with swept blades using PIV data*. Jan. 2024. DOI: [10.4121/C9631F69-8855-4E2D-8777-38338534B4EA](https://doi.org/10.4121/C9631F69-8855-4E2D-8777-38338534B4EA).
- [6] A. Langidis et al. “Design and evaluation of rotor blades for fluid structure interaction studies in wind tunnel conditions”. In: *Journal of Physics: Conference Series* 2265.2 (May 2022), p. 022079. ISSN: 1742-6588, 1742-6596. DOI: [10.1088/1742-6596/2265/2/022079](https://doi.org/10.1088/1742-6596/2265/2/022079).
- [7] S. Nietiedt, T. T. B. Wester, A. Langidis, L. Kröger, R. Rofallski, M. Göring, M. Kühn, G. Gülker, and T. Luhmann. “A Wind Tunnel Setup for Fluid-Structure Interaction Measurements Using Optical Methods”. In: *Sensors* 22.13 (July 2022), p. 5014. ISSN: 1424-8220. DOI: [10.3390/s22135014](https://doi.org/10.3390/s22135014).
- [8] C. Mertens, J. Sodja, A. Sciacchitano, and B. Van Oudheusden. “Experimental Aeroelastic Characterization of a Very Flexible Wing in Steady and Unsteady Inflow”. In: *AIAA SCITECH 2022 Forum*. San Diego, CA & Virtual: American Institute of Aeronautics and Astronautics, Jan. 2022. ISBN: 978-1-62410-631-6. DOI: [10.2514/6.2022-1344](https://doi.org/10.2514/6.2022-1344).

ACKNOWLEDGEMENTS

Throughout my journey as a PhD candidate, I have been extremely privileged to have had supportive people around me. This is particularly true for my supervisory team. **Koen**, you have always kept an eye on the details and were only satisfied when all questions were understood and answered. Your unbreakable good mood and laugh have made my PhD project all the more enjoyable. **Carlos**, you were always quick to grasp my scientific problems and guided me in tackling them. You recognised that plan A would not work, called for a plan B and, in that way, secured the smooth completion of my PhD research. **Roeland**, you made sure that the overall goal of my PhD trajectory always stayed in sight and put emphasis on me being in the driver's seat of my PhD. **Andreas**, you had no obligations towards me, and yet, you kept in close touch, always ready to support with technical knowledge and discussions. To all of you: Your efforts and guidance are greatly appreciated.

Being part of both the TNO and TU Delft worlds has given me the opportunity to interact with a large group of experts from both academic and applied research. There are many current and former TNO colleagues who have inspired me with their drive to innovate. I want to thank **Marc** and **Peter**, who thought of me as a potential PhD candidate when the TIADE project landed and **Erik**, **Rogier** and **Koen**, who gave me the freedom and time needed to finish up this dissertation. Thanks also to the TIADE colleagues with whom I have tackled pressure measurements, numeric model validation and tip designs during this challenging and inspiring project: **Carel**, **Feike**, **Johan**, **Kishore**, **Koen**, **Koen**, **Loris**, **Marco** and **Rogier**. To the aero team **Abhratej**, **Akshay**, **Edwin**, **Gerard**, **Iana**, **Kishore**, **Koen**, **Marco**, **Simone**: I love our technical discussions and I have learned a lot in these meetings over the last years. Finally, **Chen**, **Kishore**, **Koen**, **Marco**, **Nassir**, **Siddarth**, **Simone**, **Vadim**, it has been great fun to compete during futsal, padel and beach volleyball matches and to enjoy a well-deserved beer every once in a while. I am looking forward to returning from my little PhD island and working more closely with the fantastic group of experts making up the TNO Wind Energy group.

To my fellow PhD candidates at the wind group of TU Delft: I still don't know where the name **Team Cuisine** comes from. What I do know is that you are an incredibly friendly, open, smart and funny bunch of people. There is a good reason every guest researcher is sad when they have to leave again, and so am I at the end of my PhD. **Abhratej**, **Abhyuday**, **Adhyanth**, **Ali**, **Anand**, **André**, **Augustin**, **David**, **Deepali**, **Dylan**, **Felipe**, **Flavio**, **George**, **Guanqun**, **Haoyuan**, **Jatinder**, **Jelle**, **Jingna**, **Kiran**, **Likhitha**, **Livia**, **Matteo**, **Mehtab**, **Mihir**, **Oriol**, **Rention**, **Ricardo**, **Rishi**, **Seba**, **Shantanu**, **Shyam**, **Simone**, I want to thank you for all the great times in the office, over board games, in the swiss and rocky mountains, during sports, at the Karneval and while exploring the various cities that conferences brought us to. It has also been an immense pleasure to support and learn from each other during our growth as young researchers.



I also want to thank those in my life who, while not being related through work, have supported me during my PhD research by being the social net from which I draw a lot of my energy. More than anything else, the following words are my appreciation of your individual contributions to my fulfilled life:

Axel, Axel, Gregor, Marwin, Michael, Pierre, Riccardo, Simone, Stefan und Sven, ich hätte mir keinen besseren Freundeskreis während und seit dem Studium wünschen können. Wir teilen schon so viele gute und witzige Erinnerungen und jedes Mal, wenn wir uns sehen, kommen ein paar dazu. Und während ich hier an der Windenergie forsche, habt Ihr längst alle Gratisstrom und das ist auch gut so.

Akshay and Sylvia, I am really happy to have become such close friends with you over the last years. If everyone had people with your energy and enthusiasm in their life, the world would be a better place. There will always be a table-top-pizza-oven-pizza for you two at our place.

Max, uns verbinden Heidenheim, Puerto Rico, Hamburg, Aachen, Boulder, Alkmaar, Berlin und Delft, aber vor allem auch eine Vorliebe für Fußballspiele auf der Couch, Fast Food und flache Witze. Ich freu mich schon, diese Traditionen auch an Deinen und meinen nächsten Stationen fortzusetzen.

Luca, Du bist der Freund, der mich mit Abstand am besten kennt. Mit Dir in der Boulderhalle, am Billardtisch oder am Rhein die wichtigen (und weniger wichtigen) Themen des Lebens durchzuquatschen, ist immer der sicherste Weg, ehrliches Feedback zu kriegen und den eigenen Kopf zu sortieren.

Alex, Laura und Nele, mit Euch fühlt es sich immer an, als hätten wir uns erst vor zwei Wochen gesehen, selbst wenn es mal zwei Jahre sind. Meine Zeit mit Euch hat mich geprägt wie kaum eine andere und unsere Freundschaft verkörpert für mich bis heute das Gefühl von Freiheit und Freude aus Neuseeland.

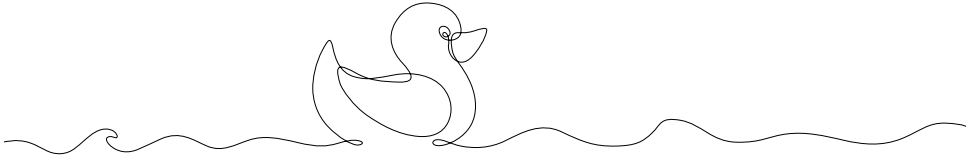
Arend, Els en Noek, vooral sinds ik naar Nederland ben verhuisd, hebben jullie me gesteund waar jullie maar konden. Tijdens spelletjes avonden in Hoofddorp en Almelo, wandelingen in Hoenderloo of beren spotten in Canada, met jullie kan ik altijd helemaal mezelf zijn. Zo'n tweede familie is echt goud waard.

Kathrin, Bettina und Petra, ich weiß, ich quäle Euch ein wenig mit der Vorbereitung, aber unser Gedichteln und die dazugehörenden Schlemmereien, Bettelrunden und Bier/Whiskey-Tastings bedeuten für mich immer Familienwohlfühloase und Erholung. Mindestens genauso wichtig finde ich die offene Art und Weise, mit der wir die schwierigen und schönen Themen bei Spaziergängen im Wald diskutieren können.

Benny, mit Dir habe ich eine Verbundenheit, wie sie eben nur mit dem Brudi besteht. Manch einer behauptet, wir seien einander zum Verwechseln ähnlich. Ich würde eher sagen, wir haben die perfekte Mischung aus so vielen Gemeinsamkeiten, dass wir bei Workouts, Knödelpackungstischtennispartien oder Discoschorlen immer Gaudi haben, aber auch jeweils so viel eigener Weg, dass es nie langweilig wird. Die Akribie und Beständigkeit, mit denen Du an Deinen immer neuen Zielen arbeitest, sind absolut faszinierend und treiben das Großer-Bruder-Ego dauernd an, die eigenen Ziele auch zu erreichen.

Regina und Richard, Ihr dürft euch einen sehr großen Anteil am Erreichen dieses Meilensteins zuschreiben. Ihr habt mich von früh an ermutigt, neugierig zu sein, meinen eigenen Weg zu gehen und aus jeder Situation das bestmögliche zu machen. Immer wieder habt Ihr mir Erfahrungen ermöglicht, von denen ich bis heute extrem profitiere. Ohne Eure bedingungslose Unterstützung wäre ich heute ganz sicher nicht, wer ich bin, nämlich ein glücklicher und zufriedener Mensch, dem eigentlich nie irgendetwas gefehlt hat. Mehr könnte ich mir nicht wünschen.

Evita, my best friend, my travel buddy, my partner in everyday silliness. This PhD would not have been possible without your unconditional support. You let me lean on you during the challenging times and were always ready to celebrate the joyful moments. You have absorbed so much of the word waterfalls that I need to release to clear my head that you should be given a master's degree in wind energy, at the least. Over the years, we have had our share of amazing adventures and I cannot wait to get going for our next one in South and Central America. I am sure it will just be one of many more to come. Thank you for being the most loving, caring and fun person I could ever wish to be with. I love you!



CURRICULUM VITÆ

Erik FRITZ

11.03.1993 Born in Heidelberg, Germany.

EDUCATION

2003–2012 Abitur
Beethoven Gymnasium, Bonn

2012–2017 Bachelor of Science in Mechanical Engineering
RWTH Aachen University

2014–2015 Erasmus semester
Queen's University Belfast

2017–2019 Master of Science in Energy Engineering
RWTH Aachen University

EXPERIENCE

2019–present Scientist Innovator
TNO Wind Energy



LIST OF PUBLICATIONS

JOURNAL AND CONFERENCE PAPERS

8. **E. Fritz**, K. Boorsma, A. Herrig, *Design of an aeroelastically tailored wind turbine blade tip for field experiments*, *Renewable Energy* (2022), under review.
7. **E. Fritz**, K. Boorsma, M. Caboni, A. Herrig, *Blade surface pressure measurements in the field and their usage for aerodynamic model validation*, *Wind Energy* (2024).
6. **E. Fritz**, C. Kelley, K. Brown, *On optimizing the sensor spacing for pressure measurements on wind turbine airfoils*, *Wind Energy Science* **9**, 8 (2024).
5. **E. Fritz**, K. Boorsma, C. Ferreira, *Experimental analysis of a horizontal-axis wind turbine with swept blades using PIV data*, *Wind Energy Science* **9**, 8 (2024).
4. **E. Fritz**, K. Boorsma, C. Ferreira, *Validation of a BEM correction model for swept blades using wind tunnel experimental data*, *Journal of Physics: Conference Series* **2767**, 022035 (2024).
3. **E. Fritz**, A. Ribeiro, K. Boorsma, C. Ferreira, *Aerodynamic characterisation of a thrust-scaled IEA 15 MW wind turbine model: experimental insights using PIV data*, *Wind Energy Science* **9**, 5 (2024).
2. **E. Fritz**, C. Ferreira, K. Boorsma, *An efficient blade sweep correction model for blade element momentum theory*, *Wind Energy* **25**, 12 (2022).
1. F. Thönnißen, **E. Fritz**, W. Schröder, *Acceleration of vortex-particle simulations using a pseudo-particle method*, *Journal of Physics: Conference Series* **1618**, 052006 (2020).

DATASETS

5. **E. Fritz**, *Documentation of a model horizontal-axis wind turbine used for wind tunnel experiments at TU Delft*, *4TU.ResearchData* (2024).
4. **E. Fritz**, C. Kelley, K. Brown, *Supporting data belonging to the publication On optimizing the sensor spacing for pressure measurements on wind turbine airfoils*, *4TU.ResearchData* (2024).
3. **E. Fritz**, K. Boorsma, C. Ferreira, *Supporting data belonging to the publication Experimental analysis of a horizontal axis wind turbine with swept blades using PIV data*, *4TU.ResearchData* (2024).
2. **E. Fritz**, A. Ribeiro, K. Boorsma, C. Ferreira, *Supporting data belonging to the publication Aerodynamic characterisation of a thrust-scaled IEA 15 MW wind turbine model: experimental insights using PIV data*, *4TU.ResearchData* (2024).
1. **E. Fritz**, C. Ferreira, K. Boorsma, *Supporting data belonging to the publication An efficient blade sweep correction model for blade element momentum theory*, *4TU.ResearchData* (2022).



